THE HONG KONG
POLYTECHNIC UNIVERSITY
香港理工大學
Pao Yue-kong Library
包玉剛圖書館

Copyright Undertaking

This thesis is protected by copyright, with all rights reserved.

By reading and using the thesis, the reader understands and agrees to the following terms:

1. The reader will abide by the rules and legal ordinances governing copyright regarding the use of the thesis.
2. The reader will use the thesis for the purpose of research or private study only and not for distribution or further reproduction or any other purpose.
3. The reader agrees to indemnify and hold the University harmless from and against any loss, damage, cost, liability or expenses arising from copyright infringement or unauthorized usage.

If you have reasons to believe that any materials in this thesis are deemed not suitable to be distributed in this form, or a copyright owner having difficulty with the material being included in our database, please contact lbsys@polyu.edu.hk providing details. The Library will look into your claim and consider taking remedial action upon receipt of the written requests.

Pao Yue-kong Library, The Hong Kong Polytechnic University, Hung Hom, Kowloon, Hong Kong

http://www.lib.polyu.edu.hk

This thesis in electronic version is provided to the Library by the author. In the case where its contents is different from the printed version, the printed version shall prevail.

THE HONG KONG POLYTECHNIC UNIVERSITY

DEPARTMENT OF INDUSTRIAL AND SYSTEMS ENGINEERING

Grinding-Aided Electrochemical Discharge Machining Of Metal Matrix Composites

LIU Jiang Wen

A thesis submitted in partial fulfilment of the requirements for the

Degree of Doctor of Philosophy

December 2009

CERTIFICATE OF ORIGINALITY

I hereby declare that this thesis is my own work and that, to the best of my knowledge and belief, it reproduces no material previously published or written, nor material that has been accepted for the award of any other degree or diploma, except where due acknowledgement has been made in the text.

______________________ (Signature)

LIU Jiang Wen (Name of candidate)

ABSTRACT

Among the many non-conventional machining methods, electrical discharge machining (EDM), wire-EDM, and electrochemical machining (ECM), are perhaps, the most promising processes for shaping metal matrix composites (MMCs). Notwithstanding the merit of these machining methods, there are still problems which need to be solved and improvements to be made before they can be effectively utilised for shaping MMCs. The main problems encountered are low material removal rate (MRR), high risk of tool breakage and the presence of various forms of defects on the machined surface.

In this research project, a new type of grinding-aided electrochemical discharge machining (G-ECDM) hybrid process has been developed, and a corresponding machining system has been designed and built. The tool-electrode has a composite coating containing a hard reinforcement phase of diamond particles, which can take various forms to suit different shape and profile requirements of the product. This process is capable of overcoming the problems encountered in machining MMCs. It is different from both the conventional electrochemical discharge grinding process, and the abrasive electrochemical grinding process. Unlike these two processes, the G-ECDM process functions under a combined action of electrochemical effects, electrical discharge erosion, and direct mechanical grinding.

The material removal mechanism of the G-ECDM process in machining particulate reinforced aluminium alloy composites has been analysed both theoretically and experimentally. The first phase of the study involved the modelling, and verification by experiment, of the relation between electrochemical effects and spark discharge initiation, with an emphasis on the prediction of the critical breakdown voltage of hydrogen bubbles. A model to reveal the electrical field acting on a hydrogen bubble in ECDM process has been established. This model was found capable of predicting the position of the maximum field strength on the bubble surface as well as the critical breakdown voltage for spark initiation. A set of experiments was performed to verify the model and the experimental results agreed well with the predicted values. The experimental results also showed that an increase in current, duty cycle, pulse duration or electrolyte concentration would promote the occurrence of arcing action in ECDM. In the second phase of the research, the effect of the grinding action of the G-ECDM process on MRR was examined. When grinding was incorporated with the ECDM process, both the MRR and the molten material throw-out coefficient increased significantly. Moreover, an examination of the machined surface quality of the MMC workpiece showed that the G-ECDM process produced much better surface finish with less defects than the ECDM process.

To further study the G-ECDM mechanism, a series of single pulse studies have been conducted. The results showed that for the G-ECDM process, the grinding action would remove the crater's built-up edge. As a consequence, the MRR of G-ECDM was higher than that of ECDM and EDM. Although, the discharge waveform of the G-ECDM process resembles a form of abnormal arcing, the machining process was found to be stable. This is attributed to the rotational motion of the tool-electrode in constantly shifting the arcing position. The differences in the distribution of craters on the machined surface for the ECDM and G-ECDM processes can be satisfactorily explained by analysing the electrical field strength.

By examining tool performance, it was found that machining chips clogged to the tool-electrode, produced by the grinding action could be removed by EDM sparks. The EDM spark thus serves the role of cleaning the tool and as a result, preventing short circuiting from occurring. Moreover, EDM sparks that occurred between the clogged material and the workpiece did not cause any noticeable damage at the interface between the diamond grit and the binding material of the tool-electrode. Therefore, the clogged material provides protection to the tool and as a consequence, a longer tool life is expected from the G-ECDM process.

ACKNOWLEDGEMENTS

I take this opportunity to express my heartfelt gratitude towards my Chief Supervisor Professor T.M. Yue whose tireless inspiration and help guided me to overcome the difficulties in my PhD study and in my life. I also express my sincere appreciation to Professor Z.N. Guo, my Co-supervisor, for his encouragement and the valuable suggestions he gave to me during the project.

My sincere thanks are due to Mr B.H. Mo, Mr G.Y. Liu, Mr Z.Y. Wan and Mr W.C. Gu of the Guang Dong University of Technology and Mr S.Y. Lau of the Materials Laboratory of PolyU for their assistance provided to me in the design and fabrication of the experimental equipment and preparation of test specimens. My thanks also go to Mr Jeremy Yeung of the Materials Research Centre for his expert guidance in electron microscopy analysis.

Many friends in the Department of Industrial and Systems Engineering have helped me throughout the period of my PhD study. Special thanks are owed to Dr Z.G. Huang, Dr Y.Z. Wu and Dr C.P. Chan for their valuable comments.

The financial support from the Hong Kong Polytechnic University for the provision of the research studentship is also greatly acknowledged.

Finally, special thanks go to my family. It is their endless love and support that gave me the courage to complete my PhD study.

TABLE OF CONTENT

LIST OF FIGURES

LIST OF TABLES

NOMENCLATURE

R	external resistor
R^*	resistance between the tool and the workpiece
$R1$	resistance of the anode
$R2$	resistance of the electrolyte
$R3$	resistance of the cathode
$C1$	double layer capacitor of the anode
$C2$	double layer capacitor of the cathode
L	gap size between the anode and the cathode
S	surface area of the exposed electrode
ρ	resistivity of the electrolyte
ϕ_a	applied voltage
φ_2	breakdown voltage
φ	arc maintaining voltage
t_{on}	pulse-on-time
φ_c	voltage of the capacitance
φ_s	steady state voltage of the capacitance
τ	time constant
E_x	external electric field outside the bubble
φ_a	electric potential across the bubble of a length a
ε_0	dielectric constant of the electrolyte

ε	dielectric constant of the hydrogen bubble
c	special heat capacity
$u(t)$	voltage between the electrodes
$i(t)$	current
t_k	pulse duration.
J	current density
σ	conductivity of the electrolyte
σ_0	initial electrolyte electrical conductivity
ξ	temperature impact index
$T(x)$	processing temperature of the processing area
β	*void fraction*
n	void fraction impact index
$v(t)$	feed velocity
l	feed depth
ω	dissolved metal volume per unit quantity
η_a	energy partition fraction of anode
η_b	energy partition fraction exhausted in the spark channel
η_c	energy partition fraction of cathode
ρ	density of the material
λ	thermal conductivity
T	temperature
t	time
$\dot{Q}$	internal heat source

h_c	coefficient of heat convection
R_e	Reynolds number
P_r	Prandtl number
Ω	flow velocity
μ	viscosity
η_f	molten material throw-out coefficient

CHAPTER 1

INTRODUCTION

1.1 Background of Research

Metal matrix composites (MMCs) are having a significant effect in the aerospace [1, 2], electronic [3, 4] and automobile industries [5]. This is primarily due to their high specific strength and stiffness, good elevated temperature properties and excellent wear resistance [1-5]. Indeed, both the physical and mechanical properties of MMCs are in many respects superior to those of their monolithic counterparts. However, the unique properties that make these materials appealing could also become hurdles when shaping them. Thus, the successful implementation of these novel materials is still largely dependent on how cost-effectively a component can be fabricated and transformed to the required final shape. It is accepted that MMCs are in general, much more difficult to machine than their monolithic counterparts, whether or not conventional or unconventional techniques are used [13, 14]. This causes no surprise, since most of the reinforcement phases are hard ceramic materials, and because of this, cubic boron nitride (CBN) and polycrystalline diamond (PCD) tools are often required. Apart from the extreme hardness of most of the reinforcement phases, the vast differences in physical, chemical and mechanical properties between the metal matrix and the reinforcement phase have positioned MMCs as a group of notoriously difficult-to-machine materials.

Using non-traditional machining techniques, such as laser [15] and water jet [16] machining, though being able to achieve a fairly high material removal rate, would often be accompanied by some serious surface and subsurface defects which in many cases are unacceptable to a final finish product and this could undermine the fatigue strength of the final product. Moreover, these two machining methods are not really ideal for 3-D shaping purposes. Among the many non-conventional machining methods, electrical discharge machining (EDM), wire-EDM, and electrochemical machining (ECM), are perhaps, the most promising processes for shaping MMCs [52-86] when surface roughness and flexibility on shaping geometry are considered. Notwithstanding the merits of these two kinds of machining methods for shaping MMCs, there are still problems which need to be solved and improvements to be made before they can be effectively utilised. The main problems encountered in EDM of MMCs are low machining rate, high risk of tool breakage [62] and the presence of various forms of defects on the machined surface. These problems are mainly caused by the non-conducting nature of the ceramic reinforcement phase and often the segregation of the ceramic phase. The problems intensify as the extent of the ceramic phase increases. Although, using the electrochemical discharge machining process (ECDM), the material removal rate can be increased [69, 77, 78] over that of EDM, the problems of close dimensional tolerance and poor surface finish still cannot be easily overcome. Recognising these problems, it is apparent that the EDM, ECM or the ECDM process must be further improved in order to meet the challenge facing the shaping of advanced composite materials.

1.2 Research Objectives

The main objective of this project is to develop a new type of ECDM process, which incorporates a mechanical grinding element that can overcome most of the problems encountered in machining MMCs: low material removal rate, and poor surface integrity. The proposed process is termed Grinding-aided Electrochemical Discharge Machining process (G-ECDM). One of the important features of this process is that the tool-electrode comprises a coating of diamond particle reinforced metal composite, instead of the normal graphite or copper electrode used for EDM. Moreover, the tool-electrode can take various forms to suit different shape and profile requirements of the product. The proposed process is different from the conventional electrochemical discharge grinding (ECDG) process [84]. The latter, though, is also a kind of combination of electrochemical and electrical-discharge material removal process, the so-called grinding wheel of the electrode is normally made of bonded fine graphite particles without any abrasive particles involved. Moreover, like any EDM process, the workpiece and the wheel of the ECDG process do not come into contact. The G-ECDM process, unlike the conventional ECDG process, functions under a combined action of electrochemical effects (ECE), electrical discharge erosion (EDE), and direct mechanical grinding (DMG). The process is also different from the electrochemical grinding (ECG) process [83] which only involves electrochemical action and grinding without the EDM action. Also, the ECG process removes the bulk material primarily by the electrolytic action and less than a few percent of the material removed by the abrasive action of the wheel.

With the G-ECDG process, it is envisaged that the hard reinforcement phase could be removed more readily under the combined action of ECE, SE and MG. As a result, high machining efficiency can be obtained. Moreover, surface/subsurface defects could be eliminated, and a good surface finish can be attained. Nevertheless, before the full benefit of the G-ECDM process can be realised, an understanding of the machining mechanism must be achieved. Before a full investigation on G-ECDM is conducted, it is necessary to have a good understanding on ECDM of MMCs since there is still no theoretical model found in the literature concerning the machining mechanism of ECDM of MMCs. Despite the fact that, much interest has been generated in applying ECDM on non-conductive and composite materials [79, 91], the research undertaken thus far has mainly focused on experimental aspects. Bearing this in mind, the first phase of the research focuses on the modelling of the ECDM mechanism of particulate composites with experimental verification; while the second phase will be on the G-ECDM process. The following summarises the main objectives of this research:

(i) to analyse and model the machining mechanism of ECDM of MMCs;

(ii) to understand and establish the machining mechanisms of shaping metal matrix composites under the combined action of electrochemical effects, electrical discharge erosion, and mechanical grinding;

(iii) to design and arrive at a G-ECDM process that utilise the combined action to shape MMCs with high machining efficiency, good surface finish and long tool life.

The scope of the research work and its outcomes are presented according to the structure of the thesis given below.

1.3 Structure of the Thesis

Chapter 1 identifies the key issues and problems being addressed with regard to the machining of MMCs and states the purpose of the proposed research and the concept of the G-ECDM process, together with the possible outcome of this research project.

Chapter 2 gives a comprehensive literature review which summarises the relevant and up-to-date research work in the field of machining MMCs. Since different machining methods have their own advantages and limitations, particular attention is paid to reviewing the merits and limitations of both traditional and non-traditional machining processes regarding the shaping of MMCs.

Chapter 3 presents the principle and approach of the development of the G-ECDM process. Moreover, the design concept of the equipment and the electrode tool is given in detail.

Chapter 4 presents the modelling and experimental verification of the relation between the electrochemical effect and electrical discharge initiation, with an emphasis on the prediction of the critical breakdown voltage of hydrogen bubbles in ECDM particulate reinforced MMCs. It also reports the relative importance of the various cutting parameters on material removal rate.

Chapter 5 studies, both theoretically and experimentally, the machining mechanism of the G-ECDM process with the emphasis placed on material removal rate.

Chapter 6 further studies the G-ECDM mechanism, in which, the discharge waveform and the distribution of craters have been studied for the ECDM and G-ECDM processes.

Chapter 7 studies the basis for the long tool life of the G-ECDM process. In which, the polarity effect and the grinding effect have been both theoretically and experimentally analysed.

The conclusions of this research are presented in Chapter 8; while suggestions for future work are given in Chapter 9.

CHAPTER 2

LITERATURE REVIEW

Despite advancements made in manufacturing technology of metal matrix composites (MMCs), such as in powder metallurgy [6, 7, 11], co-spraying [8], low pressure liquid infiltration [9] and squeeze casting [10, 12], the need for post-forming or post-casting machining of MMC components seems to be inevitable. Thus, the manufacturability of MMC components or products depends, among other things, on the ease with which these materials can be machined into the required form and shape. Machining of MMCs using various conventional means have been studied in some detail [17-44], and most studies have shown limitations such as high tool wear rates [17-36, 44], poor finish surface quality, formation of sub-surface defects [35-38], etc. Although, non-conventional methods, such as abrasive water jet machining and laser machining, seem to be able to solve some of the aforementioned problems, such as rapid tool wear and low machining rates, these alternative methods have their own problems. For instance, the non-contact nature and the extreme high energy intensity of laser beams precludes the problem of tool wear, but the intensity of the heat often produces unacceptable microstructural changes and causes undesirable thermal cracking [51-53]. As for the water jet method, the issues of poor dimensional control and limitations on shape profile are not easily overcome [53]. The following review highlights the major research work conducted in the field of machining MMCs using both conventional and non-conventional methods. The review mainly focuses on two important types of MMC materials, SiC and Al_2O_3

particles reinforced Al-alloy composites, which have high commercial potential for applications in the aerospace, automobile and sports industries. These two types of composites form the target materials of the present research study.

2.1 Conventional Machining of MMCs

2.1.1 Tool wear

Conventional machining can be defined as a process using mechanical (motion) energy, which usually involves changing the shape of a workpiece using an implement made of a harder material. In using conventional machining methods to shape MMCs, a serious problem – rapid tool wear – is often encountered. To employ common cutting-tool materials, such as high-speed steels, carbides, cubic boron nitride (CBN) and ceramics to machine MMCs, the serious problem of short tool life [17, 26, 27] is often encountered. Although for certain kinds of MMCs, the problem of short tool life could be lessened by using polycrystalline diamond (PCD) [20-25], the cost of machining is inevitably increased [18]. Fig. 2.1 shows the wear properties of a range of carbides, ceramics, high speed steels (HSS) and PCD tool materials for the machining of a SiC reinforced Al-Si based composite [27]. SiC is harder than HSS, and most carbide and ceramic tools, so that in the cutting process of SiC particle reinforced composites it will micro-cut these tools and result in a rapid tool wear. Although diamond and CBN have a much higher hardness than SiC, serious abrasive wear does not take place rapidly on these tools, however, due to the brittle nature of these two materials, they are vulnerable to breakage, especially under the pounding action of the SiC particles [27]. These results also reveal that though the

PCD tool has outperformed the rest of the materials, tool wear remains as a problem that cannot be neglected (Fig. 2.2). Perhaps it is worth noting that PCD tools are not suitable for machining ferrous material due to the chemical reaction between iron and carbon. The results obtained so far on the study of machining MMCs show that, disregarding the types of tool material, tool geometry and cutting parameters, the volume of the reinforcement phase and its size are the two main factors affecting tool life [31-36]. The higher the volume fraction and/or the coarser the size of the reinforcement phase, the more severe is the wear of the tool, and consequently, the shorter is the tool life [27].

In research for improving the wear resistance of cutting-tools in machining MMCs, a great deal of effort has been given to explore the use of various coating technologies, including CVD and PVD [28, 29, 34]. Various kinds of surface coatings have been applied to carbide tools with an aim of improving their wear resistance performance [28, 29]. Unfortunately, most of these studies show that surface coatings do not appear to be effective means for improving wear resistance. A study on the machining of an Al-alloy reinforced with Al_2O_3 particles using tungsten carbide showed that the carbide inserts, both coated and uncoated, have a very short tool life in comparison with PCD tools [17]. In this case, the brittle transitional structure at the interface between the tool and the coating acts as a source of weakness, which causes spalling and cracking of the entire coating, and as a result, the tool loses the protection of the coating after a very short machining period. Other studies attempted to employ diamond or diamond-like coatings [17-19] to improve wear resistance of the cutting tools. Both thin and thick diamond CVD coatings have been considered; the former is found to be suitable for complex-shape tools, however, due to the coating adhesion problems, tool life was shorter than that of PCD tools [17]. On the other hand, a thick diamond CVD coating tool is considered to be a competitor to PCD, but the fabrication process is not considered to be straight forward and it is not suitable for complex tool geometries [18].

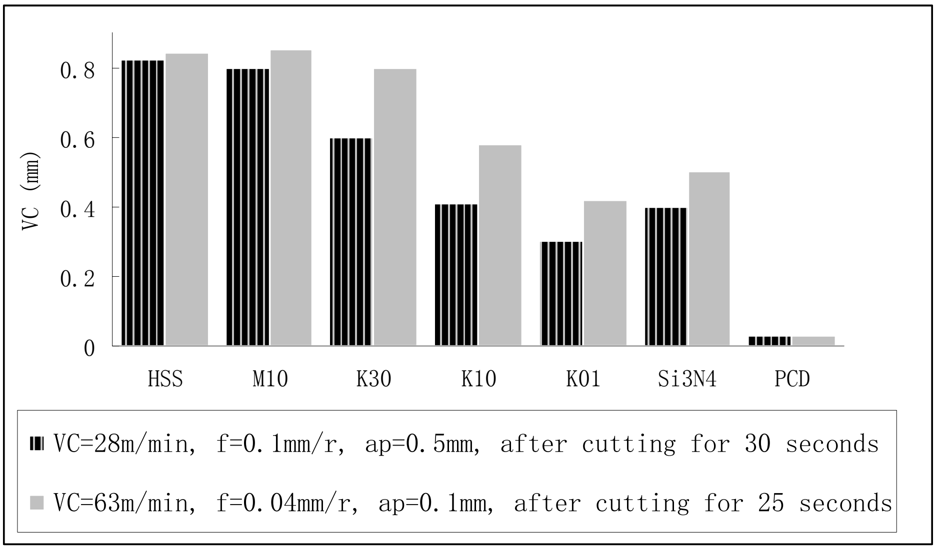

Fig. 2.1 Maximum wear and worn radius of some tools for the cutting of an Al-356/SiC composite [27]

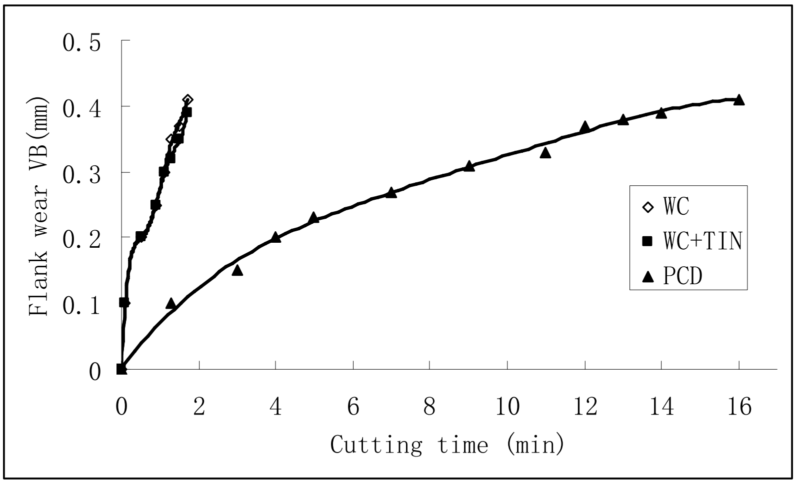

Fig. 2.2 Tool wear vs cutting time in milling of Al alloy +20% Al_2O_3 [17]

2.1.2 Surface integrity

In the machining of MMCs, surface and subsurface defects are often produced. They can appear in the form of voids, micro-cracks, fractured or crushed particles and pulled-out particles (Fig. 2.3). Fig 2.4 shows the subsurface damage in a SiC reinforced Al-alloy composite machined using PCD, which is in the form of microcracks. In fact, there are many factors that can influence the surface integrity of the MMCs, such as tool materials, cutting parameters [35, 38], tool geometry [37] and particle volume and size [41]. It is found that better surface integrity can be obtained by increasing the cutting speed and feed rate and decreasing the nose radius of the PCD tool. The tool with 0° rake angle is better than the tool with 5° rake angle or -5° rake angle for surface integrity [37]. In spite of the impressive knowledge gained on the wear mechanism in the machining of MMCs, the problem of surface damage needs to be resolved. The problem largely arises from the dislodging of the hard and abrasive reinforcement phase from the soft matrix which is smeared over the surface. This process not only will cause damage to the MMCs, but will also lead to rapid tool wear as a result of three-body abrasion. Fig. 2.5 shows a micrograph of the flank wear surface of a tungsten carbide tool in the machining of an aluminium alloy-silicon carbide metal matrix composite. The presence of scratch patches indicates the incidence of the three-body abrasion process [30].

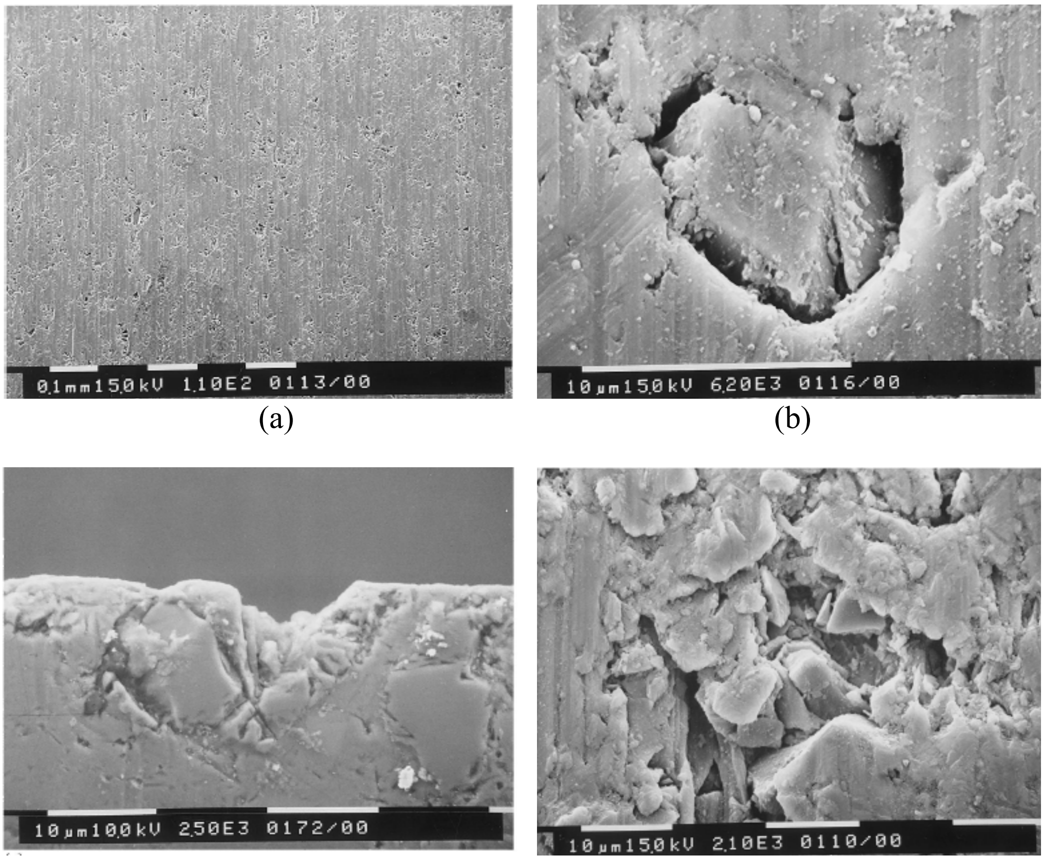

(a) (b)

(c) (d)

Fig. 2.3 Scanning Electron Microscope (SEM) images of a machined surface using PCD (a) typical topography; (b) voids around SiC particles; (c) pulled-out SiC particles; and (d) fractured/crushed SiC particles [37]

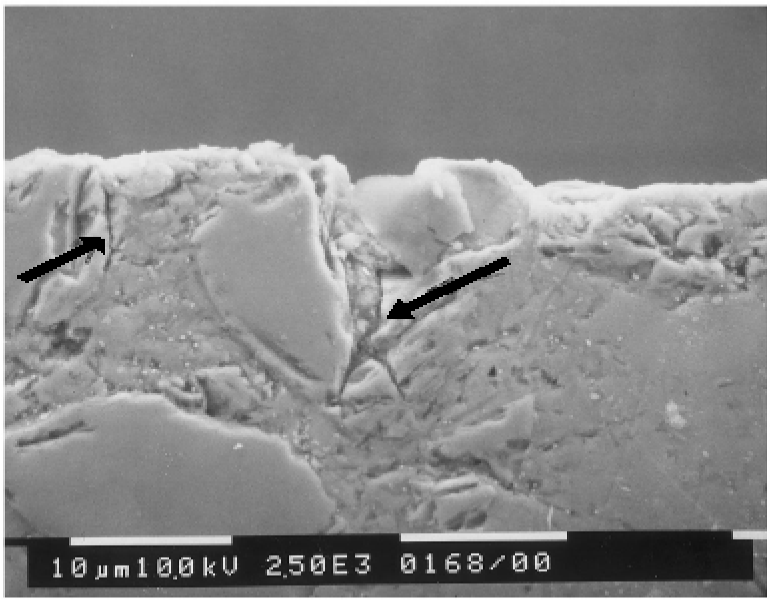

Fig. 2.4 SEM micrograph showing microcracks had developed underneath the machined surface [37]

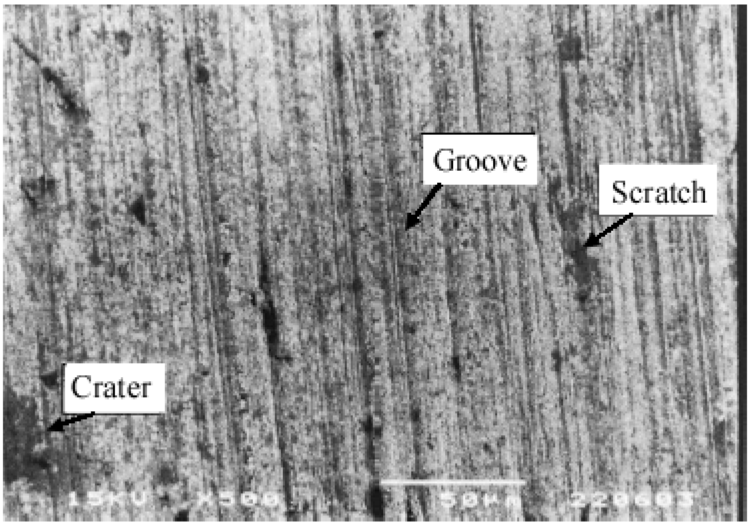

Fig. 2.5 SEM micrograph of the worn cutting tool surface [30]

2.1.3 Grinding of MMCs

Though the volume of research studying the grinding of MMCs [45-50] is much less than for turning, drilling and milling, etc, its value is of significance because normally a good surface finish with less damage can be obtained using grinding. Typical surface roughness (*Ra*) measured for rough-ground MMCs ranges between 0.15–0.70μm, and for the fine-ground condition, the roughness can be down to the range of 0.20–0.35μm [49]. Fig. 2.6 and Fig. 2.7 respectively show a ground surface and a section of it for an Al/Al_2O_3 composite material. Virtually no defects can be found at the ground surface (Fig. 2.6), nor any sub-surface damage (Fig. 2.7) [49].

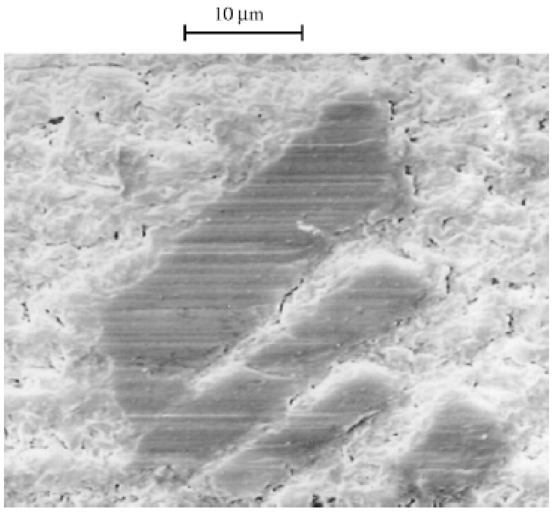

Fig. 2.6 SEM micrograph showing a grinded MMC surface (2618/Al_2O_3/20p) [49]

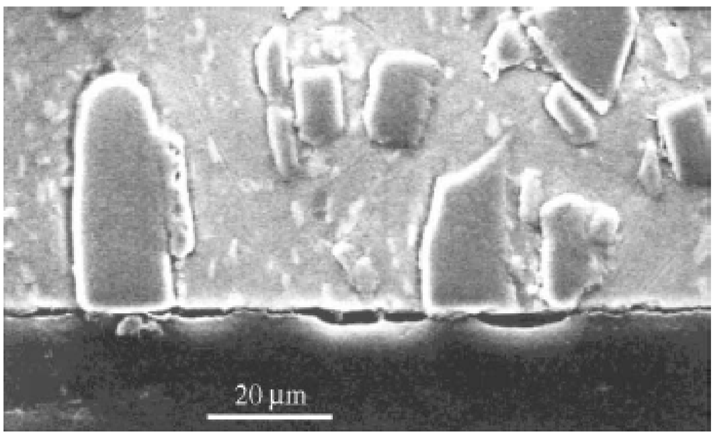

Fig. 2.7 Sub-surface of a grinded MMC (2618/Al_2O_3/20p) [49]

Despite the excellent surface quality that can be obtained by grinding, it is not really a highly versatile process for shaping complex profiles. Moreover, the material removal rate of the process is relatively low. In addition, wheel clogging is a serious problem when grinding dual phase materials in which one constituent is a soft material. It has been found that [50] the decrease in cutting ability of the grinding wheels is mainly caused by clogging of the active surface due to chip adhesion rather than by flattening of the grit caused by the abrasion of the hard reinforced particles. Very often clogging occurs before serious wear of the grit. This means that the ductile matrix is the main factor that mostly influences the grindability of MMCs, rather than the hard reinforced particles. Among the various types of grinding wheels employed for the shaping of MMCs, Al_2O_3 and SiC wheels were found to have better performance, in terms of low clogging, low grinding forces and better surface finish [50], than those of the super-abrasive types, such as CBN wheels and diamond wheels.

The potential of using SiC wheels is high, at least for rough grinding of MMCs, because SiC grains are much less expensive than diamond grains and are harder than Al_2O_3 particles. Therefore, rough grinding with a SiC wheel followed by fine grinding with a fine-grit diamond wheel has been recommended for the grinding of MMCs.

It is clear from the above review that rapid tool wear and surface damage cannot be easily disposed of if conventional machining methods are to be used. Although grinding is a promising process for giving a good surface finish, its machining efficiency is considered to be relatively low. To overcome the main problem of rapid tool wear in machining MMCs, various non-conventional machining methods have been explored.

2.2 Non-Conventional Machining of MMCs

2.2.1 Laser machining of MMCs

Laser machining is based on the interaction of the work material with an intense, highly directional coherent monochromatic beam of light, from which material is removed predominantly by melting and/or vaporization. Laser machining has been employed in cutting and drilling of MMCs [15]. Laser offers significant productivity advantages for rough cut-off applications, and since it is a "non-contact" process, the problem of tool wear does not really exist. It is apparent that lasers are of great use for high feed rates (up to $v = 3000$ mm/min) in connection with a narrow kerf width ($wk \leq 0.4$ mm) [52]. In fact, the ceramic particle reinforcement improves the ability of the laser to cut the composite, due to the reduction in the optical reflectivity of the material. However, the quality of laser machined surfaces is normally so poor that further surface finishing procedures are required. Undesirable features such as striation patterns on the cut surface and burrs at the laser exit surface (dross attachment) are commonly produced [51-53]. Moreover, significant thermally induced micro-structural changes within the composite material often occur. For example, in the case of Al/SiC composites, excessive heating will lead to the formation of a large quantity of the plate-like aluminium carbide phase (Al_4C_3) [54, 55] which would undermine the mechanical properties as well as the corrosion resistance of the material. It has been found that laser machining induces more severe thermal damage in the processed material compared to the EDM process [53]. Apart from the problem of poor machined surface quality, laser machining is not particularly suitable for shaping complex profiles.

2.2.2 Abrasive water jet machining of MMCs

Machining MMCs with an abrasive water jet (AWJ) has many advantages compared to other machining technologies. In comparison to thermal machining processes (EDM, laser), AWJ does not induce high temperatures and as a consequence there is no thermally affected zone, and no burr attachment is observed. Furthermore, AWJ can be considered to be a very efficient machining process since high feed rates are possible. However, the machined surface is relatively rough and slotted-edge damage is often produced (Fig. 2.8). The kerf width is usually larger than that obtained when using laser processing. Moreover a tapered kerf width is normally obtained, i.e. the bottom of the machined surface is less than that at the top [53]. Similar to the case of laser machining, the AWJ process is not suitable for 3D machining.

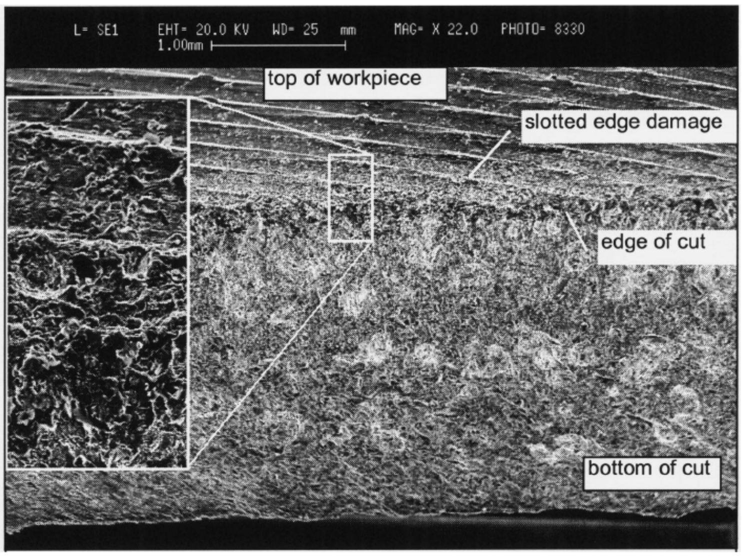

Fig. 2.8 Slotted edge damage after AWJ machining a particle reinforced MMC [53]

2.2.3 Electrical discharge machining of MMCs

Electrical discharge machining (EDM) using die sinking and wire-electrical discharge machining (W-EDM), which are capable of obtaining net shape manufacturing for intricate shapes, have been shown to be promising candidates for shaping MMCs [56, 57]. The advantage of this method is that it can avoid rapid tool wear in the course of processing. The relative tool wear when machining particle reinforced MMCs can be as low as 0.02% and the lateral spark gap can vary between 0.01 mm and 0.2 mm [58, 59]. Therefore EDM can be used to shape MMCs with a good dimensional accuracy; it is considered to be a viable machining process for composite materials in applications where close dimensional control is required. A great deal of work has been conducted in examining the effect of EDM processing parameters on material removal rate (MRR), electrode wear rate (EWR) and surface roughness [56-67] in machining MMCs. In general, these studies have found that using a high current and a long pulse-on time would increase MRR, but this would cause adverse effects on dimensional accuracy, surface roughness and EWR [61, 66].

In order to improve machining efficiency and to reduce surface roughness in the EDM of MMCs, various electrode designs have been proposed. Among these, a rotary eccentric electrode for hole drilling has been developed (Fig. 2.9). Experimental results confirm that EDM blind-hole drilling with an eccentric through-hole electrode can accelerate the debris discharge during machining so that it has a higher MRR. However, no apparent improvement in surface roughness was obtained when compared to the case where a solid electrode was used. Nonetheless, it is still a viable technique for blind-hole drilling of MMCs, despite the electrode wear rate being higher than that of EDM with a solid electrode [64]. A study of using a rotary EDM with a hollow tube electrode to drill a SiCp/6025 composite was conducted by Mohan et al [61]. The results confirm that, with injection flushing, a high material removal rate was obtained when using a rotary tube electrode. He also studied the effects of current, pulse duration and the electrode rotation speed on MRR, EWR and surface roughness. The results of the study showed that MRR increased with an increase of current and a decrease in pulse duration. A better surface finish can also be obtained if the electrode rotational speed was increased [61].

Another interesting design employs a rotary hollow-tube electrode with a ZrO_2 ball attached above the electrode (Fig. 2.10). The function of the ball is to provide an additional burnishing effect, which has been proven to be an effective technique for improving surface roughness in the machining of MMCs [65]. With the aid of the grinding effect of the ZrO_2 ball, the surface roughness (*Ra*) can be reduced to a level of a couple of microns.

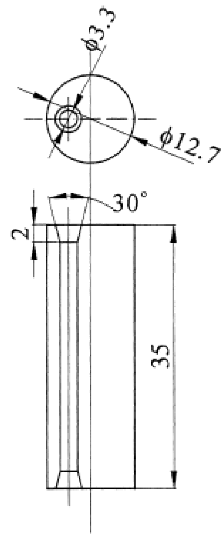

Fig. 2.9 Schematic diagram of the rotary electrode for EDM blind-hole drilling [64]

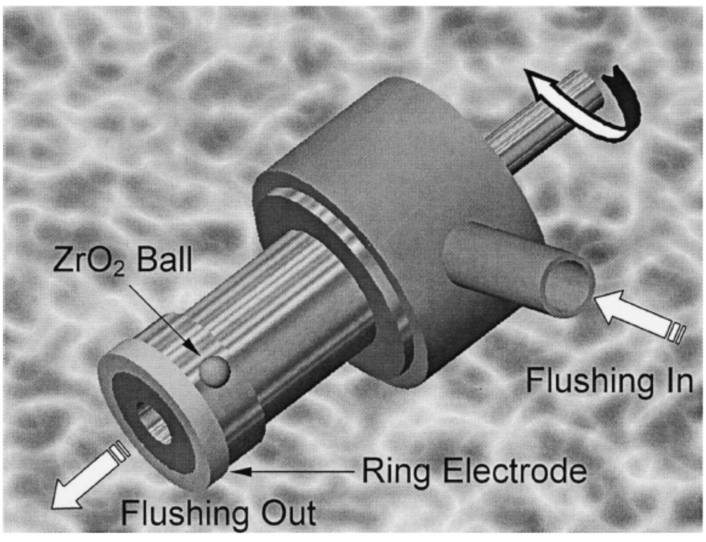

Fig. 2.10 Rotary hollow-tube electrode with a ZrO_2 grinding ball [65]

Apart from the concerns on MRR and surface roughness, the problems of high tool breakage risk, abnormal arcing and the presence of various forms of undesired surface defects need to be addressed [61]. These problems arise mainly due to the fact that the ceramic reinforcement phases are normally electrical insulators, and many of their physical properties such as melting and vaporisation points are usually a few times higher than that of the matrix material. In the EDM of particle reinforced metals, the ceramic particles do not melt during the machining process. The removal of the particles occurs through melting and vaporizing of the matrix material around the ceramic particle up to a point that the entire particle becomes detached. In fact, in the machining process, the ceramic particles can shield the matrix material, and because of this the removal rate decreases with increase of particle content [60]. The material removal rate and the cutting speed can be reduced by as much as 40% as compared to the unreinforced material [61, 62].

The exposure of ceramic particles at the surface during EDM often results in a tendency for arcing to occur. Besides, a conductive path between the electrodes is formed under the condition of inadequate flushing where the metal droplets and the detached ceramic particles are trapped within the spark gap. Under such a condition, abnormal arcing would occur [61]. Arcing will produce large discharge craters on the surface of the tool wire (Fig. 2.11), and this could cause premature breaking of the wire. Previous studies have shown that larger craters would form as the percentage of the reinforced particle is increased.

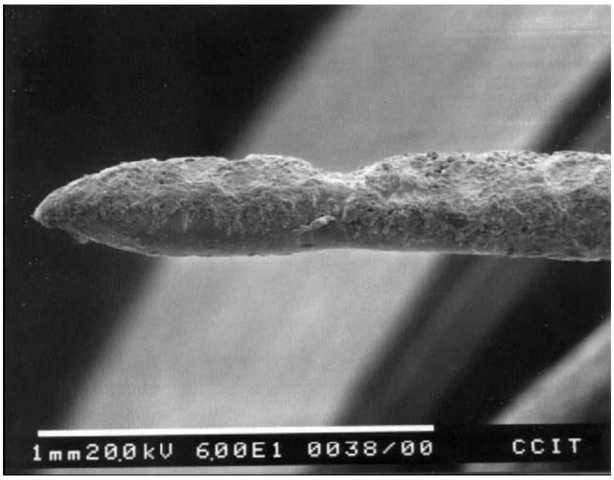

Fig. 2.11 SEM micrograph of the surface of a wire electrode after machining an Al-20%Al_2O_3 composite material [62]

Banding is another surface defect that often occurs in the EDM of MMCs. The problem arises when the advancing of the wire along its feed path is impeded by the protruding reinforced particles within the discharge gap. This causes the wire to shift and as a result, banding is formed. An example of this is during the machining of an Al_2O_3 particle reinforced Al-alloy 6061, and is shown in Fig. 2.12 [62].

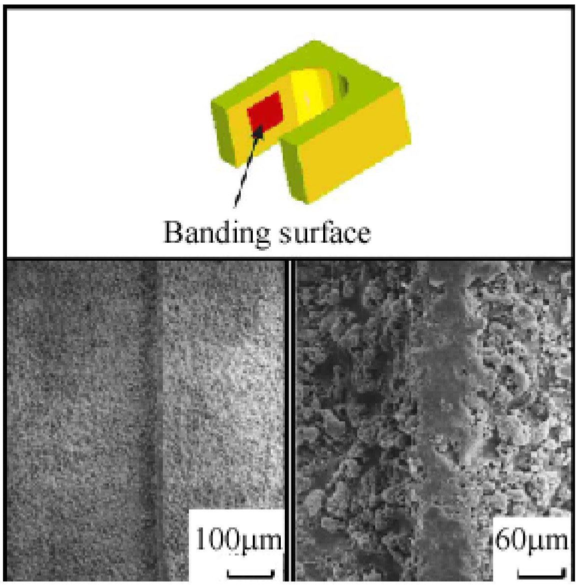

Fig. 2.12 SEM micrographs showing surface banding on an Al/Al_2O_3 composite after W-EDM [62]

With regard to microstructural defects, EDM can produce considerable microstructural changes at the surface as well as underneath it. This could significantly affect the mechanical properties of the product. The formation of a re-cast layer is one of such major defects [52]. Very often, micro-cracks are found within the re-cast layer (Fig. 2.13). Those micro-cracks are caused by the high tensile residual stress exceeding the ultimate tensile strength of the material. In addition, voids, which may be due to imperfect joining of the molten droplets or resulting from trapped gas during re-solidification, are also common features found in the re-cast layer.

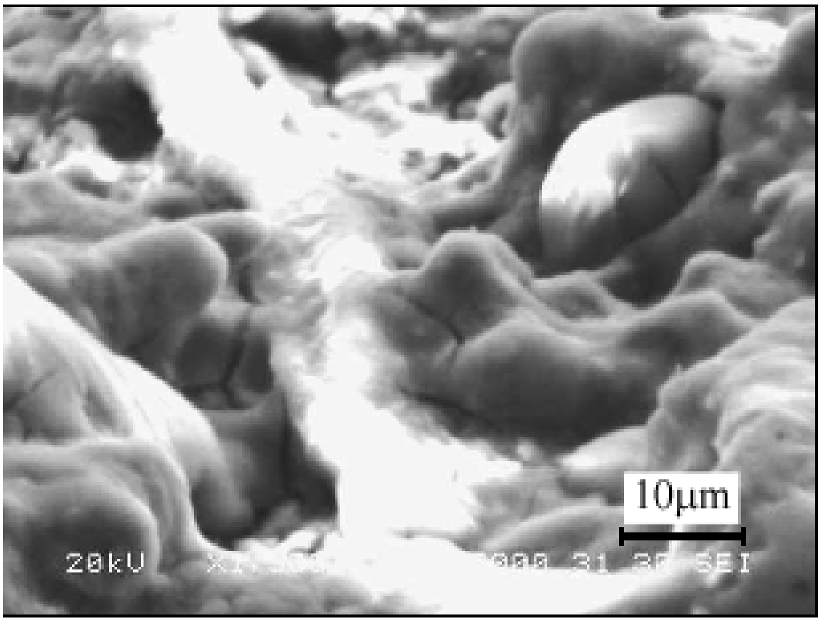

Fig. 2.13 Recast layer with micro-cracks [66]

Ramulu [67] has studied the effect of surface quality on the fatigue strength of a SiC/Al MMC. The fatigue strength of the material significantly reduced after being processed by EDM. It was found that surface roughness is one of the most important factors governing the fatigue life. On the other hand, the condition of the re-cast layer could also significantly affect the mechanical properties of the machined component or product. Normally, the rougher the surface, the lower is the fatigue life. This also means that a high MRR condition would lead to a reduction in fatigue life. Despite the fact that the problems of low material removal rate, poor surface finish and severe sub-surface damage could seriously limit the employment of EDM for machining MMCs, the advantages of the EDM process of being capable of producing intricate shapes in one single pass and having a much longer tool life than that of traditional methods, cannot be easily obtained from other machining methods. Recognising this, it is the aim of this research study to develop a new EDM based process that would overcome the problems and limitations mentioned above.

2.2.4 Electrochemical machining of MMCs

In electrochemical machining **(**ECM), metal removal is achieved by electrochemical dissolution of an anodically polarised workpiece which forms part of an electrolytic cell [68-71]. With ECM even hard metals can be shaped and the rate of machining does not depend on their hardness. The beauty of ECM is that the tool electrode used in the process does not wear, and therefore soft metals can be used as tools to form shapes on harder materials. The basic principle of the electrochemical machining process is presented in Fig. 2.14.

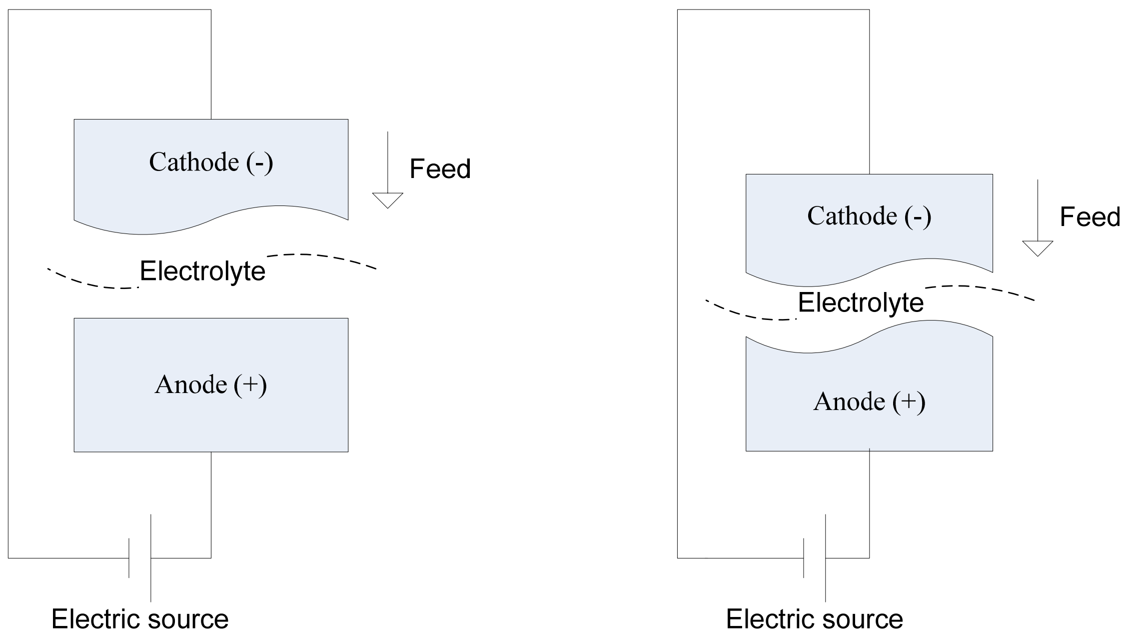

Fig. 2.14 Principle of the electrochemical machining process

As shown in Fig. 2.14, the workpiece and the tool are the anode and cathode, respectively, and a constant potential difference is applied across the two electrodes. During the process of electrolysis, the cathode shape remains unchanged; while the anode will undergo dissolution following the profile of the cathode. An electrolyte is pumped through the gap between the electrodes to remove the products of machining and to diminish unwanted effects, such as those that arise with cathodic gas generation and electrical heating. The rate at which metal is then removed from the anode is approximately in inverse proportion to the distance between the electrodes.

Indeed, ECM has established itself as one of the major alternatives to conventional methods for machining difficult-to-cut materials and/or of generating complex contours, without inducing residual stress and tool wear. The processing efficiency can be 5 to 10 times higher than that of EDM. It has been applied in diverse industries such as aerospace, automotive and electronics, to manufacture airfoils and turbine blades, dies and moulds, artillery projectiles, and surgical implants and prostheses [69]. Moreover, ECM with recent advances in machining accuracy and precision can be effectively used for micro-machining components in the electronics and precision industries [72-75].

With regard to the machining of MMCs, very few research studies have been conducted [76]. The complication in the design of the cathode tool and the intrinsic corrosion nature of the process together with the difficulty in controlling the machining gap are some major hurdles to be overcome. Moreover, the ceramic reinforcement particles that have been dislodged from the matrix cannot be readily removed from the machining gap. This could seriously hamper the electrochemical process. On the other hand, the electrolyte has to be filtered carefully to remove the ceramic particles.

It is considered that the main problem facing ECM in machining MMCs is how to improve the quality of the surface finish. After ECM, a large number of ceramic particles are commonly found protruding from the machined surface. The problem arises because the ceramic phase is not removed through dissolution, but rather by a loosening effect. This means that the surface roughness is governed very much by the volume fraction and the size of the reinforcement phase. Nonetheless, it is considered that ECM would be an excellent method for shaping MMCs, if the surface finish quality can be significantly improved, for its machining efficiency is many times higher than that of EDM. Recognising this, in the present research, the working principle of ECM[1] would be incorporated into the design of the G-ECDM method.

2.2.5 Hybrid electro machining methods

Recently, hybrid electro-machining methods, which are combinations of electro machining and one or more machining processes, have attracted special attention of those who are working in the field of machining advanced engineering materials. These processes are being developed to exploit the potential advantages

[1] In the final design of the G-ECDM process, the element of ECM is considered not to be important. In the G-ECDM process, the main function of the electrochemical effect is to obtain a relatively large spark gap environment to facilitate the removal of the reinforcement particles.

and to overcome the potential disadvantages associated with the individual constituent processes. For successful applications of the hybrid electro-machining methods, a proper understanding of the role of each constituent process is imperative. All the hybrid electro-machining methods have been developed by the combination of making use of electro energy and one or more than one types of other energies, such as thermal and mechanical. Hybrid electro-machining methods can be classified in two categories: those in which all constituent processes are directly involved in the material removal; and those in which only one of the participating processes directly removes the material while others only assist in removal by changing the conditions of machining.

Among the few hybrid methods, electro-chemical arc machining (ECAM) is an electrical based hybrid process used for electrically conductive materials. The process incorporates material removal by electro-chemical action as well as by electric arc. The productivity of ECAM is reported [77, 78] to be 5 to 50 times greater than the productivity using individual processes of ECM and EDM alone, while the main problem of this method is that the constituent ratio of ECM and EDM in the process cannot be easily controlled [69]. A similar method to ECAM is the electro-chemical spark machining (ECSM), which again is an electrical based hybrid process in which material is removed by the heat produced by sparking in the vicinity of the workpiece. In this case, the electrochemical action helps in the generation of the bubbles at the cathode for the production of sparks [79, 80]. Again, for this process it is also difficult to control the EDM and ECM actions independently [69]. Other hybrid methods make use of ultrasonic energy or mechanical energy. The ultrasonic assisted EDM (UEDM) combines ultrasonic machining (USM) and EDM, and has been found to be able to increase material removal rate (MRR) and decrease tool wear [81, 82]. However, for the UEDM process, the strict requirement on gap size prohibits the discharge debris to be readily removed and this problem would be worsened when machining MMCs. The problem of the reinforcement particle protruding from the surface also needs to be addressed.

Much interest has also been shown in the development of the electrochemical discharge grinding process (ECDG). ECDG is a combination of electrochemical grinding and electrical-discharge machining [84]. The process is very similar to conventional EDM except a grinding-wheel type of electrode is used. The grinding wheel of the electrode is normally made of bonded fine graphite particles without any abrasive particles involved. Like any EDM process, the workpiece and the grinding wheel do not come into contact. Although, using an abrasive grinding wheel has been mentioned in connection of ECDG [87], no other detailed information about the process can be found in the literature. Other hybrid processes that actually involve a grinding action are the electrochemical grinding (ECG) process [83, 85, 86] and the abrasive electrodischarge grinding (AEDG) process [87]. For the former, the bulk of material removal is by electrolytic action and only a few percent of the material are removal is by the abrasive action of the wheel. Whereas for the latter, electrochemical actions are not involved. Although these processes can be applied to machine MMCs, it is considered that a high MRR could not be readily obtained, and a rapid tool wear would be encountered.

2.3 Summary

Rapid tool wear and poor surface quality are the two main problems when conventional machining methods such as turning, milling and drilling etc. are employed to process MMCs. Although the grinding method can obtain better surface quality than others, its processing efficiency is very low. Moreover the abrasive wheel is easy to be clogged by the soft matrix metal. On the other hand, non-conventional methods can avoid rapid tool wear; however, the surface quality needs much improvement.

Among the many non-conventional methods, it is considered that the EDM method is a versatile and valuable process for shaping composite materials. However, it is obvious that both the processing efficiency and surface quality need to be improved. Another potential candidate which is also considered suitable for machining MMCs is ECM. Its efficiency is much higher than EDM. Hybrid processes which combine the actions of EDM and ECM have been found to be able to increase the machining efficiency by 5 to 50 times greater than that of using individual processes of ECM and EDM alone.

Recognising this, it is believed that by incorporating the abrasive grinding action into the hybrid process of ECDM, difficult-to-machine materials such as MMCs can be effectively machined with good surface quality and dimensional tolerance. With this in mind, this research study aims to develop and design such an integrative process and system.

CHAPTER 3

PRINCIPLE AND DESIGN OF THE G-ECDM EQUIPMENT

3.1 Principle of the G-ECDM Process

The main problems encountered in EDM of MMCs are low machining rate, high risk of tool breakage [62] and poor surface quality with the presence of various forms of defects on the machined surface. On the other hand, close dimensional control is one of the important issues that needs to be addressed in ECM [69, 78]. These problems are mainly caused by the non-conducting nature of the ceramic reinforcement phase and often the segregation of the ceramic phase. The distinctive differences in physical and mechanical properties between the relatively soft metal matrix and the hard ceramic reinforcement phase also contribute to the poor machinability of MMCs. The problems intensify as the extent of the ceramic phase increases. This research presents a new type of grinding-aided electrochemical discharge machining (G-ECDM) process that could overcome most of the problems encountered in machining MMCs. The process is capable of meeting different shape and profile requirements of the product.

The principle of the G-ECDM method is illustrated in the schematic diagram in Fig. 3.1, which is composed of three fundamental constituents, namely the electrochemical effect (ECE) element, the electrical discharge machining (EDM) element and the direct mechanical grinding (DMG) element. In the G-ECDM process, the electrolyte bath provides limited conduction between the tool and the workpiece. Although the ECE has the action of dissolving the metal phase around the reinforcement phase, its prime function is to enable EDM sparking to be operable under a relatively large spark gap size condition, and thus facilitates the removal of machined debris. During machining, normally, the tool is made the cathode, while the workpiece acts as the anode.

The relative strength of ECE and EDM in the process can be controlled by varying the processing parameters. During EDM, the material would be melted, vaporised and form EDM chips, however, it is normal that a significant amount of molten material would be re-cast around the spark eroded crater. However, the sparking action could also remove foreign material at the cathode surface, and this is beneficial in minimising tool clogging. The subject of tool clogging will be presented in Chapter 7. When it comes to the grinding phase, the re-cast material in the vicinity of the crater could be mechanically removed. The grinding action is provided by the abrasive particles embedded in the tool-electrode. In this research, diamond particles are used. With this additional grinding action, the material removal rate of ECDM would be increased. Moreover, the grinding action would improve the surface quality and finish.

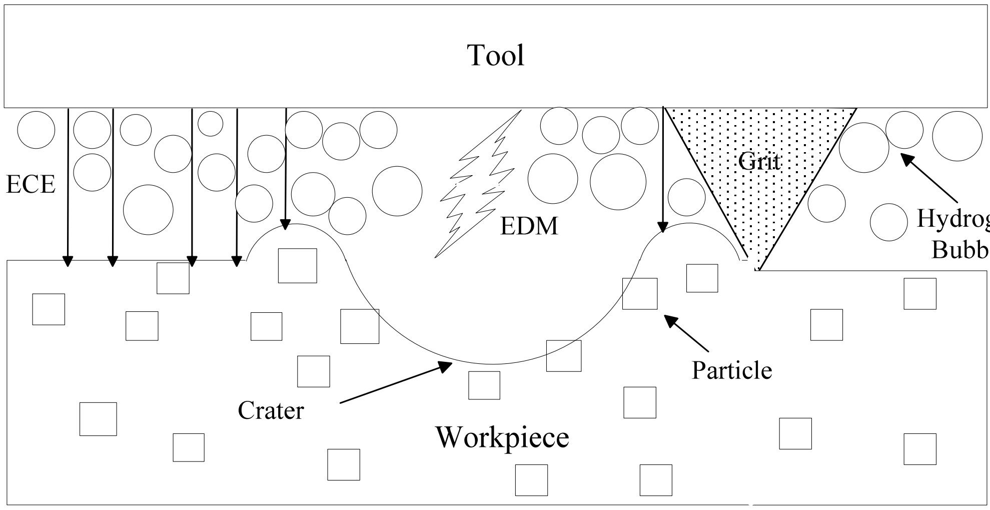

Fig. 3.1 Schematic diagram showing the combined action of the electrochemical effect (ECE), electrical discharge machining (EDM) and direct mechanical grinding (DMG)

3.2 The Tool-Electrode Design

According to the principle of G-ECDM process, the tool-electrode can adopt various forms, such as a travelling wire (Fig. 3.2), a solid drill (Fig. 3.3), a hollow drill (Fig. 3.4), a helix drill (Fig. 3.5), etc. In general, the ECDM element and the grinding element would be integrated together to form the tool-electrode. These different designs have a common characteristic that the functional part of the tool is not continuous. Such a design would provide a more stable machining condition during processing, since the open gap between the cutting elements would facilitate the removal of machined debris that are trapped between the tool and the workpiece. In this research, a continuous type of functional part is adopted because it is easier to manufacture (Fig. 5.8). The structure of the tool-electrode has an essential composite coating containing a hard reinforcement phase. The thickness of the coating typically ranged between tens of micron to a few millimetres. Here, diamond, in the form of particle, is chosen to be the reinforcement phase. The nominal size of the reinforcement particle dictates the spark gap during G-ECDM processing, which has a strong relation to the size of the reinforcement phase of the MMCs.

If a drill is employed, it will be set to rotate at a desired speed, and the three effects: electrolytic, electro-discharge and mechanical grinding will operate independently. Although, these three actions work separately, they would compensate each other.

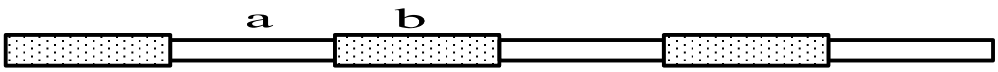

Fig. 3.2 Travelling wire [Metal phase (a), G-ECDM Section (b)] (not in scale)

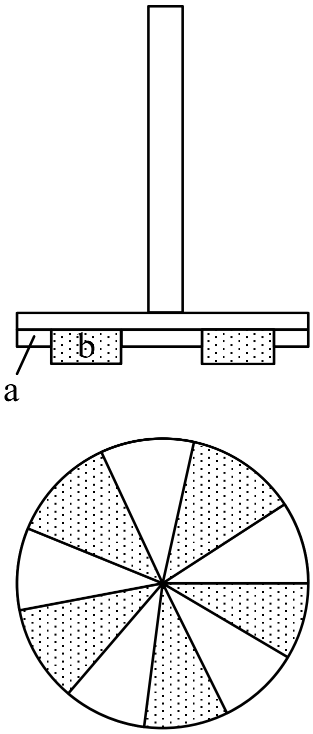

Fig. 3.3 Solid drill [Metal phase (a), G-ECDM Section (b)] (not in scale)

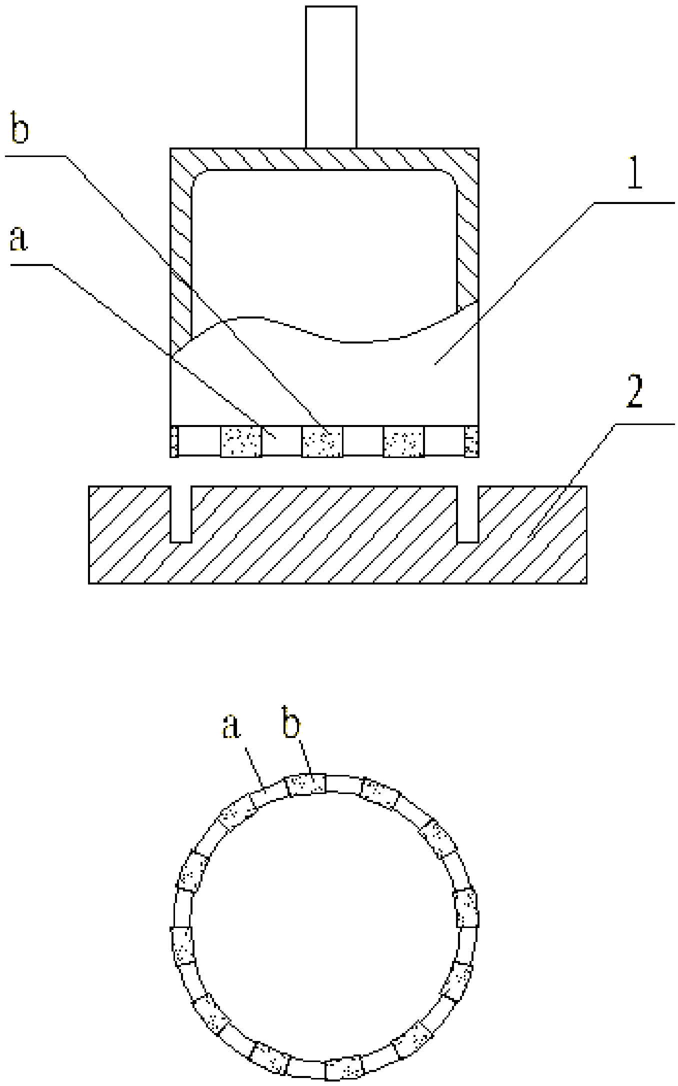

Fig. 3.4 Hollow drill [Tool (1), Workpiece (2), Metal phase (a), G-ECDM Section (b)] (not in scale)

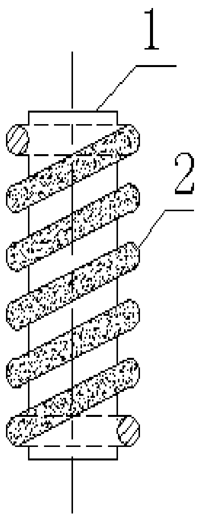

Fig. 3.5 Helix drill [Metal phase (1), G-ECDM Section (2)] (not in scale)

3.3 The Design of the G-ECDM Equipment

Fig. 3.6 presents a schematic diagram of the equipment; while Fig. 3.7 shows the actual in-house built ECDM equipment. It has a spindle (Fig. 3.8, Fig. 3.9) which is fixed to the Z-axis, onto which a cylindrical steel tool is held. The motorized spindle is capable of rotating over a wide range of speeds. During the course of processing, the electric current flows through a conduction bush (Fig. 3.10) that is placed inside an electrical insulating bearing housing (Fig. 3.8), to the tool-electrode. During operation, the springs of the bush set up push the bush into tight contact with the shaft. With such a design, unwanted sparking between the bush and the shaft can be avoided. Moreover, with such a spindle design, the working current will be confined to the processing area.

During the course of machining, the electric current flows from an electric transmission system, placed on a plastic insulated seat, to the tool. The resistance of the electric transmission system is negligible. A pulse number controllable electrical source has been designed for the experiments, in which the current can be adjusted without changing the applied voltage. The average current output of this electrical source can be adjusted from 0.5A to 100A. The pulse duration ranges between 4μs and 400μs, while the duty cycle can be operated between 1:1 and 1:10. Some major specifications of the ECDM equipment are given in Table 3.1. To facilitate the study of the ECDM process, the experimental set up allows the number of electrical pulse to be preset.

The electrolyte is pumped into the processing area through the nozzle with the aid of an electrolyte circulation system. After the electrolyte has been properly filtered, it will return to the electrolyte circulation system.

Table 3.1 Major specifications of the ECDM equipment

	X-axis	Y-axis	Z-axis	Spindle	Electrical source	Electrolyte bath
Travel (mm)	250	250	100			
Repeatability position accuracy (μm)	5	5	1			
Position accuracy (μm)	15	15	2			
Speed (rpm)				0-20000		
gripping range (mm)				Ø 0.5-10		
Power (kW)				1.5		
Peak current (A)					0.5-100	
Voltage (V)					20-120	
Pulse duration (μs)					4-400	
Duty cycle					1:1-1:10	
Maximum liquid level (mm)						200
Medium						Emulsion Electrolyte
Circulator flow (L/min)						0-20

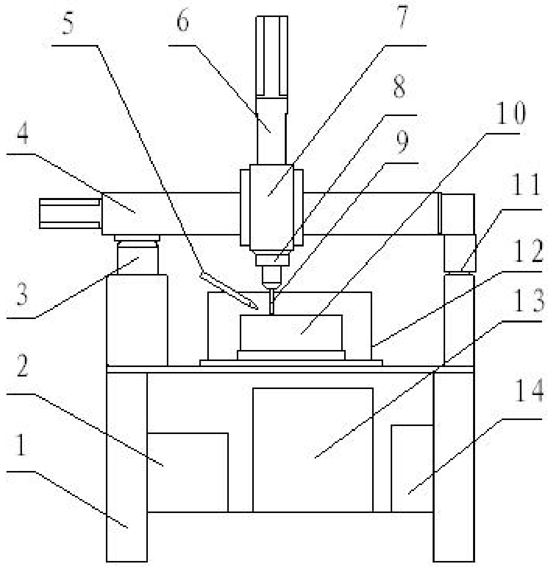

Fig. 3.6 ECDM set up [Working table (1), Electrolyte system (2), Y axis (3), X axis (4), Nozzle (5), Z axis (6), Tool holder (7), Electric transmission system (8), Tool (9), Workpiece (10), Slide rail (11), Electrolyte bath (12), Control system (13), Power source (14)]

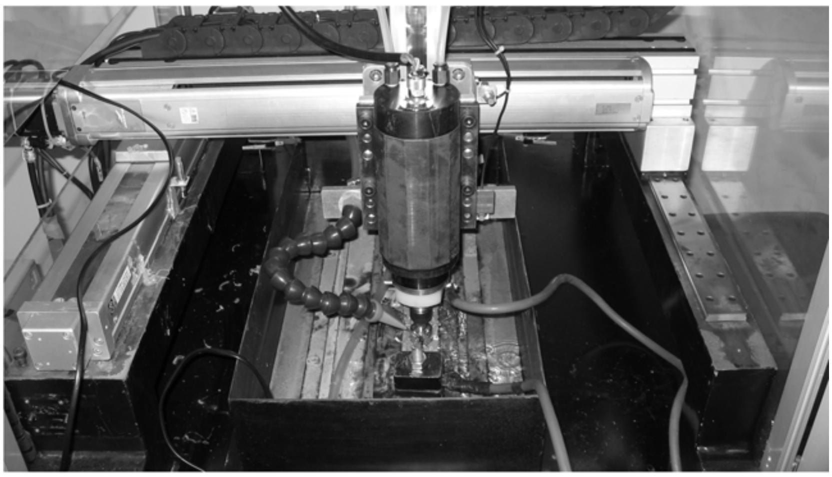

Fig. 3.7 Photo showing the set-up of the G-ECDM equipment

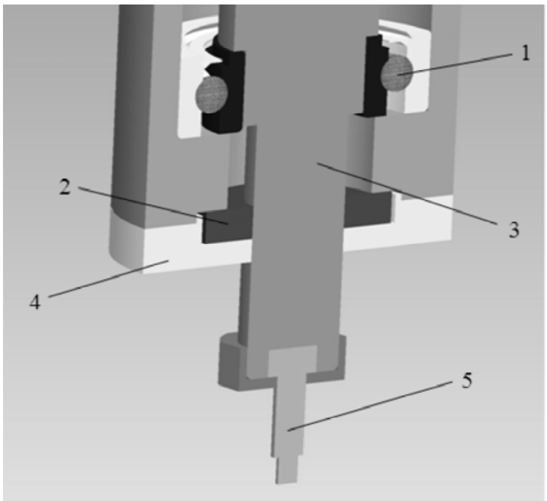

Fig. 3.8 Illustration of the design of the spindle where an electric insulating bearing system is employed to insulate the shaft from other components of the spindle. [Ceramic ball bearing (1), Insulation cover (2), Shaft (3), Insulating bearing housing (4), Tool (5)]

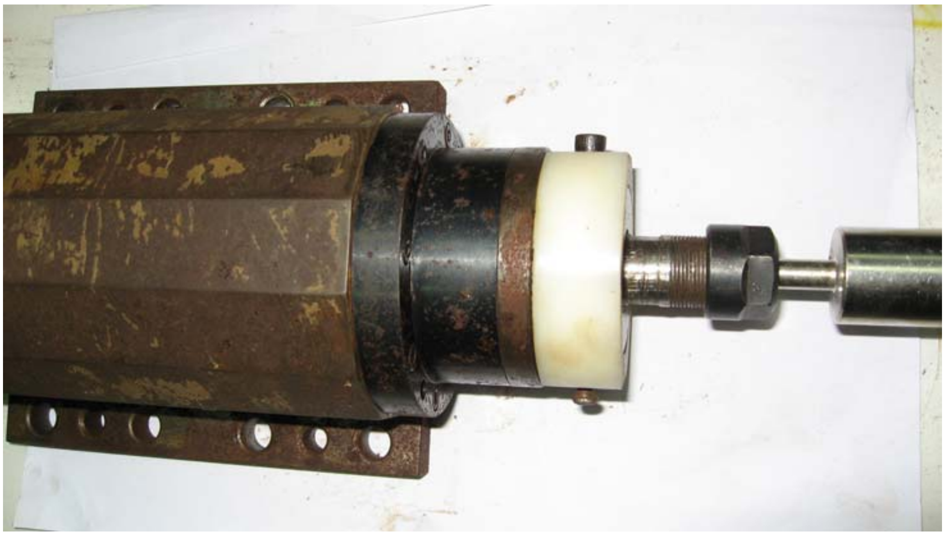

Fig. 3.9 Photo showing the spindle of the G-ECDM equipment

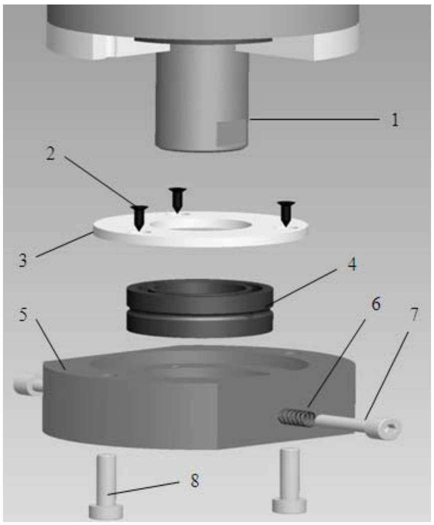

Fig. 3.10 Structure of the electrical bush [Spindle shaft (1), Push bolt (2), Insulated cover (3), Conducting bearing (4), Insulating bearing housing (5), Spring (6), Conductive bolt (7), Fixing bolt (8)]

Another important aspect of the design is the fluid bath which holds the electrolyte. The workpiece is placed on an insulated pad, and is fastened to the fixture of the fluid bath (Fig. 3.11). The joint plate and the fluid container are welded together and are fixed onto an insulating plate by bolts. The insulation plate together with the pads can prevent the working current from flowing to the worktable.

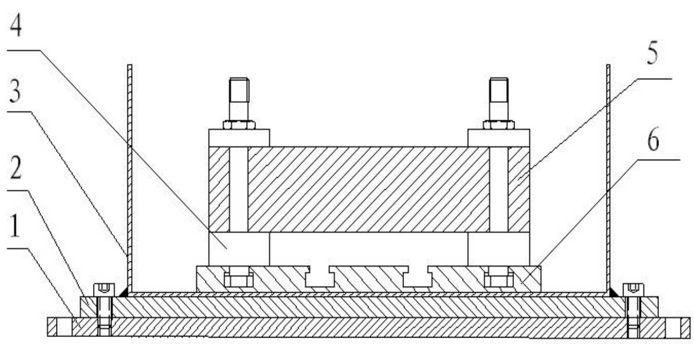

Fig. 3.11 Design of the electrolyte bath [Insulation plate (1), Joint plate (2), Fluid container (3), Insulation pad (4), Workpiece (5), Fixture (6)]

Associated with the G-ECDM experimental setup is a tailored-made power source. Its pulse duration can be adjusted from 4μs to 400μs and operates with a 100A peak current, whereas the working voltage ranges between 20V-110V, with the duty cycle capable of working between 1:1 and 1:10. A typical waveform of this power source is shown in Fig. 3.12.

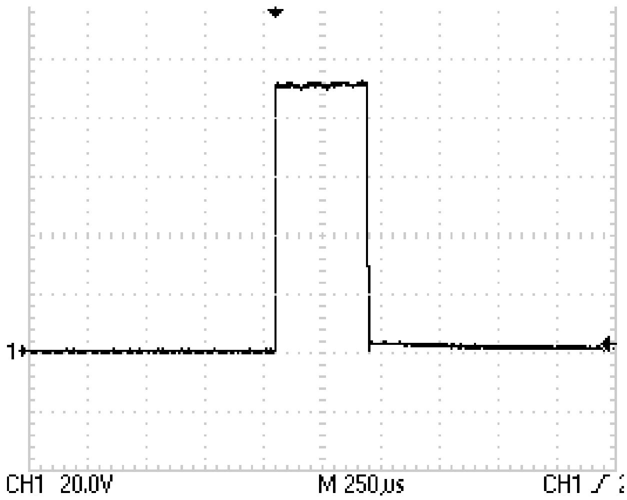

Fig. 3.12 Typical waveform of the power source

During G-ECDM, if the machining debris cannot be discharged from the spark gap in time, then short-circuiting would occur. Fig. 3.13 indicates the voltage characteristics during processing under different machining conditions. If it is under a stable machining condition (I), the processing voltage fluctuates between φ_1 and φ_2. While for an unstable condition (II), it would normally be maintained for a short period of time. If the unfavourable processing situation persists, i.e. condition (II), the voltage will drop further and finally short-circuiting would occur, i.e. condition (III), in which, the voltage would drop sharply from φ_3 to φ_4. With this problem in mind, the electrode control system of the G-ECDM is so designed that it can monitor the change of voltage and provides appropriate remedial actions to avoid short circuiting from happening. Should an unstable processing condition be encountered, the servo control system would command the tool to retract instantly so as to improve debris discharge through a wider machining gap. The retract speed and the distance can be controlled according to the unstable processing condition encountered.

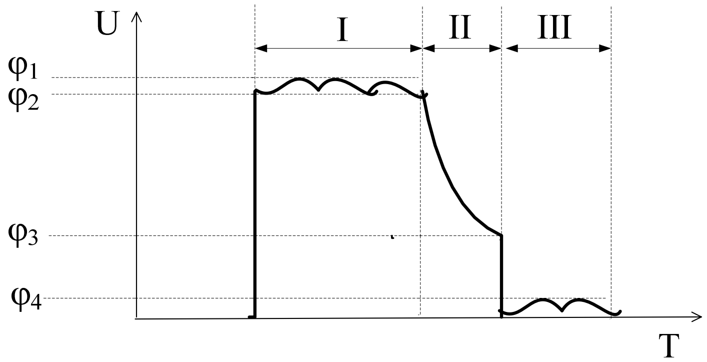

Fig. 3.13 Voltage behaviour for different processing conditions. [Stable processing condition (1), Unstable processing condition (2), Short-circuiting (3)]

The following describes the working principle of the process control system. A voltage collection card is employed to monitor the processing voltage. Initially, the processing voltage data are collected and those voltages which are too high or too low will be filtered out. Then the average voltage value is calculated using the following equation:

$$U = \frac{\sum_{j=1}^{i} U_j}{i} \tag{3.1}$$

The average voltage obtained is used to determine the status of the processing condition. If the value found matches that of the unstable condition, the control system will signal the tool to retract. The monitoring flowchart below summarises the working sequences of the process control system (Fig. 3.14).

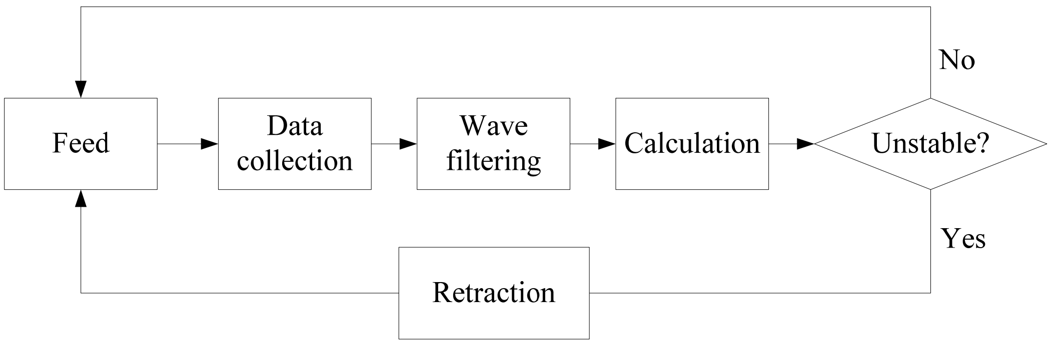

Fig. 3.14 Monitoring process flowchart

In fact, the data collection card and the movement control card are integrated into a computerised control system (Fig. 3.15); the processing voltage between the tool and the workpiece is monitored by the data collection card. The collected data is then calculated and analysed by a computer program. If the voltage determined is in a stable processing state, the tool will keep feeding. On the other hand, if an unstable condition is detected, the computer will give a signal to the driver through the movement control card such that the servo-actuator will be activated and the tool will retract.

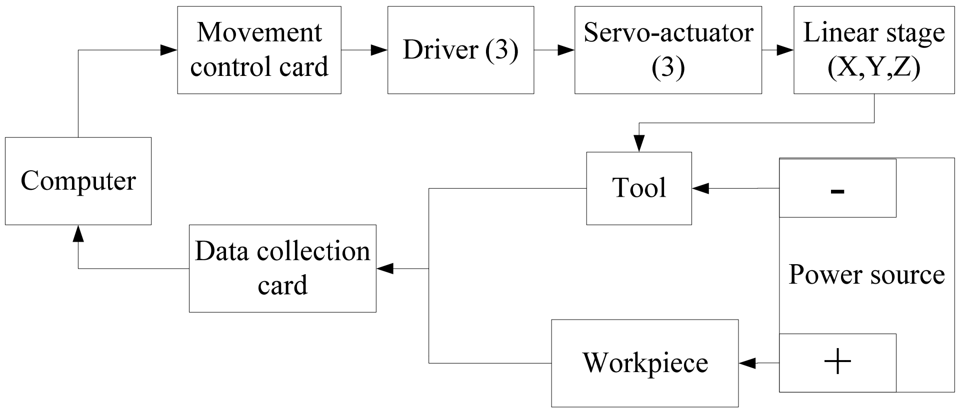

Fig. 3.15 Movement control flowchart

The control program flowchart with the corresponding computational logics is shown in Fig. 3.16, whereas the computer program written for that is given in Appendix A. Right at the start, the tool and the workpiece will be adjusted to a suitable processing position. Then the tool will be fed with an initial set speed and the feed distance being continuously logged. If no unstable condition is encountered, then the same processing condition will be maintained, or alternatively, with the auto speed control (ASC) command, the feed speed can be progressively increased to increase the machining rate until an unstable condition starts appearing. Unstable processing conditions are detected by monitoring a sudden drop of the processing voltage. When an unstable condition is encountered, the tool will retract instantly according to the command of the ASC, so as to provide a larger discharge gap for the debris to be washed out. After the process is resumed, the feed speed will be reduced automatically to avoid any unstable processing condition to occur again. Apart from the main control function, the system has the ability to compensate any inherent movement errors of the lead screw.

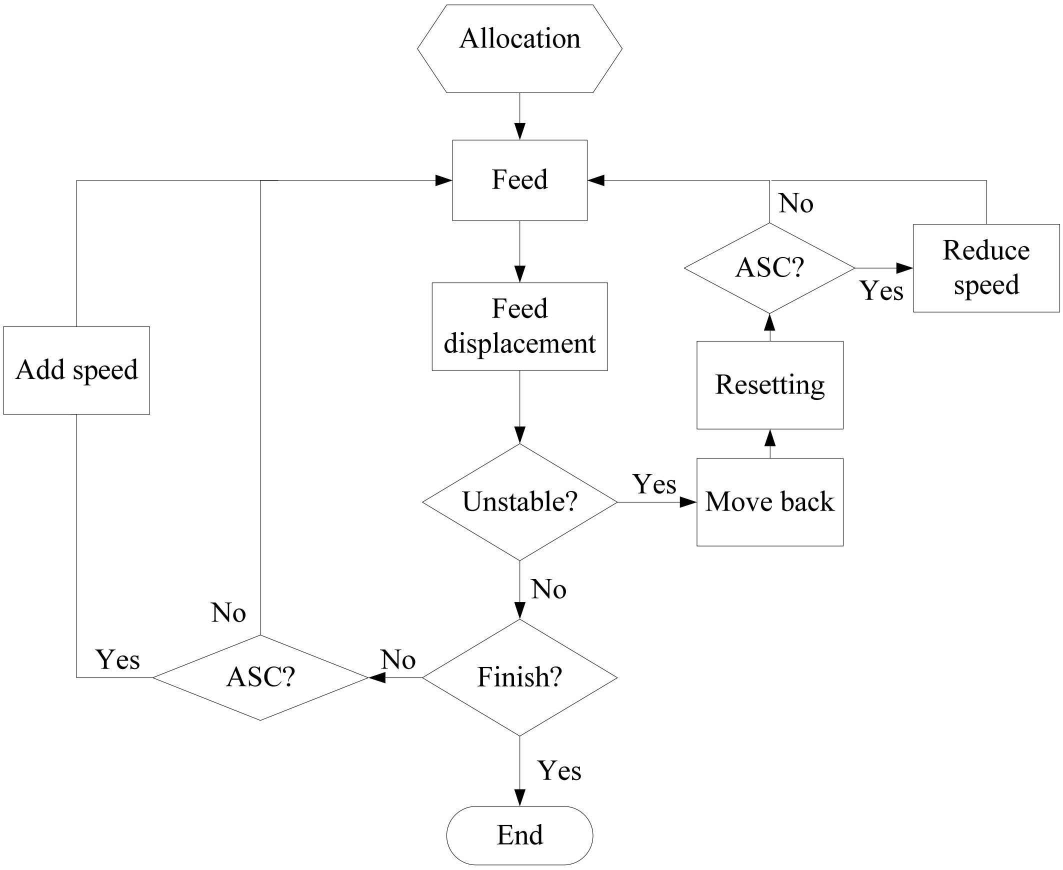

Fig. 3.16 Control program flowchart

CHAPTER 4

ELECTROCHEMICAL DISCHARGE MACHINING OF PARTICULATE REINFORCED METAL MATRIX COMPOSITES

In order to fully understand the complex interactions between the three effects, namely, electrochemical, electrospark and grinding, of the G-ECDM process when machining particulate reinforced MMCs, it was decided to break down the research into several phases of studies. They are the analysis of the ECDM mechanism, the analysis of the G-ECDM mechanism, and the study of tool performance of the G-ECDM process. There is no doubt that ECDM plays a very important role in G-ECDM of MMCs. In fact, the machining mechanism of ECDM of MMCs has not been studied in detail and little is known about the material removal mechanism. In this chapter, detailed research work on ECDM is presented; its scope encompasses the analysis of ECDM spark generation mechanism, and the study of material removal under single pulse and continuous pulse conditions.

4.1 Analysis of Discharge Mechanism

4.1.1 Background

A number of studies have been conducted to analyse the electrochemical discharge machining (ECDM) process as well as the material removal mechanism [88, 79, 80, 89]. Among these, the early work of Crichton and McGeough [88] involved high-speed photography to analyse the various stages of the discharging process. On the other hand, Allesu et al. [90] attempted to establish a classification of the various material-removal processes based on the ECD phenomenon. Despite a considerable amount of experimental research being conducted on the study of ECDM, relatively little theoretical modelling work has been performed. With regard to modelling the ECDM process, Basak and Ghosh [89] developed a simplified idealistic model of the process capable of predicting the critical voltage and current for spark initiation. They treated the discharge phenomenon as a switching off process, in which the current drops to zero for a very short time. Taking a different approach, Jain et al. [79] considered each gas bubble as a valve, which after its breakdown due to a high electric field produces a discharge in the form of an arc; their study mainly focussed on the aspects of energy and current during sparking. Although the models proposed by Basak and Jain have shed useful light on the discharge mechanism in electrochemical discharge machining, Kulkarni et al. [80] argued that their models cannot explain the observation of the dependence of the arc on the immersion depth of the tool. Moreover, in Basak's work, despite the theoretical predicted values comparing quite well with experimental observations, the model developed still has some major deficiencies according to a recent review paper by WÜthrich [91]. It is apparent that the basic mechanism of the process is not yet completely understood and more research work is deemed necessary.

4.1.2 Theoretical analysis

4.1.2.1 Assumptions

Previously, Basak and Ghosh [89] modelled the ECDM discharge phenomenon as a switching off process, while Kulkarni et al [80] studied in some detail the ECDM mechanism experimentally. In Basak's model, it is hypothesized that, as a consequence of vapour blanketing of the electrode, a switching off situation occurs and the current through the circuit, within a very short time span, drops to zero. Similarly, Kulkarni proposed that when an isolating film of hydrogen gas bubble covers the cathode tip portion in the electrolyte, the tip is covered by a gaseous layer. At this time, a large dynamic resistance is present and the current through the circuit becomes almost zero. However, according to experiment observations and analysis, this phenomenon only exists in some special situations, such as when the energy of the power supply is low and/or the electrode area is small. Jain et al. [79] also have the same opinion in that the current does not need to drop to zero or almost zero. Taking a different approach to analyse spark initiation, Jain [79] put forward an arc discharge valve model to explain the ECSM process, and it has satisfactorily explained some of the experimental results. However, the model mainly focuses on the analysis of the start point of sparking, and the bubble effect on the distribution of the electric field has not been studied. Recognising this, the present research work aims to provide a deeper understanding of the ECDM mechanism in the machining of MMCs. In the analysis, the effects of bubbles and the reinforcement phase on the electric field are considered.

In this study, the gap between the electrodes is assumed to be constant, and the surfaces of the tool and the workpiece is in parallel. While the bubble takes a spherical shape. The distribution of bubbles on the electrode and in the gap is considered to be random, and a hundred percent bubble coverage of the cathode is not assumed. Also assumed is the energy of the power supply is sufficient for the ECDM process to be continuous.

Normally, the ECDM consists of several stages. The initial stage is essentially a pure ECE, during which the resistance between the anode and cathode gradually increases because of an increase of the number of hydrogen bubbles resulting from the ECE. As a result, the voltage between the anode and cathode will increase accordingly. Once it reaches the breakdown voltage, a spark would be produced; the value of this critical breakdown voltage can be obtained by using the model developed in this study. The following sections present details of the theoretical analysis of the model.

4.1.2.2 Theoretical model of the discharge mechanism

Fig. 4.1 shows a schematic diagram of the ECDM process, which is the subject of this study, in which the workpiece is the anode and the tool is the cathode. During processing, an electric double layer is assumed to exist on both surfaces of the workpiece and the tool (Fig. 4.1b). For the cathode, initially, the electric double layer is in a stable condition since there is no current flowing to the cathode (Fig. 4.2a). When the process starts, electrons will flow towards the cathode (Fig. 4.2b), and most of these electrons will charge up the electric double layer capacitor of the tool. When the electric double layer capacitor has been fully filled, electrons are used to produce H_2 (Fig. 4.2c). Fig. 4.3 presents the equivalent circuit of the ECDM process, where C_1 and C_2 represent the electric double layer capacitors of the anode and cathode respectively. R_1 and R_3 represent the resistance of the electrochemical reactions at the anode and cathode respectively. R_2 is the resistance of the electrolyte. R is an external resistor, and R^* is used to represent the resistance between the tool and the workpiece.

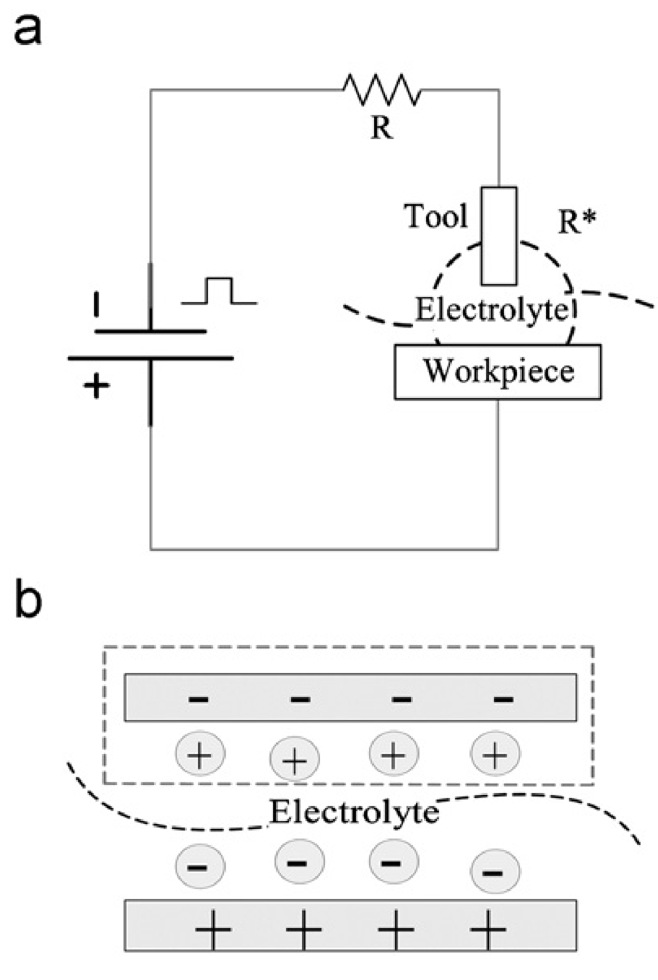

Fig. 4.1 Schematic diagram showing [(a) the overall ECDM process, where R represents an external resistor, R^* is the resistance between the tool and the workpiece; (b) the electric double layers exist on both surfaces of the workpiece and the tool]

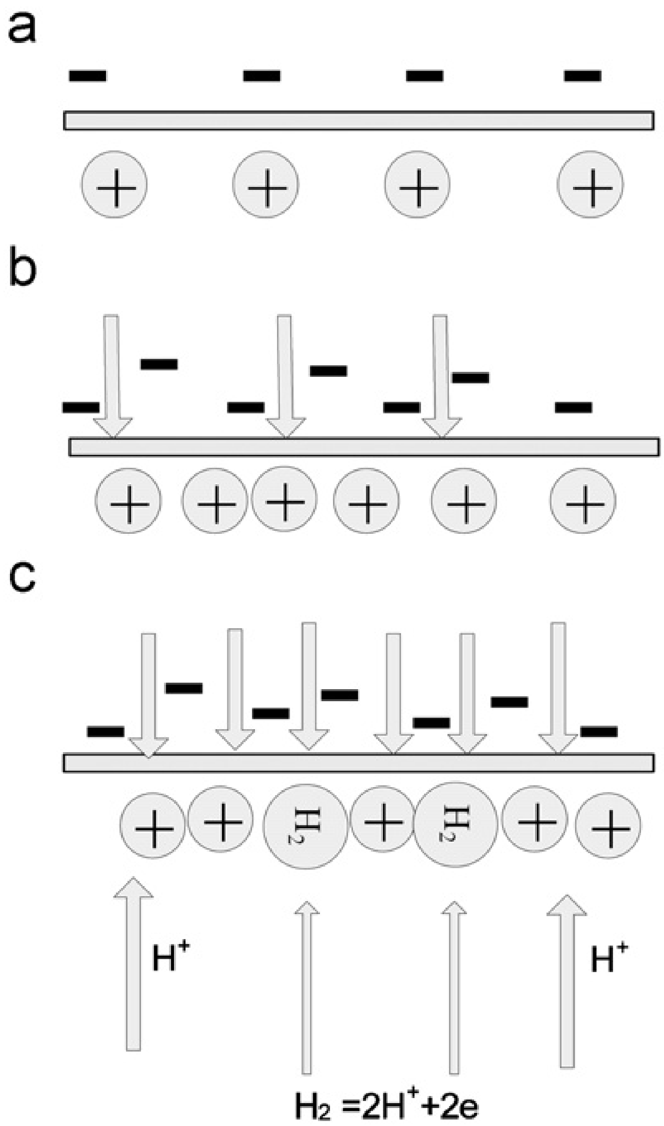

Fig. 4.2 Electric double layer of the cathode (a) initially, the electric double layer is in a stable condition; (b) when the ECDM process starts, electrons will flow towards the cathode; (c) when the electric double layer capacitor has been fully filled, H_2 gas starts to form

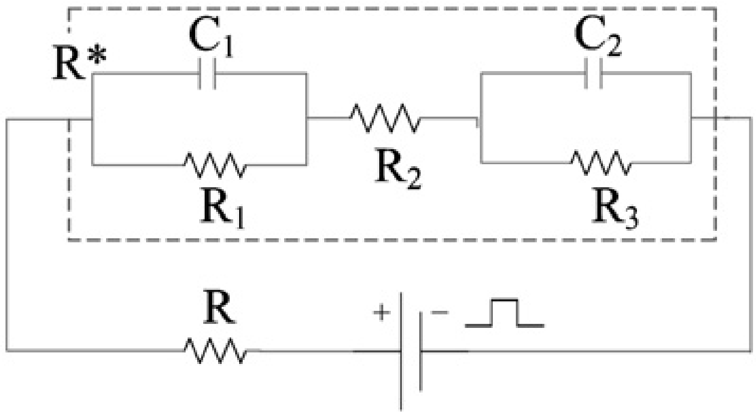

Fig. 4.3 Equivalent circuit of the ECDM, where *C*1 and *C*2 represent the double layer capacitors of the anode and cathode respectively. *R*1 and *R*3 represent the electrochemical reaction resistances of anode and cathode, respectively. *R*2 is the resistance of the electrolyte. *R* is an external resistor, and *R** represents the resistance between the tool and the workpiece

During the ECDM process, some bubbles will break and disappear, but more bubbles will be produced, and as such the open area between the workpiece and the tool will decrease. According to equation (4.1), *R** will increase (where *L* is the gap size between the two electrodes; *S* is the surface area of the exposed electrodes; ρ is the resistivity of the electrolyte). As a result, the voltage between the cathode and anode will increase accordingly, and if the voltage reaches the breakdown voltage, sparks will be produced and the voltage will drop to a value that will just be sufficient to maintain arcing.

$$R^* \propto \rho \frac{L}{S} \tag{4.1}$$

If ϕ_a is the applied voltage, and φ_2 is the breakdown voltage and φ is the arc maintaining voltage, then the voltage waveform for ECDM could resemble the form as shown in Fig. 4.4(a), in which the pulse-on-time is t_{on}. During Stage I, the voltage between the anode and cathode will gradually increase. Once it reaches the breakdown voltage, a spark will be produced and the voltage will drop to the arc maintaining voltage immediately. At this point in time, Stage II sets in, and the arc discharge will persist till the end of the pulse-on-time if the energy of the power supply can sustain the current at the arc maintaining voltage. At the end of the pulse-on-time, due to the electric capacity effect, the voltage between the anode and cathode will gradually drop to zero (Stage III).

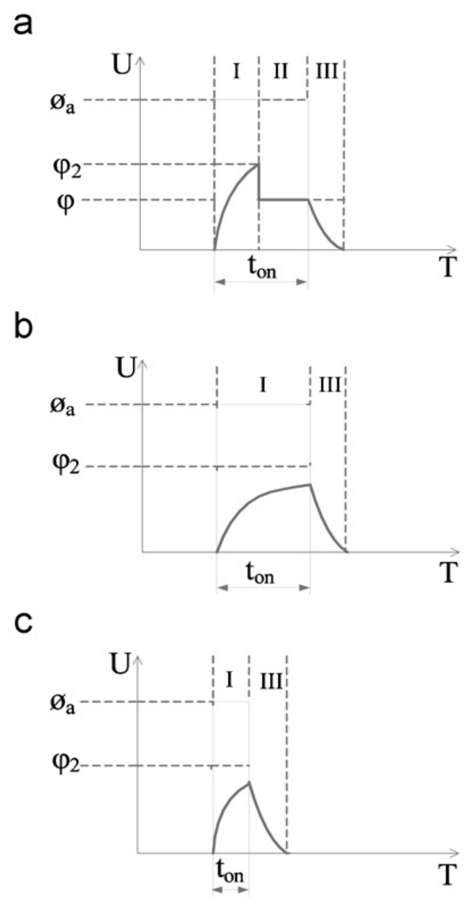

Fig. 4.4 Three possible voltage waveforms occurring in ECDM [(a) typical ECDM waveform; (b) waveform for cases where the voltage increasing rate is low; (c) waveform for cases of short pulse-on time.]

The voltage of the capacitance (φ_c) between the two electrodes can be determined by equation (4.2), where φ_s is the steady state voltage of the capacitance and τ is a time constant.

$$\varphi_c = \varphi_s(1 - e^{-\frac{t}{\tau}}) \tag{4.2}$$

However, in the case where the rate of voltage increase is low, during the pulse-on-time, the voltage will not reach φ_2 (Fig. 4.4b), and as such, sparking will not occur, and should this do so, the voltage waveform will resemble that of Fig. 4.4(b). Likewise, if the pulse-on-time is too short, the voltage will fall short of φ_2 and again sparking will not occur (Fig. 4.4c).

4.1.2.3 Critical breakdown voltage

In this study, the power supply is ensured as being capable of providing enough energy for generating an arc at the breakdown site. Under such a condition, the breakdown voltage (φ_2), which is a critical parameter for the study of the ECDM mechanism, can be determined. To comprehend an arc discharge event, the effects of hydrogen bubbles present between the two electrodes and the ceramic phase existing in the workpiece, on the electric field strength during ECDM are investigated. Fig. 4.5 shows a schematic diagram for modelling the electric field in ECDM.

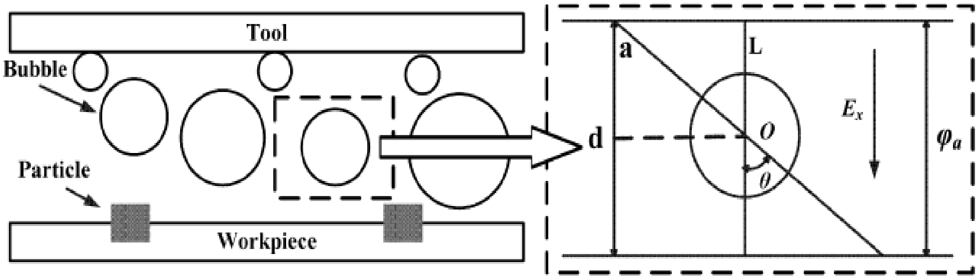

Fig. 4.5 Schematic model for studying the electric field in ECDM of a particulate reinforced composite (E_x is the external electric field outside the bubble, φ_a is the electric potential across the bubble of a length a).

Initially, the voltage between the two electrodes can be described by Laplace's Equation:

$$\nabla^2\varphi = \frac{\partial}{\partial r}(r^2\frac{\partial v}{\partial r}) + \frac{1}{\sin\theta}\frac{\partial}{\partial\theta}(\sin\theta\frac{\partial v}{\partial\theta}) + \frac{1}{\sin^2\theta}\frac{\partial^2 v}{\partial\phi^2} = 0 \tag{4.3}$$

The general solution of this equation in spherical coordinates can be represented by equation (4.4), which can be found in related mathematical physics books [92]:

$$\varphi(r,\theta,\phi) = \sum_{n,m}\left(A_{nm}r^n + \frac{B_{nm}}{r^{n+1}}\right)\mathrm{P}_n^m(\cos\theta)\cos m\phi + \sum_{n,m}\left(C_{nm}r^n + \frac{D_{nm}}{r^{n+1}}\right)\mathrm{P}_n^m(\cos\theta)\sin m\phi \tag{4.4}$$

where A_{nm}, B_{nm}, C_{nm}, D_{nm} are arbitrary constants.

Under the ECDM condition, due to the symmetry of the bubble, the electric potential φ can be described by equation (4.5) [92]:

$$\varphi = \sum_n\left(A_n r^n + \frac{B_n}{r^{n+1}}\right)\mathrm{P}_n(\cos\theta) \tag{4.5}$$

Furthermore, using equation (4.5), the potentials outside the bubble (φ_{out}) and inside the bubble (φ_{in}) can be described by equations (4.6) and (4.7) respectively:

$$\varphi_{out} = \sum_n \left(A_n r^n + \frac{B_n}{r^{n+1}} \right) \mathrm{P}_n(\cos\theta) \tag{4.6}$$

$$\varphi_{in} = \sum_n \left(C_n r^n + \frac{D_n}{r^{n+1}} \right) \mathrm{P}_n(\cos\theta) \tag{4.7}$$

where $P_n(\cos\theta)$ has the form of a Legendre Function:

$$P_0 = 1, \quad P_1(\cos\theta) = \cos\theta, P_2(\cos\theta) = (3\cos^2\theta - 1)/2 \tag{4.8}$$

Also the following boundary conditions apply:

(1) The electric potential at the bubble surface is equal to:

$$\varphi_{out} = \varphi_{in} \quad \text{(when } r = R \text{ and } R \text{ is the bubble diameter)} \tag{4.9}$$

(2) At the bubble surface, the electric induction intensity in the normal direction is equal to:

$$\varepsilon_0 \frac{\partial \varphi_{out}}{\partial r} = \varepsilon \frac{\partial \varphi_{in}}{\partial r} \tag{4.10}$$

where ε_0 and ε are the dielectric constants of the electrolyte and the hydrogen bubble.

(3) The electric potential is uniform in the space far away from the bubble, i.e.:

$$\varphi_{out} \to -E_\chi r\cos\theta \quad \text{(when } r \to \infty\text{)} \tag{4.11}$$

When the effect of bubble density and the particles on the electric field is considered, the external electric field outside the bubble can be expressed by E_x (as shown in Fig. 4.5). In fact, these effects are primarily reflected on the value of d.

(4) The electric potential in the centre of the bubble has a finite value of,

$$\varphi_{in} \neq \infty \quad \text{(when } r = 0\text{)} \tag{4.12}$$

(5) The electric potential across a bubble of length "*a*" is determined by both φ_{in} and φ_{out}.

$$\varphi_a = (\varphi_{in}\Big|_0^R + \varphi_{out}\Big|_R^a) \tag{4.13}$$

Using equations (4.6) and (4.7), and according to boundary condition (1), the following equation is obtained:

$$\varphi_{out} = \sum_n \left(A_n R^n + \frac{B_n}{R^{n+1}} \right) \mathrm{P}_n(\cos\theta) = \sum_n \left(C_n R^n + \frac{D_n}{R^{n+1}} \right) \mathrm{P}_n(\cos\theta) = \varphi_{in} \tag{4.14}$$

It is known that $\varepsilon_0 \approx 80$, $\varepsilon \approx 1$ [93], and using equation (4.14) and based on boundary condition (2), the following equation is obtained:

$$80\frac{\partial\varphi_{out}}{\partial r} = 80\sum_n \left(nA_n R^{n-1} + (n+1)\frac{B_n}{R^{n+2}} \right) \mathrm{P}_n(\cos\theta) = \frac{\partial\varphi_{in}}{\partial r} = \sum_n \left(C_n nR^{n-1} + (n+1)\frac{D_n}{R^{n+2}} \right) \mathrm{P}_n(\cos\theta) \tag{4.15}$$

Now, according to boundary condition (3) and for $P_1(\cos\theta) = \cos\theta$, i.e. equation (4.8), the following is obtained:

$$\varphi_{out} \to -E_\chi r\cos\theta = -E_\chi r\mathrm{P}_1(\cos\theta) \tag{4.16}$$

Using equations (4.6) and (4.16), A_1 and A_n can be determined,

$$A_1 = -E_\chi, \qquad A_n = 0 \ \ (n \neq 1)$$

Using equation (4.7) and according to boundary condition (4), D_n must be zero.

Now, let $A_1 = -E_x$, $A_n = 0$ $(n \neq 1)$ and $D_n = 0$, equations (4.14) and (4.15) can be simplified to:

$$E_\chi R\mathrm{P}_1(\cos\theta) + \sum_n \frac{B_n}{R^{n+1}}\mathrm{P}_n(\cos\theta) = \sum_n C_n R^n \mathrm{P}_n(\cos\theta) \tag{4.17}$$

$$-E_\chi \mathrm{P}_1(\cos\theta) - \sum_n \frac{(n+1)B_n}{R^{n+2}} \mathrm{P}_n(\cos\theta) = \frac{1}{80} \sum_n nC_n R^{n-1} \mathrm{P}_n(\cos\theta) \tag{4.18}$$

Based on equations (4.17) and (4.18), the following equations are obtained:

$$-E_\chi R + \frac{B_1}{R^2} = C_1 R \tag{4.19}$$

$$-E_\chi - \frac{2B_1}{R^3} = \frac{1}{80} C_1 \tag{4.20}$$

With equations (4.19) and (4.20), B_1 and C_1 can be evaluated,

$$B_1 = \frac{-79}{161} E_\chi R^3, \qquad C_1 = -\frac{240}{161} E_\chi$$

Furthermore, according to equations (4.17) and (4.18) when $n \neq 1$, B_n and C_n should be equal to zero. Having obtained A_1, A_n ($n \neq 1$), B_1, B_n ($n \neq 1$), C_1, C_n ($n \neq 1$) and D_n, equations (4.6) and (4.7) can be written as:

$$\varphi_{out} = -E_\chi r\cos\theta + \frac{-79}{161} \frac{E_\chi R^3 \cos\theta}{r^2} \tag{4.21}$$

$$\varphi_{in} = -\frac{240}{161} E_\chi r\cos\theta \tag{4.22}$$

Based on equation (4.22), E_{in} is formulated:

$$E_{in} = -\frac{\partial \varphi_{in}}{\partial z} = -\frac{\partial \varphi_{in}}{\partial (r\cos\theta)} = \frac{240}{161} E_\chi \tag{4.23}$$

Now, according to boundary condition (5) and using equations (4.21) and (4.22), equation (4.13) thus becomes:

$$\varphi_a = -\frac{240}{161}E_\chi R\cos\theta + (-E_\chi r\cos\theta + \frac{-79}{161}\frac{E_\chi R^3\cos\theta}{r^2}\Big|_R^a) \tag{4.24}$$

$$\varphi_a = -(E_\chi a\cos\theta + \frac{79}{161}\frac{E_\chi R^3\cos\theta}{a^2}) \tag{4.25}$$

Since,

$$2\,\varphi_a = -E_0 d \quad \text{and} \quad a = \frac{d}{2\cos\theta} \tag{4.26}$$

where E_0 is the original electric field strength.

Then using equations (4.25) and (4.26), the following equations are obtained:

$$-2(E_\chi a\cos\theta + \frac{79}{161}\frac{E_\chi R^3\cos\theta}{a^2}) = -E_0 d \tag{4.27}$$

and E_x becomes:

$$E_\chi = \frac{E_0 d}{d + \dfrac{316R^3\cos^3\theta}{161d^2}} \tag{4.28}$$

And according to equation (4.28), it is apparent that the maximum value of E_x (Max E) occurs at $\theta = 90°$, which is equal to E_0. Then equation (4.23) becomes:

$$\text{Max}\,E_{in} = \frac{240}{161}MaxE_\chi = \frac{240}{161}E_0 \tag{4.29}$$

Equation (4.29) can also be written as:

$$E_0 = \frac{161}{240}MaxE_{in} \tag{4.30}$$

Given that the dielectric strength of hydrogen is about 3×10^6 V/m (i.e. $MaxE_{in}$), and based on equation (4.30), when E_0 reaches 2.013×10^6 V/m, the bubble will breakdown; this value is independent of the interactions that the reinforcement particle may have on the electric field. Nevertheless, the reinforcement phase will affect the amount, distribution and possibly the size of the hydrogen bubbles. To verify the model and to determine the breakdown voltage experimentally, experiments were conducted under different processing conditions and the results are given in the following section. According to the model, when the gap between the electrodes is 15±2μm, the predicted breakdown voltage φ_2 should range between 26.2V and 34.2V.

4.1.3 Experimental verification

4.1.3.1 Experimental approach

Basically, the experiment set up described in Section 3.3 was employed. Fig. 4.6 shows a schematic diagram of the ECDM equipment. It has a fine adjustment device, onto which a cylindrical tool-electrode made of carbon steel having a diameter of 5 mm is held by the tool holder. The precision of the fine adjustment device is 1μm. The major difference between ECDM and G-ECDM is that the tool-electrode of the former does not have abrasive particles. To facilitate the study of the ECDM process, a pulse number controllable electrical source has been designed for the experiment (Fig. 4.7), i.e. the number of pulses can be preset, and using which the current can be adjusted without changing the applied voltage. The pulse number can be varied from 1 to 99999. The peak current output of this electrical source can be adjusted from 0.5A to 100A. The pulse duration ranges between 4μs and 400μs, while the duty cycle can be operated between 1:1 and 1:10.

The workpiece material, i.e. the MMC, is a particulate reinforced aluminium alloy 359 with 20-vol% SiC. The material was supplied in the form of 10mm thick rolled plates with the reinforcement phase having a nominal size of 10μm. The workpiece is placed on an insulated pad. The electrolyte used for the experiment was $NaNO_3$ solution, and its concentration was varied between 1wt% and 1.6wt%. The electrolyte is pumped into the processing area through a nozzle with the aid of a circulation system. After the electrolyte has been properly filtered, it returns to the electrolyte circulation system. In the experiment, the effects of current, pulse duration, duty cycle and electrolyte concentration on ECDM were studied. The various conditions employed are given in Table 4.1. Moreover, a comparison of the discharge waveforms was made between the ECDM and EDM processes.

Before the start of the experiment, the tool surface and the workpiece surface were adjusted to ensure they were parallel. The spark gap was initially set by moving the surface of the tool-electrode to come to contact with the workpiece using a contact sound buzzer. Then, the fine adjustment device is used to move the tool away from the workpiece at a specified displacement which determines the initial spark gap.

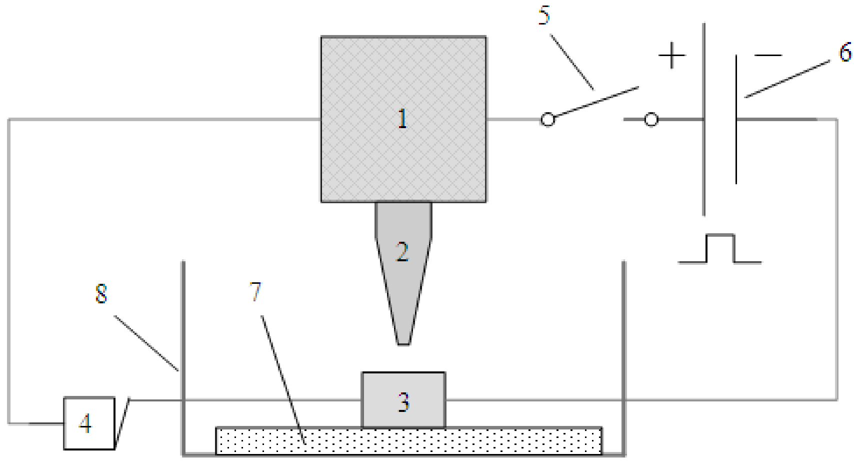

Fig. 4.6 Schematic diagram of the ECDM experiment device [Fine adjustment device (1), Electrode (2), Workpiece (3), Buzzer (4), Switch (5), Power source (6), Insulation plate (7), Electrolyte bath (8)]

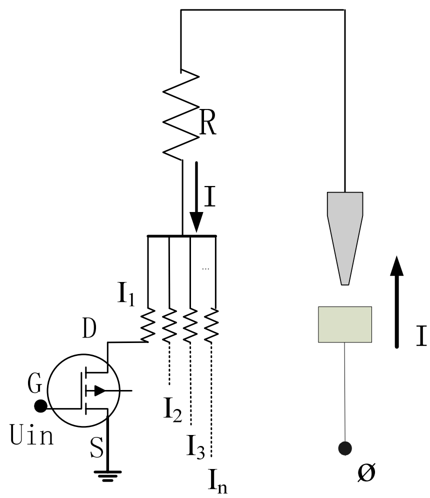

$$I = I_1 + I_2 + I_3 + \cdots + I_n$$

Fig. 4.7 Design of the electrical source

4.1.3.2 Experimental results and discussion

ECDM and EDM Waveforms

A comparison of the voltage waveforms was made between ECDM and EDM of the SiC particulate reinforced composite. For the EDM process, the machining conditions were similar to those of Condition A2 (Table 4.1), except that an emulsion medium was used instead of the $NaNO_3$ solution and the spark gap size was 5μm. Fig. 4.8 shows the typical waveforms of the applied voltage, the ECDM voltage and the EDM voltage. According to Fig. 4.8b, the three stages that are expected of a typical ECDM waveform (Fig. 4.4a) were obtained. The recorded breakdown voltage was about 30V which compared well with the theoretical predicted value of 26.2V to 34.2V; the experimental results also show that the arc maintaining voltage was about 20V. It was also found that the peak voltage in ECDM was significantly lower than the applied voltage. This indicates that the current between the two electrodes was not zero. On the other hand, the waveform resulting from the EDM process shows that Stage I and Stage II in the ECDM waveform were absent (Fig. 4.8c). This is considered to be simply due to the high electrical resistance of the emulsion used in EDM. Moreover, due to the fact that the dielectric strength of the emulsion is significantly higher than that of the hydrogen bubbles formed in the ECDM process, a much higher breakdown voltage (110V) was recorded than in the ECDM process (30V) despite the fact that the former has a much smaller spark gap. Nonetheless, the fact that the two processes have a similar maintaining voltage of about 20V after breakdown indicates that the discharge mode of these two processes is in the form of an arc.

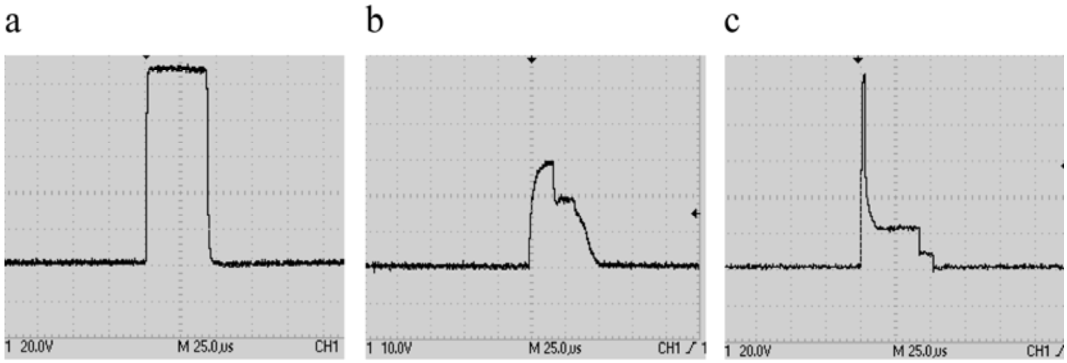

Fig. 4.8 Typical waveforms of (a) applied voltage, (b) ECDM (machining Condition A2), (c) EDM

Parameters Studies

Figs. 4.9-4.12 show the effects of current, duty cycle, pulse duration and electrolyte concentration on the resulting ECDM waveforms. The results show that an increase in current, duty cycle, pulse duration or electrolyte concentration would promote the action of ECDM. This can be recognised by the presence of the Stage II ECDM mechanism in the waveforms when these parameters were increased to a certain value. The results further show that under the conditions of this study, when the values of peak current, duty cycle, pulse duration and electrolyte concentration reached a level of 30A, 1:6, 40μs, 1.4%, respectively, the Stage II mechanism was observed. This could be explained on the basis that an increase of these parameters would lead to an increase of the number of hydrogen bubbles which would cause the voltage between the two electrodes to be increased. This creates a favourable condition for the bubbles to reach the breakdown voltage and thus initiates the occurrence of sparks. The breakdown voltage obtained for all the conditions of this study ranged between 26V and 30V, which agrees well with the theoretical predictions.

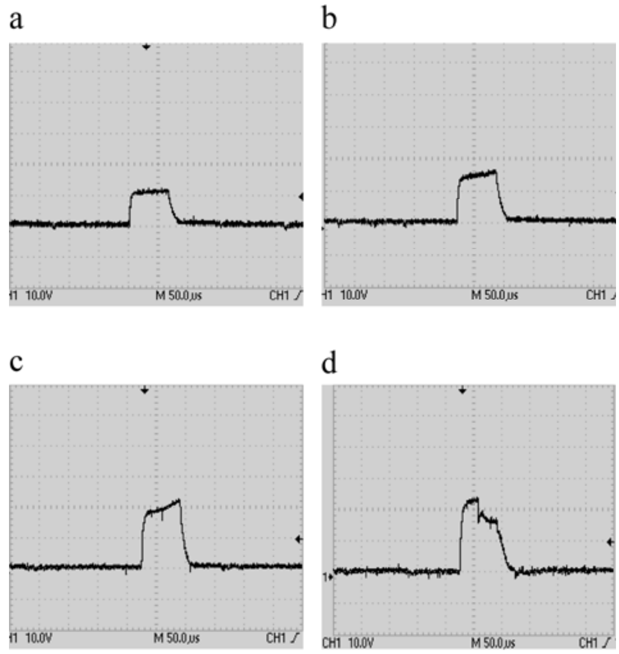

Fig. 4.9 Effect of current on ECDM spark waveform (machining Condition B) [(a)12A, (b)18A, (c)24A, (d)30A]

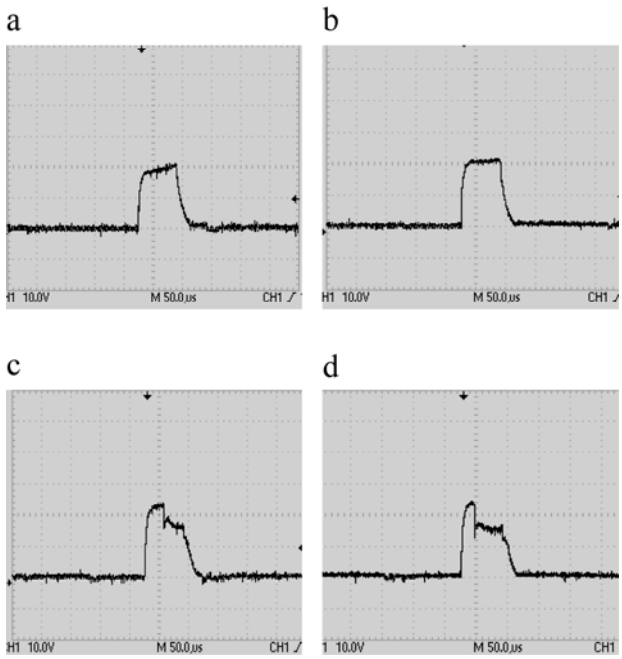

Fig. 4.10 Effect of duty cycle on ECDM spark waveform (machining Condition C) [(a)1:10, (b)1:8, (c)1:6, (d)1:4]

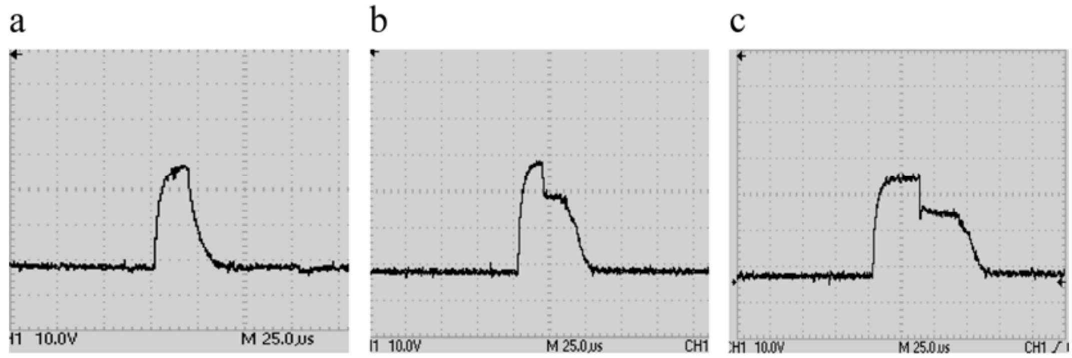

Fig. 4.11 Effect of pulse duration on ECDM spark waveform (machining Condition A) [(a) 24μs, (b) 40μs, (c) 72μs]

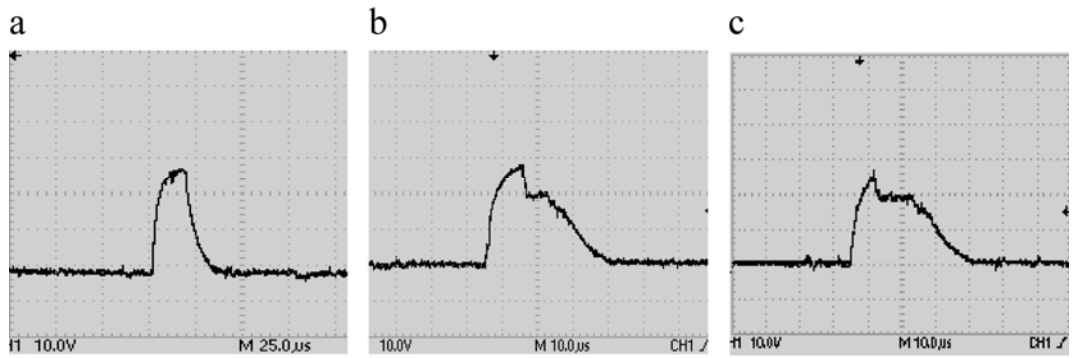

Fig. 4.12 Effect of electrolyte concentration on ECDM spark waveform (machining Condition D) [(a) 1%, (b) 1.4%, (c) 1.6%]

Table 4.1 Processing conditions for the study of the ECDM mechanism

Processing Conditions		Applied Voltage (V)	Pulse Duration (μs)	Duty Cycle	Electrolyte Concentrate (wt%)	Peak Current (A)
A	1	110	24	1:6	1	30
	2		40			
	3		72			
B	1	110	72	1:6	1.6	12
	2					18
	3					20
	4					30
C	1	110	72	1:10	1.6	30
	2			1:8		
	3			1:6		
	4			1:4		
D	1	110	24	1:6	1	30
	2				1.4	
	3				1.6	

Craters and Debris

Figs. 4.13 (a) and (b) show typical machined surfaces of MMCs by ECDM and EDM respectively. The craters resulting from single pulse ECDM and EDM resemble a circular shape with a rough projection at the circumference; the morphology is typical of an arc effect. This observation is evidence that the discharge mode of both the ECDM and EDM processes is in the form of an arc. The crater volume was measured using a three dimensional optical device (Alicona IFM G4). The equipment measured the volume of the cavity below the workpiece surface. Five measurements were taken for both processes, and the relative standard deviation (RSD) of the measurements was found to be within 2%. The measurements for ECDM were all lower than those of the EDM. The average values obtained for

ECDM and EDM were 5.8×10^5 μm^3 and 8.1×10^5 μm^3 respectively. It is apparent that under a similar single pulse processing condition, the EDM process resulted in the removal of a larger volume of material. Since for ECDM, the total energy is roughly divided into two parts, the electrochemical energy and the arc energy, therefore it is within expectation that the crater volume of ECDM is smaller than that of EDM. It is considered that, due to the nature of ECM, which is a time consuming dissolution process, the ECM phase would not increase the material removal rate considerably. Therefore, in theory, the EDM process is likely to have a higher material removal rate than the ECDM process. However, in practice, the overall material removal rate of ECDM was found to be higher than that of EDM in machining particulate MMCs [94]. This is made possible due to a more stable machining condition can be obtained for the ECDM process, for a large machining gap is present and thus improves the condition for the ceramic reinforcement to be washed away from the gap. A more detailed study on material removal volume for different processing conditions was conducted under single pulse and continuous pulsing conditions, and the results are presented in Sections 4.2 and 4.3 respectively.

In examining both the ECDMed and EDMed surfaces, it is obvious that re-solidification occurred. Moreover, some re-solidified debris can also be found on the surfaces. Therefore melting and vaporization should be the major material removal mechanism. However, micro-cracks observed in both the surfaces suggest that spalling might also be involved in the material removal process (Fig. 4.14). Fig. 4.15a and Fig. 4.15b show some of the debris that had been collected during ECDM and EDM, respectively. For both the ECDM and EDM experiments, a continuous pulsing time of three minutes was employed. The similarity in morphology of the debris resulting from these two processes support the idea that the discharge modes of the ECDM and EDM processes are alike and in the form of an arc. The debris size was measured using a particle size distribution analyzer (Horiba CAPA-700). Five measurements were taken for both debris collected after the EDM and ECDM experiments, the median particle diameter and the maximal particle diameter of the former were both found to be larger than those of the latter (Fig. 4.16). The median diameter of the debris for EDM and ECDM was 35μm and 23μm, respectively, while the maximal diameter for EDM was above 100μm and which for ECDM was about 80μm. The smaller median and maximal debris sizes for the ECDM process indicate that the arc energy of ECDM is likely to be smaller than that of the EDM process. Again, this can be argued from the total energy point of view, as discussed above.

To study any phase change that might have occurred during ECDM and EDM, the x-ray diffraction (XRD) patterns of the machined surfaces of both the ECDM and EDM specimens were obtained. A comparison of the XRD patterns shows that an Al_4C_3 phase is present in the EDM specimen but not in the ECDM specimen (Fig. 4.17). An examination of the EDM specimen confirms that the needle-like Al_4C_3 phase is present in areas directly next to the machined surface (Fig. 4.18). This indicates that aluminium reacted with the SiC particles due to the arc heating effect in the EDM process. However, the Al_4C_3 phase was not detected in the ECDM specimen. This is probably due to the fact that the arc energy of the ECDM process was lower than that of the EDM process. As a result, the re-melt zone and the heat affected zone would be smaller, and the amount of aluminium carbides formed greatly reduced and below the detection limit. Another reason could be that the ECM effect of the ECDM process could dissolve material of the machined surface, and Al_4C_3, even if formed, could have been debonded from the matrix.

a b

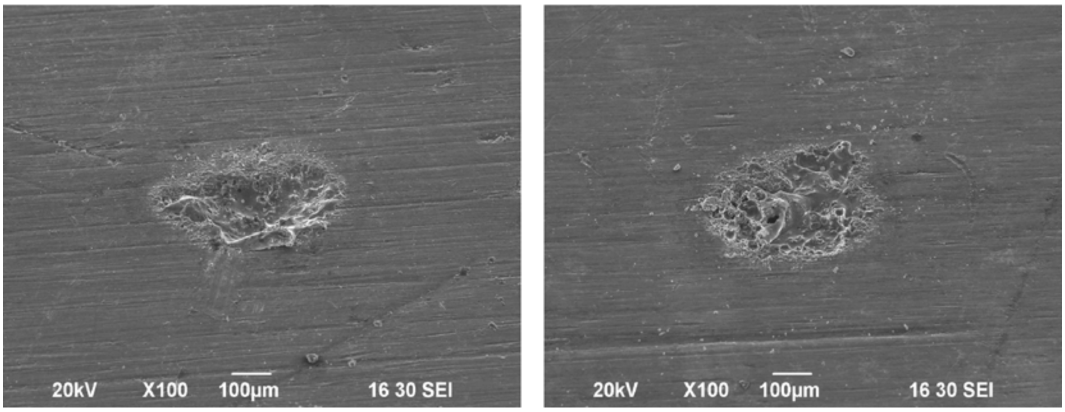

Fig. 4.13 Craters generated by single pulse (a) ECDM and (b) EDM

a **b**

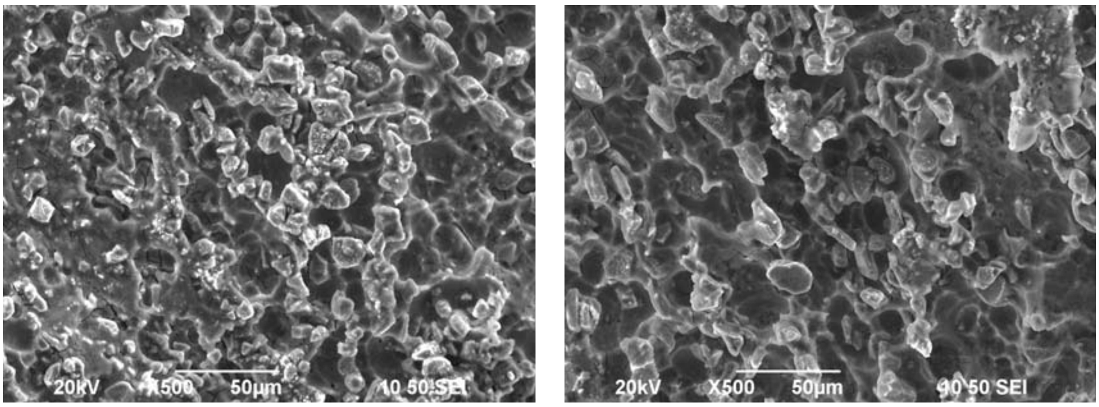

Fig. 4.14 Typical machined surface, showing the presence of re-solidified debris and micro-cracks [(a) ECDMed surface and (b) EDMed surface]

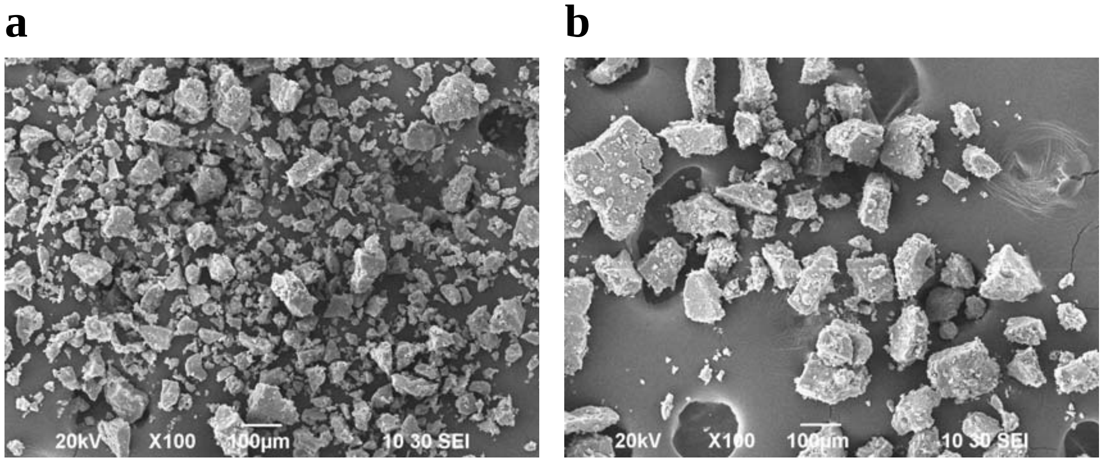

Fig. 4.15 Debris collected from (a) ECDM process and (b) EDM process

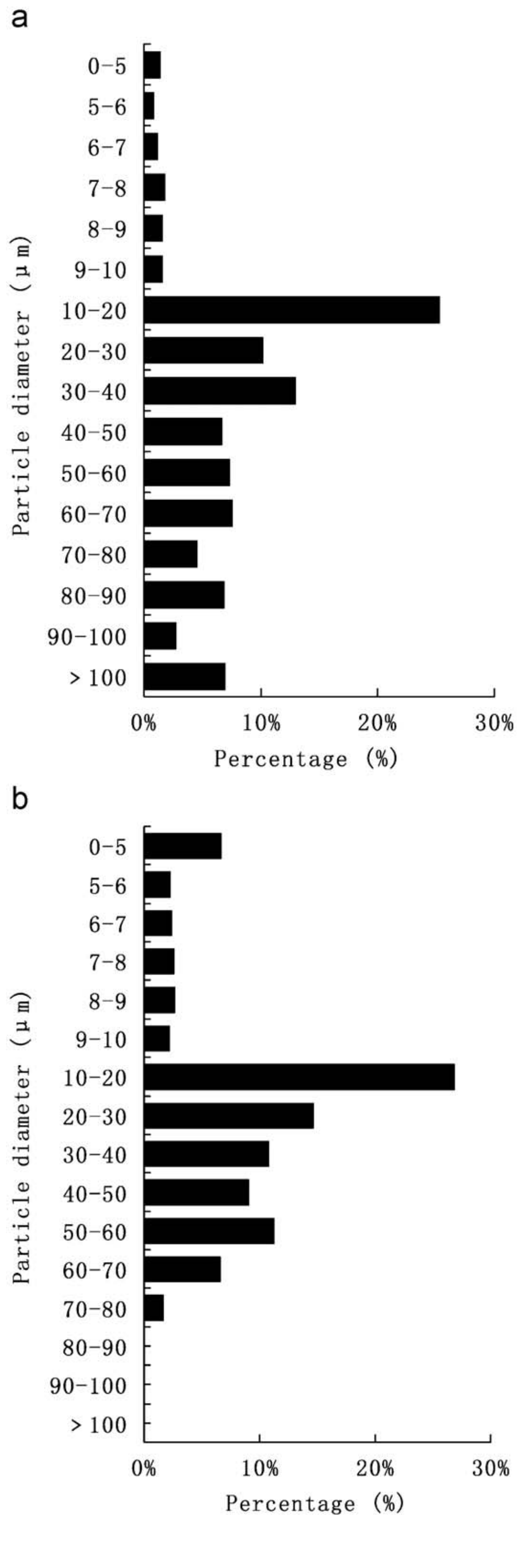

Fig.4.16 Measurements of the distribution of the particle size of the debris collected from the (a) EDM experiment and (b) ECDM experiment

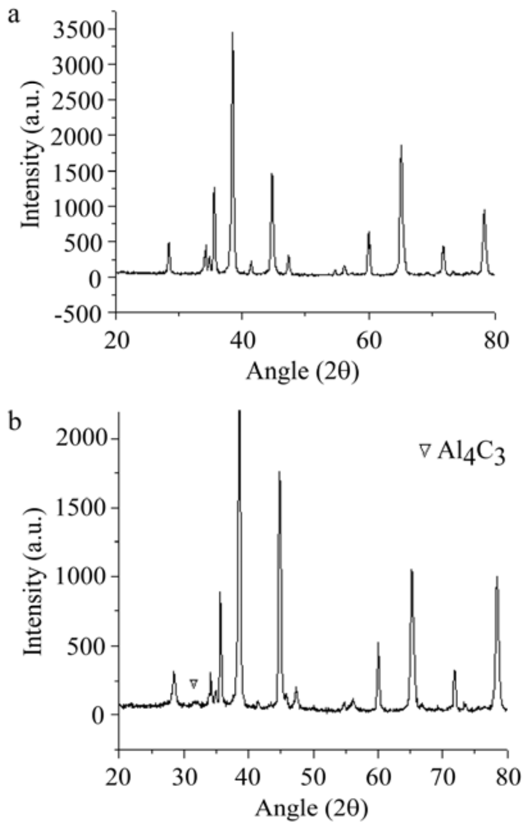

Fig. 4.17 XRD patterns obtained for (a) ECDM specimen, and (b) EDM specimen

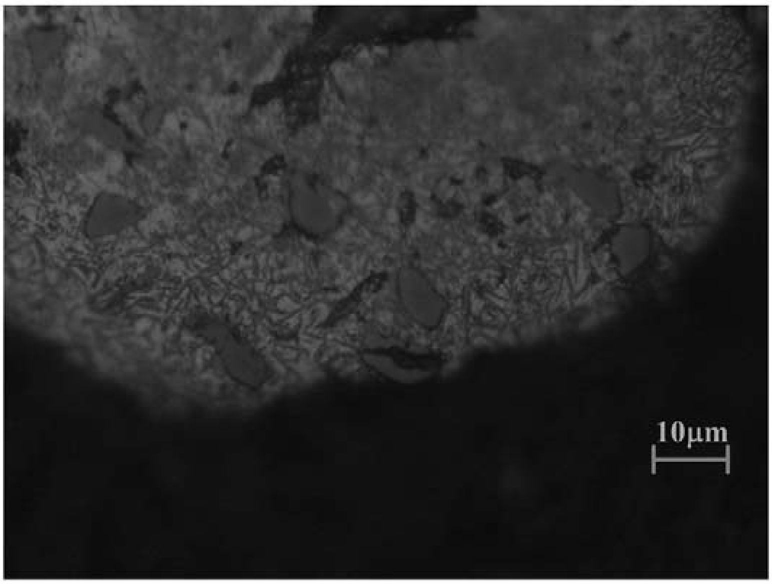

Fig. 4.18 Microstructure in regions close to the EDMed surface, in which needle-like Al_4C_3 phase is observed

4.2 Single Pulse Study of Spark Crater

This section further studies the effects of spark gap and electrical processing parameters on discharge behaviour as well as spark crater volume under the ECDM environment.

4.2.1 Experimental approach

For the ECDM experiments, a $NaNO_3$ electrolyte was employed as the spark dielectric medium. For comparison purposes, experiments were also conducted using a water-based emulsion to represent an EDM processing condition with a relatively weak electrolysis action. The tool-electrode used was a 1mm diameter carbon steel cylinder. The workpiece material was a particulate reinforced aluminium alloy 6061 with 10-vol% Al_2O_3. The material was supplied in the form of 10mm thick rolled plates with the reinforcement phase having a nominal size of 21μm. The crater volume was measured using a 3 dimensional optical device (Alicona IFM G4). The equipment measured the volume of the cavity below the workpiece surface. Five measurements were taken for each single processing condition and the mean value was obtained. The processing conditions are given in Table 4.2.

Table 4.2 Processing conditions for the study of gap distance on crater volume

Processing Conditions		Media	Pulse Duration (μs)	Applied Voltage (V)	Peak Current (A)	Gap Distance (μm)
	1					1
A	2	Emulsion	200	90	35	2.5
	3					7.5
	1	Electrolyte				2.5
B	2		200	90	35	10
	3	(2.5%$NaNO_3$)				20
	4					30

.

4.2.2 Results and discussion

4.2.2.1 Effect of spark gap on crater volume

Figs. 4.19, 4.20, 4.21 show the morphology of some typical single pulse formed carters processed in emulsion with different spark gaps of 1μm, 2.5μm and 7.5μm, respectively. Their processing conditions are given in Table 4.2, which correspond to Conditions A1, A2 and A3, respectively. The volumes of the cavity measured for these three conditions were $25.5\times10^5\mu m^3$, $30\times10^5\mu m^3$ and $39\times10^5\mu m^3$ respectively (Fig. 4.22). The RSD of the volume measurements was found to be within 2%. The results indicate that the larger the spark gap, the higher was the volume of removal. Moreover, a more uniform crater with less re-solidified material around the perimeter was obtained when the spark gap was increased to 7.5μm. All these results show that, under an EDM predominately processing condition and within the range of this study, a wider gap would facilitate the removal of material from the crater. At this stage the reason(s) for this is still not clear, however, it is considered that the dynamic characteristics of the ionised column of emulsion fluid may play an influential role, and further investigation is required.

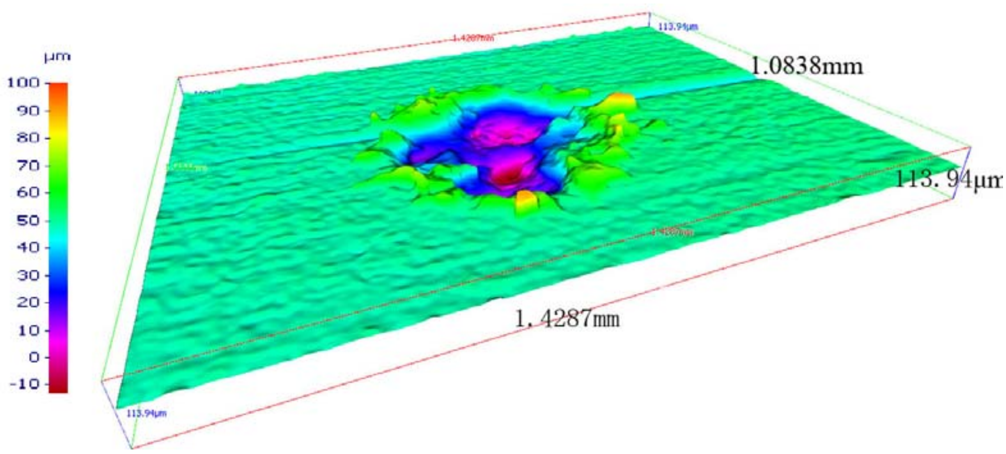

Fig. 4.19 Morphology of the crater produced using the water-based emulsion and a spark gap of 1 μm

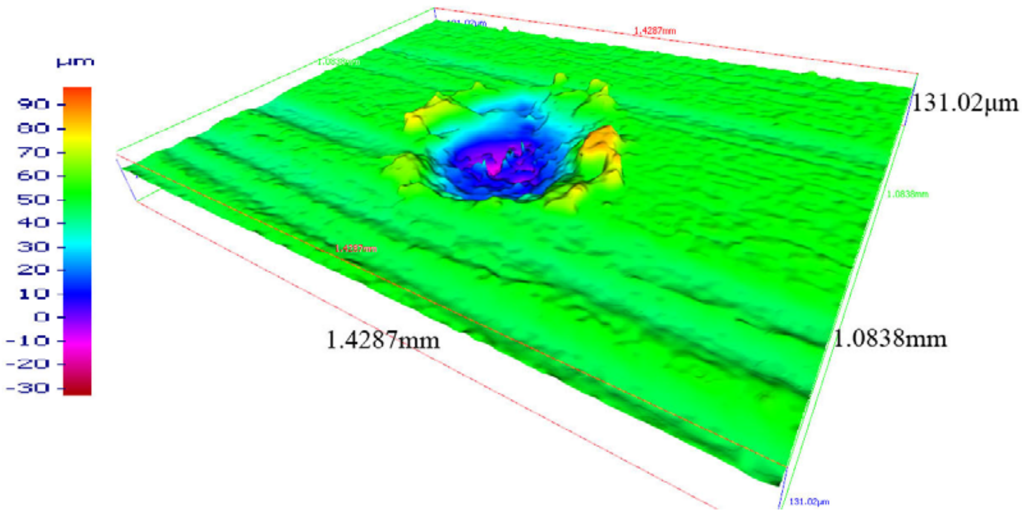

Fig. 4.20 Morphology of the crater produced using the water-based and a spark gap of 2.5μm

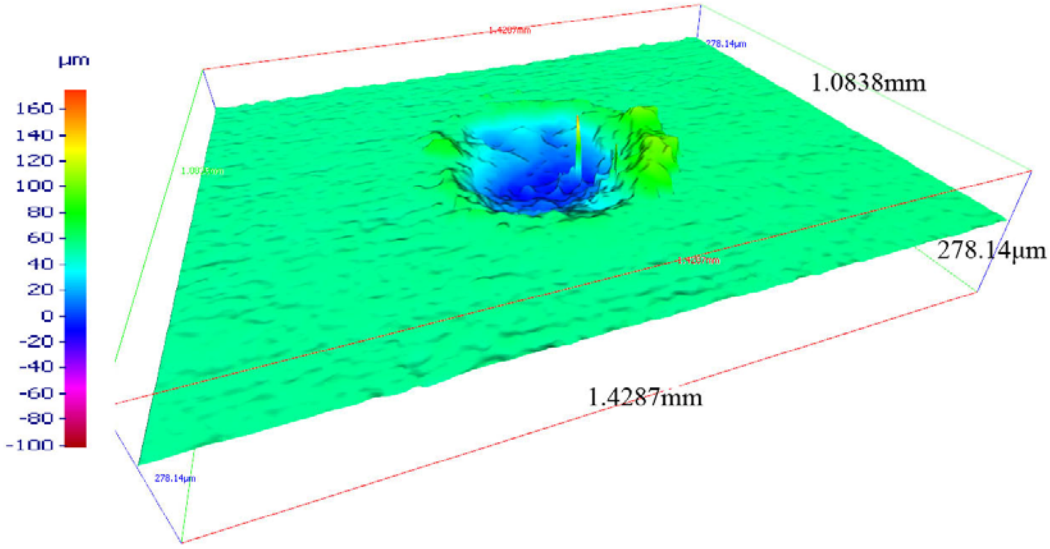

Fig. 4.21 Morphology of the crater produced using the water-based emulsion and a spark gap of 7.5μm

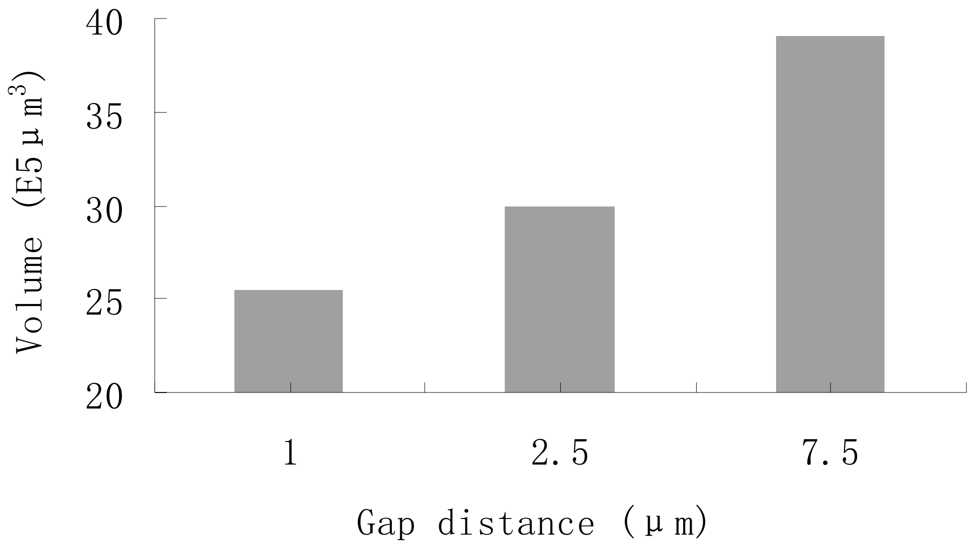

Fig. 4.22 Volume of the cavity measured for EDM craters of different gap distances

Turning now to ECDM processing, Fig. 4.23, Fig. 4.24, Fig. 4.25 and Fig.

4.26 show the morphology of the craters under different spark gaps conditions of 2.5μm, 10μm, 20μm and 30μm, respectively. Their respective processing conditions are given in Table 4.2 as conditions B1, B2, B3, and B4. The crater volumes measured for these conditions follow the sequence of 10μm (volume: 52.5×10^5 μm^3) > 2.5μm (volume: 33×10^5 μm^3) > 20μm (volume: 31×10^5 μm^3) > 30μm (volume: 20×10^5 μm^3) (Fig. 4.27). Differ from the EDM process, the ECDM results show that the crater volume decreased with increasing spark gap distance when the spark gap was relatively large.

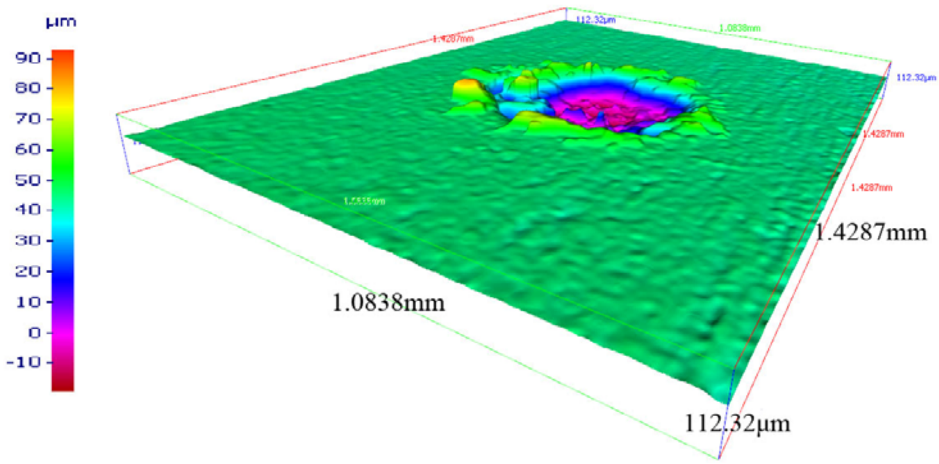

Fig. 4.23 Morphology of the crater produced using the $NaNO_3$ electrolyte and a spark gap of 2.5μm

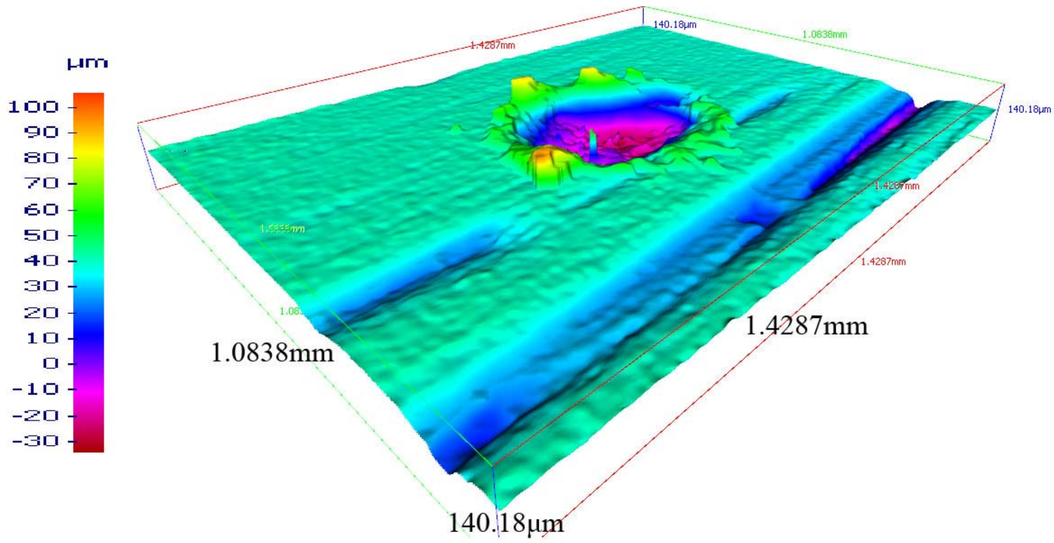

Fig. 4.24 Morphology of the crater produced using the $NaNO_3$ electrolyte and a spark gap of 10µm

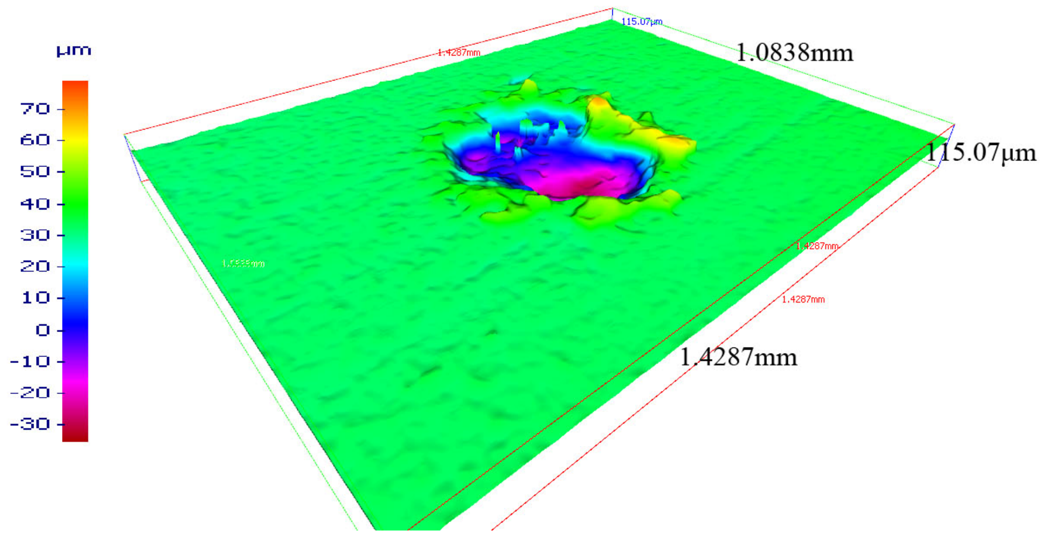

Fig. 4.25 Morphology of the crater produced using the $NaNO_3$ electrolyte and a spark gap of 20µm

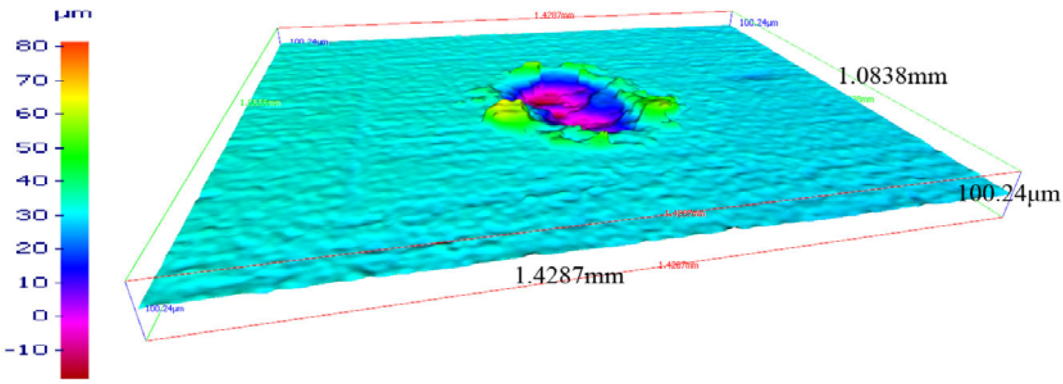

Fig. 4.26 Morphology of the crater produced using the $NaNO_3$ electrolyte and a spark gap of 30µm

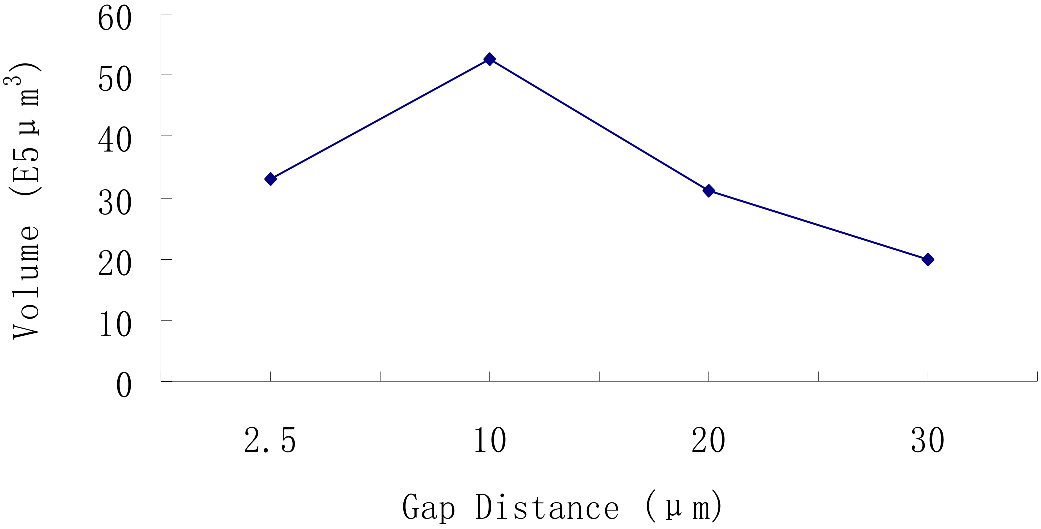

Fig. 4.27 Volume of the cavity measured for ECDM craters of different gap distances

The reason for a smaller crater volume when processing at large gaps (between 10µm and 30µm) is elucidated by analysing the voltage waveform with respect to spark ignition-delay for a range of spark gaps. Figs. 4.28 (a-d) show the voltage waveforms obtained for processing spark gaps of 2.5µm, 10µm, 20µm and

30μm, respectively. These figures clearly show that ignition-delay increases with the increasing of spark gap distance. In other words, when the spark gap increases, the arc maintaining period is reduced. This also means that the spark energy would be reduced. As a result, the crater volume would become smaller when the processing gap is relatively large (Fig. 4.29). On the other hand, spark ignition-delay is not obvious for the conditions of small spark gaps, for these cases, other factors, such as the characteristics of the ionised fluid column might govern the crater removal volume.

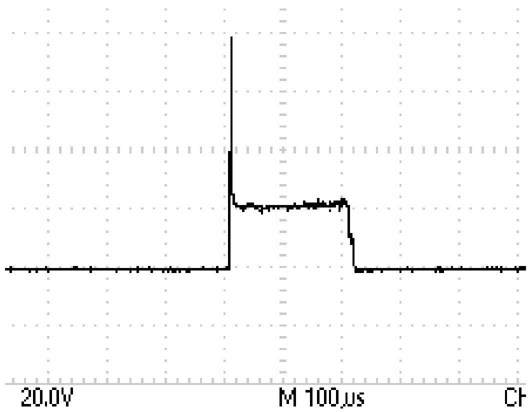

(a)

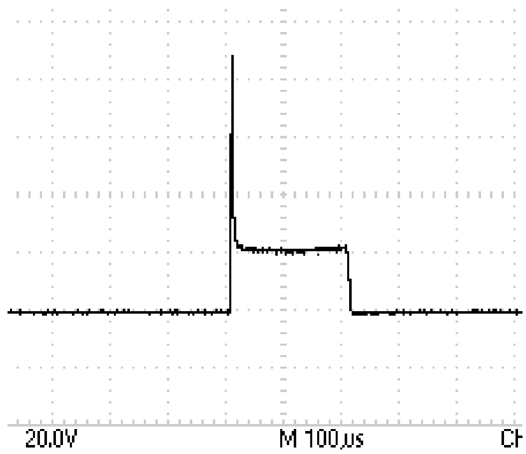

(b)

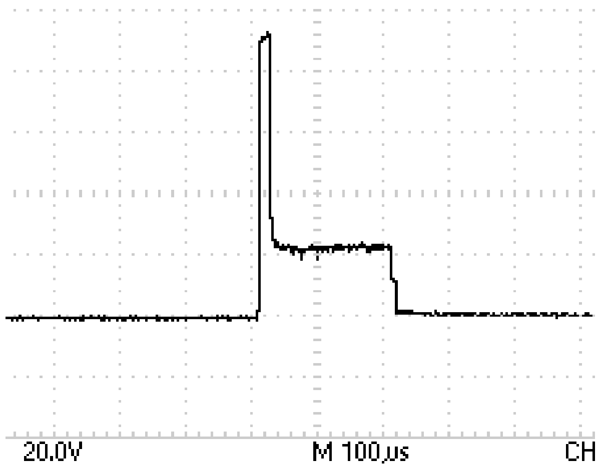

(c)

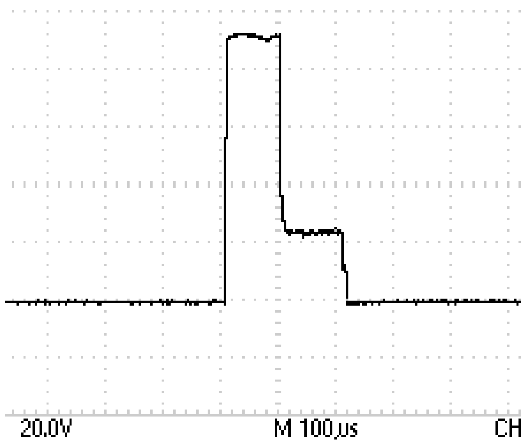

(d)

Fig. 4.28 Typical voltage waveforms obtained for the conditions of spark gap distances of (a) 2.5μm, (b) 10μm, (c) 20μm, (d) 30μm; the applied voltage was set at 90V for all these cases

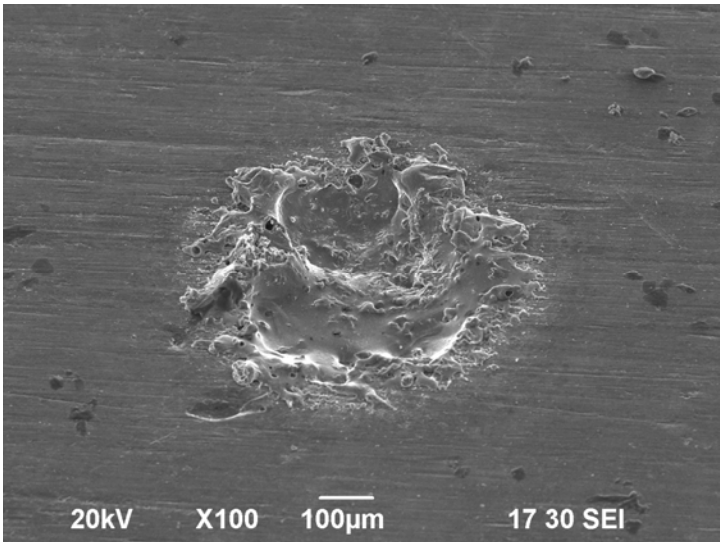

(a)

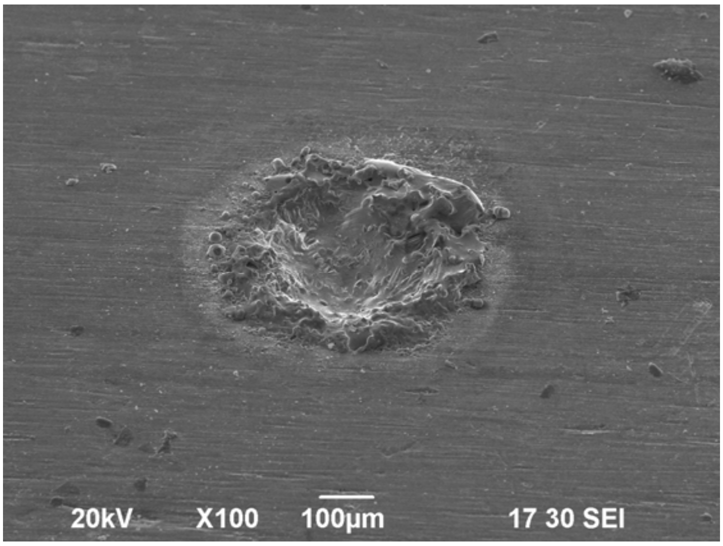

(b)

Fig. 4.29 SEM images of the craters produced using [(a) spark gap of 20µm, and (b) spark gap of 30µm]

In this investigation, it was also found that the processing temperature, i.e. the bath temperature, has a significant effect on ignition delay. The voltage waveforms obtained for a range of processing temperatures between 25°C and 60°C are presented in Figs. 4.30 (a-c). Other processing parameters were, the applied voltage was fixed at 90V, while the spark gap was fixed at 20μm (Table 4.3). Figs. 4.30 (a-c) clearly show that the ignition-delay decreases with an increase in processing temperature. For the case of processing temperature of 60°C (Fig. 4.30c), ignition-delay virtually disappeared. At this stage, the reasons for this temperature effect is still not clear, however, it is considered that an increase in temperature might have an effect on the electrochemical reactions of the ECDM process and as such could affect the hydrogen bubble formation and growth rate. This would directly influence the discharge behaviour. Moreover, an increase in temperature could accelerate bubbles to arrive at positions of high electric field strengths. As a result, the ignition delay time would be reduced. In other words, when the processing temperature increases, the arc maintaining period is prolonged. This means that the total spark energy would be increased. This would result in an increase in crater volume.

Table 4.3 Processing conditions for the study of processing temperature effect

Processing Conditions	Media	Pulse Duration (μs)	Applied Voltage (V)	Peak Current (A)	Gap Distance (μm)	Temp (^{0}C)
A	2.5%$NaNO_3$	200	90	35	20	25
B	2.5%NaNO3	200	90	35	20	40
C	2.5%$NaNO_3$	200	90	35	20	60

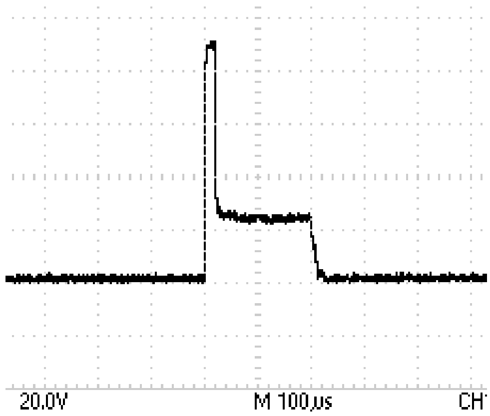

(a)

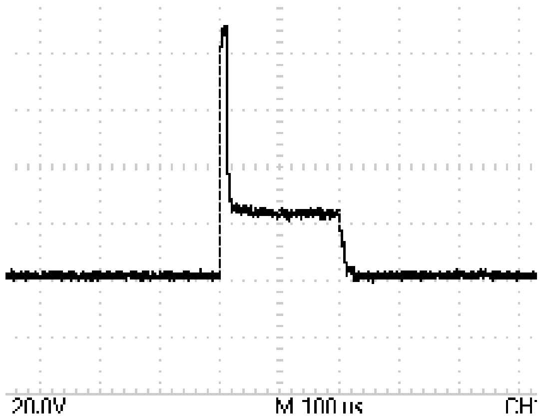

(b)

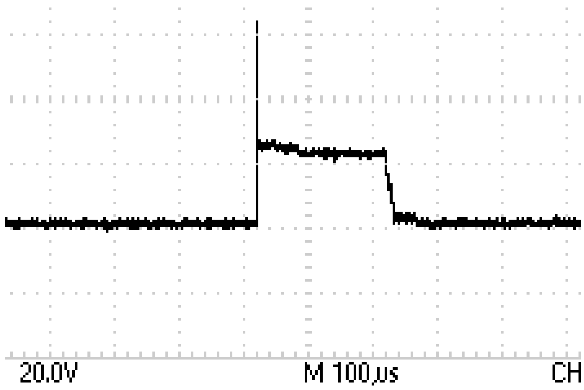

(c)

Fig. 4.30 Typical voltage waveforms obtained for processing temperatures of (a) 25^0C, (b) 40^0C, (c) 60^0C

4.2.2.2 *Effect of current and pulse duration on crater volume*

Figs. 4.31(a-e) show the craters created by single pulse for a range of peak currents between 30A and 6A, whereas the pulse duration, the applied voltage and the spark gap were fixed at 200μs, 90V and 10μm, respectively (Table 4.4). All the craters resemble a circular shape with re-solidified material found at the surface. These figures also show that the crater volume decreased considerably when the current was decreased from 30A to 6A (Fig. 4.32). This is believed to be simply due to a reduction of total energy because of the decrease of current.

Table 4.4 Processing conditions for the study of peak current effect

Processing Conditions	Media	Pulse Duration (μs)	Applied Voltage (V)	Peak Current (A)	Gap Distance (μm)
A	2.5%$NaNO_3$	200	90	30	10
B	2.5%$NaNO_3$	200	90	24	10
C	2.5%$NaNO_3$	200	90	18	10
D	2.5%$NaNO_3$	200	90	12	10
E	2.5%$NaNO_3$	200	90	6	10

A similar energy effect was also found if the pulse duration was reduced. Figs. 4.33 (a-d) show the craters produced by single pulse for pulse durations between 320μs and 48μs, whereas the current, the applied voltage and the spark gap were fixed at 30A, 90V and 10μm, respectively (Table 4.5). It is clear from these figures that the crater volume decreased greatly when the pulse duration decreased from 320μs to 48μs (Fig. 4.34). Again, this was attributed to a decrease in the total ECDM energy when the pulse duration was reduced. In fact, the ECDM energy composes of ECM energy and EDM arc energy, and they play a different role in material removal. Their role and contribution to material removal is discussed in Chapter 5.

Table 4.5 Processing conditions for the study of pulse duration effect

Processing Conditions	Media	Pulse Duration (μs)	Applied Voltage (V)	Peak Current (A)	Gap Distance (μm)
A	2.5%$NaNO_3$	320	90	30	10
B	2.5%$NaNO_3$	200	90	30	10
C	2.5%$NaNO_3$	120	90	30	10
D	2.5%$NaNO_3$	48	90	30	10

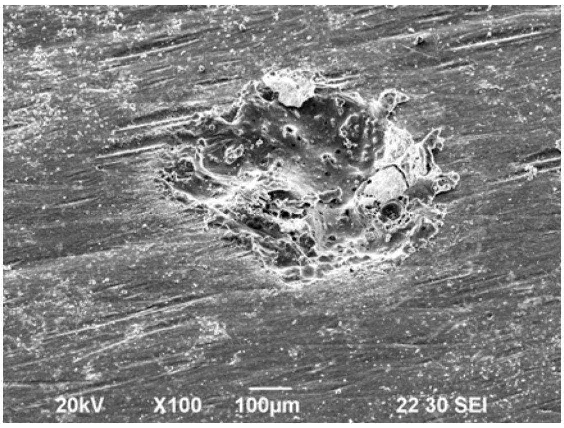

(a)

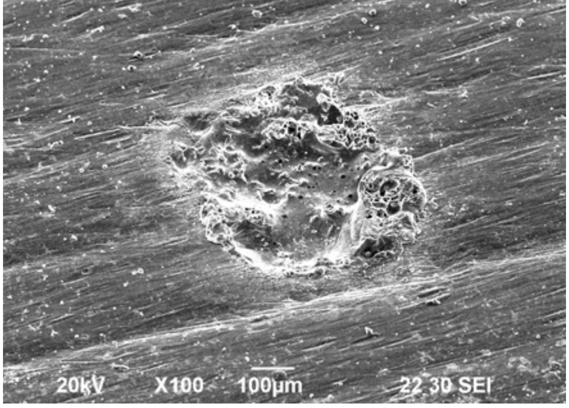

(b)

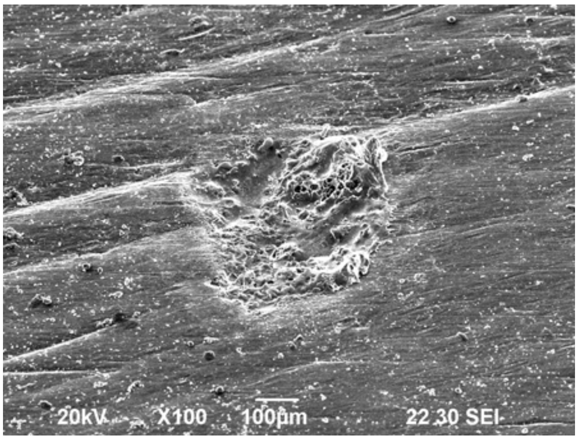

(c)

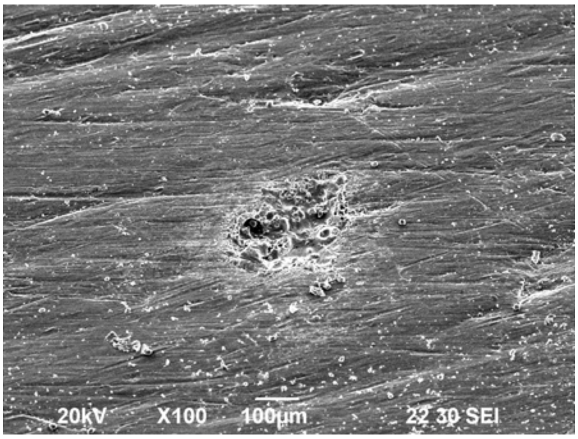

(d)

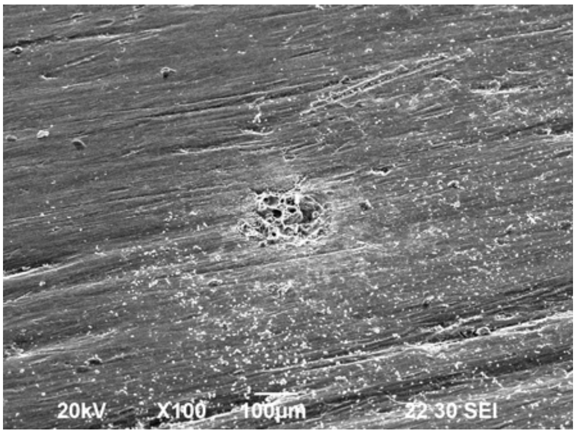

(e)

Fig. 4.31 SEM micrographs of the craters produced using peak currents of (a) 30A (b) 24A, (c) 18A, (d) 12A, (e) 6A

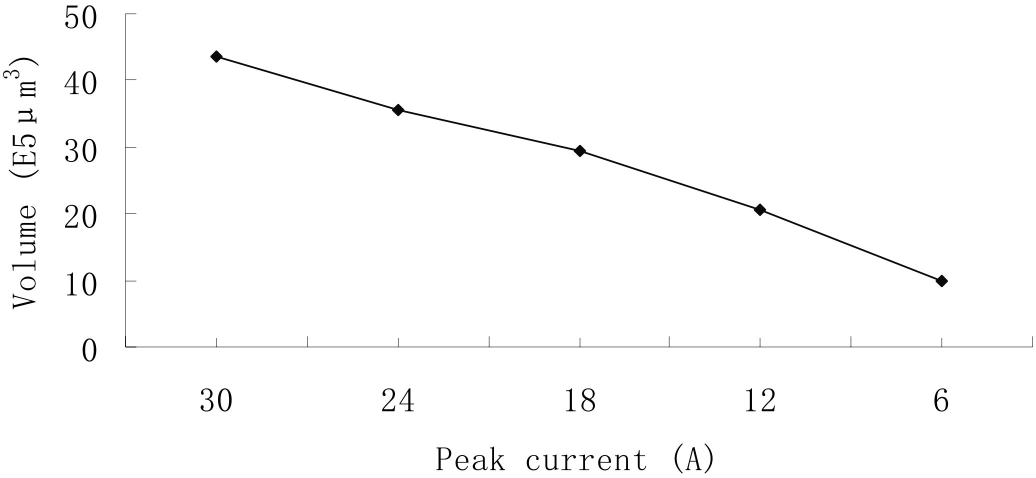

Fig. 4.32 Crater volume as a function of peak current

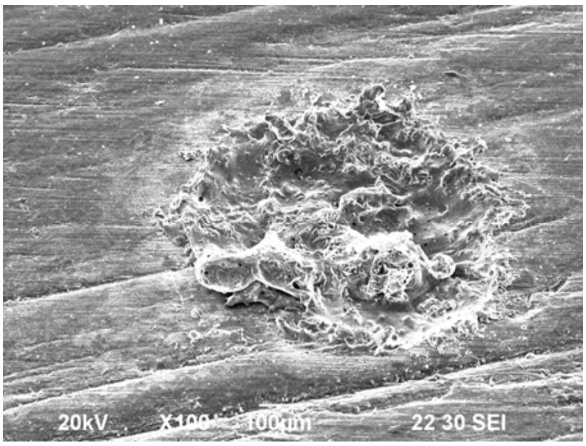

(a)

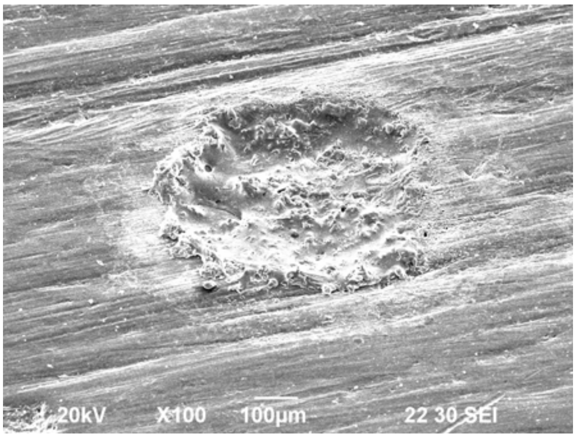

(b)

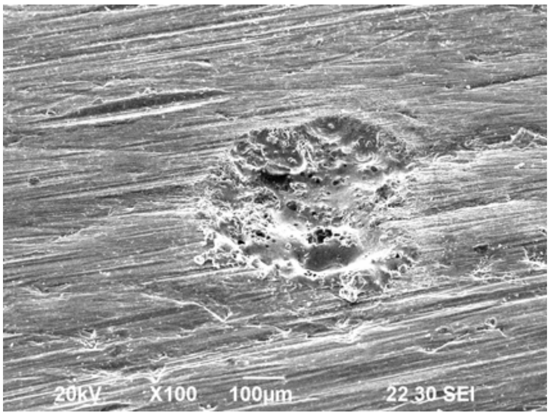

(c)

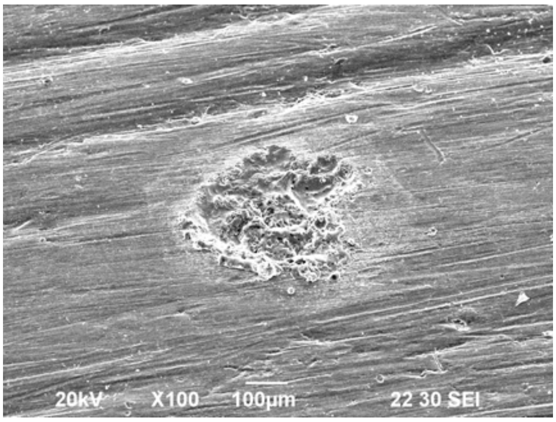

(d)

Fig. 4.33 SEM micrographs of the craters produced using pulse durations of (a) 320μs, (b) 200μs, (c) 120μs, (d) 48μs

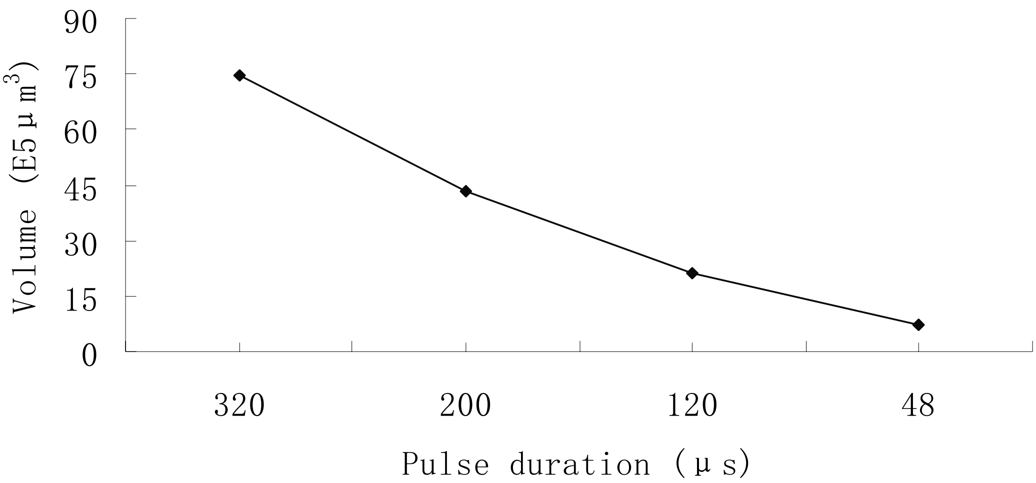

Fig. 4.34 Crater volume as a function of pulse duration

4.3 Continuous Pulse Studies of MRR in ECDM

In the previous section, the relationship between crater volume and various processing parameters under single pulse conditions were studied. However, under single pulse conditions, the effect of ECM could not be easily assessed because the ECM process is a time consuming dissolution process. Recognising this, the effects of processing parameters on material removal rate (MRR) in practical ECDM were therefore studied using continuous pulse experiments and orthogonal analysis. The study also investigated the separate effect of EDM and ECM on material removal.

4.3.1 Experimental details

The MMCs employed in this experiment are particulate reinforced aluminium 6061 with 10-vol% Al_2O_3 (10ALO) or 20vol% Al_2O_3 (20ALO). The materials were in the form of rolled plates, having a thickness of 36mm, with reinforcement particles of nominal size 21μm. For the machining experiment, a widely used W-EDM machine, which employs an extremely high travelling speed of 8m/s of molybdenum wire (0.18mm in diameter) as the tool electrode, was used (WEDM-HS). The advantage of using a fast travelling wire is that a relatively stable spark gap condition could be obtained. This is due to the fact that the eroded debris can be readily removed by the fast travelling wire [95]. Using such a machine, the material removal rate could be readily obtained. In the experiment, a water-based emulsion was employed as the machining fluid instead of deionised water that is normally used for W-EDM. The emulsion has an electrical resistance of 700Ω.cm. Since the electrical conductivity of the emulsion used is some 20 to 500 times higher than that of deionised water, the discharge process would be accompanied by relatively weak electrolysis action.

It is considered that the relative strength of the ECM component of the WEDM-HS process would have a significant effect on the overall machining behaviour. To assess the effect of ECM, $NaNO_3$ is added to the emulsion to increase its electrical conductivity. The amount of $NaNO_3$ varies between 0.25wt% and 1wt%. In so doing, the electrical resistance of the emulsion will change from 240Ω.cm to 80Ω.cm. Moreover, an orthogonal experimental design was adopted to investigate the effects of the various discharge parameters, as well as the concentration of the electrolyte on machining efficiency.

4.3.2 Results and discussion

4.3.2.1 Effects of pulse duration on material removal rate

Fig. 4.35 summarizes the effect of pulse duration on MRR of both the 10ALO and 20ALO composites under the condition of a peak pulse current of 9A and an applied voltage of 100V. As was expected, a higher ceramic phase percentage resulted in a drop in MRR, however, somewhat unexpectedly, the MRR decreased with an increase of pulse duration when the duration exceeded 8μs. This is rather different from the normal behaviour in cutting monolithic metallic materials. The results were not anticipated because a higher pulse duration means a higher energy input and should result in a higher MRR. In fact, the results of the single pulse experiment show that a longer pulse duration would lead to a larger crater volume (see Fig. 4.33 and Fig.4.34). The major reason for a lower MRR at relatively long pulse durations under the continuous pulse condition could be that, though initially a relatively large volume of material could be removed from the workpiece, the MRR would drop if debris, which comprises the reinforcing ceramic phase, is trapped in the spark gap and cannot be carried away quickly enough by the cutting fluid. It is likely that this phenomenon occurred in the experiment, since the nominal size of the ceramic reinforcement phase is 21μm which is large when compared to the size of the spark gap existing in WEDM-HS, which is considered to range from 10μm to 20μm [96]. In a situation where a significant number of ceramic particles are trapped in the gap, the cutting process becomes unstable and material removal is reduced. Thus, it appears that in order to benefit from the high cutting rate under the condition of long pulse duration, the size of the reinforcement phase should be smaller than the spark gap.

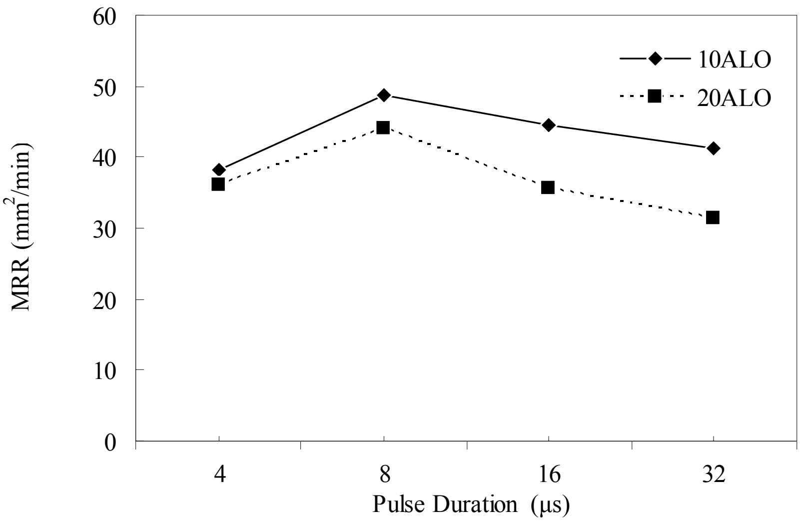

Fig. 4.35 Effect of pulse duration on MRR

4.3.2.2 Effect of current on material removal rate

Fig. 4.36 shows the effect of cutting current on MRR, where the pulse duration and the applied voltage were fixed at 16μs and 100V, respectively. It is apparent that the MRR for both composites increased greatly when the peak current increased from 3A to 18A. One would expect that, similar to the effect of pulse duration, an increase in current would result in a drop in MRR, as a higher energy input is provided. However, the results show that MRR increased when the current was increased. This means that the machining condition was stable, and effective material removal was achieved at high cutting currents.

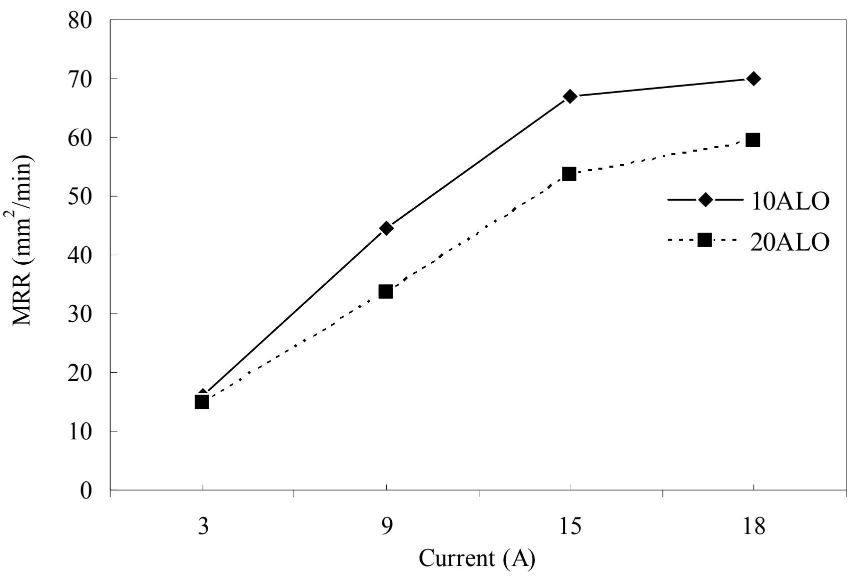

Fig. 4.36 Effect of current on MRR

The reason for the high MRR at conditions of high currents can be elucidated by analyzing the discharge voltage waveform. The typical waveforms obtained at conditions of 3A and 18A for material 20ALO are shown in Fig. 4.37a and Fig. 4.37b, respectively. For the low current condition, the material removal process was mainly dominated by the EDM effect, in which about half of the waveforms show a kind of unstable discharge condition (second waveform in Fig. 4.37a). That is to say, under the condition of low current, energy utilization was low, and this could be due to inefficient removal of the eroded debris. However, for the high current condition, virtually all waveforms exhibit a stable discharge condition characteristic (Fig. 4.37b), and such a condition would facilitate the action of ECM. In the present experiment, due to the conductive nature of the emulsion, and a high current condition, the ECM effect is manifested. It is believed that the ECM effect not only increases the amount of material to be eroded, but also enlarges the cutting gap. Once the cutting gap is enlarged, the ceramic particles can be discharged more readily and hence a stable cutting condition is maintained.

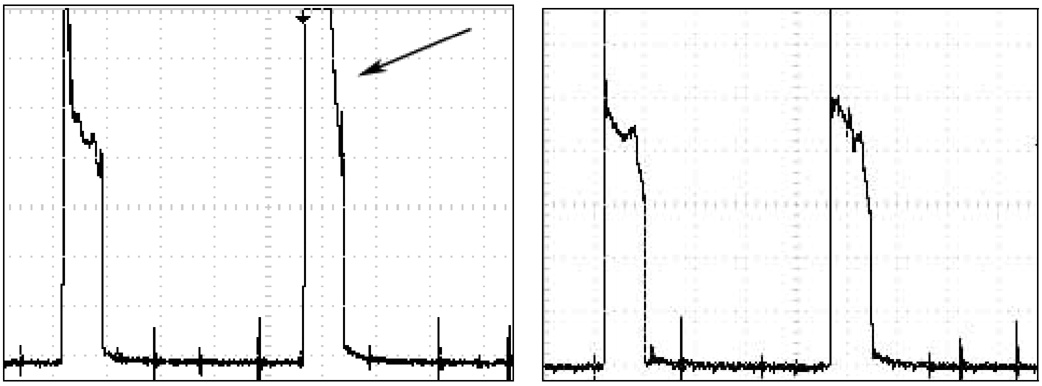

(a) (b)

Fig. 4.37 Voltage waveforms obtained for peak currents (a) 3A, and (b) 18A of the 20ALO material

4.3.2.3 Effect of electrolyte concentration on material removal rate

The effect of ECM on material removal in ECDM process was further studied by varying the amount of $NaNO_3$ (electrolyte) in the emulsion. In the experiment, the pulse duration and the peak current were kept at 16μs and 18A, respectively, while the applied voltage was fixed at 100V. Fig. 4.38 shows the results of the 20ALO composite: the MRR exhibits an up-and-down trend as the amount of $NaNO_3$ is increased.

This finding can be explained by studying the voltage waveforms in Fig. 4.39a to Fig. 4.39d. It is apparent from the figures that the ECM effect increased and the EDM effect decreased when the concentration of the electrolyte was increased. In fact, the EDM effect appears to have disappeared at concentrations of 0.5wt% and 1wt%.

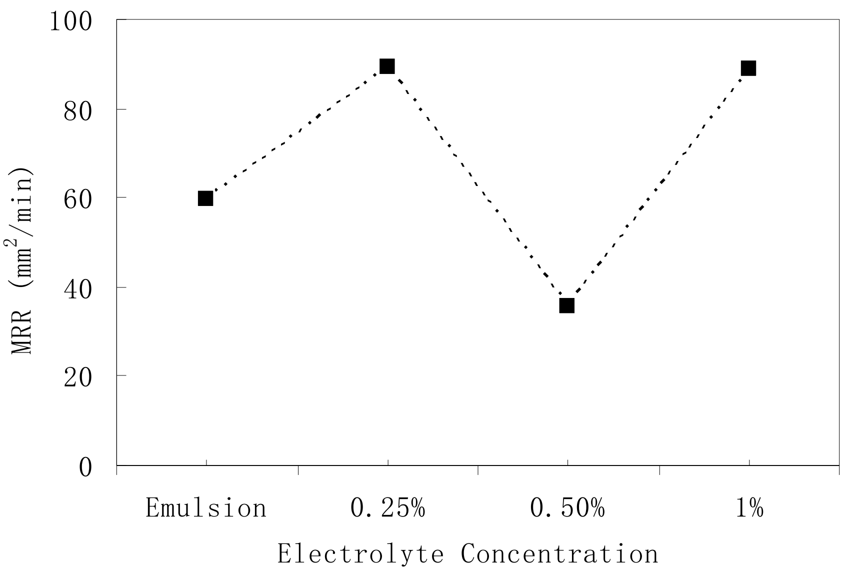

Fig. 4.38 Effect of the concentration of electrolyte on MRR for the 20ALO material

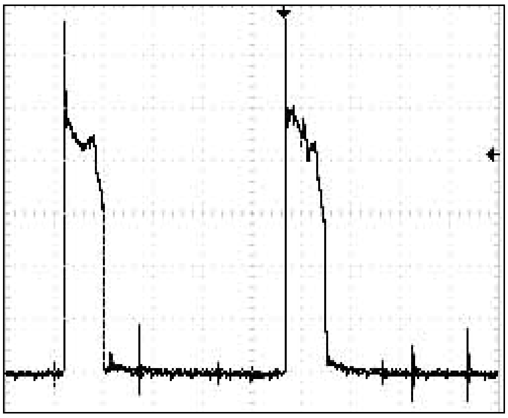
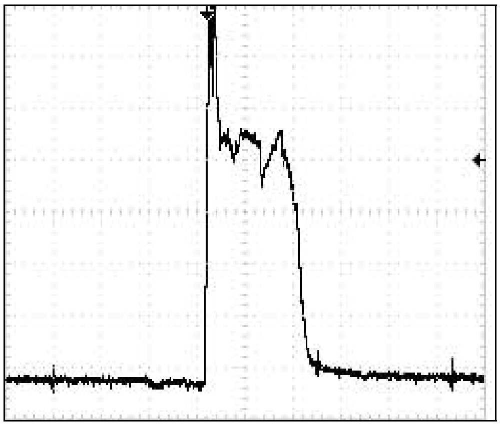

(a) (b)

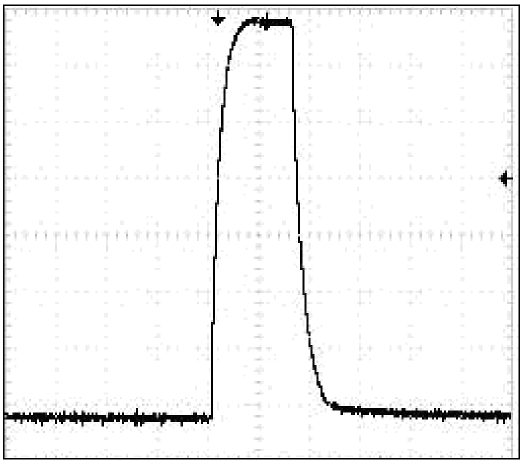


(c) (d)

Fig. 4.39 Voltage waveforms for the conditions of different electrolyte concentrations for the 20ALO material, (a) zero %, (b) 0.25%, (c) 0.5%, (d) 1%

Without the addition of $NaNO_3$, the ECM effect was found to be relatively weak (Fig. 4.39a). When the electrolyte concentration was increased to 0.25wt%, a relatively high discharge current, together with a rather strong ECM effect, were experienced (Fig. 4.39b). At a concentration of 0.5wt%, the EDM effect virtually disappeared (Fig. 4.39c) and the material removal mechanism was basically controlled by ECM. It is worth noting that in this condition, a relatively low current was experienced in the ECM process, that is to say only weak ECM action occurred. As the concentration was further increased to 1wt%, the situation was rather similar to that of the 0.5wt% condition, and the current was significantly higher (Fig. 4.39d). This means that a strong ECM action would be obtained. Therefore, it can be concluded that a high MRR would be obtained providing that either a strong EDM effect is coupled with a moderate ECM effect (Fig. 4.39b), or a strong ECM effect is present (Fig. 4.39d). In the case of a weak ECM effect, without the action of EDM (Fig. 4.39c), the MRR was found to be on the low side. It is considered that under a low ECM current and without the aid of the EDM action, the matrix material will be slowly eroded and it will take some time before the ceramic particles can be totally exposed to the surface. As a result, a low MRR is obtained. The situation is vastly improved when the concentration is 1wt% (Fig. 4.39d). Under this condition, a high current density was used in the ECM process, and the dissolution rate of the matrix material was expected to increase significantly, and this would facilitate the removal of the ceramic phase, and hence a high overall MRR was obtained. The SEM photographs of the machined surface of the 20ALO composite for the four conditions are presented in Fig. 4.40(a-d). These figures show that when both the EDM and ECM are relatively active (Fig. 4.40b), or a strong ECM effect is involved (Fig. 4.40d), less Al_2O_3 particles are present at the surface. This supports the view that a strong ECM activity would give a positive effect on the removal of reinforcing particles.

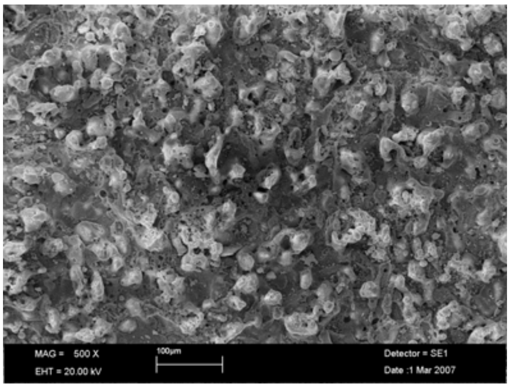

(a)

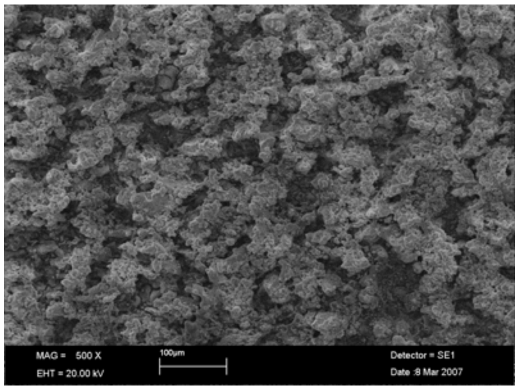

(b)

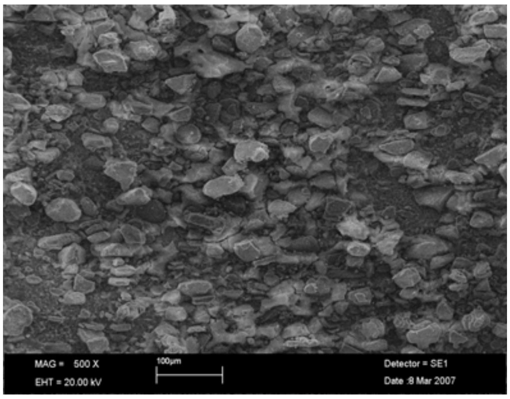

(c)

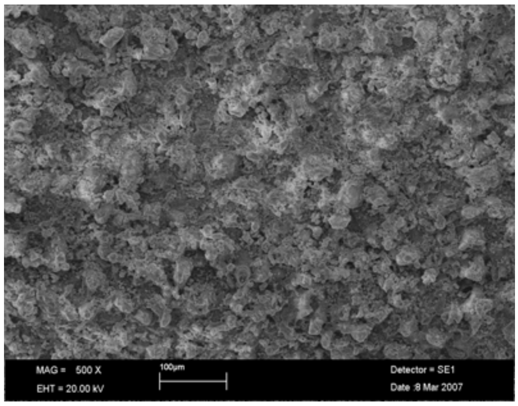

(d)

Fig. 4.40 Corresponding SEM photographs of the machined surface of the four conditions as labelled in Fig. 4.39

4.3.2.4 Orthogonal analysis

An orthogonal design was adopted to determine how significant the effects of the various cutting parameters on MRR were. In the analysis, the concentration of the electrolyte, the pulse duration and the working current were selected to be the three factors to be examined. Each factor is presented at three levels (Table 4.6). Therefore a L_9 (34) table of orthogonal design is established, and the aim is to optimize MRR. Based on this objective, an orthogonal analysis is performed and the results are given in Table 4.7 and Table 4.8 respectively.

With the 10ALO composite, the impact of the different factors follows the sequence of current > pulse duration > electrolyte concentration. At conditions of a peak current of 18A, pulse duration of 32μs and 0.25% electrolyte, the highest MRR is obtained. As for the 20ALO composite, the ranking of the significance of the three factors follows the sequence of current > electrolyte concentration > pulse duration. Within the conditions of the study, the optimum conditions for achieving the highest MRR are: peak current of 15A, pulse duration of 8μs, and 1% concentration.

Table 4.6 Parameter levels for the numerical analysis

Factors/levels	1	2	3
A (Medium)	0.25	0.5	1
B （Pulse duration）	8[μs]	16[μs]	32[μs]
C （Peak Current）	12[A]	15[A]	18[A]

Table 4.7 Results of the orthogonal analysis on MRR for the 10ALO material

Factors Series no.	A 1	B 2	C 3	D 4	MRR [mm^2/min]
1	1	1	1	1	48.7
2	1	2	2	2	59.5
3	1	3	3	3	89.3
4	2	1	2	3	53.5
5	2	2	3	1	66.9
6	2	3	1	2	59.5
7	3	1	3	2	59.5
8	3	2	1	3	35.7
9	3	3	2	1	59.5
Ⅰj	197.5	161.7	143.9		
Ⅱj	179.9	162.1	172.5		
IIIj	154.7	208.3	215.7		
Ⅰj= Ⅰj/3	65.8	53.9	48		
Ⅱj=Ⅱj/3	60	54	57.5		
IIIj=IIIj/3	51.6	69.4	71.9		
R	42.8	46.6	71.8		

Table 4.8 Results of the orthogonal analysis on MRR for the 20ALO material

Factors Series no.	A 1	B 2	C 3	D 4	MRR [mm^2/min]
1	1	1	1	1	44.6
2	1	2	2	2	59.5
3	1	3	3	3	89.3
4	2	1	2	3	59.5
5	2	2	3	1	35.7
6	2	3	1	2	53.5
7	3	1	3	2	107.1
8	3	2	1	3	53.5
9	3	3	2	1	53.5
Ij	193.4	211.2	133.8		
IIj	148.7	148.7	220.1		
IIIj	214.1	196.3	202.3		
Ⅰj= *Ij/3*	64.5	70.4	44.6		
Ⅱj= *IIj/3*	49.6	49.6	73.4		
IIIj=*IIIj/3*	71.4	65.4	67.4		
R	65.3	62.5	86.3		

The results of the above analysis suggest that to achieve the highest MRR for both the 10ALO and 20ALO composite materials using WEDM-HS, and within the conditions of this study, the applied current is the most influential factor between current, pulse duration, and concentration of electrolyte. This result is considered to be reasonable due to the fact that both the EDM and ECM actions are directly governed by the magnitude of the applied current. Therefore, regardless of which of these two actions is dominant in the machining process, current will still play an important role. With regard to the effect of the concentration of electrolyte, the results show that its effect becomes more important as the amount of reinforcing phase increased from 10% to 20%. This could mean that, when machining the 20ALO composite, the ECM activity is dominant over the EDM action in removing the material. Indeed, this was found to be the case when the voltage waveforms of the two materials are compared for different concentrations of the electrolyte (c.f. Fig. 4.39 and Fig. 4.41). For the cutting of the 20ALO composite, a strong ECM activity is observed when the concentration reaches 1% (Fig.4.39d); while for the 10ALO composite, the ECM activity stayed at relatively low levels even at the condition of 1% concentration (Fig. 4.41d). In fact, for the 10ALO composite, the waveforms show that the EDM action was there in the machining process regardless of any change in concentration. In contrast, for the 20ALO composite, the EDM effect disappeared when the concentration reached 0.5% (Fig. 4.39c and Fig. 4.39d). The reasons for this difference in behaviour at this stage it is still not certain, however, it is considered that the current density, the spark gap width, and the amount of hydrogen produced at the cathode are important influential factors. For the 20ALO composite, because of a higher volume of ceramic particles, the surface area of the matrix phase which is exposed to the electrolyte is less than that of the 10ALO composite. As a result, a higher current density would be experienced by the 20ALO composite, and this would favour the ECM action. If a strong ECM action is present, a relatively wide spark gap would be produced. This would discourage EDM action. Moreover, with the 20ALO material, due to a relatively small surface area of the matrix phase, less hydrogen gas is produced at the cathode. This again could suppress the condition for the formation of sparks.

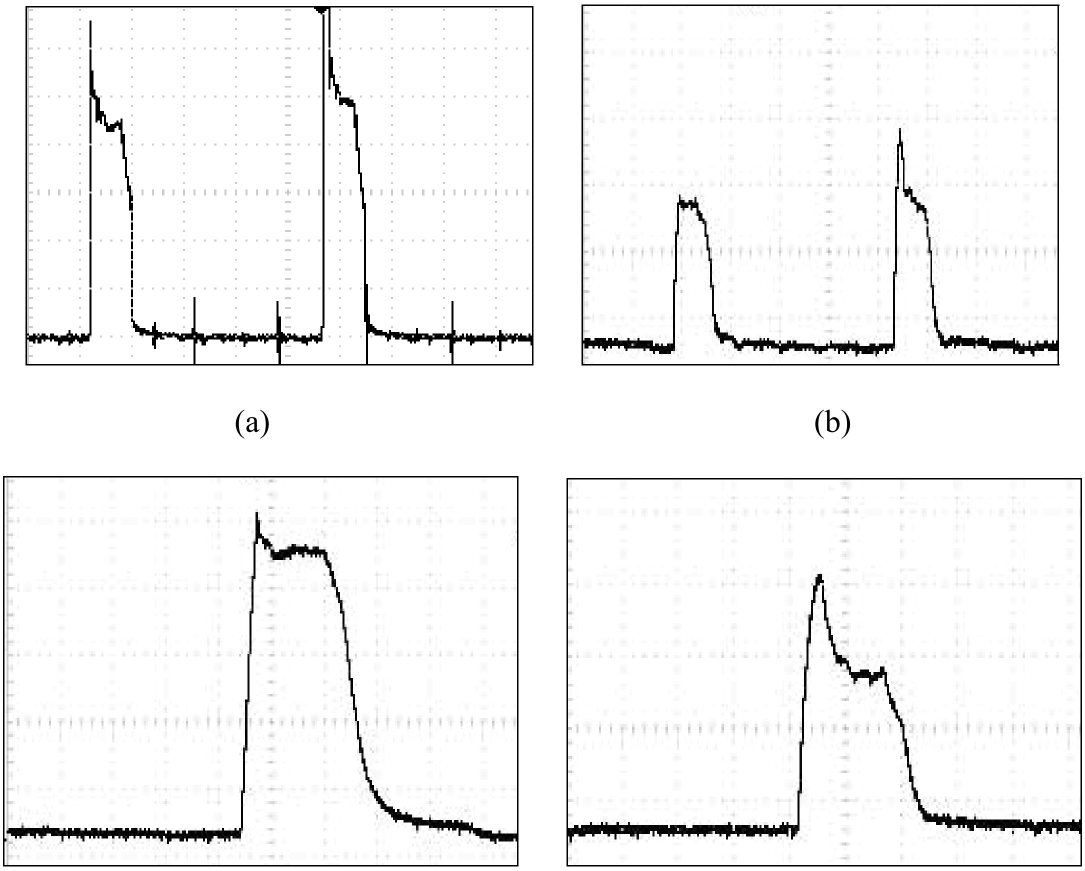

(a) (b) (c) (d)

Fig. 4.41 Voltage waveforms for the conditions of different electrolyte concentrations for the 10ALO material, (a) zero %, (b) 0.25%, (c) 0.5%, (d) 1%

4.4 Summary

The first part of this chapter focuses on the modelling of the discharge mechanism with an emphasis on prediction of the critical breakdown voltage of hydrogen bubbles in electrochemical discharge machining of a particulate reinforced metal matrix composite. The model was found capable of predicting the position of the maximum field strength on the bubble surface as well as the critical breakdown voltage for spark initiation. A set of experiments was performed to verify the model and the experimental results agreed well with the predicted values. The experimental results also showed that an increase in current, duty cycle, pulse duration or electrolyte concentration would promote the occurrence of arcing action in ECDM. Moreover, by studying the waveform of ECDM and surface craters, one can confirm that the spark action is in the form of an arc. In the second part of this chapter the relative importance of the various cutting parameters on material removal rate was reported. As far as MRR is concerned, the applied current is found to be the most influential factor among current, pulse duration and electrolyte concentration. The results of the study also show that although ECDM could achieve a reasonably high MRR when compared to the EDM process, the machined surface quality needs to be improved. In the next chapter, the advantages of the G-ECDM process, in terms of MRR and surface quality, over the ECDM process will be examined.

CHAPTER 5

MATERIAL REMOVAL MECHANISM OF GRINDING-AIDED ELECTROCHEMICAL DISCHARGE MACHINING OF MMCS

Several studies were conducted with the aim to understand the material removal mechanism of the G-ECDM process. These studies cover the conditions of single pulse and continuous pulsing on the analysis of the ECDM process with and without grinding.

Due to the constraints of the WEDM-HS machine, a greater electrolyte concentration than 1% cannot be used. Moreover, it is difficult to fix the spark gap distance with the WEDM-HS machine when grinding is incorporated into the ECDM process. Recognising this, the purposely designed equipment presented in Chapter 3, with some simple cylindrical shape tool-electrodes that have an abrasive coating would be used for studying the G-ECDM process.

5.1 Theoretical Analysis

5.1.1 Physical model of ECDM

The principle of the G-ECDM method is illustrated in the schematic diagram in Fig. 3.1 which is composed of the constituents of the electrochemical effect (ECE), electrical discharge machining (EDM) and direct mechanical grinding (DMG). In the G-ECDM process, the electrolyte bath provides limited conduction between the tool and the workpiece. Although the ECE has the action of dissolving the metal phase around the reinforcement phase, its major function is to enable EDM sparking to be operable under a relatively large spark gap size condition, and thus facilitating the removal of machined debris. In analysing the material removal mechanism of the G-ECDM process, the actions of ECE, EDM and DMG are studied separately. A representation of the physical model of ECDM is shown in Fig. 5.1. During EDM, the temperature in the spark channel is so high that the electrolyte in the channel will be vaporised and as a result ECE is not expected to play an important role in the EDM spark area. In considering the EDM effect, most of the energy at the electrode surface is assumed to transform into heat energy. A large part of the heat energy transfers to the tool and the workpiece through heat conduction and this will cause the melting and vaporisation of the corresponding materials, while some of the heat energy transfers to the electrolyte through convection and radiation.

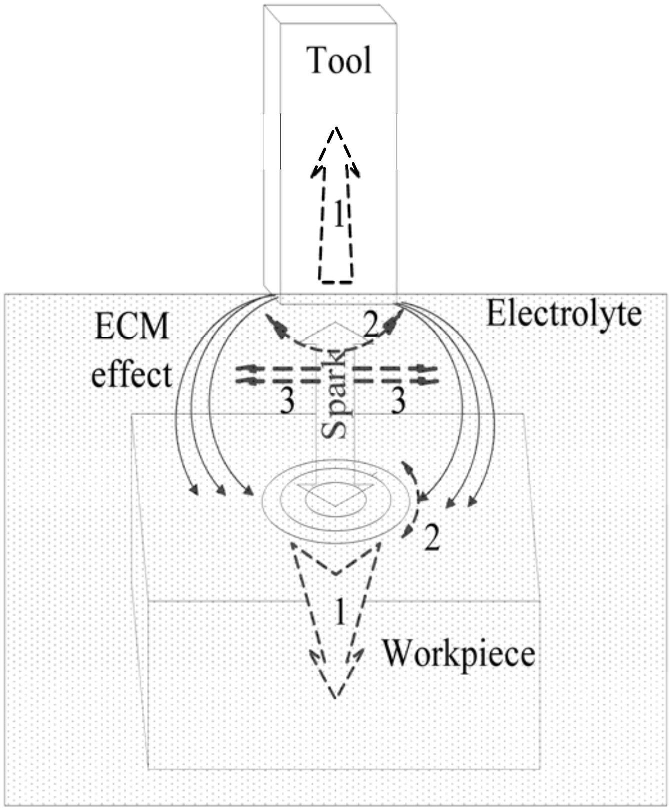

Fig. 5.1 Physical model of ECDM [Heat conductivity (1), Heat convection (2), Heat radiation (3)]

5.1.2 Pulse energy for ECM

Equation (5.1) gives the total energy of a single pulse

$$W = \int_0^{t_k} u(t)\, i(t) dt \tag{5.1}$$

$$W = W_1 + W_2 \tag{5.2}$$

where $u(t)$ is the voltage between the electrodes, $i(t)$ is the current and t_k is the pulse duration. The energy is divided into two parts, electrochemical energy W_1 and electrical discharge energy W_2. The proportion of W_1 and W_2 is related to the electrode area, the processing voltage, the gap size and the electrolyte concentration. For both the ECM and EDM actions, it is assumed that they have the same voltage *u(t)*. Since the ignition delay is very short, *u(t)* can be taken to be the processing voltage during the pulse-on period, which is normally around 22V for any applied voltage. Accordingly, the value of $i(t)$ governs the amount of energy for the ECM and EDM actions. To determine the ECM energy (W_1), the current density during machining was evaluated using the finite element method. A simple two-dimensional model, consisting of a flat anode immersed in a bath of electrolyte, was used for the analysis (Fig. 5.2).

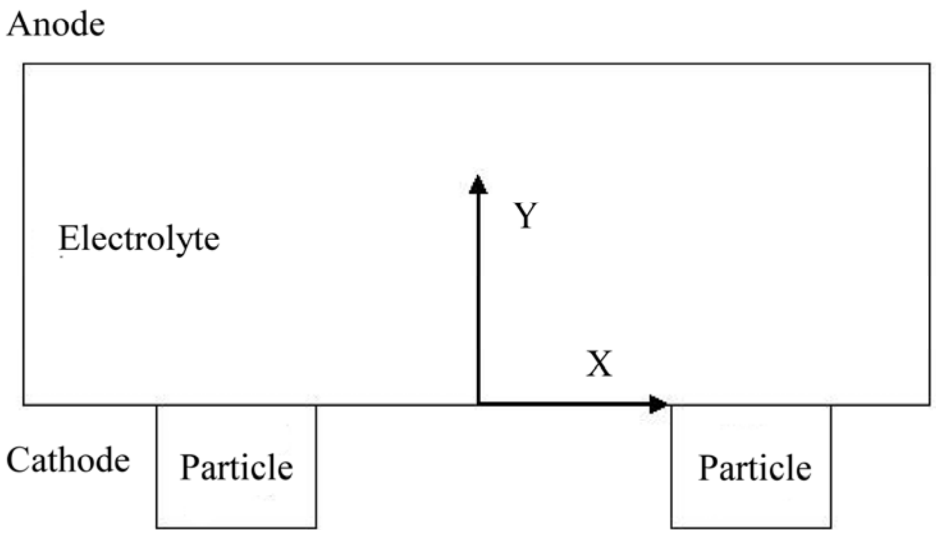

Fig. 5.2 Two-dimensional model of the ECM effect

In the area of interest, nonconductive ceramic particles are assumed to be embedded in the anode. The length of the ceramic particle is assigned to be L_1 and the distance between two particles is L_2. The machining process is assumed to be stable and the conductivity of the electrolyte is assumed to be constant and uniform throughout the analysis. Under these conditions, the electrical potential (ϕ) in the processing area can be described by:

$$\frac{\partial^2 \phi}{\partial x^2} + \frac{\partial^2 \phi}{\partial y^2} = 0 \tag{5.3}$$

and the boundary conditions are:

$$\phi_C = 0 \tag{5.4}$$

$$\phi_A = U \quad (L_1 + \frac{L_2}{2} \langle |X| \langle \infty \cup |X| \langle \frac{L_2}{2}) \tag{5.5}$$

$$J = -\sigma \square \phi \tag{5.6}$$

where ϕ_c and ϕ_A are the electrical potentials at the surfaces of the cathode and anode, respectively. J is the current density and σ is the conductivity of the electrolyte. U is the processing voltage, which is 22V. The gap size is assumed to be 0.05mm. The concentration of the electrolyte, $NaNO_3$, ranges between 0.5wt% and 5wt%. In so doing, the electrical resistivity of the emulsion varies from 170Ω·cm to 20Ω·cm [78]. The Al_2O_3 ceramic particle is assumed to take a square shape of size 21μm. The electrical resistivity of the ceramic particle is assumed to be infinitely large. According to Xu et al [78], the electrolyte electrical conductivity has the following relationship:

$$\sigma = \sigma_o \left[1 + \xi(T(x) - T_o)\right]\left[1 - \beta\right]^n \tag{5.7}$$

where σ_o is the initial electrolyte electrical conductivity, ξ is the temperature impact index, which is assumed to be 0.02 [78]. T_o is the initial temperature of the processing area, which is 20^0C, $T(x)$ is the processing temperature of the processing area, which is 40 ^{0}C. β is the void fraction and is assumed to be 0.75, and was determined using a bubble volume fraction of 0.2 [78] and a grit volume fraction of 0.55. n is the void fraction impact index which is taken to be 2 [78]. Based on these conditions and assumptions, the current density for different electrolyte concentrations which appear in ECM was determined using the Ansys software. The simulation results are presented in Fig. 5.3. With these, the ECM current can be calculated [78]:

$$i(t) = JA(t) \tag{5.8}$$

where $A(t)$ is the workpiece working area. Here,

$$A(t) = \alpha(A_b + A_s) \approx \int_0^{t_k} 1.6\alpha\left[1 + v(t)\right]dt \approx 1.6a(1+l) \tag{5.9}$$

where α is the area fraction of the metal matrix of the composite. In this study, the composite contains 10%(vol) of Al_2O_3 particles, and α is therefore assumed to be 0.9. A_b, A_s are the base area and the lateral area of the tool; $v(t)$ is the feed velocity and l is the feed depth.

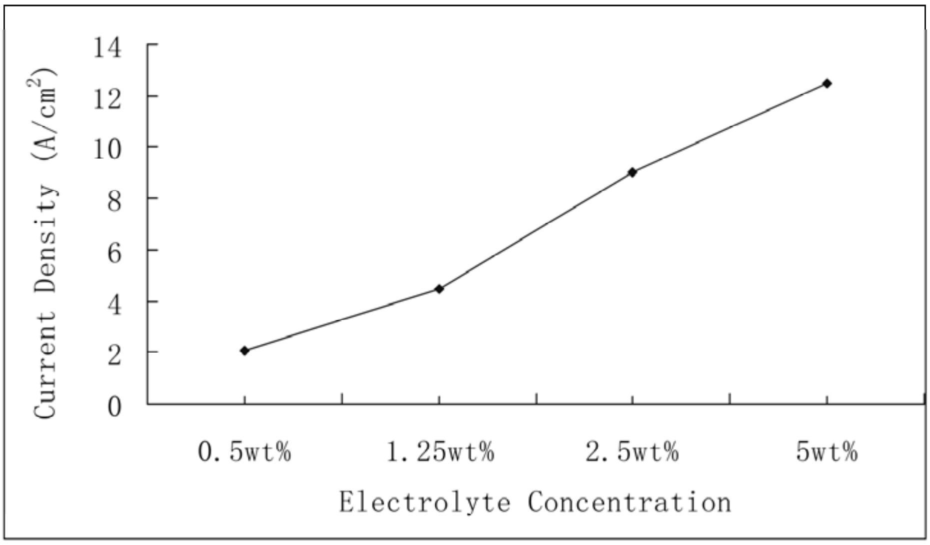

Fig. 5.3 Simulation results of current density as a function of electrolyte concentration

5.1.3 Material removal by ECM

The material removal volume due to ECM is determined using the proposed relationship of Xu et al. [78]:

$$V_c(t) = \int_0^{t_k} \omega i(t)dt \approx \omega J A_a t \tag{5.10}$$

$$A_a \approx \frac{A_0 + A_f}{2} \tag{5.11}$$

where V_c is the dissolved metal volume of the anode. ω is the dissolved metal volume per unit quantity of electricity. A_a, A_0 and A_f are the average area of the workpiece, the original working area, and the final working area respectively. It is known that for pure aluminium $\omega_{Al} = 2.1(mm^3 / A \cdot \min)$ [78]. It is also assumed that a particle would be removed if the metal phase around it has been dissolved, therefore the actually removed volume of the composite material was calculated to be

$\omega_{10ALO} \approx 2.3(mm^3 / A \cdot \min)$.

5.1.4 Spark energy of EDM

In the EDM process, the spark energy W_2 is divided into three parts [97]: namely, the energy at the anode surface (W_a), the energy at the cathode surface (W_b), and the energy exhausted in the spark channel (W_c).

$$W_2 = W_a + W_b + W_c \tag{5.12}$$

Further, W_a, W_b and W_c can be determined using equation (5.13):

$$W_{a,b,c} = \eta_{a,b,c}\left(\int_0^{t_k} u(t)i(t)dt - W_1\right) \tag{5.13}$$

where $\eta_{a,\ b,\ c}$ is the energy partition fraction. In this study, the interest is in the material removal rate of the workpiece, so only W_a was considered, for which η_a was assumed to be 40% [98]. It is assumed that all the energy at the electrode surface transforms into heat energy and takes the form of a heat source which is composed of a volumetric heat source and a plane heat source. The volumetric heat source appears only in those conditions where the processing current changes rapidly, such as at the very beginning of the process or when the processing conditions are unstable. Since such conditions are not the prevailing machining conditions under normal stable machining [99], it is therefore assumed that all the energy at the electrode surface appears as a plane heat source. The plane heat source is created as a result of the bombardment of high speed charged particles at the electrode surface. In this study, the heat flux density profile of the plane heat source is assumed to take the form of a Gaussian distribution [100].

5.1.5 Simulation of temperature profile of the workpiece

Equation (5.14) represents the heat transfer differential equation which is based on Fourier heat transfer theory, and is employed to simulate the temperature profile of the composite workpiece. c, ρ, λ, T, t, $\dot{Q}$ are the special heat capacity, density of the material, thermal conductivity, temperature, time and internal heat source respectively.

$$c\rho\frac{\partial T}{\partial t}=\frac{\partial}{\partial x}(\lambda\frac{\partial T}{\partial x})+\frac{\partial}{\partial y}(\lambda\frac{\partial T}{\partial y})+\frac{\partial}{\partial z}(\lambda\frac{\partial T}{\partial z})+\dot{Q} \tag{5.14}$$

Since, under the EDM condition, the heat source is axisymmetric and equation (5.14) can be simplified to:

$$c\rho\frac{\partial T}{\partial t}=\lambda(\frac{1}{r}\frac{\partial T}{\partial r}+\frac{\partial^2 T}{\partial r^2}+\frac{\partial^2 T}{\partial z^2})+\dot{Q} \tag{5.15}$$

where r and z are circular cylindrical coordinates.

5.1.5.1 Heat source model, boundary conditions and spark position analysis

Owing to the symmetry of the heat source, a two-dimensional model can be employed to study the heating effect of the spark (Fig. 5.4). The initial condition and the boundary conditions are given below:

Initial condition:

$$T = T_0 \qquad \text{(when t=0)} \tag{5.16}$$

Boundary conditions:

$$-\lambda\frac{\partial T}{\partial \vec{n}}=q_s \qquad \text{(when } r\le R\text{)} \tag{5.17}$$

$$-\lambda\frac{\partial T}{\partial \vec{n}}=h_c(T-T_0) \qquad \text{(when } r> R\text{)} \tag{5.18}$$

$$-\lambda\frac{\partial T}{\partial \vec{n}}=0 \qquad \text{(at surfaces as shown in Fig.5.4)} \tag{5.19}$$

Given that the heat flux has a Gaussian distribution, it can be determined by the following equation (5.20) [101],

$$q_s(r)=q_m\exp(-a\frac{r^2}{R^2})=\frac{a}{\pi R^2}\eta P\exp(-a\frac{r^2}{R^2}) \tag{5.20}$$

where q_m is the maximum heat flux which occurs at the centre of the spark channel and r is the radial distance from the centre of the spark. The heat flux decreases with increasing r. R is the spark channel radius which is assumed to be 100μm [79]. P is the spark energy (i.e. W/t), η_a is the energy partition coefficient and a is the heat source intensity coefficient which is assumed to be equal to 3 [97].

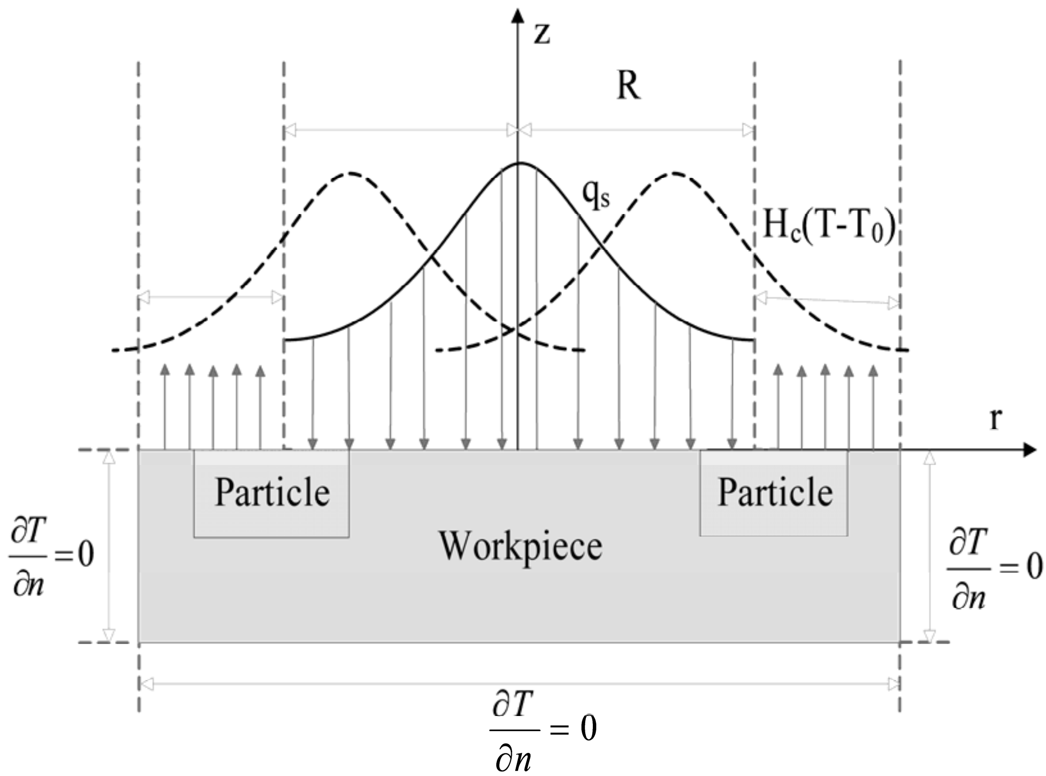

Fig. 5.4 Two-dimensional model of heat flux and convection at the composite surface

In the model, a spark discharge begins with a Townsend breakdown, and then it turns to a Streamer breakdown [103]. Based on the Streamer breakdown theory, if the anode material is composed of a MMC, electrons will stay away from the non-conductive ceramic particles and enter into the metal phase. As such, photoionization will mainly occur above the metal phase. This means that the centre of the spark will have a greater chance to appear at the metal phase, although its exact position is difficult to determine. In the model, it is assumed that the spark occurs in the middle of two ceramic particles.

Since heat radiation only consumes very little energy. Therefore in this study, only heat conductivity and heat convection have been considered.

Accordingly, the heat lost of the spark to the electrolyte through heat convection can be determined by equation (5.18).

The coefficient of heat convection h_c can be determined using equations (5.21)-(5.23) [102].

$$h_c(x) = C\frac{\lambda}{x}R_e^{1/2}P_r^{1/3} \tag{5.21}$$

$$R_e = \frac{\rho\omega x}{\mu} \tag{5.22}$$

$$P_r = \frac{\mu c}{\lambda} \tag{5.23}$$

where x is the coordinate position. The coefficient C relates to the surface conditions, λ is the thermal conductivity, R_e is the Reynolds number, P_r is the Prandtl number, ρ is the fluid density, ω is the flow velocity, μ is the viscosity and c is the specific heat. The coefficient of heat convection, h_c, along the X-axis in relation to the Y co-ordinate is shown in Fig. 5.5.

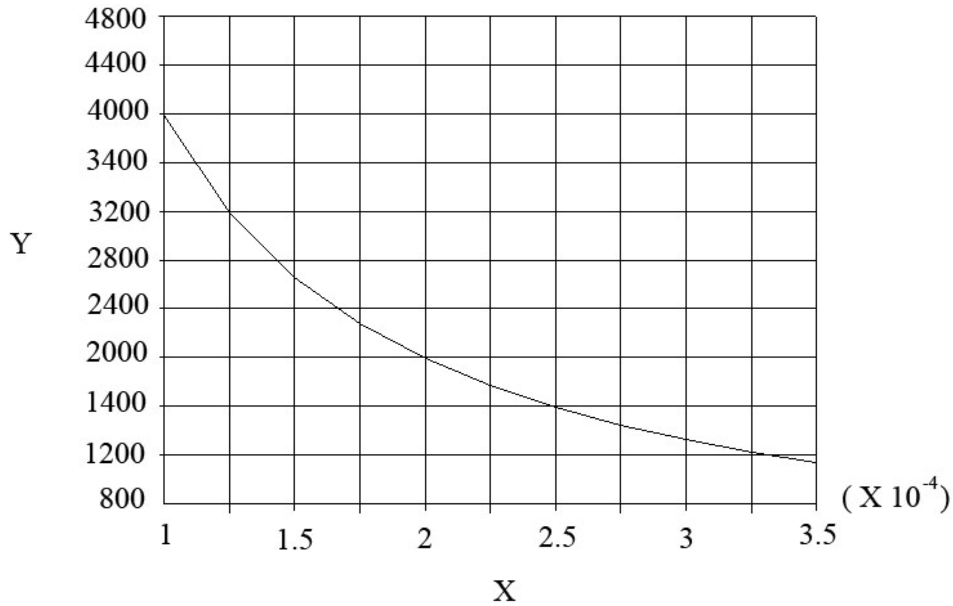

Fig. 5.5 Coefficient of heat convection along the X-axis

5.1.5.2 Simulation of temperature field induced by a spark

The heating effect of an EDM spark on the temperature field of the anode was analysed using ANSYS. The flowchart representing the analysis is shown in Fig. 5.6 that follows.

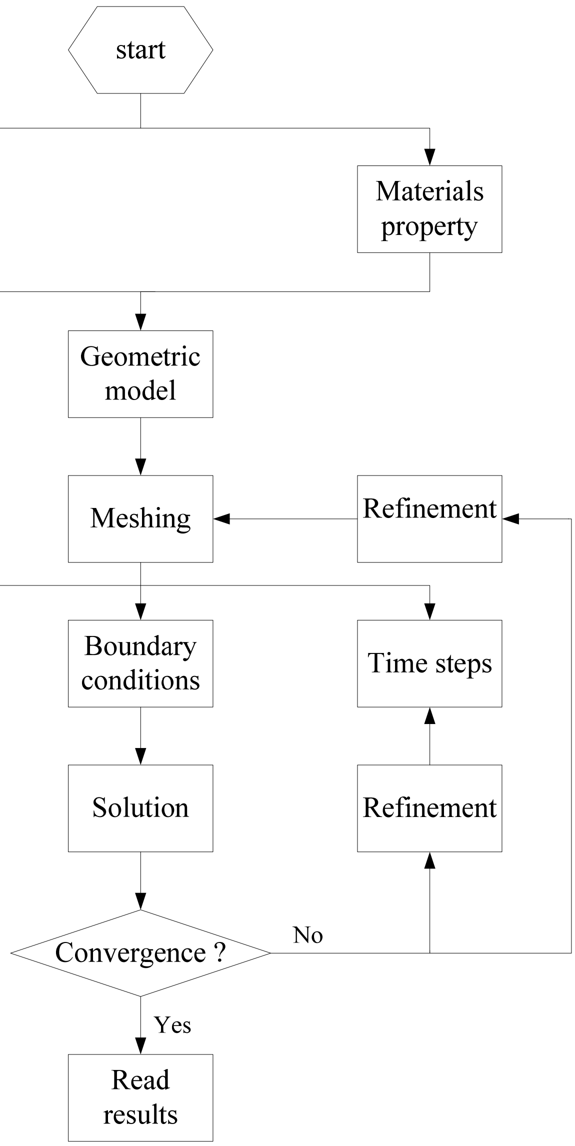

Fig. 5.6 ANSYS analysis flow chart

The material properties of the matrix material and the ceramic phase for the analysis are given in Table 5.1. The anode is an Al-6061/10(vol)% Al_2O_3 composite. The nominal size of an Al_2O_3 particle is 21μm, which is assumed to take the form of a square and is uniformly distributed in the composite (see Fig. 5.7). The uniformity is ensured by equally spacing out the particles in each layer of the model with no overlapping of particles between layers. The processing conditions employed were: processing voltage of 22V, average current of the pulse-on time of 10A and pulse duration of 48μs. Fig. 5.7 shows the simulation results of the temperature field of the processing area. It is apparent that the ceramic particles have the effect of restraining heat from passing through. This would make the volume of the molten pool to be smaller than that of the material without the ceramic reinforcement phase.

Table 5.1 Material properties of the matrix and the ceramic phase [104-105]

Properties	Al_2O_3	6061Al
Thermal Conductivity (W/(m·k))	25	167
Density(kg/m^2)	3800	2700
Specific Heat (J/kg·k)	880	900

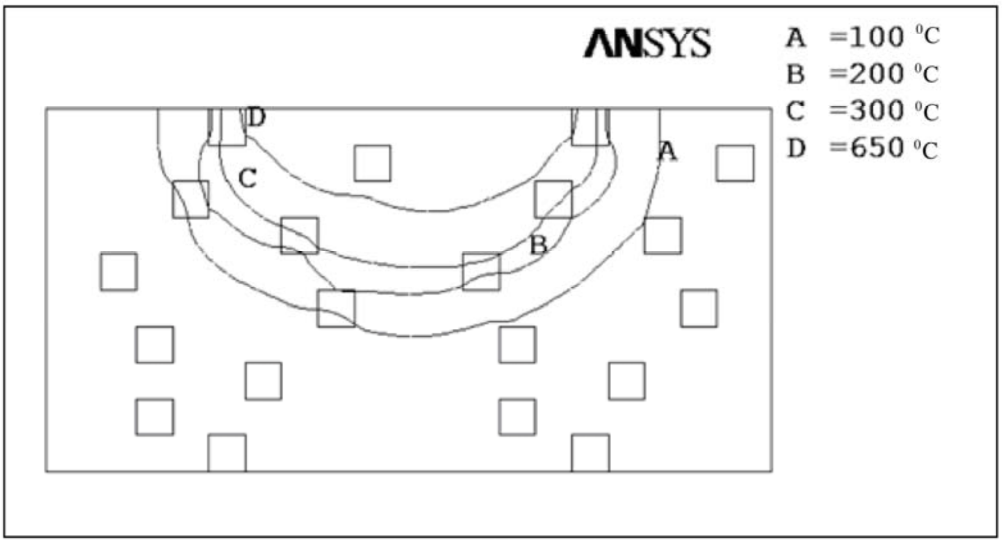

Fig. 5.7 Simulation results of the temperature field of the composite when subject to an EDM spark

5.1.6 Volume of material removed by ECDM

Based on the temperature simulation results in Section 5.1.5, the depth and width of the molten pool can be obtained. Using this, and assuming that the molten pool takes a hemispherical form, the volumes of molten material and the material removed by a single spark can then be determined using equations (5.24) and (5.25), respectively [81, 106].

$$V_m = \frac{1}{6}\pi H(\frac{3}{4}L^2 + H^2) \tag{5.24}$$

$$V_s = \eta_f V_m \tag{5.25}$$

where V_m is the volume of the molten material, V_s is the volume of the material removed by a spark without re-depositing back on the surface, and η_f is defined to be the molten material throw-out coefficient. H is the depth of the molten pool, while L is the width. Since η_f has been found by experiment to be smaller than 0.15 [107], in this study, it is assumed to be 0.1.

Now, the theoretical volume of material removed (V) by a single pulse under ECDM is simply equal to,

$$V = V_c + V_s \tag{5.26}$$

The MRR in one minute (V_{MRR}) can therefore be determined:

$$V_{MRR} = (V_c + V_s)(\frac{60}{T}) \tag{5.27}$$

where T is the pulse cycle.

When considering the G-ECDM process, the grinding mechanism will aid removal of extra material which has not been taken away by the spark, especially the built-up materials around the craters. As a result, the MRR will increase. To verify the theoretical model, a number of experiments have been conducted.

5.2 Experimental Approach

According to the working principle of the G-ECDM process, an appropriate drill tool has been designed (Fig. 5.8). The tool forms the cathode which in this case is an iron based hollow cylinder of diameter 26mm with a thickness of 2mm. The surface of the tool is deposited with a 100μm thick composite coating of Ni with up to 55vol% of diamond particles of a nominal size of 120μm. The tool is held by a spindle, and the current flows to the tool through a special electric transmission system which has negligible resistance. The electrolyte is pumped into the processing area through the nozzle with the aid of an electrolyte circulation system. After the electrolyte has been properly filtered, it will return to the electrolyte circulation system. More details of the design and the operation schemes of the G-ECDM equipment can be found Chapter 3.

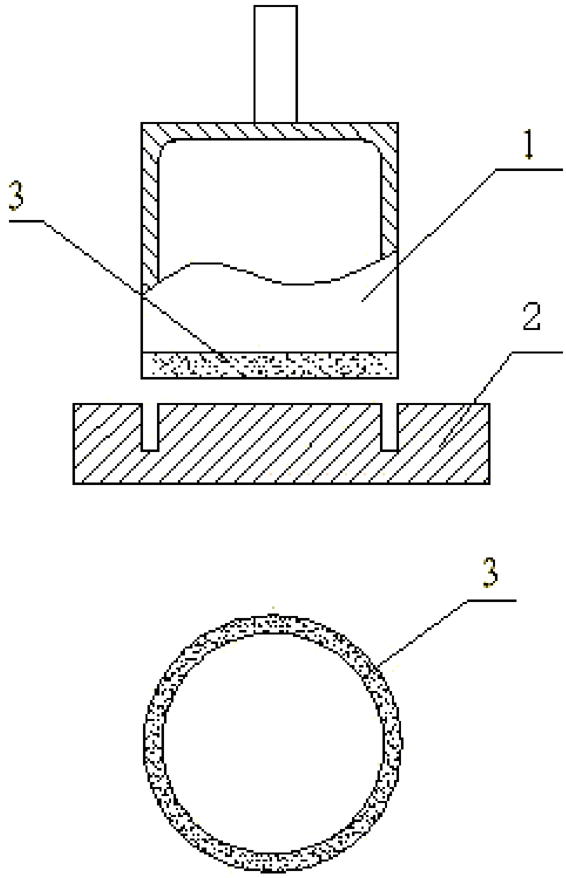

Fig.5.8 Schematic drawing showing the G-ECDM drill [Tool (1), Workpiece (2), G-ECDM Section (3)]

The relative strength of ECM and EDM in the process can be controlled by varying the processing parameters. During EDM, the material would melt, vaporise and form EDM chips. However, it is normal that a significant amount of molten material would be re-cast around the spark eroded crater. However, the sparking action could also remove foreign material at the cathode surface, and this is beneficial in minimising tool clogging. Accordingly, when it comes to the grinding phase, the re-cast material in the vicinity of the crater could be mechanically removed. The grinding action would thus increase the material removal rate.

Moreover, the grinding action would improve the surface quality and finish.

During G-ECDM, if the machining debris cannot be discharged from the spark gap in time, then short-circuiting would occur. Fig. 3.11 indicates the voltage characteristics during processing under different machining conditions. If it is under a stable machining condition (I), the processing voltage fluctuates between φ_1 and φ_2. While for an unstable condition (II), it would normally be maintained for a short period of time. If this unfavourable processing situation persists, i.e. Condition (II), the voltage will drop further and finally short-circuiting would occur, i.e. Condition (III), in which, the voltage would drop sharply from φ_3 to φ_4. With this problem in mind, the control system of the G-ECDM is so designed that it can monitor the change of voltage and provides appropriate remedial actions to avoid short circuiting from occurring. Should an unstable processing condition be encountered, the control system would command the tool to retract instantly so as to improve debris discharge through a wider machining gap.

In the experiment, the MMC workpiece acts as the anode. The MMC employed in this study is particulate reinforced aluminium 6061 with 10 (vol)% Al_2O_3. The material was supplied in the form of rolled plates with the reinforcement phase having a nominal size of 21μm. The electrolyte used for the experiment was $NaNO_3$ solution, and its concentration was varied between 0.5wt% and 2.5wt%.

An additional experiment was conducted to study whether the detrimental Al_4C_3 phase would be present at the machined surface after G-ECDM of SiC reinforced composites. The material used for this study was a particulate reinforced aluminium alloy 359 with 20(vol%) SiC; the reinforcement phase has a nominal size of 10μm.

5.3 Experimental Results and Discussion

5.3.1 ECDM of MMCs

An ECDM experiment without grinding was conducted to verify the ECDM model. The processing conditions were: applied voltage 110V, pulse-on time 48μs and a duty cycle of 1:7. The average gap size between the anode and cathode was about 0.05 mm and this dimension was maintained by the physical presence of the grits. The electrolyte concentration was 0.5wt%, the spindle speed was 15rpm and the depth of feed was 0.5mm (Table 5.2). When the spindle speed is so low, the grinding effect on MRR can be ignored. Under these conditions and based on the simulation results and the use of equation (5.8), the ECM current for each pulse was found to be 3A, and knowing the ECM current, the EDM current can also be obtained. Accordingly, the MRR for ECDM was calculated using equation (5.27). The predicted and experiment results of MRR for different average currents of the pulse-on time are shown in Fig. 5.9. Although the former was found to be slightly higher than that of the latter, a reasonably good agreement between them was obtained. A likely reason for the difference could be that the molten material throw-out coefficient (η_f) used for the prediction was slightly too high. Nonetheless, the results confirm that for the case of ECDM, the value of η_f is around 0.1, which is in agreement with the study of Rebelo et al [107].

Table 5.2 Processing conditions for the study of MRR of ECDM

Processing Conditions	Spindle Speed (rpm)	Duty Cycle	Pulse Duration (μs)	Applied Voltage (V)	Peak Current (A)	Gap Distance (μm)
A	15	1:7	48	110	12.5	50
B	15	1:7	48	110	15	50
C	15	1:7	48	110	17.5	50
D	15	1:7	48	110	22.5	50
E	15	1:7	48	110	27.5	50

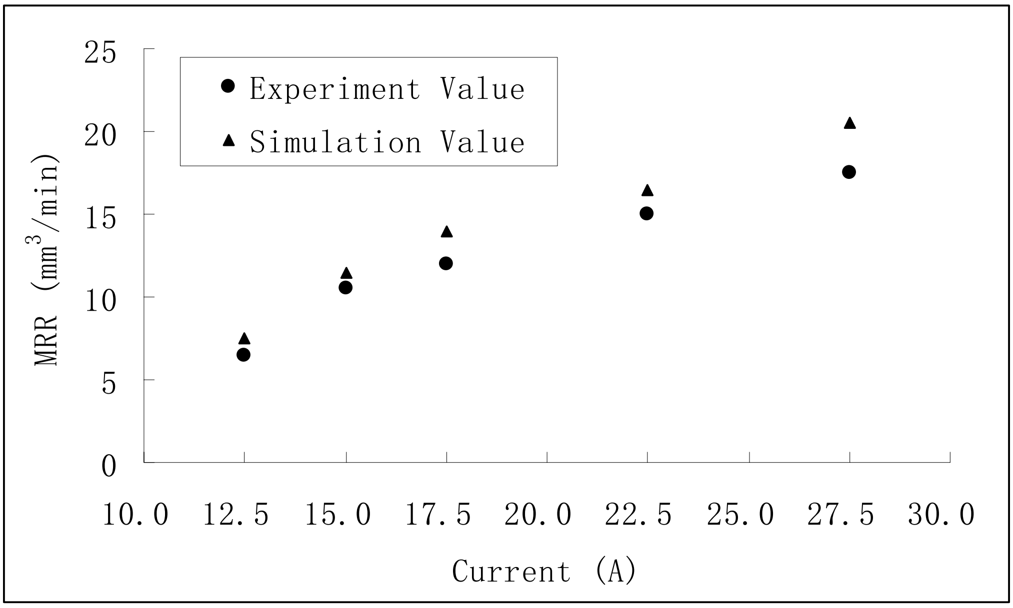

Fig. 5.9 Simulation and experimental results of MRR for ECDM of the composite

5.3.2 G-ECDM of MMCs

A series of experiments were conducted to study the effects of the various processing parameters on MRR and the material removal efficiency of G-ECDM. The G-ECDM experimental conditions are given in Table 5.3. For all these conditions, the same processing voltage of 80V, with a spindle speed of 1500rpm and a feed depth of 0.5mm, were employed. Each experiment was repeated ten times. Table 5.3 also shows the results of η_f and the number of unstable machining occurrences. In the case of G-ECDM, η_f not only takes the material removed by the sparks into account but also includes the material removed by the grinding action.

Table 5.3 Experimental results of G-ECDM

Condition	Pulse-on-time (μs)	Duty cycle	Electrolyte concentration (wt.%)	Current (A)	η_f	MRR (mm^3/min)	No. of unstable occurrences in 0.5mm drill depth
A	48	1:7	2.5	42	0.25	61	0
				35	0.28	59	2
				28	0.36	58	4
B	48	1:7	0.5	28	0.25	57	5
			1.25		0.28	59	3
			2.5		0.36	58	4
			5.0		0.90	53	14

The experimental results show that the MRR of G-ECDM increased with an increase in current (Table 5.3). The relative standard deviation (RSD) of the experimental results is within 2%. According to equation (5.8), the ECM current for each pulse is about 18A, under which the material dissolved by ECM would be 5.9 mm^3/min (equation (5.10)). For a case where the processing current is 42A, the EDM current in each pulse is about 28A, since the ECM current remains at 18A. Based on equation (5.25) and the ANSYS simulation results, the actually volume of the molten material removed by a spark would be 22.0 mm^3/min. According to the above analysis, and based on equation (5.27), the theoretical MRR of ECDM would be 27.9

mm^3/min. Accordingly, the experiment results of G-ECDM show that the processing condition was stable even when the material removal rate reached 60mm^3/min, which is significantly higher than the theoretical and the experimental values of ECDM without the grinding effect. This has led to η_f increasing from about 0.1 for the condition of no grinding to 0.25 with grinding. The values of η_f for other processing currents were also obtained and are given in Table 5.3. The results show that when η_f reaches a critical value of 0.25, any attempt to increase this value would lead to the occurrence of unstable processing conditions. The greater the value of η_f, the higher the frequency of unstable processing occurrences being encountered. Under these conditions, the control system would respond immediately to retract or reduce the feed speed accordingly.

The results of test Condition B show that the maximum MRR occurred at an electrolyte concentration of around 1.25%, and it appears that a concentration higher or lower than this level would result in a lower MRR (Fig. 5.10). At low concentrations, a relatively short arc discharge time was experienced and hence the amount of molten material produced would be less than that for the conditions with high concentrations. The short discharge time is considered to be caused by the fact that at low concentrations, the hydrogen formation rate at the cathode would be relatively low. As a consequence, a longer time is required during the pulse-on-period for generating enough bubbles so as to increase the resistance between the two electrodes and reaching the critical breakdown voltage. That is to say, the discharge time would be correspondingly reduced. On the other hand, under the conditions of high concentrations, the ECM action would be enhanced, and the

EDM effect would be weakened. Since EDM plays a more important role in material removal than ECM, a weakening in EDM would result in a drop in MRR.

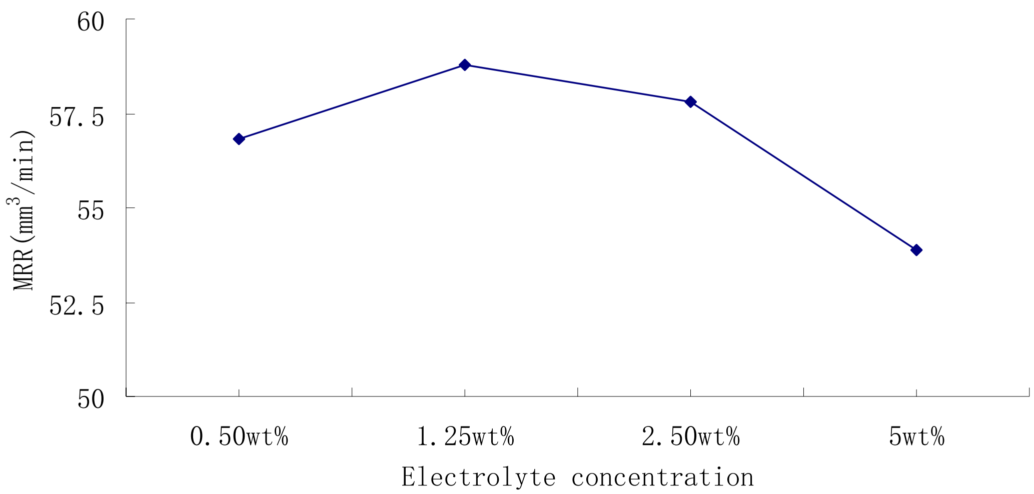

Fig. 5.10 Relationship between electrolyte concentration and MRR

During the G-ECDM process, it was noticed that the processing condition could become unstable if the tool is clogged with the debris of removed material and/or debris is seriously trapped in the spark gap. Fig. 5.11 shows some typical types of unstable processing waveforms. It was observed that an unstable situation could turn to a stable one even within a pulse (Fig. 5.11a, b). The exact reason for this is still uncertain, but it is believed to be attributed to the spinning effect of the tool. The swirling effect brought about by the spinning tool could effectively unknot short-circuit situations. In the case where seriously unstable conditions are encountered (Fig. 5.11c), the control system would respond instantly to redress the processing condition to become stable by retracting the tool as well as reducing the feed speed.

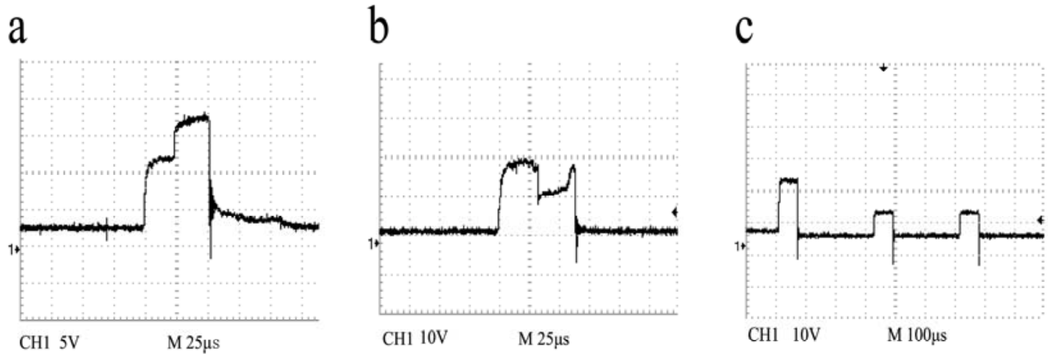

Fig. 5.11 Typical unstable waveforms appearing in G-ECDM

An examination of the machined surface of the specimens of machining Condition A (Table 5.3) was conducted using scanning electron microscopy (SEM). A few marks were observed on the 35A specimen (Fig. 5.12a), while for the specimen processed under a higher current of 42A, many more grinding marks could be found (Fig. 5.12b). This indicates that increasing the current increases the grinding effect. This is somewhat expected, since a higher current means more molten material is produced and hence a larger crater; moreover, more re-cast material is expected to form around the crater and as such, the effect of grinding would become more apparent. A single pulse experiment shows that without the grinding effect, considerable re-cast material is formed around the edge of the crater, and this was not found for the case of G-ECDM (Fig. 5.13) (The processing conditions are given in Table 5.4).

a

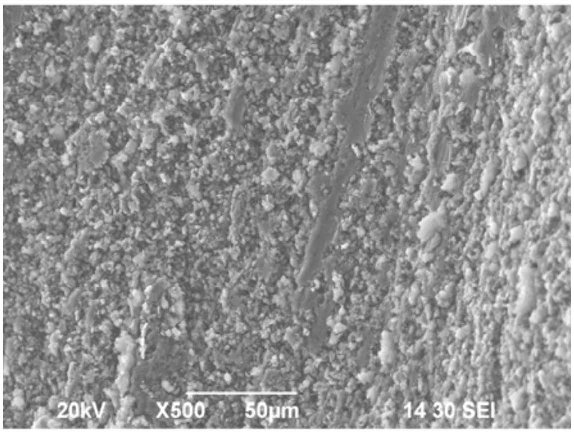

b

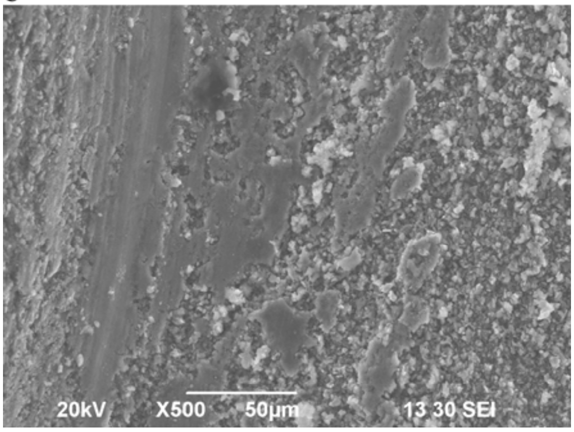

Fig. 5.12 Typical surface topography of the specimens machined under a peak pulse current [(a) 35A; (b) 42A]

Table 5.4 Processing conditions for the study of the machined surface under single pulse

Processing Condition	Media	Duty Cycle	Pulse Duration (µs)	Applied Voltage (V)	Peak Current (A)	Spindle Speed (rpm)
A(ECDM)	2.5% $NaNO_3$	1:7	200	90	35	0
B(G-ECDM)	2.5% $NaNO_3$	1:7	200	90	35	15000

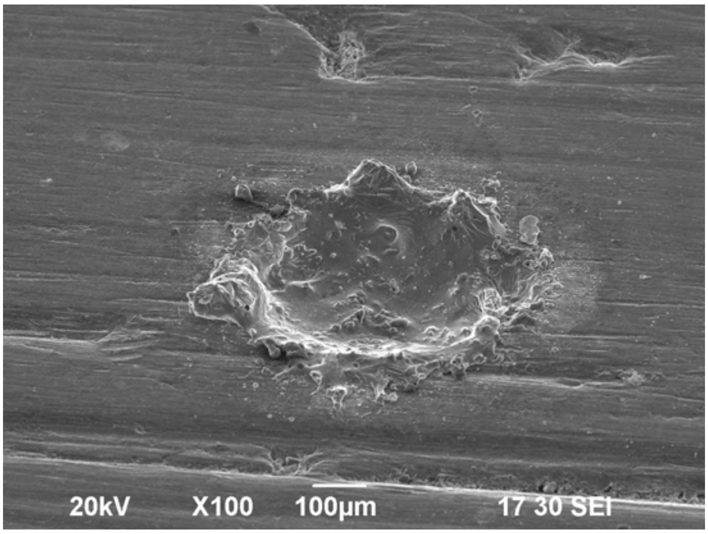

(a)

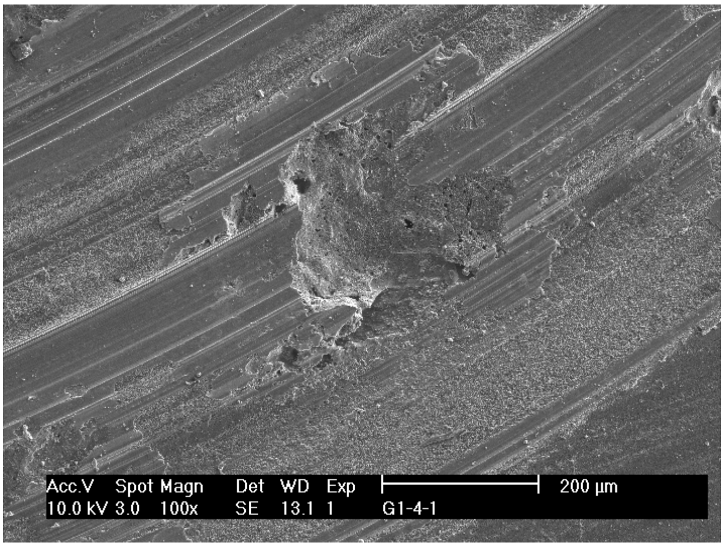

(b)

Fig. 5.13 Machined surfaces [(a) without grinding effect, and (b) with grinding effect, under a single pulse processing condition]

5.3.3 Machined surface quality

To ascertain that the G-ECDM process can produce a good surface finish for MMC materials, a comparison study of the quality of the G-ECDMed and

ECDMed surfaces of the Al-6061/10(vol)% Al_2O_3 composite was made. The processing conditions for G-ECDM and ECDM are given in Table 5.5. In the experiment, positive electrode polarity was employed because this would facilitate the cleaning of clogged materials in the tool. A detailed study on tool cleaning is presented in Section 7.3. Although, with such a polarity arrangement, the material removal rate of the workpiece would be reduced, a better surface finish is expected.

Fig. 5.14 shows that the surface roughness (R_a) measured for the G-ECDM specimen (0.26μm) was found to be much better than that of the ECDM specimen (2.5μm). Moreover, defects such as micro-cracks, voids, and the amount of re-solidified material that were found on the surface of the ECDM specimen (Fig. 5.15) were largely eliminated from the surface of the G-ECDM specimen (Fig. 5.16). There is no doubt that more experiments are needed to optimise the processing parameters in order to achieve the best surface finish, nonetheless the results of this preliminarily study confirms that G-ECDM can produce better surface finish with much less surface defects than the ECDM process.

Table 5.5 Processing conditions for the study of machined surface quality

Processing Conditions	A	B
Processing Mode	G-ECDM	ECDM
Polarity (electrode)	Positive	Positive
Peak Current (A)	35	35
Applied Voltage (V)	80	80
Pulse Duration (μs)	48	48
Media	2.5%$NaNO_3$	2.5%$NaNO_3$
Duty Cycle	1:7	1:7
Spindle Speed (rpm)	1500	1500
Feed Speed (μm/min)	240	240
Machining Depth (mm)	0.5	0.5

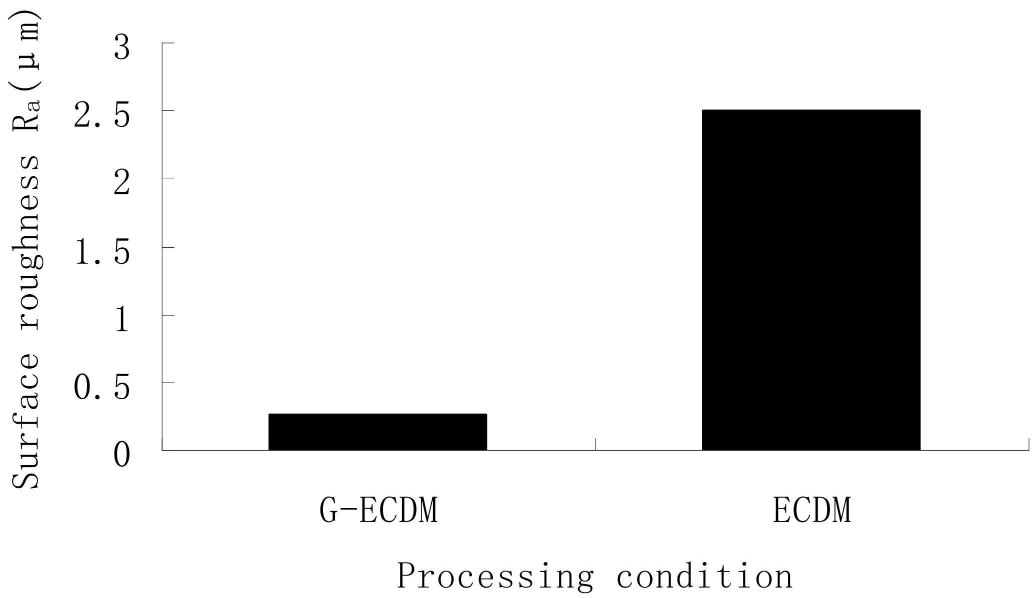

Fig. 5.14 Surface roughness measured for the machined surfaces produced by G-ECDM and ECDM

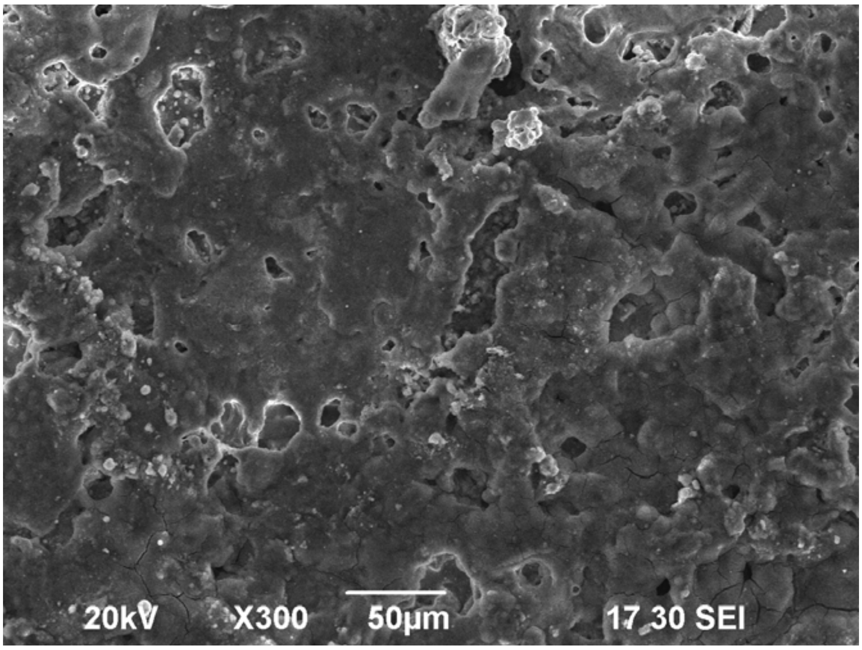

Fig. 5.15 Typical machined surface produced by ECDM

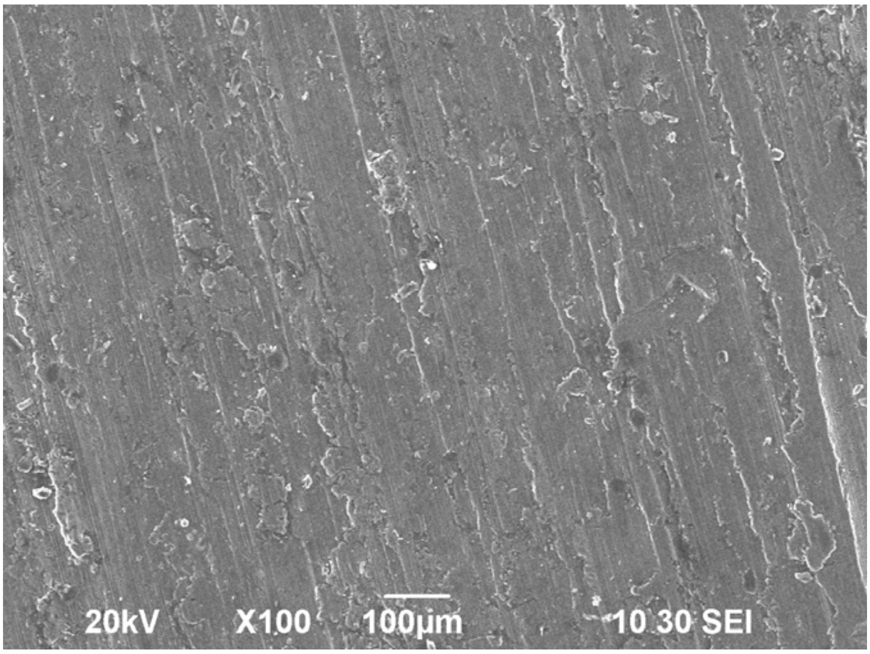

Fig. 5.16 Typical machined surface produced by G-ECDM

Turning to the concern of the presence of the harmful Al_4C_3 phase at the machined surface after processing; both the surfaces of the ECDM and G-ECDM specimens were examined using the XRD technique. The processing conditions for these specimens are given in Table 5.6. The XRD patterns for the ECDM and G-ECDM specimens are shown in Figs. 5.17(a)-(c).

Although the XRD results (Fig. 5.17a) show that the Al_4C_3 phase was not detected in the ECDM specimen when the machining time was 3 minutes (processing Condition A). In fact, similar results were found and were presented in Chapter 4 (section 4.1.3), when a relatively low peak current and a short machining time were employed. However, when the machining time was prolonged and a high peak current was used (processing condition B), the XRD results (Fig. 5.17b) show that the Al_4C_3 phase was present at the surface of the ECDM specimen. The results thus suggest that Al would react with SiC and form the Al_4C_3 phase if an intense heating condition exists during processing. In the present case, a long processing time and high peak current provide a favourable condition. However, for the case of G-ECDM, the XRD results (Fig. 5.17c) show that even after a relatively long processing time with a high peak current (processing condition C), no Al_4C_3 was detected. The reason for the absence of the Al_4C_3 phase is believed to be due to the grinding action of the G-ECDM process removes most of the re-cast and heat affected materials at the machined surface.

Table 5.6 Processing conditions for the study of the presence of Al_4C_3 phase at the machined surface

Processing Conditions	A	B	C
Processing Mode	ECDM	ECDM	G-ECDM
Processing Time (min)	3	10	10
Peak Current (A)	30	36	36
Applied Voltage (V)	110	110	110
Pulse Duration (μs)	40	40	40
Media	1% $NaNO_3$	1% $NaNO_3$	1% $NaNO_3$
Duty Cycle	1:6	1:6	1:6
Spindle Speed (rpm)	1500	1500	1500
Original Feed Speed (μm/min)	240	240	240

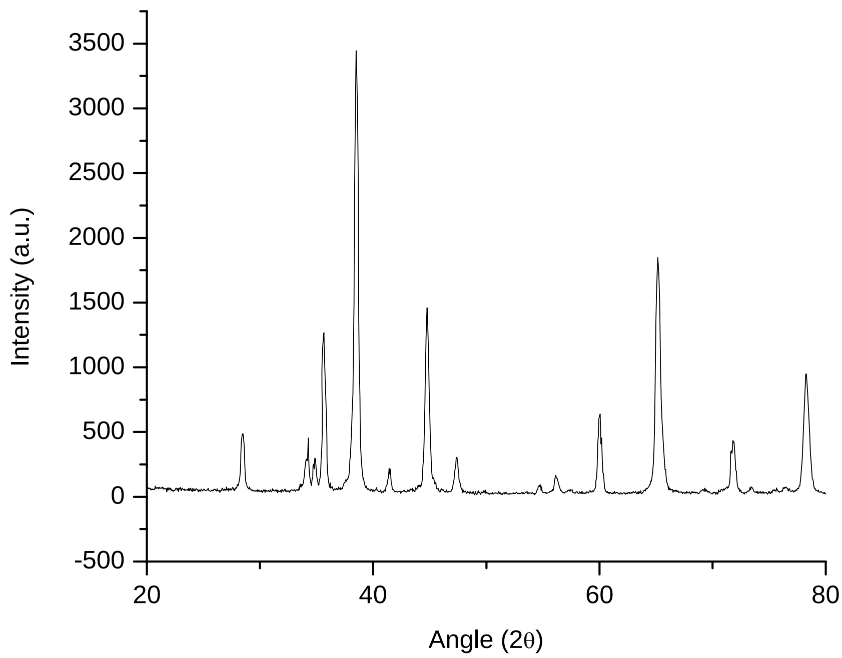

(a)

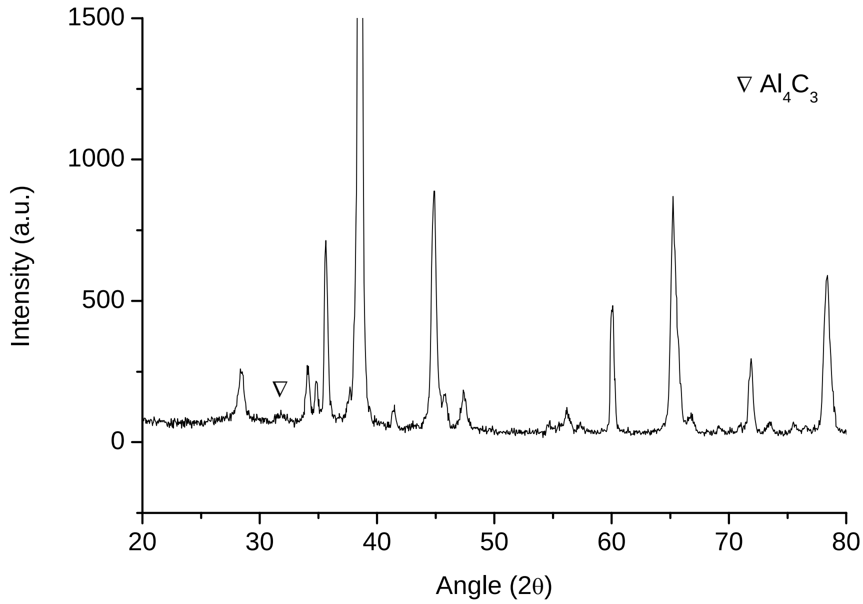

(b)

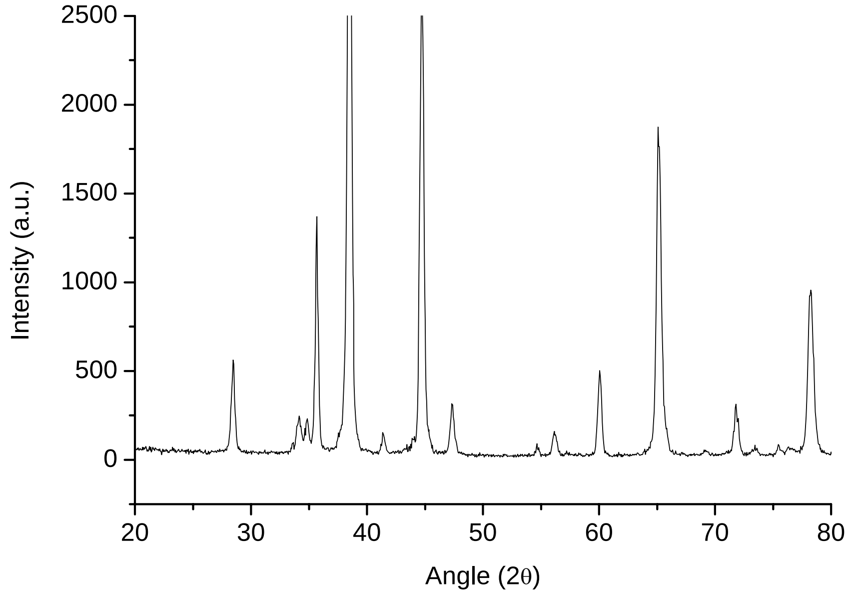

(c)

Fig. 5.17 XRD patterns obtained for (a) Processing Condition A, (b) Processing Condition B, and (c) Processing Condition C

5.4 Summary

When grinding is incorporated with the ECDM process, both the MRR and the molten material throw-out coefficient significantly increased. The material removal mechanism of grinding-aided electrochemical discharge machining (G-ECDM) of MMCs has been modelled, and the individual contribution of ECM and EDM to the material removal rate has been established. The theoretical results show that EDM plays a more significant role in material removal when the removal rate was considered. With regard to the EDM action, both the experimental and predicted results showed that the molten material throw-out coefficient of the ECDM process was about 0.1. This is in agreement with previous experimental studies. During G-ECDM of composites, unstable conditions could occur. However, the spinning effect of the spindle could unknot short-circuit situations and restore the stable machining condition. Should seriously unstable conditions occur, the electrode servo control system would act instantly to retract the spindle, and this was found to be effective in overcoming the problem. In summary, the G-ECDM process is superior to the ECDM process in machining metal matrix composites, with a higher machining efficiency and a better surface quality. Notwithstanding the success of the G-ECDM process, there are still limitations of the process. The design of a suitable tool-electrode to meet different shape and profile requirements of the product could be challenging. And the tool design also depends on the material of the product. If a very high spindle speed is required, then electrical transmission between the bush and the spindle might become a problem.

CHAPTER 6

SINGLE PULSE STUDY OF G-ECDM

To further study the G-ECDM mechanism, a series of single pulse studies were conducted and the results are presented in this chapter. The crater volume, the discharge waveform, and the distribution of craters have been studied for the ECDM and G-ECDM processes.

6.1 Experimental Approach

The abrasive cathode electrode is a steel cylinder of diameter 10mm, which is coated with a 100μm thick composite coating of Ni with up to 55% of diamond particles of a nominal size of 120μm; while the same electrode but without the diamond abrasive is employed for the ECDM experiment (Fig. 6.1). The workpiece material is a particulate reinforced aluminium alloy 6061 with 10-vol% Al_2O_3 (10ALO). The nominal size of this reinforcement phase is 21μm. The material was supplied in the form of 10mm thick rolled plates. The processing parameters for ECDM and G-ECDM are, applied voltage 90V, peak current 35A, pulse-on-period 200μs, an electrolyte concentration of 2.5% $NaNO_3$ Three rotating speeds of the cathode were used. They were (a) the low spindle speed condition, 15rpm, (b) the moderate spindle speed condition, 600rpm, and (c) the high spindle speed condition, 15000rpm (Table.6.1).

Table 6.1 Processing conditions for the study of spindle speed effect on crater profile

Processing Conditions	Media	Pulse Duration (μs)	Applied Voltage (V)	Peak Current (A)	Spindle Speed (rpm)
A	2.5%$NaNO_3$	200	90	35	15
B	2.5%$NaNO_3$	200	90	35	600
C	2.5%$NaNO_3$	200	90	35	15000

The profiles of the craters formed by G-ECDM and ECDM were measured using a 3 dimensional optical device (Alicona IFM G4). This instrument measured the volume of the cavity below the ground surface of the workpiece. Five measurements were taken to obtain an average value.

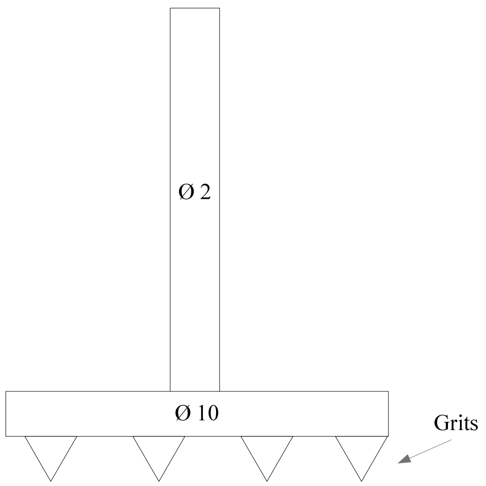

(a)

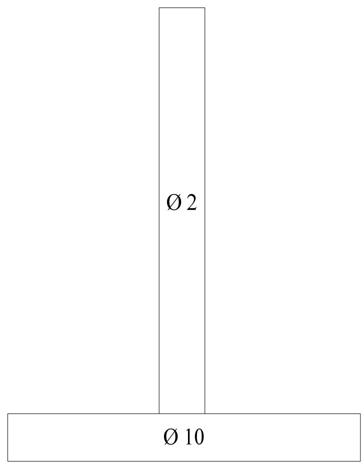

(b)

Fig. 6.1 Schematic drawings showing the (a) G-ECDM tool-electrode, and (b) the ECDM tool-electrode

6.2 Results and Discussion

6.2.1 Effect of spindle speed on crater volume

The tool-electrode rotational effect of the G-ECDM process on crater profile was studied by varying the spindle speed of the electrode. Fig. 6.2, Fig. 6.3 and Fig. 6.4 show the craters produced by a single pulse for the conditions of low (15rpm), moderate (600rpm), and high (15000rpm) spindle speed conditions, respectively. These three spindle speeds corresponding to maximum relative displacements of the two electrodes of 1.5μm, 60μm, and 1500μm in one pulse period, respectively. The low spindle speed condition actually resembles the ECDM process, i.e. without the grinding effect. Despite the relatively large displacement that occurred in the high speed condition, the shape of the crater was not significantly different from those of the low and moderate conditions. Although the reasons for this are still not completely certain, it is considered that when the plasma channel was formed between the two electrodes, its anchoring positions on the electrode surfaces would not change appreciably throughout the pulse-on-period. This proposed concept is illustrated in the schematic diagram (see Fig. 6.5). Assuming this concept, the arc energy would not be dispersed outside the original spark area.

It is also interesting to note that the crater formed in the high speed condition was larger than those of the lower speed conditions. The crater volumes measured for the low, moderate, and high speed conditions were 25×10^5 μm^3, 41×10^5 μm^3, and 57×10^5 μm^3, respectively (Fig. 6.6). The RSD of the experimental results was within 2%. The increase is believed to be associated with an increase of the thrown out efficiency of the molten material. It is considered that the fluid flow force induced by the spinning electrode would facilitate the thrown out of molten material. As the speed was increased so was the fluid flow rate and force. The results thus indicate that in order to obtain a high material removal rate (MMR), a high electrode spinning speed is to be preferred.

From the re-constructed profiles of the craters produced under different spindle speeds (Figs. 6.2-6.4), it is apparent that the built-up re-solidified material around the crater was reduced as the speed increased. The results thus illustrate the role of the grinding action in removing re-cast material of the ECDMed surface, and the higher the spindle speed, the stronger the grinding effect would be. Such a grinding effect not only would increase MRR, also it would improve the surface quality since, defects such as cracks and porosity are normally present in the re-cast layer.

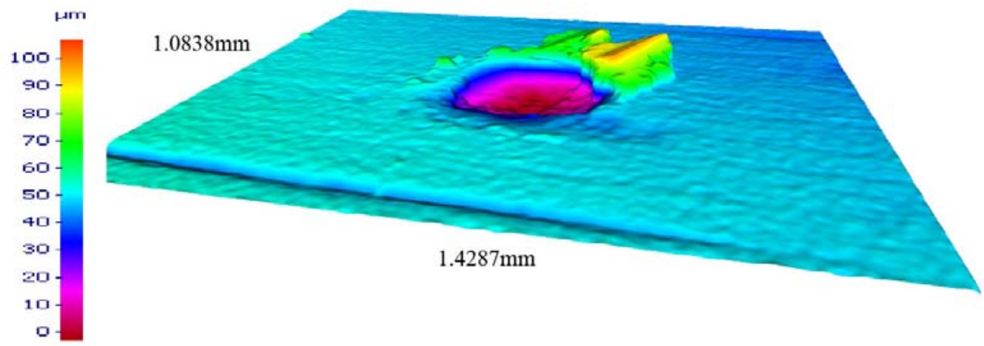

Fig. 6.2 Profile of a re-constructed crater produced under the low spindle speed condition (15rpm)

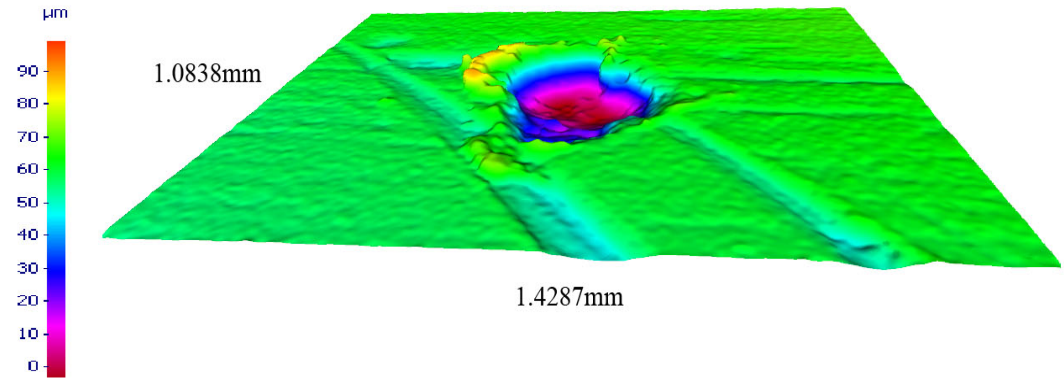

Fig. 6.3 Profile of a re-constructed crater produced under the moderate spindle speed condition (600rpm). A couple grinding marks are present

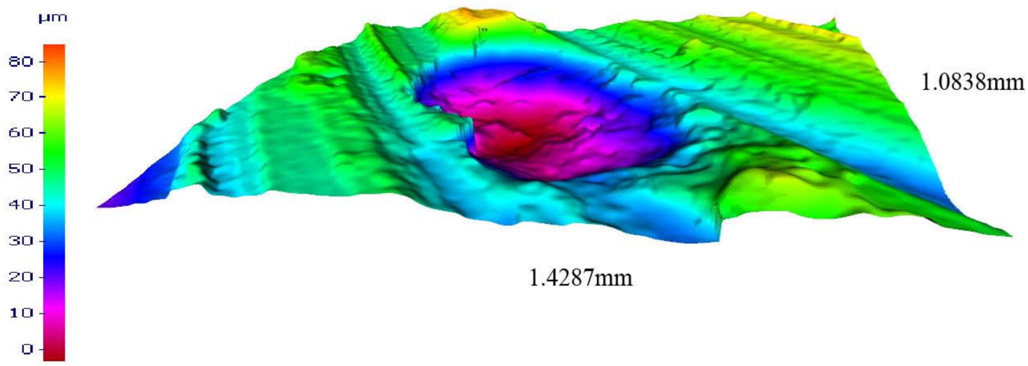

Fig. 6.4 Profile of a re-constructed crater produced under the high spindle speed condition (15000rpm)

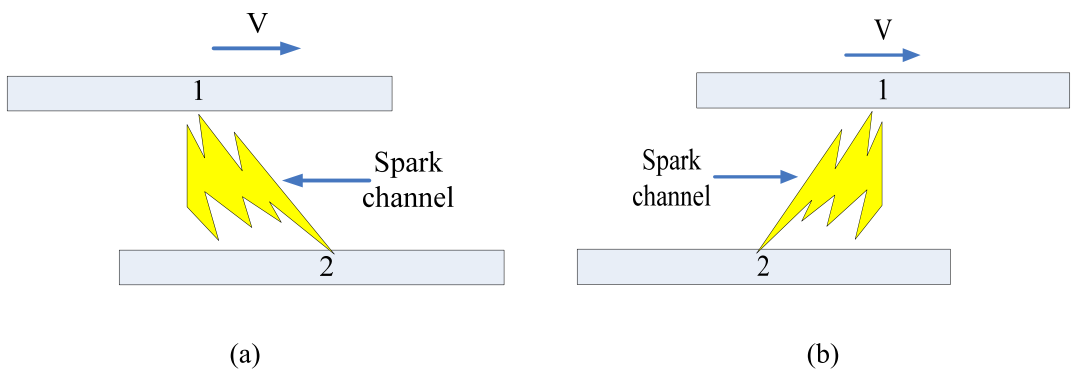

Fig. 6.5 Plasma channel position during the pulse-on-period

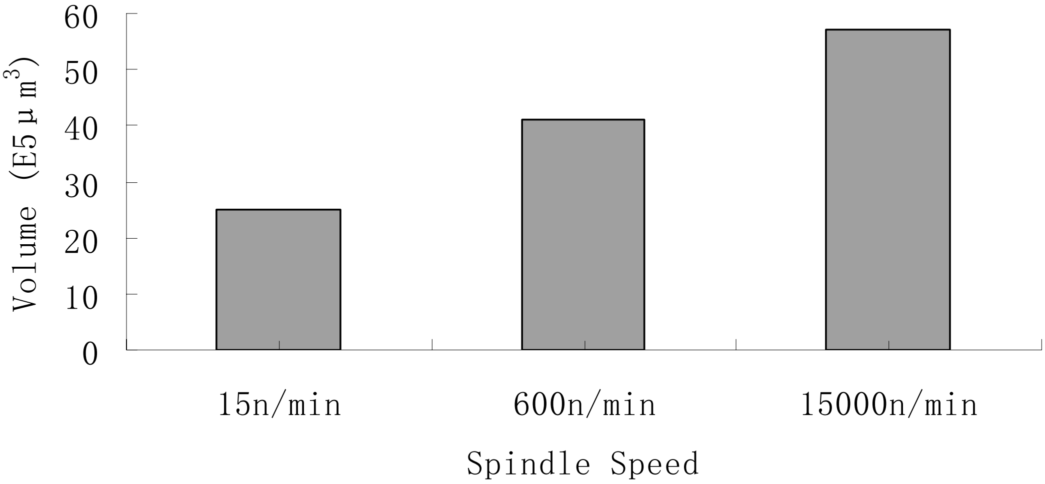

Fig. 6.6 Crater volume obtained for different spindle speed conditions

6.2.2 Comparison of voltage waveform

To further study the G-ECDM mechanism, some experiments have been conducted to study the voltage waveform of G-ECDM. In the study, the applied voltage was fixed at 60V and the processing temperature was 20^0C. Other processing parameters are given in Table 6.2. Typical waveforms obtained for the ECDM and G-ECDM processes are presented in Fig. 6.7(a) and Fig. 6.7(b) respectively. These figures show that the ignition delay occurred in the ECDM process, whereas G-ECDM has no such phenomenon.

Table 6.2 Processing conditions for the study of voltage waveform

Processing Conditions	Media	Temp (^{0}C)	Pulse Duration (μs)	Applied Voltage (V)	Peak Current (A)	Spindle Speed (rpm)
A(ECDM)	2.5% $NaNO_3$	20	64	60	35	0
B(G-ECDM)	2.5% $NaNO_3$	20	64	60	35	15000

In traditional EDM processes, pulse waveforms without ignition delay are considered to be a consequence of abnormal arcing. For which the abnormal arc position is thought to be unchanged due to the reason that the condition occurs between the former arc point could facilitate the forming of another arc in the same place. This means that an abnormal arc will continue remove materials at the same location and hence burned machined surface and serious tool wear will result. Fig. 6.7(b) shows that the G-ECDM waveform resembles to that of EDM abnormal arcing. However somewhat unexpectedly, the craters distribute randomly over the entire G-ECDM area (Fig. 6.8), i.e. arcing did not occur at the same locality. This is rather different from the abnormal arcing behaviour of the traditional EDM process. At this stage, the reasons for why abnormal arching in the G-ECDM process results in random craters is still not certain. However, it is considered that the high relative velocity of the electrodes and the relatively high processing temperature are important contributing factors.

Under a high relative velocity condition, though the plasma channel anchoring positions on the electrodes are considered to be fixed during the pulse on period, the relative distance between the two anchoring points at the anode and cathode surfaces significantly increased. Accordingly, the next arcing would not easily occurr at the former positions due to a considerable shift in relative position. Therefore, the high relative velocity helps to change the arcing positions, and results in a random distribution of craters. With regard to high processing temperature conditions, it was found in Section 4.2.2 that a high temperature leads to a decrease in ignition delay time. In the case of G-ECDM, it is believed that the grinding effect could increase the temperature of the processing area, thus causing ignition delay to disappear. Thus, for the G-ECDM process, the occurrence of ‘abnormal arc waveform’ is believed to be due to a high processing temperature. The random distribution of craters suggests that even with abnormal arcing, the processing condition of G-ECDM process is stable, and a burned machined surface and serious tool wear did not occur. Furthermore, as mentioned in Section 4.2.2, the absence of ignition delay means a relatively long arc maintaining period is obtained, and under such a condition, more molten material is produced. The result is that a high MRR would be obtained from the G-ECDM process.

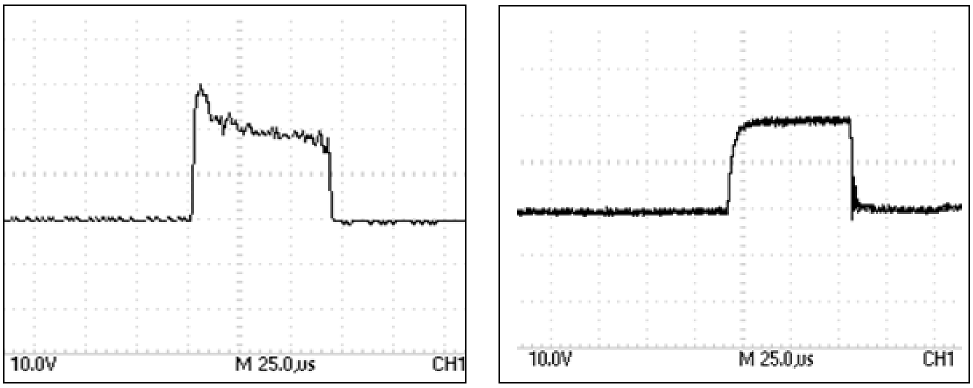

(a) (b)

Fig. 6.7 Typical voltage waveforms obtained for the (a) ECDM process, (b) the G-ECDM process

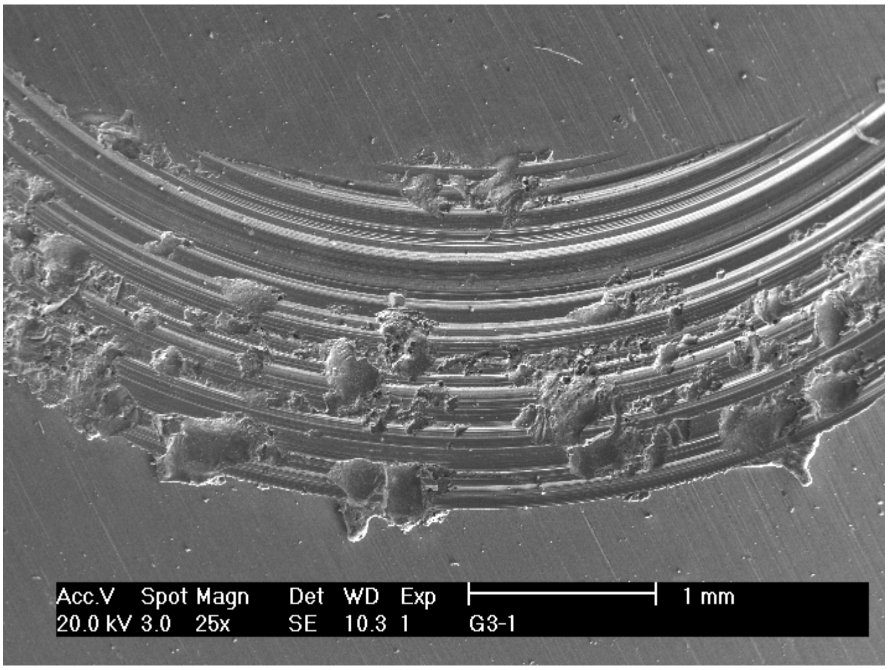

Fig. 6.8 SEM micrograph showing the distribution of craters on a G-ECDMed surface

6.3 Craters Distribution

To further study the scientific basis of craters distribution on the ECDM and G-ECDM machined surfaces of particulate MMCs, an ideal two-dimensional model consisting of parallel electrodes is employed to simulate the electrical field strength of the machining surface, i.e. the anode (Fig. 6.9). Nonconductive ceramic particles are assumed to be embedded in the anode. The processing condition is assumed to be stable and the electrolyte conductivity is assumed to be constant and uniform. The electric potential in the processing area can be described by:

$$\frac{\partial^2 \phi}{\partial x^2} + \frac{\partial^2 \phi}{\partial y^2} = 0 \tag{6.1}$$

and the boundary conditions are:

$$\phi_C = 0 \tag{6.2}$$

$$\phi_A = U \tag{6.3}$$

where ϕ_C is the electric potential at the surface of the cathode, and ϕ_A is the electric potential at the metal phase surface of the anode. J is the current density and σ is the conductivity. In the present study, U is the applied processing voltage, which is 110V. The ceramic particle is assumed to have a square shape of size 21μm. The electrical resistance of the ceramic particle is assumed to be infinitely large; while the resistance of the electrolyte is assumed to be 4Ω.cm. The machining gap between the electrode surfaces is 50μm. The height of the crater built-up edge is assumed to be 20μm for ECDM, and zero for G-ECDM (the built-up edge is assumed to have removed by grinding). The crater diameter and depth are assumed to be 180μm and 40μm, respectively and the distance between the centres of the two reinforcement particles is assumed to be 460μm. The above assumed dimensions are based on the actual measurements of the processed specimens. Based on these conditions and assumptions, the simulated results of the distribution of the electric field strength at the anode surface was obtained using the software ANSYS. The results of the field strength distribution can be used to predict the positions where arcing is likely to occur.

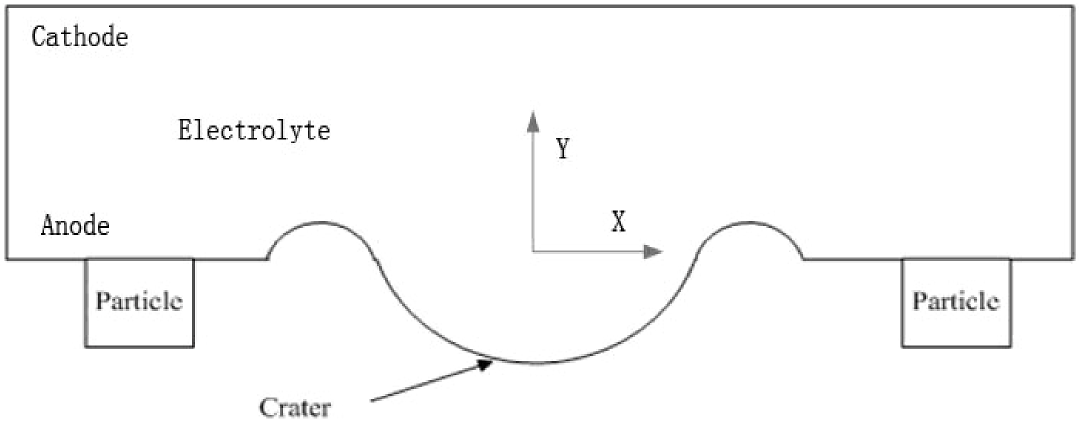

Fig. 6.9 2-D model for the analysis of electric field strength distribution on the machined surface

6.3.1 Simulation results of electric field

Fig. 6.10(a) and Fig. 6.10(b) show the simulation results of the distribution of electric field strength for the cases of ECDM and G-ECDM, respectively. Fig. 6.10(a) reveals that for the ECDM process, high electric field strength is experienced around the build-up edge of craters. While for the G-ECDM process, high electric field strength is found to occur at the interface between the matrix and the ceramic particle (Fig. 6.10b). The reason for this difference is primarily due to the fact that the build-up edge has been removed by grinding in the case of G-ECDM. Without the build-up edge, the results show that a strong electric field is established at the matrix-particle interface.

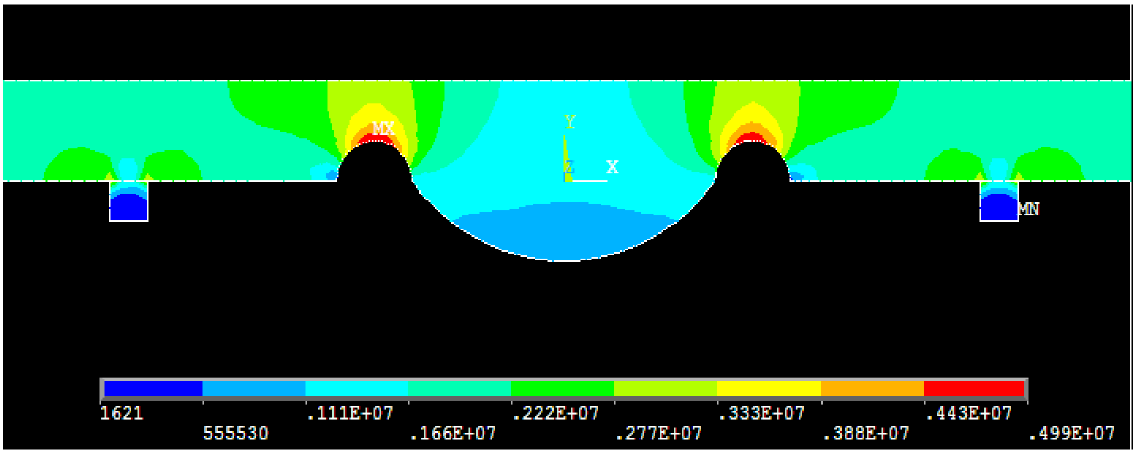

(a)

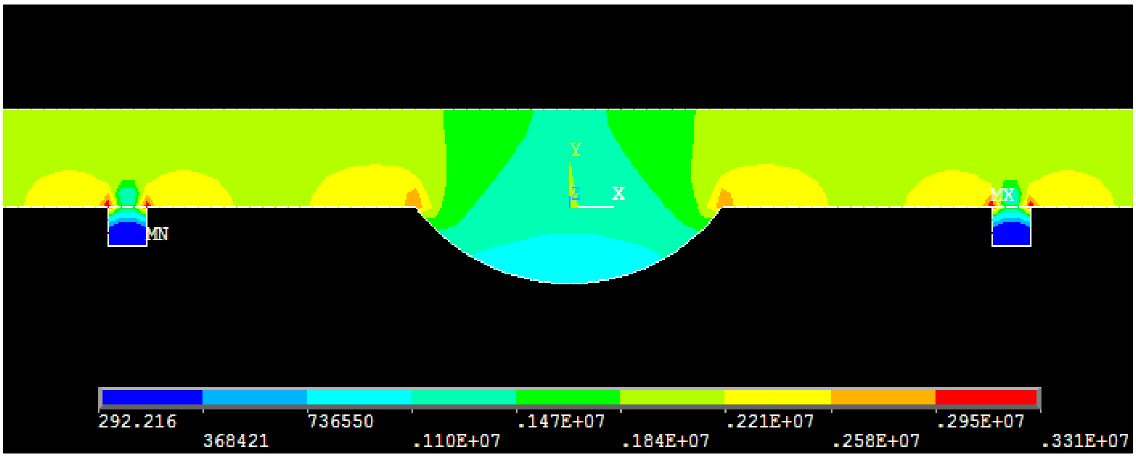

(b)

Fig. 6.10 Simulation results of electric field strength distribution for (a) ECDM, and (b) G-ECDM

6.3.2 Experimental verification

The SEM photographs of the machined surfaces of ECDM and G-ECDM specimens are presented in Fig. 6.11(a) and Fig. 6.11(b) respectively (the processing conditions are given in Table 6.3); they have been subject to five consecutive discharge pulses. Fig. 6.11(a) clearly shows that the craters on the ECDMed surface are connected to each others. This supports the view that under the ECDM condition, discharge occurs at crater built-up edges where the highest electric field strength is present. As a result, discharge craters tend to connect together. While for the G-ECDM process, separated craters were observed on the machined surface. This suggests that the previously formed craters have little effect on the following discharge site. These results therefore support the above theoretical analysis of electric field strength of the ECDMed and G-ECDMed surfaces.

Table 6.3 Processing conditions for the study of craters distribution

Processing Conditions	Media	Duty Cycle	Pulse Duration (μs)	Applied Voltage (V)	Peak Current (A)	Gap Distance (μm)
A(ECDM)	2.5% $NaNO_3$	1:7	200	110	35	50
B(G-ECDM)	2.5% $NaNO_3$	1:7	200	110	35	50

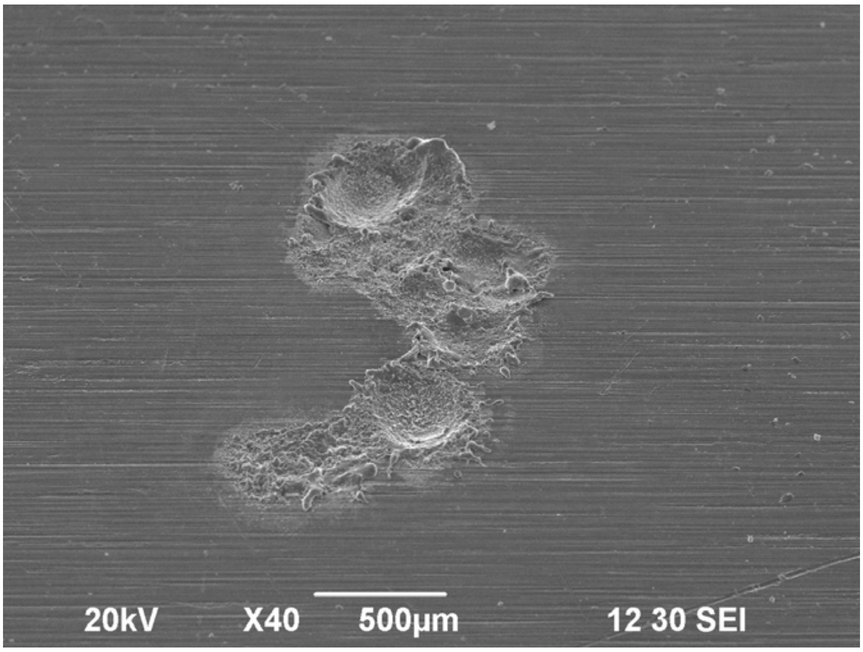

(a)

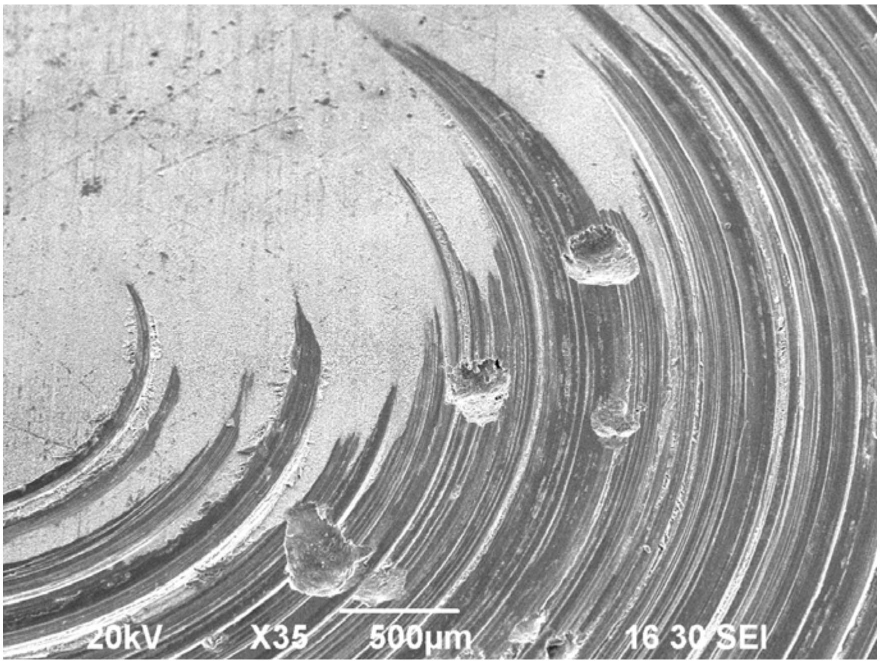

(b)

Fig. 6.11 SEM micrographs showing craters distribution on the MMC surfaces after (a) ECDM, (b) G-ECDM

6.4 Summary

To further study the G-ECDM mechanism, a series of single pulse studies have been conducted. The crater morphology and the distribution of craters of the ECDM and G-ECDM machined specimens have been analysed. The results show that for the G-ECDM process, the grinding action could remove the crater built-up edge. As a result, the MRR of G-ECDM is higher than that of ECDM and EDM. Although, the discharge waveform of the G-ECDM process resembles a form of abnormal arcing, the machining process is found to be stable and a burnt surface did not occur. This is attributed to the rotational motion of the cathode-electrode in constantly shifting the arcing position which results in a random distribution of craters. The differences in the distribution of craters on the machined surfaces of ECDM and G-ECDM specimens are satisfactory explained by analysing the electrical field strength in the machining of MMCs.

CHAPTER 7

TOOL PERFORMANCE OF G-ECDM

During the course of G-ECDM, if the grinding debris cannot be removed in time, some could adhere to the cathode-tool surface and when the trapped debris or chips between the diamond grits has increased to a certain amount, short-circuiting would occur. A schematic drawing showing grinding debris trapped in the tool is presented in Fig. 7.1. It is believed that EDM sparks could remove the clogged material that is trapped in the tool surface, and as such, stable machining conditions can be maintained. Recognising this, an analysis on tool performance of G-ECDM of MMCs was conducted. The scope of the study covers the aspects of tool cleaning and tool protection mechanism; also both theoretical and experimental studies have been conducted.

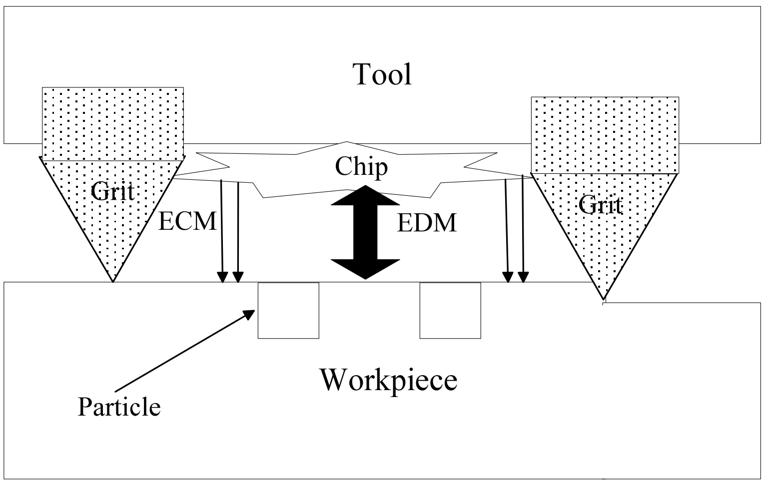

Fig. 7.1 Schematic diagram showing machining debris trapped between diamond grits

7.1 Theoretical analysis

Fig. 7.2 shows the physical model used to study the cleaning action of tool clogging by a spark. The tool is made the cathode and the workpiece is the anode with negative electrons flow to the anode and positive ions to the cathode. A high temperature plasma spark channel is formed between two diamond grits where there is a chip. Initially, because the expansion force is larger than the binding force, the channel will expand, and moreover, owing to the frictional force at the electrode surface, the spark channel will take the form of a drum (broken lines in Fig. 7.2). After a period of expansion, the channel will reach a quasi stable state, at which the channel size at the cathode end is smaller than that at the anode end [108]. As a result, a tornado shape channel is formed (solid lines in Fig. 7.2)

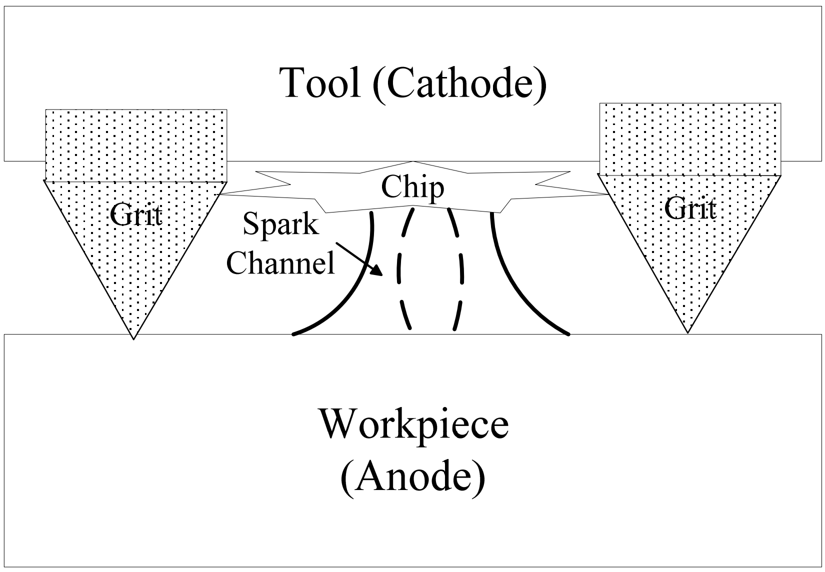

Fig. 7.2 Physical model used to study the tool cleaning effect.

To study the tool cleaning action by a spark, the EDM spark energy transferred to the cathode-tool needs to be determined. Employ a similar approach as is described in Section 5.1.4 where EDM spark energy W_{EDM} can be divided into three parts: namely, the energy at the anode surface (W_a), the energy at the cathode surface (W_b), and the energy exhausted in the spark channel (W_c).

$$W_{EDM} = W_a + W_b + W_c \tag{5.12}$$

The energy appears in the cathode surface (W_b) mainly comes from ion bombardment. Part of W_b will be used up for emission electrons, while a significant portion of which transforms into heat energy. Therefore, W_b can be divided into two components: electron emission energy W_e and heat energy W_h, i.e.,

$$W_b = W_h + W_e \tag{7.1}$$

The heat energy at the cathode can be treated as a heat source which composes of a bulk heat source and a surface heat source. The bulk heat source appears only in the conditions that the processing current changes rapidly, such as at the beginning of the process or when the processing conditions are unstable. Under a stable processing condition, the bulk heat source energy is negligible. It is therefore assumed that all the energy at the cathode surface appears as a surface heat source which is generated by the bombardment of ions, and it can be determined by:

$$W_h = \eta_h W_{EDM} \tag{7.2}$$

where η_h is the energy partition coefficient (refer to section 5.1.4), which is assumed to be 14% [108].

As a consequence, the heat energy generated in the cathode could melt or even evaporate any trapped debris material between the diamond grits. Naturally, a small amount of heat energy will be transferred to the electrolyte through heat convection and heat radiation. In this study, the surface heat source of the cathode is assumed to take the form of a Gaussian distribution.

7.1.1 Heat source model, boundary conditions

The heating source model of a spark and the corresponding boundary conditions used to simulate the temperature profile of the workpiece that are described in Section 5.1.5 are employed here to establish the temperature profile of the cathode. Fig. 7.3 shows a 2-D heating model of the cathode. The energy of a spark is assumed to have been absorbed by a chip that is adhered to the tool between two diamond grits. The heat energy then conducts through the binding material to the steel tool. Heat loss from the chip to the surrounding electrolyte through convection is also taken into account in the model.

Base on the Townsend breakdown and Streamer breakdown theories [103], ions will be kept away from the diamond grits and will enter into the metal phase of the cathode-tool. Therefore, the centre of the spark has a greater probability to occur at the metal phase, though its exact position is difficult to be determined. In this study, it is assumed that the spark occurs in the middle of two grits (Fig. 7.3).

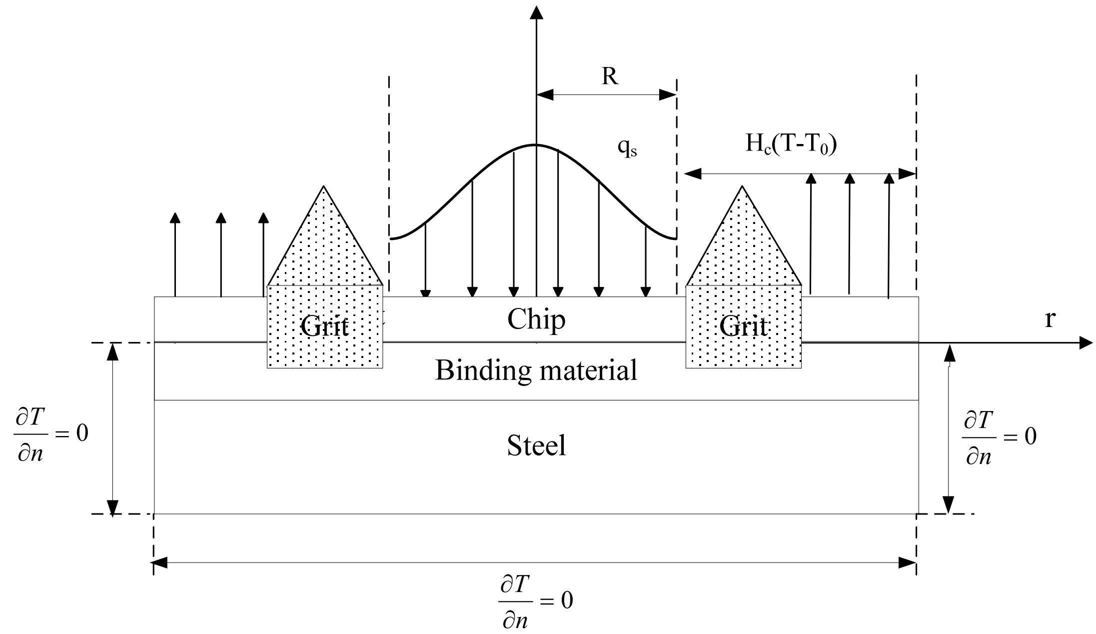

Fig. 7.3 Two-dimensional EDM heating model for the cathode

Similar to the heating of the anode, i.e. the workpiece (section 5.1.5), the heat flux distribution can be determined by the following equation:

$$q_s(r) = q_m \exp(-a\frac{r^2}{R^2}) = \frac{a}{\pi R^2}\eta_h W_{EDM} \exp(-a\frac{r^2}{R^2}) \qquad (5.20)$$

where q_m is the maximum heat flux which occurs at the centre of the spark channel and r is the radial distance from the centre of the spark. The heat flux decreases with increasing r. R is the spark channel radius at the cathode end which is considered to be smaller than that at the anode end, and is assumed to be 50μm. Whereas a is the heat source intensity coefficient and is assumed to be equal to 3 [97].

Since some heat energy is transferred to the electrolyte through heat convection, the heat lost will therefore be considered in the calculation of the temperature profile. Based on the fact that heat radiation consumes only very little energy, in this study, only heat conductivity and heat convection have been considered.

Now, the heat lost of the spark to the electrolyte through heat convection can be determined by equation (5.18) in Section 5.1.5.

The coefficient of heat convection h_c can be determined using equations 5.21-5.23, previously given in Section 5.1.5, i.e.

$$h_c(x) = C\frac{\lambda}{x}R_e^{1/2}P_r^{1/3} \tag{5.21}$$

$$R_e = \frac{\rho\omega x}{\mu} \tag{5.22}$$

$$P_r = \frac{\mu c}{\lambda} \tag{5.23}$$

7.1.2 EDM energy of a single pulse

Before the simulation of the temperature profile of the cathode can be performed, it is necessary to determine W_{ECM}. In the G-ECDM process, there is a combined action of ECM etching and EDM spark erosion for every pulse. Equation 7.3 gives the total energy of a single pulse

$$W = \int_0^{t_k} u(t)i(t)dt \tag{7.3}$$

where *u(t)* is the voltage between the two electrodes. *i(t)* is the current and t_k is the pulse duration. The energy is divided into two parts, ECM energy W_{ECM} and EDM spark energy W_{EDM}:

$$W = W_{ECM} + W_{EDM} \tag{7.4}$$

In this study, both the ECM and EDM actions are assumed to have the same voltage *u(t)*. Since the ignition delay is very short, *u(t)* can be taken to be the processing voltage during the pulse-on period, which is normally around 22V for any applied voltage. Accordingly, the value of $i(t)$ governs the amount of energy for the ECM and EDM actions. It was found that the ECM current in this study is 18A. Accordingly, W_{EDM} can be determined by:

$$W_{EDM} = \int_0^{t_k} u(t)(i(t) - 18)dt \tag{7.5}$$

7.1.3 Simulation results of heating effect of a spark

The heating effect of a spark is analysed using the ANSYS software. The material properties of the diamond grit, 10ALO chip, the grit binding material (Ni) and carbon steel (tool substrate material) for the analysis are given in Table 7.1. The diamond grit is assumed to have a square shape with a nominal size of 120μm. The diamond grits are embedded in the Ni binding material of the tool, with part of the grit exposed at the tool surface. It is assumed that the unconcealed height of the grit is 50μm. The average distance between the grits is 100μm; this was obtained by measurements of the cathode-tool. While the thickness of the chip and the thickness of the binding material are taken to be 30μm and 100μm, respectively. Other processing conditions are given in Table 7.2.

Table 7.1 Material properties of diamond grit, binding material Ni, 10ALO chip and carbon steel tool substrate [104-105]

Parameters	Grit	10ALO	Ni	Carbon Steel
Thermal Conductivity (W/(m·k))	2200	156	82.9	47
Density(kg/m^3)	3520	2810	8910	7800
Specific Heat (J/kg·k)	550	897	461	490
Melting point (^{0}C)	-	650	1450	1460
oxidizing temperature (^{0}C)	720-800	-	-	-

Table 7.2 Processing Conditions for the study of heating effect of a spark

Processing Conditions	Processing Voltage (V)	Pulse Duration (μs)	Peak Current(EDM) (A)
A	22	48	10
B	22	48	20

Fig. 7.4 shows the simulation results of the temperature field of machining Condition A. The positions of the grit and the layer of the binding material are superimposed on the figure. According to the results, a large portion of the chip will be melted with a small amount vaporised, while the Ni binding material remains unchanged because the maximum temperature reached (860^{0}C Fig. 7.5) is still lower than the melting point of Ni. Since the maximum temperature occurs in the grit (250^{0}C Fig. 7.6) is lower than the oxidation temperature of diamond so the grit also remains unchanged. The results thus suggest that for this machining condition, tool clogging would be relieved without damaging the binding material and the grit.

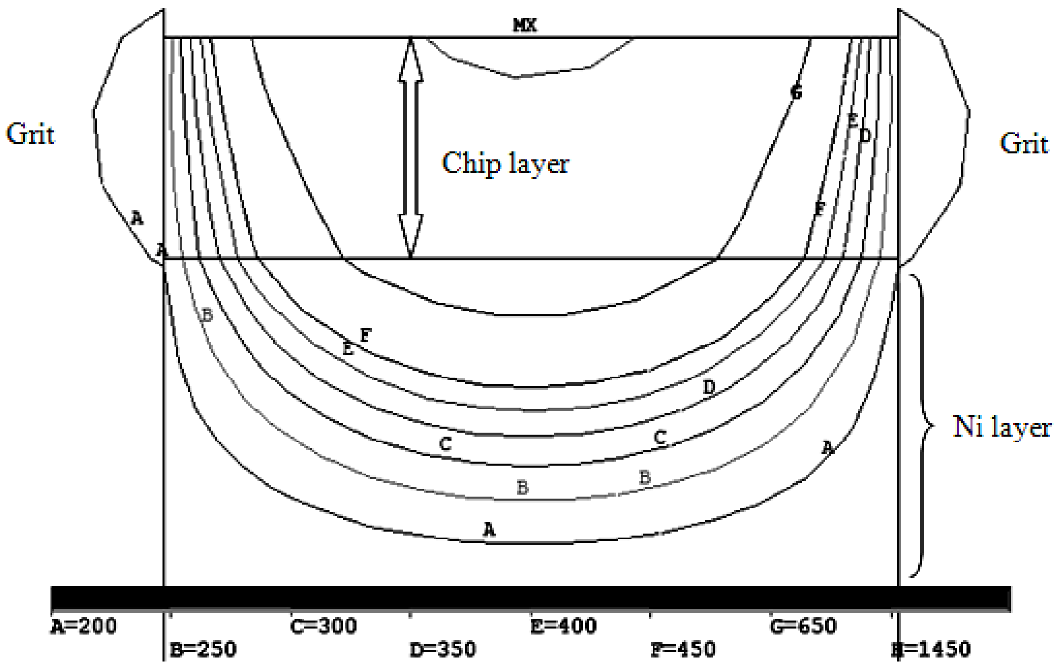

Fig. 7.4 Simulation results of the temperature fields of the chip and the binding material for machining Condition A

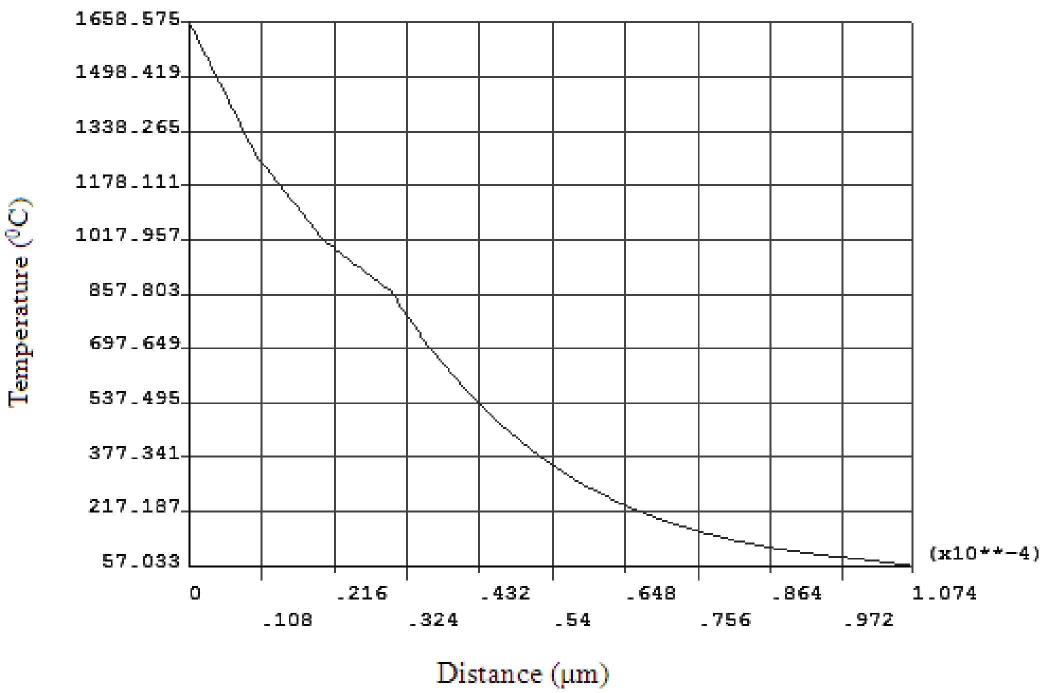

Fig. 7.5 Temperature profile as a function of distance along Y-axis

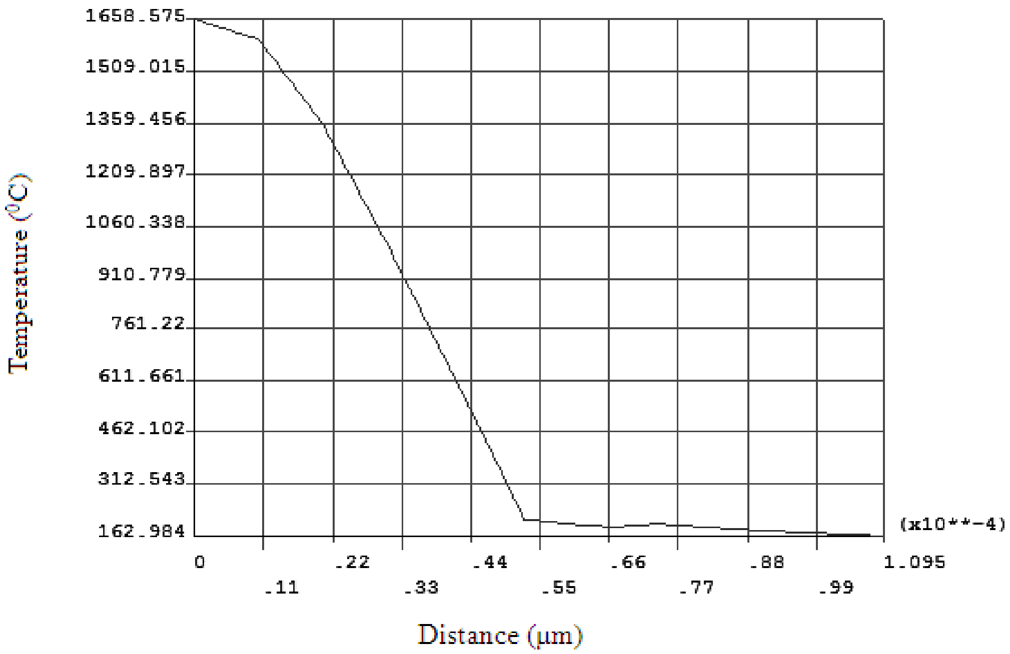

Fig. 7.6 Temperature profile as a function of distance along X-axis

As the peak EDM current was increased to 20A in machining Condition B, according to the simulated temperature field (Fig. 7.7), a larger portion of the chip would be vaporised when compared to Condition A of which the EDM current was at 10A. Also, a small amount of binding material would be melted, as evident from Fig. 7.8 that the temperature of the binding material can reach as high as 1450^0C at a depth of 10µm. However, the maximum grit temperature, which is about 450^0C (Fig. 7.9) is still less than the oxidation temperature, and therefore the grit is largely unchanged. The results thus show that machining Condition B, i.e. a higher peak current, would provide a more effective tool cleaning effect.

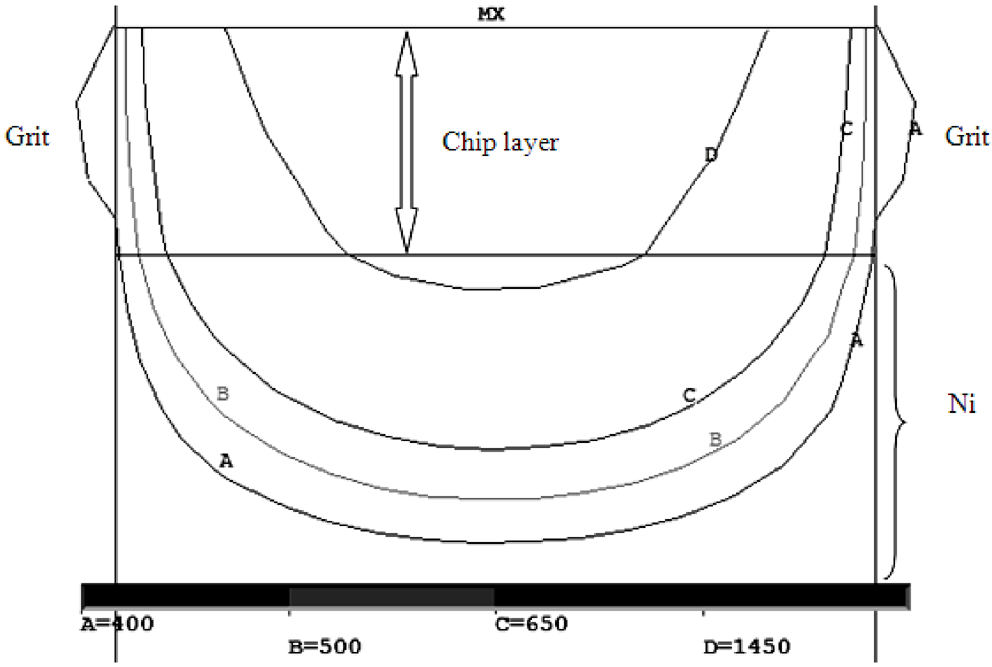

Fig. 7.7 Simulation results of the temperature fields of the chip and the binding material for machining Condition B

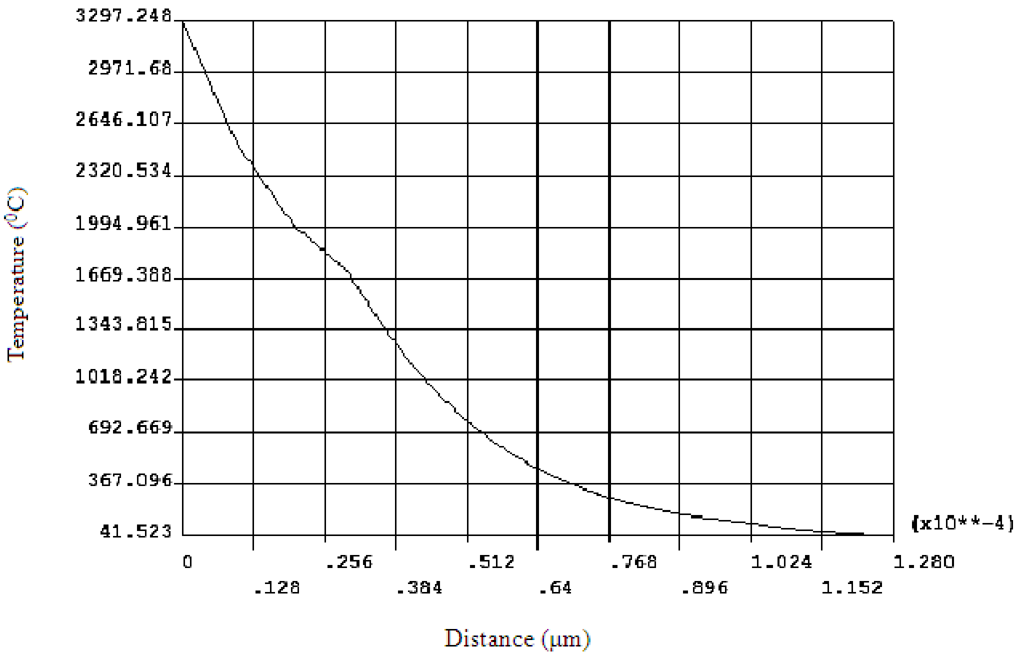

Fig. 7.8 Temperature profile as a function of distance along Y-axis for Condition B

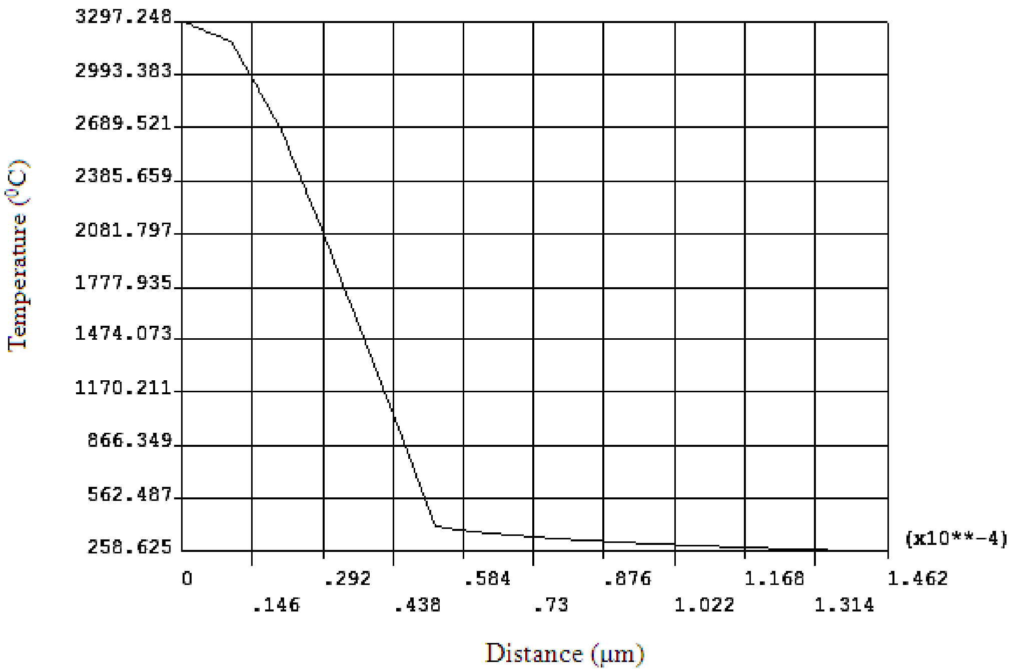

Fig. 7.9 Temperature profile as a function of distance along X-axis for Condition B

The above simulation results show that a large EDM current would remove more chip debris that is trapped between the diamond grits, and because of this, a more stable processing condition would be attained. For Condition B, where a high current is employed, though a small portion of the binding material would be melted, it should not affect the grinding action too seriously. So, it is believed that machining conditions as that of Condition B would give a better tool performance in G-ECDM. To verify some of these findings, some experiments have been conducted.

7.2 Experimental Verification

7.2.1 Conditions

The MMCs employed in this study was a particulate reinforced aluminium 6061 with 10-vol% Al_2O_3 (10ALO). The material was in the form of rolled plates with the reinforcement particle having a nominal size of 21μm. According to the working principle of the G-ECDM process, an appropriate steel drill tool with its surface reinforced with diamond grits of nominal size 120μm has been designed. The diameter of the composite drill tool is 26mm; the surface diamond reinforced layer is about 100μm thick (Fig. 7.10).

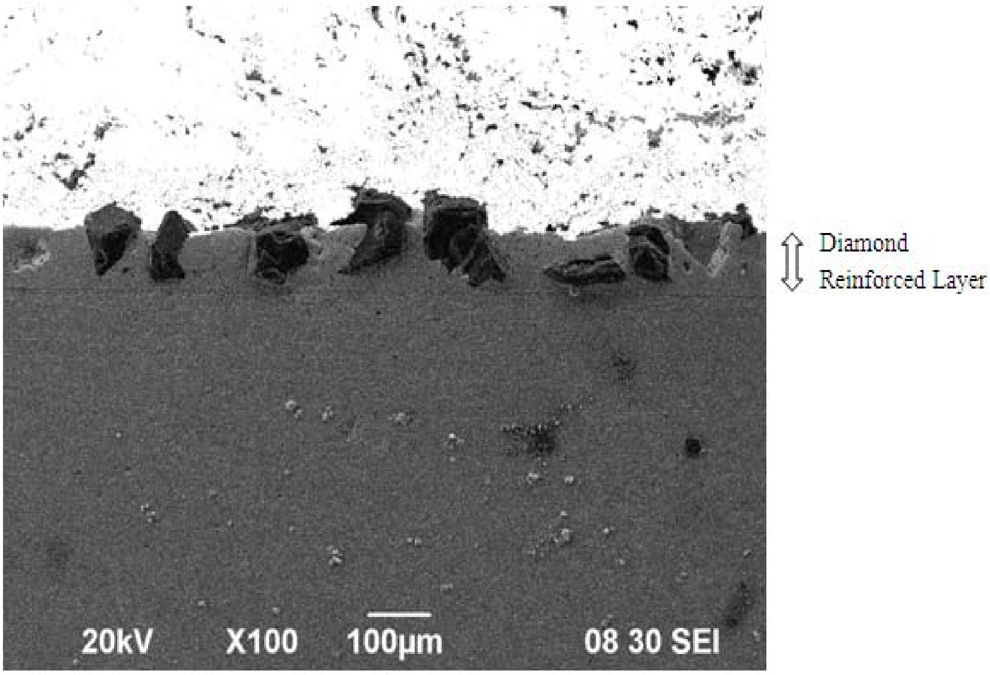

Fig. 7.10 SEM image showing the diamond reinforced layer of the tool-electrode

In the experiment, a 2.5wt% $NaNO_3$ electrolyte was used. Where other processing parameters are: processing voltage 80V, pulse on time 48μs, duty cycle 1:7, machining gap size 0.05mm, spindle speed 1500rpm, machining depth 0.5mm. The original feed speed was set at 240μm/min, but this would vary and is automatically adjusted by the electrode servo control system which would act instantly to respond to unstable machining conditions.

7.2.2 Experimental results and discussion

7.2.2.1 Effect of EDM current

Fig. 7.11 shows the effect of peak current on the number of incidents of unstable machining conditions that had been encountered (the processing conditions are given in Table. 7.3.). The result shows that the incident of unstable conditions considerably reduced as the peak current increased. This agrees with the simulation results presented in Section 7.1.3 that clogged chips are more likely to be removed by a high EDM current, as a result a more stable processing condition can be obtained.

Table 7.3 Processing Conditions for the study of unstable machining conditions

Processing Conditions	A	B	C	D
Peak Current (A)	21	28	35	42
Applied Voltage (V)	80	80	80	80
Pulse Duration (µs)	48	48	48	48
Media	2.5% $NaNO_3$	2.5% $NaNO_3$	2.5% $NaNO_3$	2.5% $NaNO_3$
Duty Cycle	1:7	1:7	1:7	1:7
Spindle Speed (rpm)	1500	1500	1500	1500
Feed Depth (mm)	0.5	0.5	0.5	0.5
Original Feed Speed (µm/min)	240	240	240	240

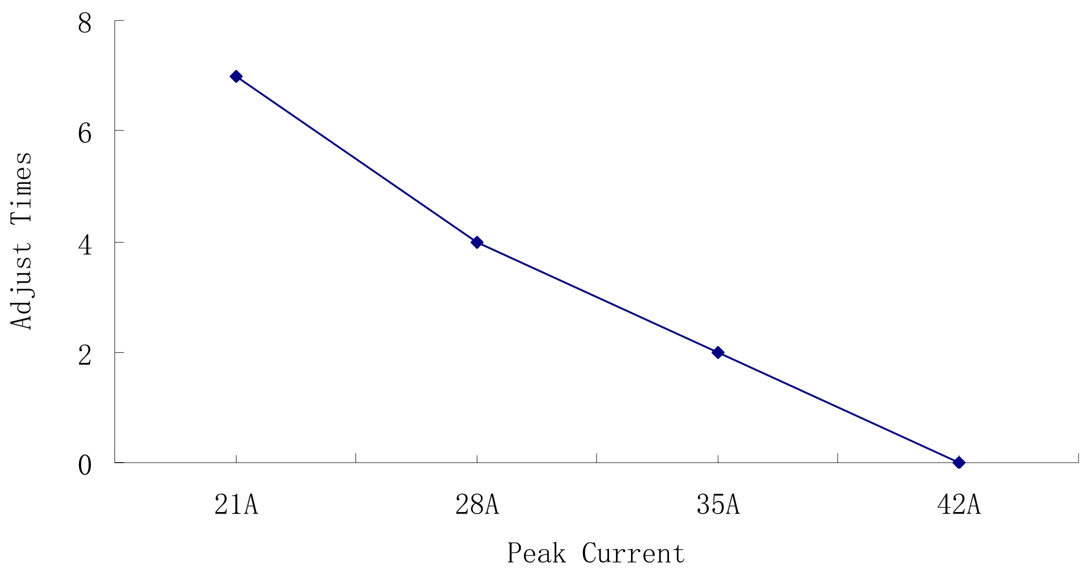

Fig. 7.11 Relationship between number of incidents of unstable machining and current

An examination of the machined surfaces of the MMCs that were produced using a low peak current of 28A (Table 7.4, Condition A) and a high peak current of

38A (Table 7.4, Condition B) shows that for the former hardly any grinding marks can be found (Fig. 7.12a), while for the latter, obvious grinding marks were observed (Fig. 7.12b). The results thus indicate that high EDM amperes enhanced the grinding effect while still maintaining a stable machining condition. With a high EDM current, not only is a strong grinding action of material removal obtained, the high energy spark also increases the material removal rate. All this is made possible because the high energy spark serves the role of tool cleaning, and has therefore overcome the problem of short-circuit recurrence and allows the servo system to drive the tool-electrode at a relatively high pace. On the other hand, if a low EDM current was used, tool clogging could become a problem, and should this happen, an unstable condition is encountered. As a result, the servo system would retract the tool and this would undermine the grinding action. This is considered to be the reason why very few grinding marks can be found on the machined surface of the specimen processed at a low EDM peak current.

Table 7.4 Processing conditions for the study of grinding effect on machined surface topography

Processing Conditions	A	B	C	D
Peak Current (A)	28	38	28	38
Applied Voltage (V)	80	80	80	80
Pulse Duration (μs)	48	48	48	48
Media	2.5% $NaNO_3$	2.5% $NaNO_3$	2.5% $NaNO_3$	2.5% $NaNO_3$
Duty Cycle	1:7	1:7	1:7	1:7
Spindle Speed (rpm)	1500	1500	1500	1500
Feed Depth (mm)	0.5	0.5	0.5	0.5
Original Feed Speed (μm/min)	240	240	360	360

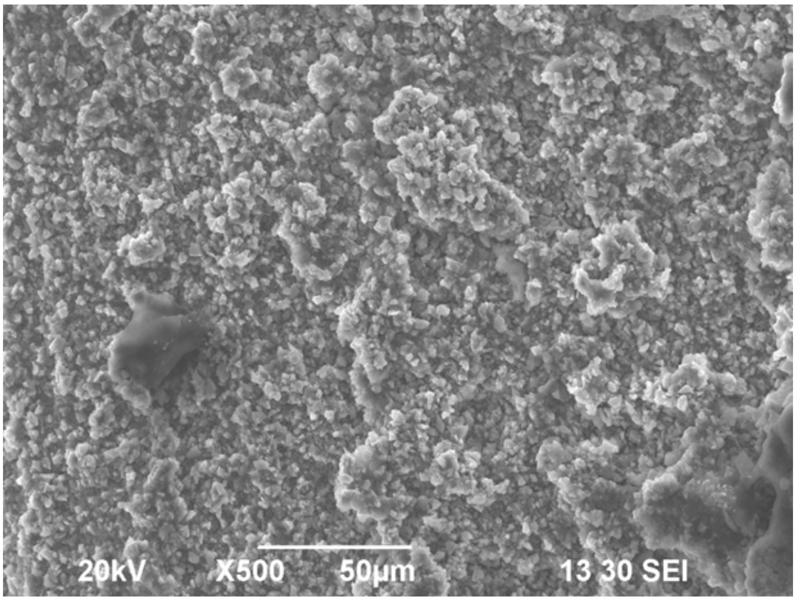

(a)

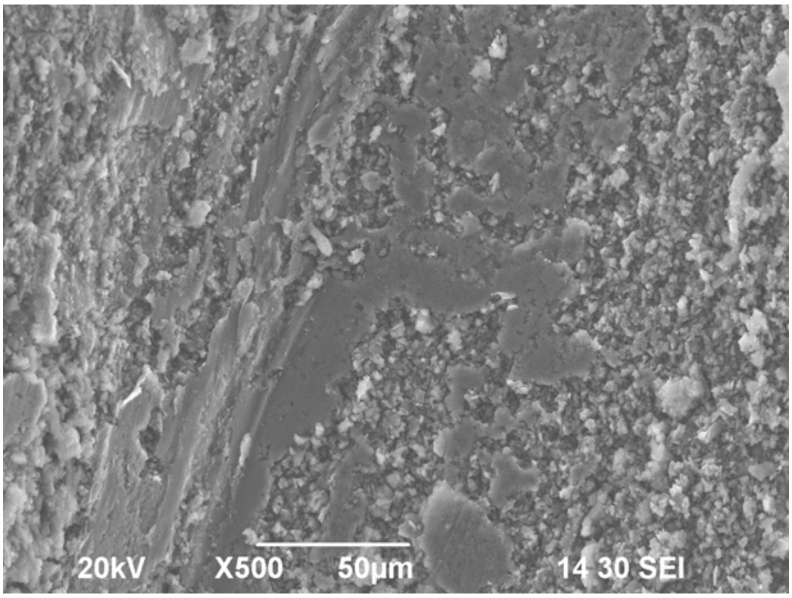

(b)

Fig. 7.12 Machined surfaces produced under a peak current of (a) 28A, (b) 38A, with electrode servo control

Another experiment was conducted without the operation of the electrode servo system, and the electrode was made to advance at a preset speed of 360 μm/min. Under this condition, the total MRR for the low (Table 7.4, Condition C) and high current (Table 7.4, Condition D) conditions will be the same. Contrary to the case where electrode servo control is employed, numerous grinding marks can be found on the machined surface of the low EDM current specimen (Fig. 7.13a), and very few was observed on the high EDM current specimen when servo control is absent (Fig. 7.13b). The results thus show that the grinding effect decreases with an increase in current. With a high EDM current, again, more material would be removed by spark vaporisation, but with a preset speed and without the servo control, the electrode would not accelerate its advancement. As a result, a relatively large machining gap results, and because of this, the grinding action becomes inactive, thus very few grinding marks can be found on the machined surface of the high EDM current specimen. For the low EDM current case, the material removed by spark vaporisation is much less; therefore a relatively small machining gap is expected. Without the servo control, the electrode would be driven close to the workpiece surface, and this would enhance the grinding action, hence numerous grinding marks are found. But without a high EDM current spark to remove clogged chips between the diamond grits, the problem of short-circuit is quickly established.

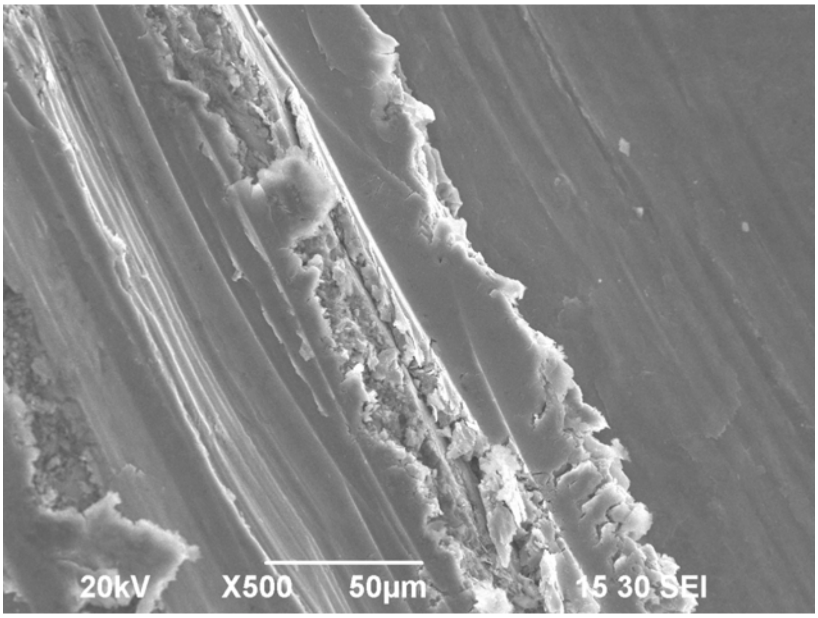

(a)

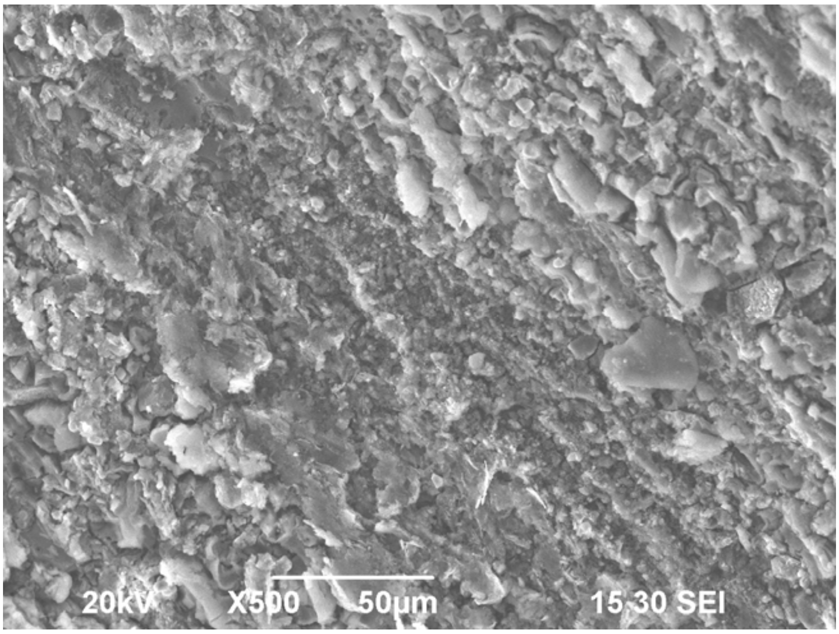

(b)

Fig. 7.13 Machined surfaces produced under a peak current of (a) 28A, (b) 38A, without electrode servo control

7.2.2.2 Examination of tool surface

Figs 7.14 (a, b, c), show the surfaces of the tools after direct grinding without the ECDM action (Table 7.5 Condition A), G-ECDM for 30 minutes (Table 7.5 Condition B), and G-ECDM for 60 minutes (Table 7.5 Condition C), respectively.

Table 7.5 Processing conditions for the study of tool surface condition

Processing Conditions	A	B	C	D	E
Processing Mode	Grinding	G-ECDM	G-ECDM	G-ECDM	ECDM
Peak Current (A)	-	35	35	35	35
Applied Voltage (V)	-	80	80	80	80
Pulse Duration (μs)	-	48	48	200	48
Media	2.5% $NaNO_3$	2.5% $NaNO_3$	2.5% $NaNO_3$	2.5% $NaNO_3$	2.5% $NaNO_3$
Duty Cycle	-	1:7	1:7	1:7	1:7
Spindle Speed (rpm)	1500	1500	1500	1500	1500
Original Feed Speed (μm/min)	240	240	240	240	240
Processing Time (min)	1	30	60	30	5

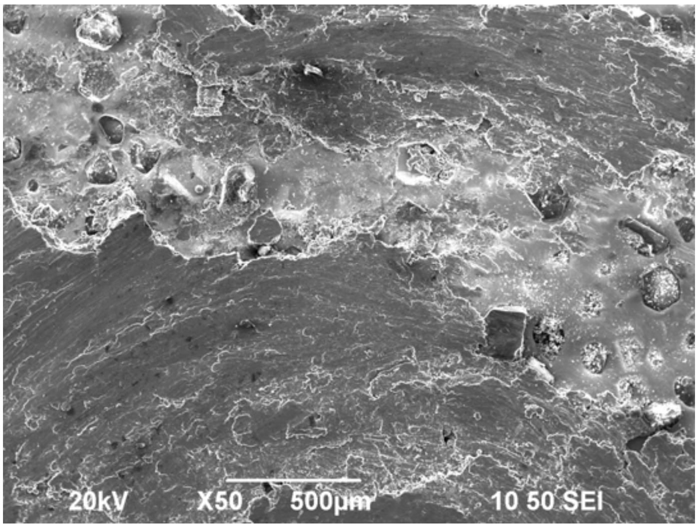

(a)

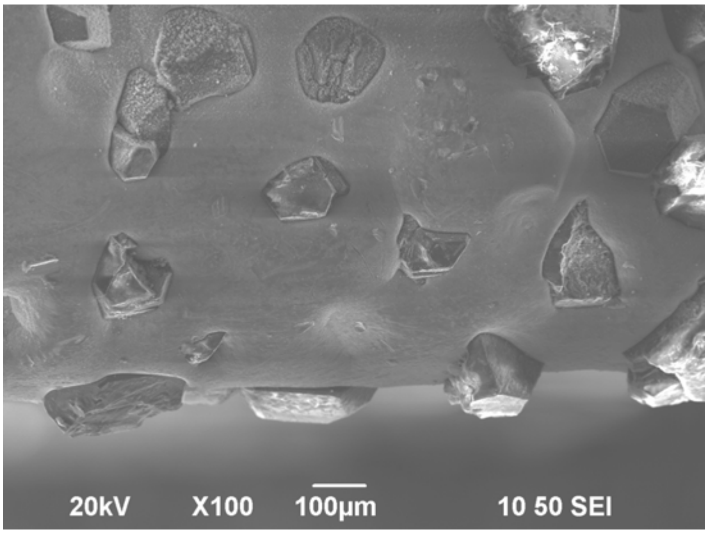

(b)

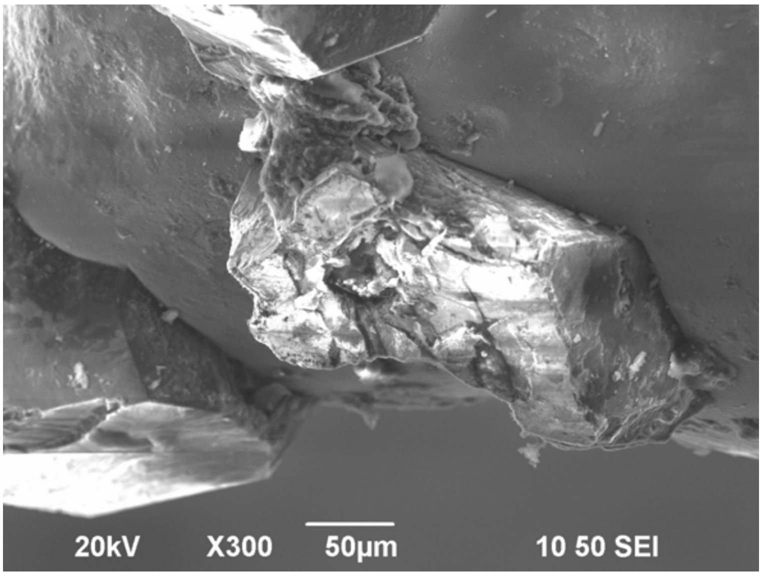

(c)

Fig. 7.14 SEM photographs showing the tool surfaces after machining the MMC under (a) processing condition A, (b) processing condition B, and (c) processing condition C

Fig. 7.14(a) shows that without ECDM, the problem of tool clogging is immense, even only after one minute grinding time, all the grits are covered by machining debris. However, tool clogging can hardly be observed on the tool after 30 minutes G-ECDM of the MMC (Fig. 7.14b). An SEM-EDS mapping of Al element of the surfaces of the direct grinding tool (Fig. 7.15) and the G-ECDM tool (Fig. 7.16) conforms that the chips are Al-based and therefore belongs to the workpiece. This clearly demonstrates the tool cleaning effect from EDM sparks. Moreover the temperature profile simulation results show that the EDM effect mainly serves the function of re-melting and vaporisation of trapped chips and without causing serious damage to the underlying tool material.

In the presence of ECDM, even after G-ECDM for 60 minutes, only a small amount of debris can be found on the tool (Fig. 7.14c). Moreover, there is no sign of serious damage at the interface between the diamond grit and the binding material.

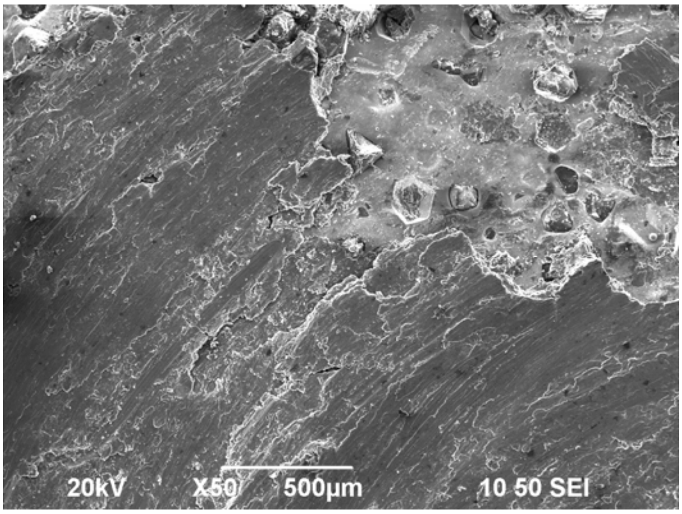

(a)

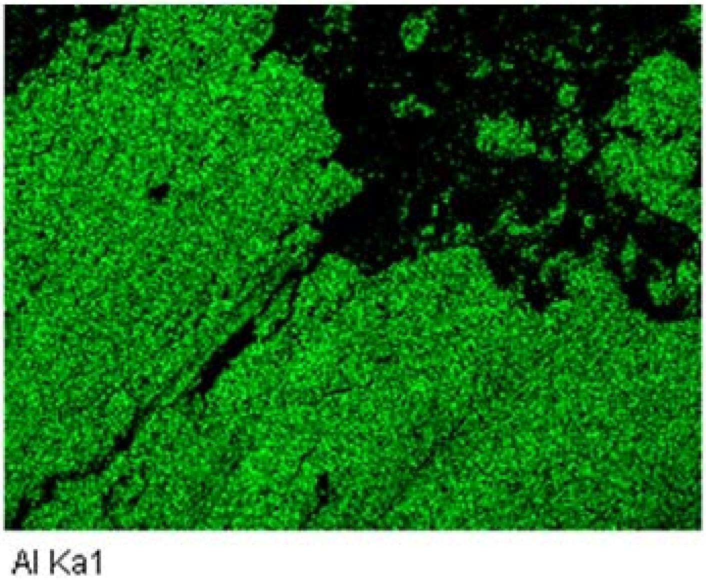

(b)

Fig. 7.15 EDS mapping of Al of the direct grinding tool surface: (a) an image of the tool surface after 1 minute of grinding, (b) mapping of Al

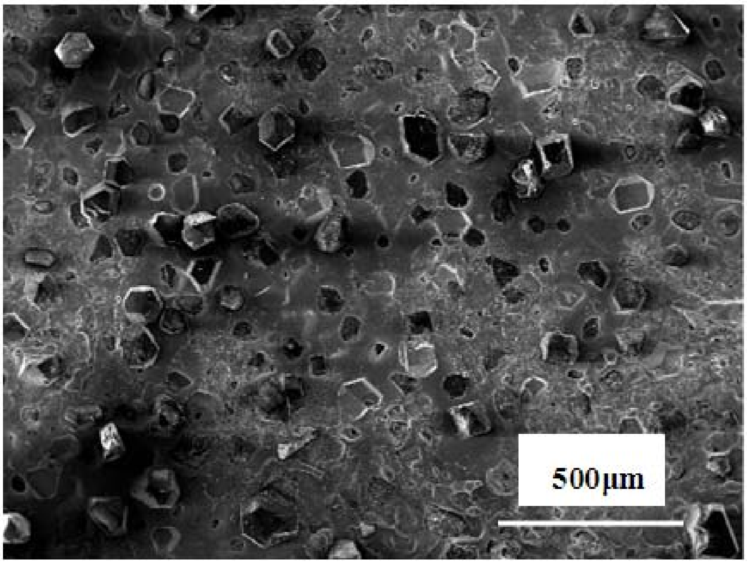

(a)

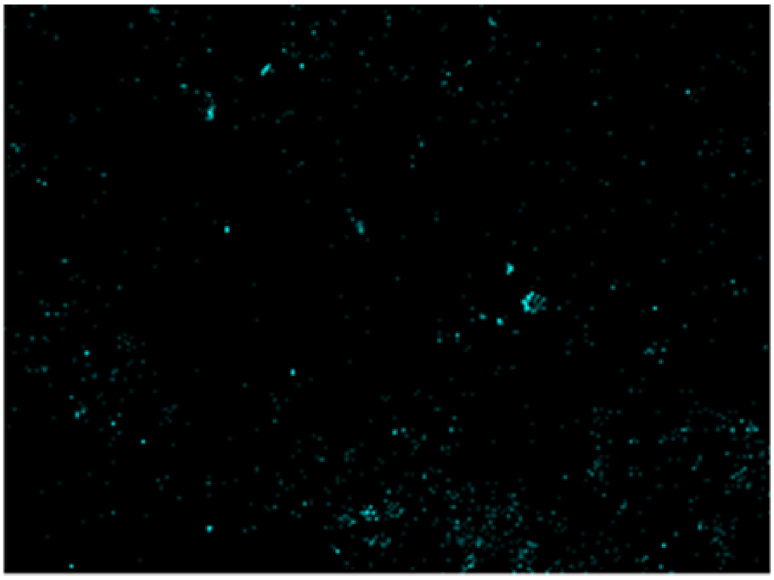

Al Ka1

(b)

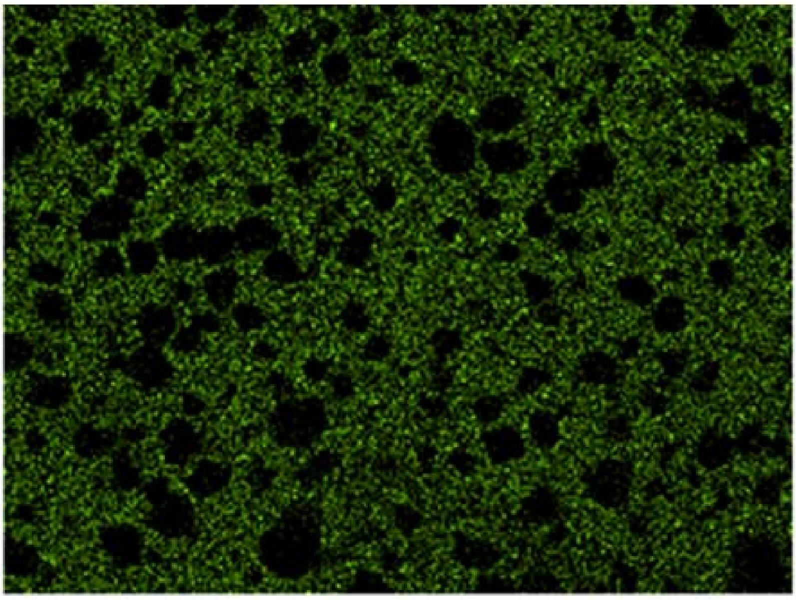

(c)

Fig. 7.16 EDS mapping of Al and Ni of the G-ECDM tool surface: (a) an image of the tool surface after 30 minutes of machining, (b) mapping of Al on the tool, (c) mapping of Ni on the tool

However, occasionally, microcracks can be observed on the G-ECDM tool surface (Fig. 7.17) (The processing conditions are given in Table.7.5, Condition D.). This is likely to be due to EDM sparking had occurred near/at the chip-diamond grit interface. Therefore, if the amount and the volume of the clogged material is small and the arc energy is large, high thermal stresses could develop and result in thermal cracking. To avoid such a problem, further study is required to establish the condition where, on one hand there is enough chips to protect the tool-electrode from excessive thermal stresses, while on the other hand a stable machining condition is maintained.

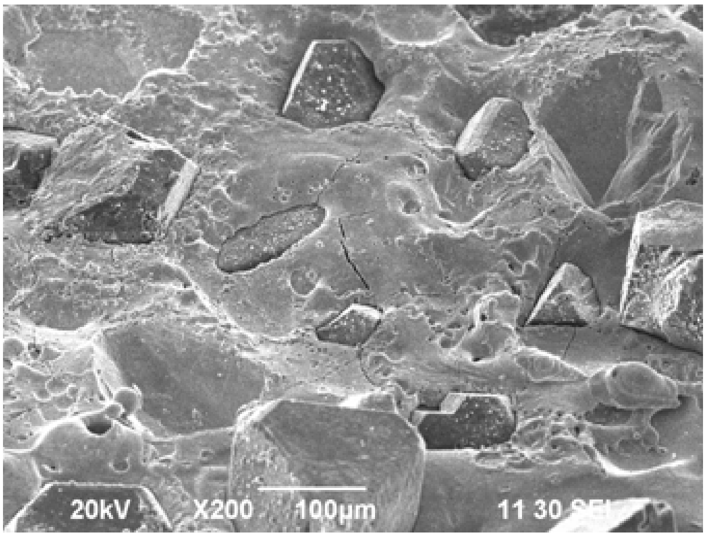

Fig. 7.17 SEM photography of the G-ECDM tool surface where microcracks are found (processing Condition D)

To further give support to the theory that machining chips can provide protection to the tool-electrode in G-ECDM, a series of ECDM experiments were conducted with a steel electrode coated with a Ni layer (Table 7.5, Condition E).

Fig. 7.18, Fig. 7.19 and Fig. 7.20 show the original tool surface, a crater on the tool surface produced by a single pulse, and the tool surface after a machining time of 5 minutes, respectively. It was found that for the case of a single pulse, there was virtually no Ni detected in the crater (Fig. 7.19); while for the case of 5 minutes processing time, it is clear that the Ni layer has been removed and the base material, i.e. Fe, has been exposed at the surface of the tool (Fig. 7.20). This clearly shows that EDM sparks could seriously damage the tool, in this case has removed the Ni binding material. As such rapid tool wear would occur. This is different to the case of ECDM. For the case of G-ECDM, it was found that even, after a machining time of 30 minutes, the Ni layer still remains on the tool (Fig. 7.16). So, once again, this demonstrates that the Ni layer on the G-ECDM tool surface has been protected by the clogged material between the diamond grits. This means that the tool life of the G-ECDM tool would be governed by tool wear of the diamond grit and not so much by the ECDM action on the metal phase of the tool. It is therefore believed that good tool life is expected of the G-ECDM process.

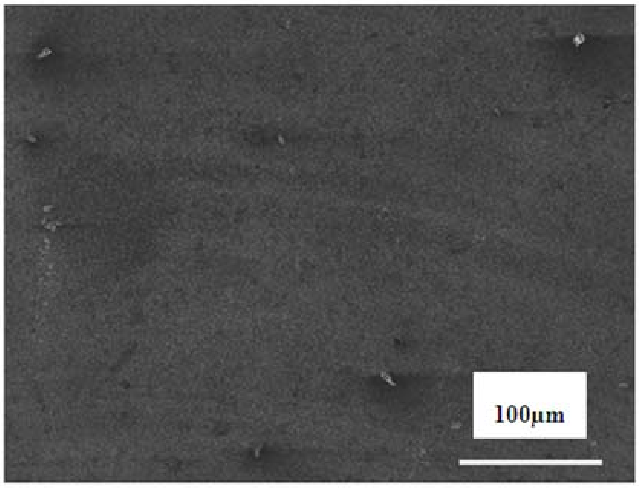

(a)

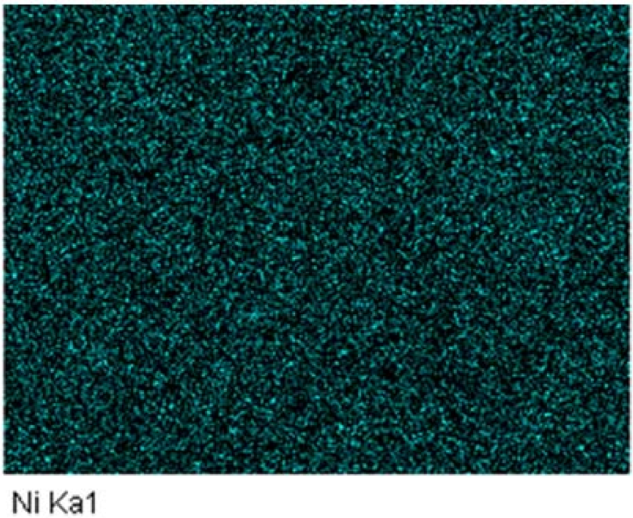

(b)

Fig. 7.18 EDS mapping of Ni on an original tool surface: (a) image of tool surface, (b) Ni mapping

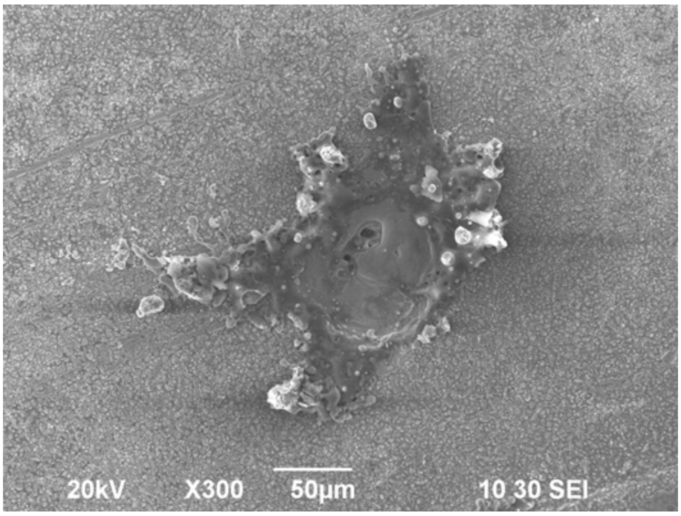

(a)

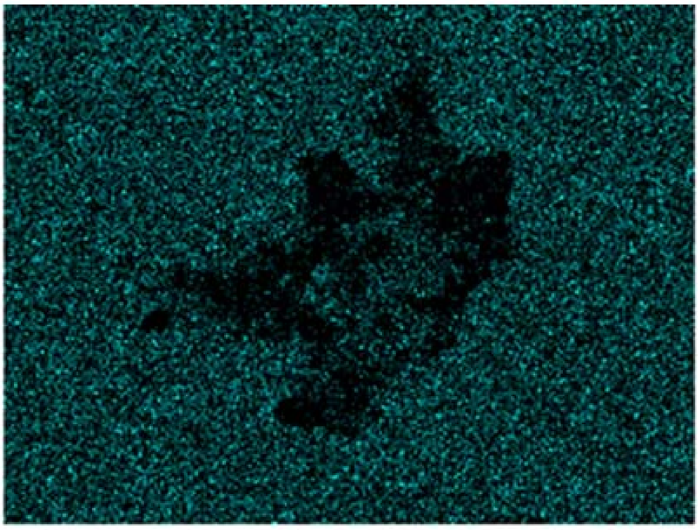

(b)

Fig. 7.19 EDS mapping of Ni of an ECDM crater on the tool surface

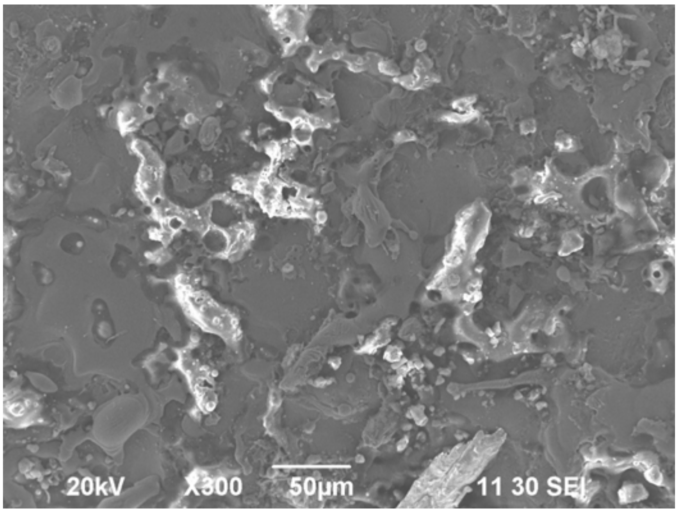

(a)

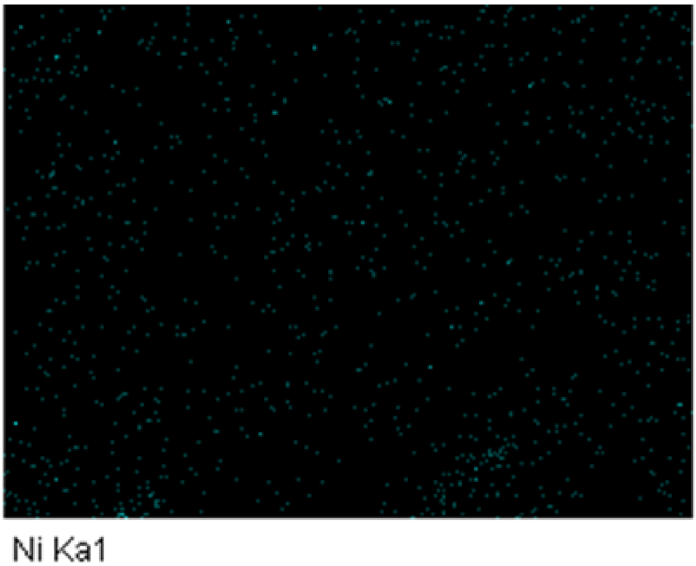

(b)

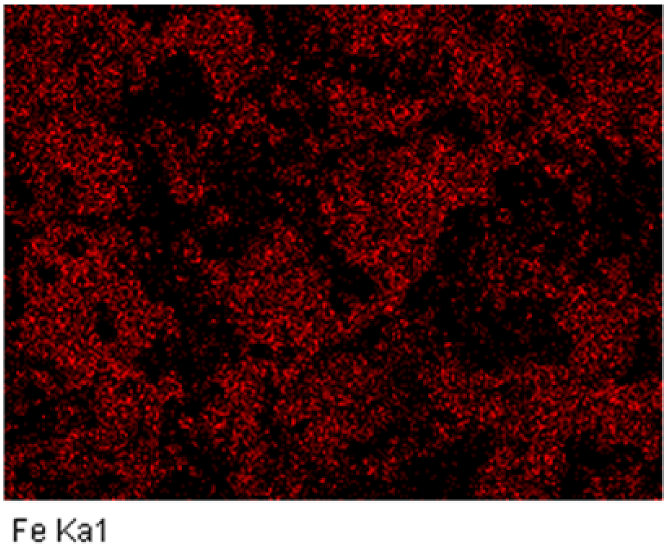

(c)

Fig. 7.20 EDS mapping of Ni and Fe of the tool surface after 5 minutes machining (processing condition E): (a) image of the machined surface, (b) Ni mapping, (c) Fe mapping

7.2.2.3 Tool performance

Figs. 7.21 (a, b, c) show the re-constructed surface topologies of the original tool surface, the tool after G-ECDM for 30 minutes (processing Condition B), and G-ECDM for 60 minutes (processing Condition C), respectively. The average diamond grit heights measured for these three conditions were 48µm, 51µm, and 56µm, respectively (Fig. 7.22). The results show that the longer the processing time, the higher the grit height. It is believed that during G-ECDM, though the binding Ni layer of the tool is protected by the clogged material between the diamond grits, some material would still be removed by the ECDM action. The diamond grit volume fractions for three conditions were measured to be 0.55, 0.48, and 0.46 respectively (Fig. 7.23). Although there was a relatively large decrease in grit volume after 30 minutes into the machining, further machining only caused a very mild reduction. The relatively high detachment rate of diamond grit at the early stage of the machining is believed to be due to the fact that some grits were not well bonded to the Ni binding layer, and as a result, those loose grits detached from the tool. After the run in period, the grit volume fraction hardly changed. This also leads to the conclusion that though some Ni binding material on the tool surface was removed by the ECDM action, most of the diamond grits remained firmly bonded by the Ni matrix. This means that the tool life of the G-ECDM tool is primarily governed by the tool wear of the diamond grit itself.

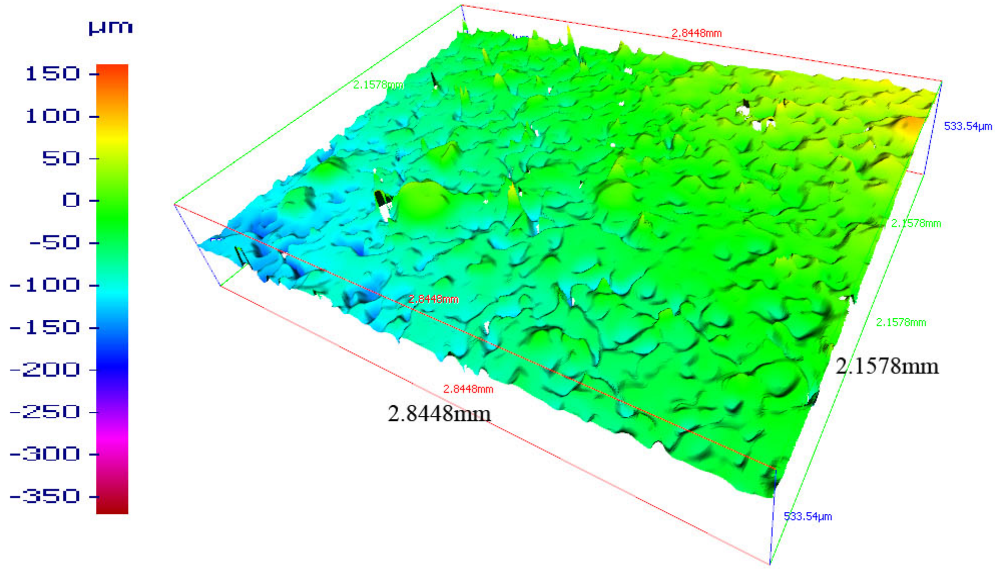

(a)

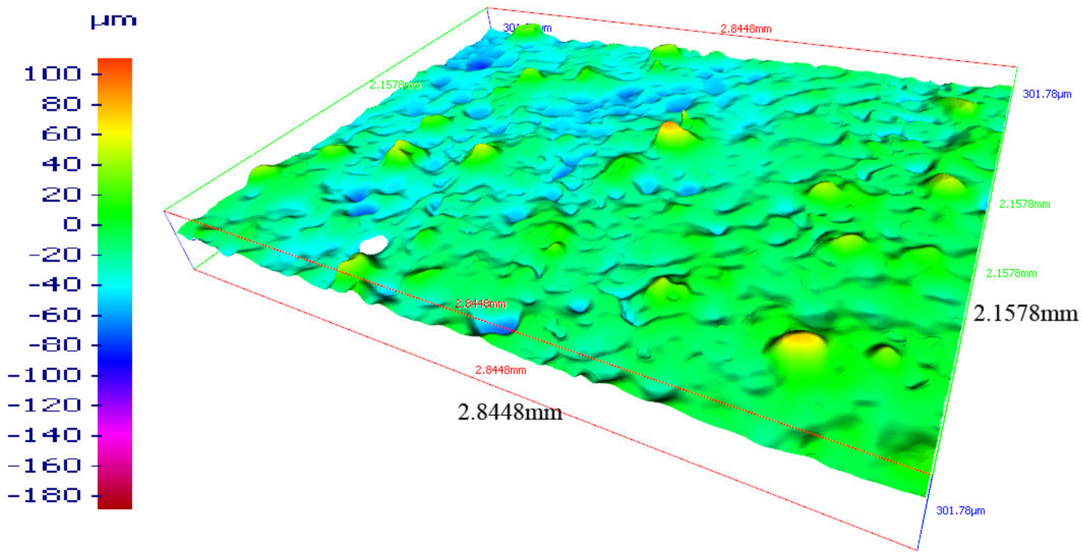

(b)

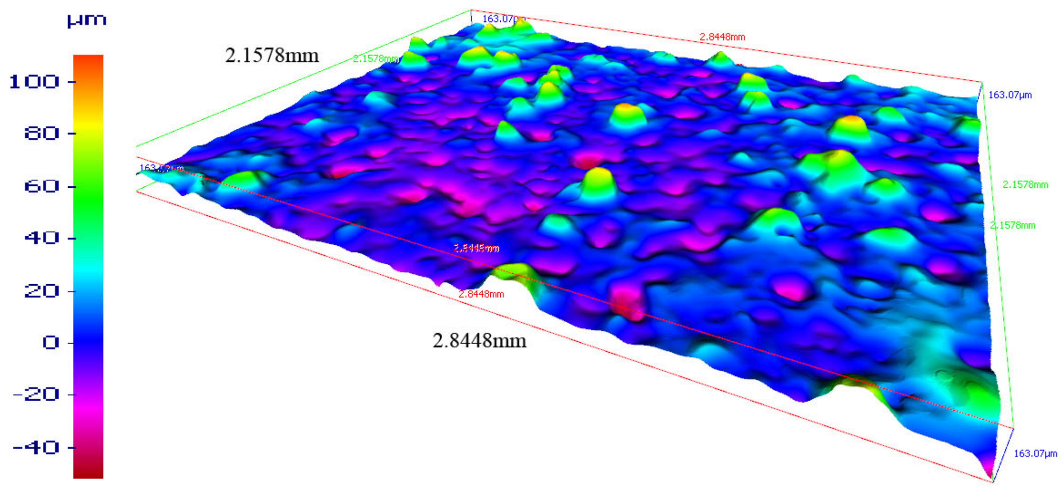

(c)

Fig. 7.21 Re-constructed surface topologies of (a) original tool, (b) tool after machining the MMC under processing conditions (B), (c) tool after machining under processing conditions of (C)

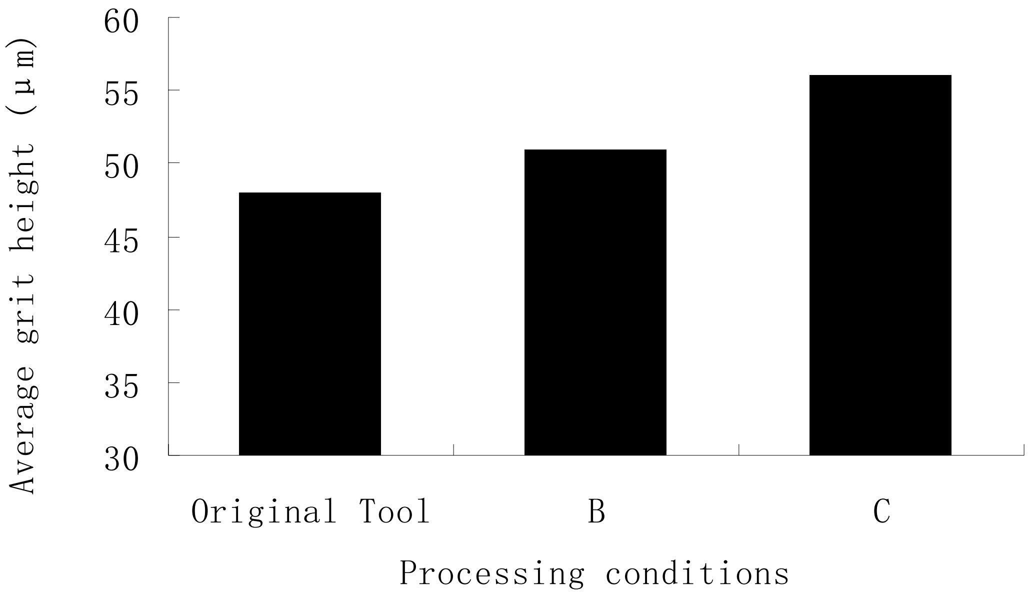

Fig. 7.22 Average grit height measured of the tool for the various processing conditions

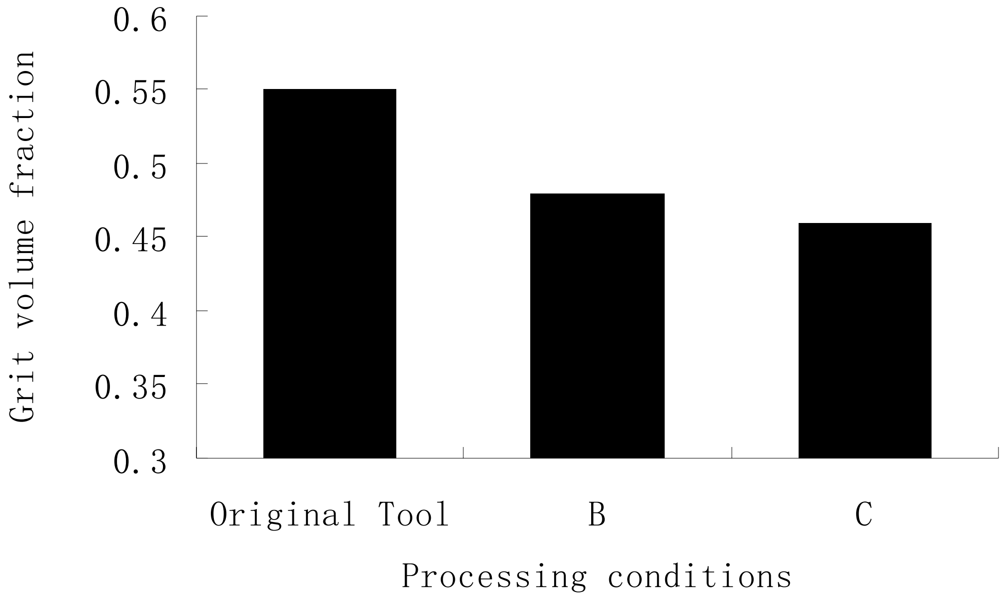

Fig. 7.23 Grit volume fraction remains on the tool for the various processing conditions

7.3 A further Study on Tool Damage

The study presented in Section 7.2 shows that when the workpiece is in positive polarity, while the electrode tool is in negative polarity, i.e. negative electrode polarity, the EDM spark would remove materials both of the workpiece and the tool. The latter action could provide a cleaning function to eliminate chips that are trapped at the tool surface, and the action allows the G-ECDM process to be able to operate in stable machining conditions. The present study aims to further investigate the removal volume of the clogged material if the electrode polarity is reversed.

7.3.1 Experimental conditions

In the study of electrode polarity effect on removal volume of clogged material, it is assumed that the tool is covered with the MMC material. In the experiment, both the tool electrode and the workpiece were made of the same MMC material having a diameter of 10 mm, which is a particulate reinforced aluminium alloy 6061 with 10-vol% Al_2O_3 (10ALO). With such a set-up (Fig. 7.24), the polarity effect on crater volume can be realised by examining the craters on both the tool electrode and the workpiece without the need to reverse the polarity. The processing conditions are given in Table 7.6.

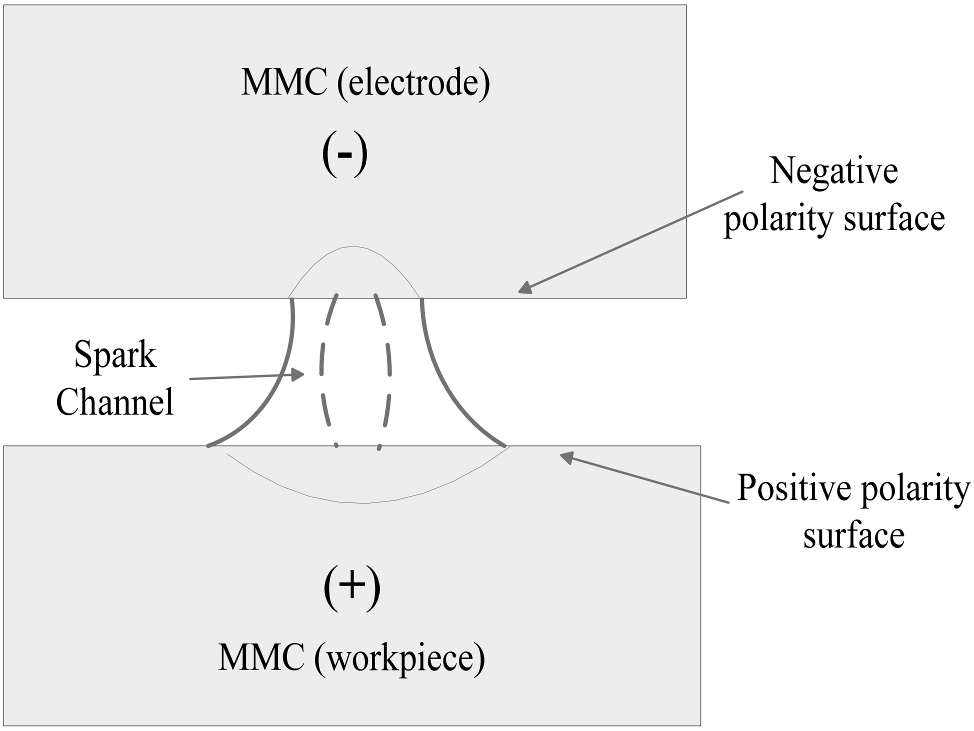

Fig. 7.24 Experiment set-up for studying the polarity effect

Table 7.6 Processing conditions for the study of polarity effect

Processing Conditions	A	B	C
Processing Mode	ECDM	ECDM	G-ECDM
Media	2.5%$NaNO_3$	2.5% $NaNO_3$	2.5% $NaNO_3$
Applied Voltage (V)	90	90	90
Pulse Duration (μs)	48	200	200
Spindle Speed (rpm)	-	-	15000
Gap Distance (μm)	15	15	50
Peak Current (A)	35	35	35

7.3.2 Results and discussion

Fig. 7.25 and Fig. 7.26 show the typical craters produced on the MMC, with positive polarity, and negative polarity, respectively with a pulse duration of 48μs under the ECDM condition. The average volumes measured (from five measurements) for the craters are 6.5×10^5 μm^3 and 3×10^5 μm^3 respectively. The RSD of the experimental measurements is within 2%. The results show that positive polarity resulted in a higher material removal rate of the MMC material. This supports the view that the arc energy on the positive polarity surface is higher than that on the negative polarity surface. The reason for higher arc energy on the former can be explained by the movement of electrons and ions. It is known that negative electrons flow to the positive polarity surface while positive ions flow to the negative polarity surface during the EDM process. With the mass of an electron being a thousand times lighter than that of an ion, a much faster movement of electrons occurs, and therefore fewer positive ions than electrons arrive at the corresponding surface during sparking. Since electrons are considered the primary source of energy for EDM material removal, larger craters are expected to occur on the positive polarity surface.

When the pulse duration was increased to 200μs, though, the situation was found to be rather similar to that of the 48μs condition: the crater on the positive polarity surface (42×10^5 μm^3) was again larger than that on the negative polarity surface (33×10^5 μm^3) (Figs. 7.27, 7.28), the percentage difference between the two is smaller when compared to that of the condition of the 48μs pulse duration (Fig. 7.29b). This suggests that the energy difference during sparking at the anode and cathode surfaces becomes less under relatively long pulse durations as relatively more ions can now reach the cathode surface.

It is also interesting to note that there are small pits found at the bottom of the craters produced on the positive polarity surfaces for both short and long pulse duration conditions, (Figs. 7.25, Fig. 7.27). Whereas, the craters produced on the negative polarity surface, was found to have a relatively smooth bottom without pits (Figs. 7.26, Fig. 7.28). The formation of pits under on the positive polarity surface is considered to be due to plasma channel jumping on the anode surface [109].

Turning to the craters produced using G-ECDM on the positive polarity surface, it was found that unlike the ECDM process, the bottom of the craters were relatively smooth and without pits (Fig. 7.30). The reason for this difference between ECDM and G-ECDM, at this stage, is still not certain. However, it is considered that the dynamic behaviour of the plasma channel under the operation of a high speed rotational electrode in the case of G-ECDM could be quite different from the case of ECDM, and the phenomenon of plasma channel jumping could have been removed by the rotational effect of the G-ECDM process.

Based on the above findings, it is clear that in order to achieve a more effective removal of clogged materials, i.e. a larger crater volume, from the tool; the tool should have positive polarity. Also long pulse durations should be used so as to obtain a high removal volume on the negative polarity surface, i.e. the workpiece.

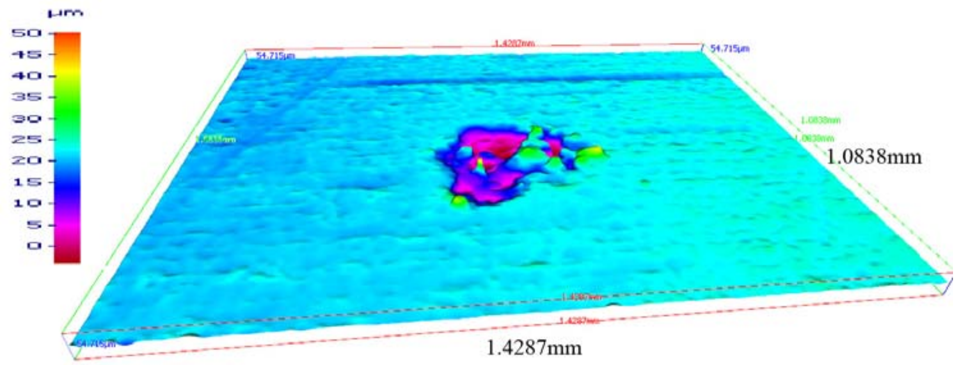

(a)

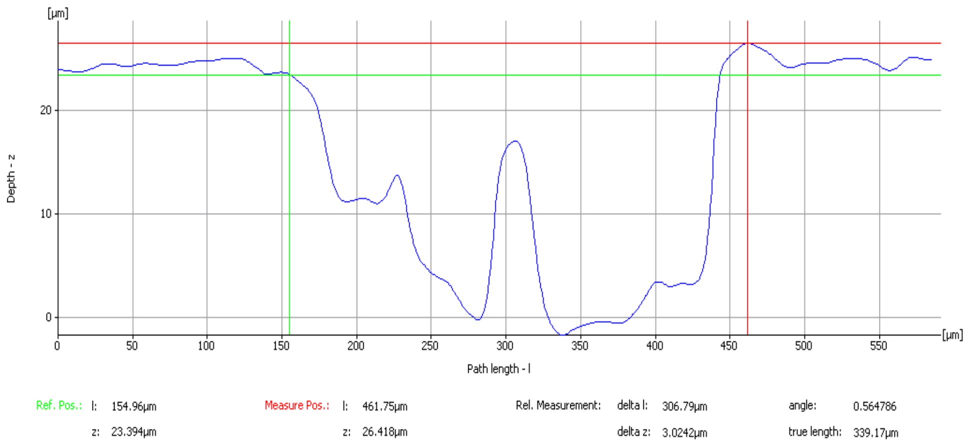

(b)

Fig. 7.25 3-D re-construction of (a) a crater generated on the positive polarity surface under the ECDM condition with a pulse duration of 48µs, (b) a cross-sectional profile of the crater

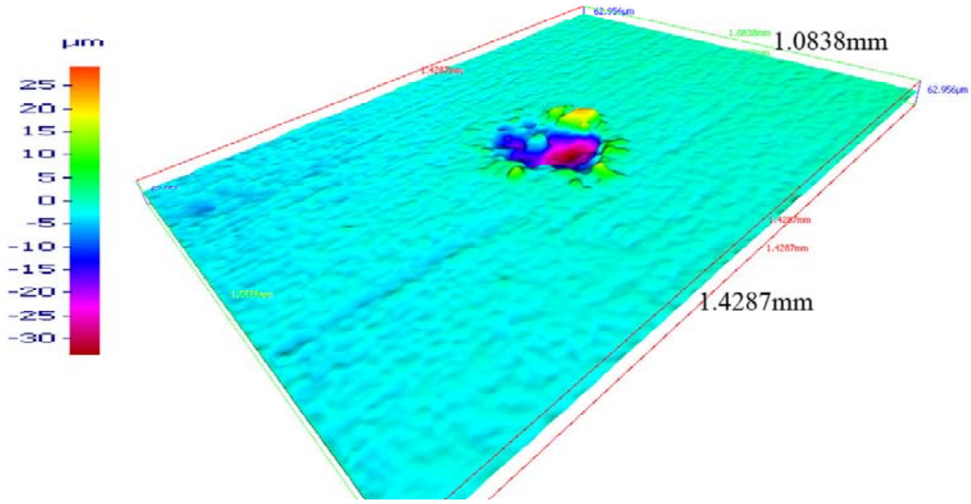

(a)

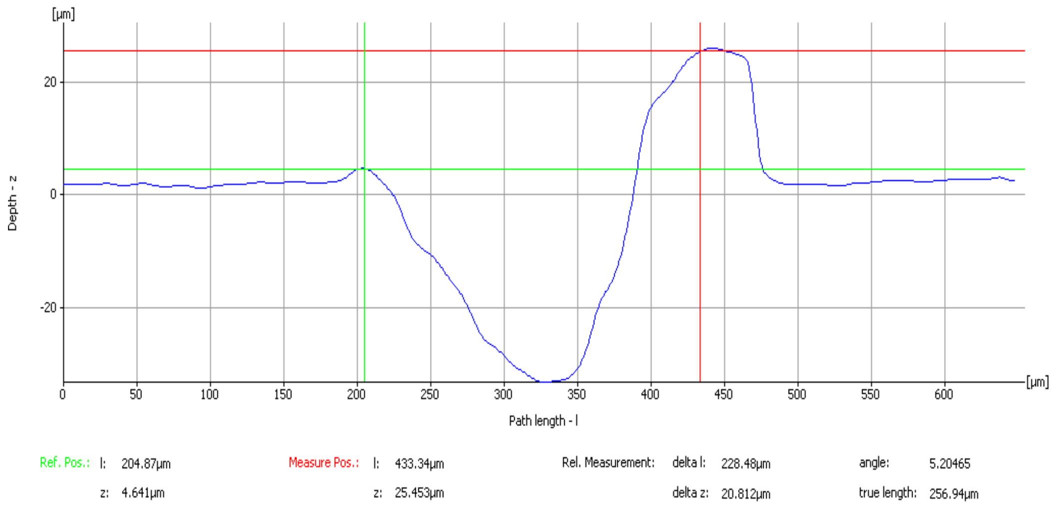

(b)

Fig. 7.26 3-D re-construction of (a) a crater generated on the negative polarity surface under the ECDM condition with a pulse duration of 48µs, (b) a cross-sectional profile of the crater

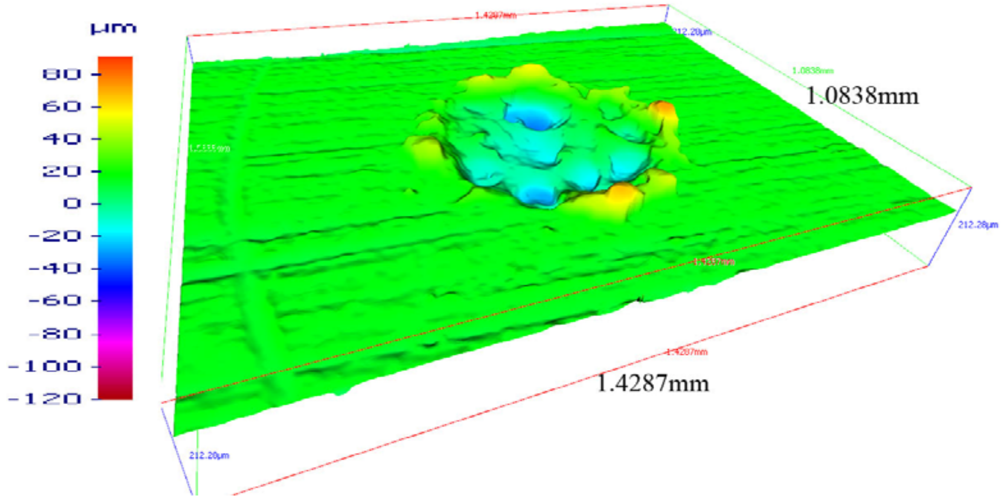

(a)

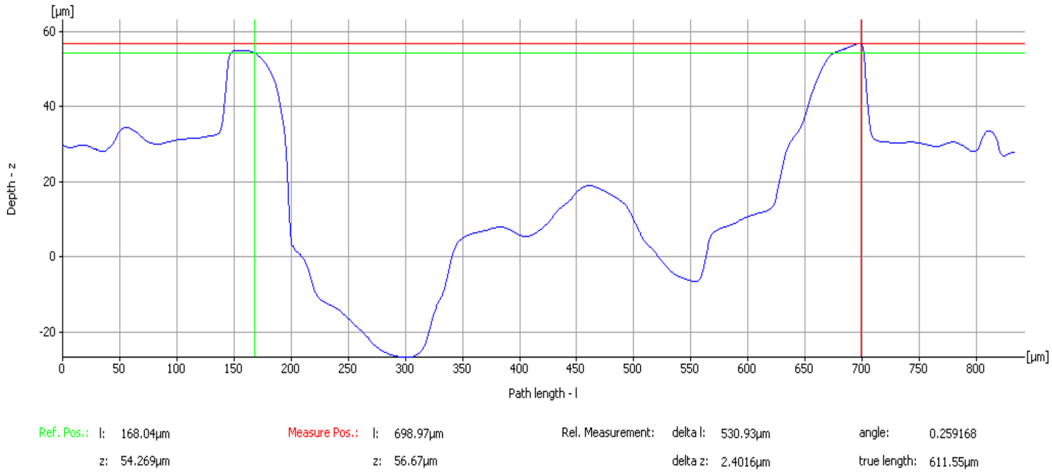

(b)

Fig. 7.27 3-D re-construction of (a) a crater generated on the positive polarity surface under the ECDM condition with a pulse duration of 200µs, (b) a cross-sectional profile of the crater

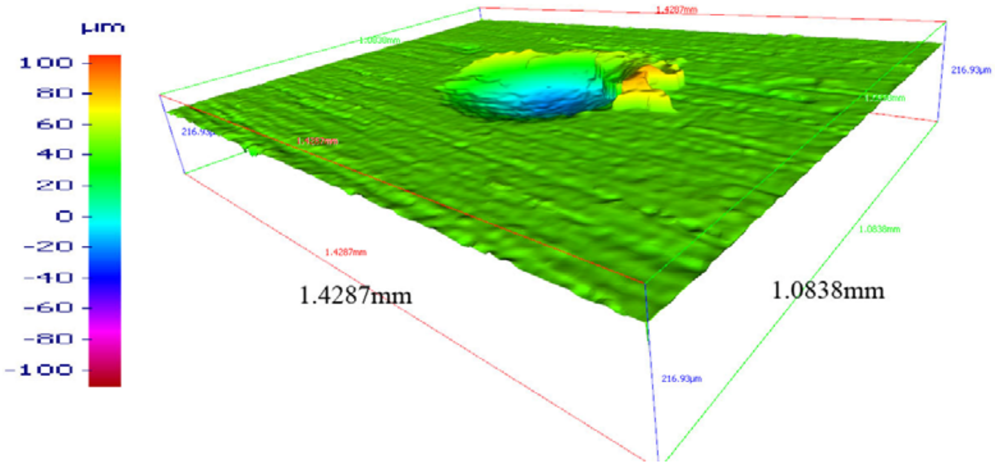

(a)

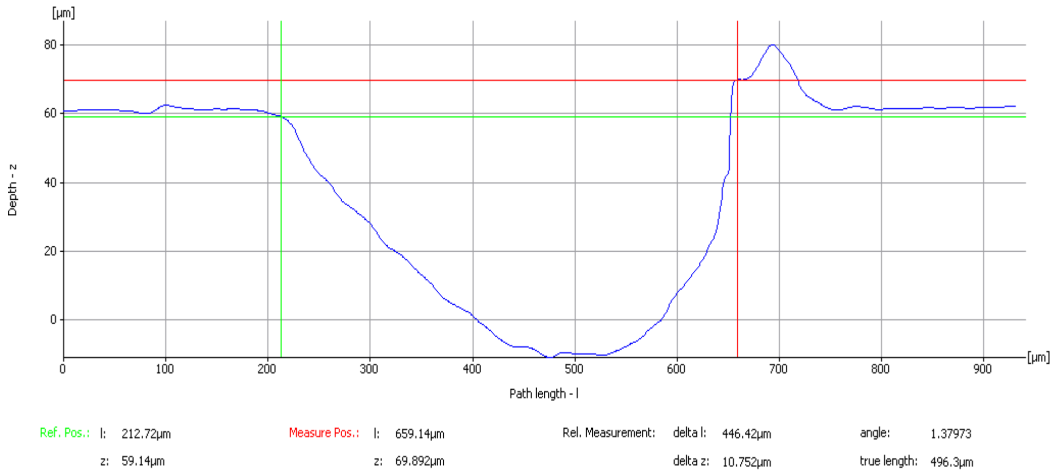

(b)

Fig. 7.28 3-D re-construction of (a) a crater generated on the negative polarity surface under ECDM condition with a pulse duration of 200μs, (b) a cross-sectional profile of the crater

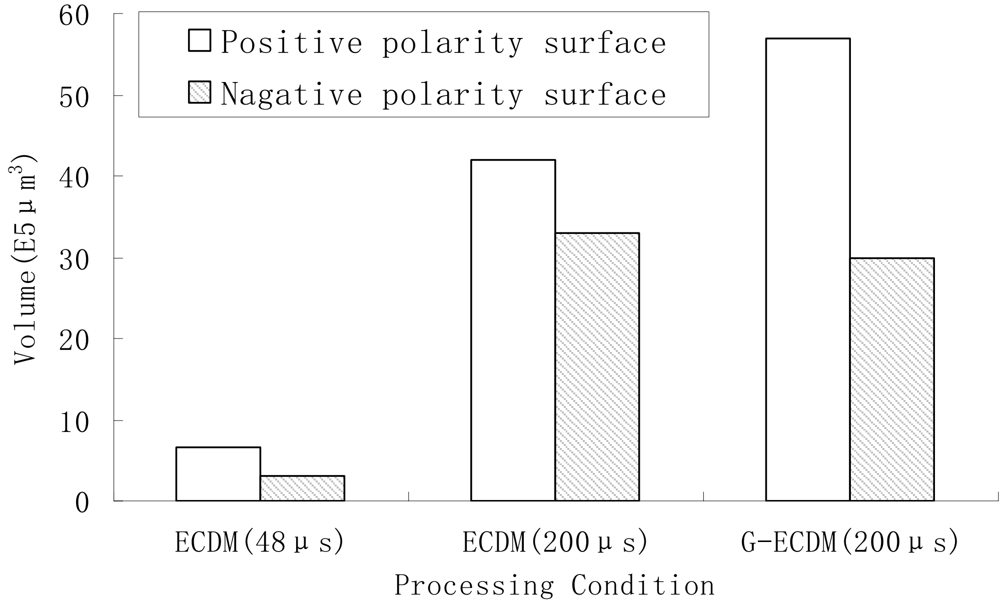

(a)

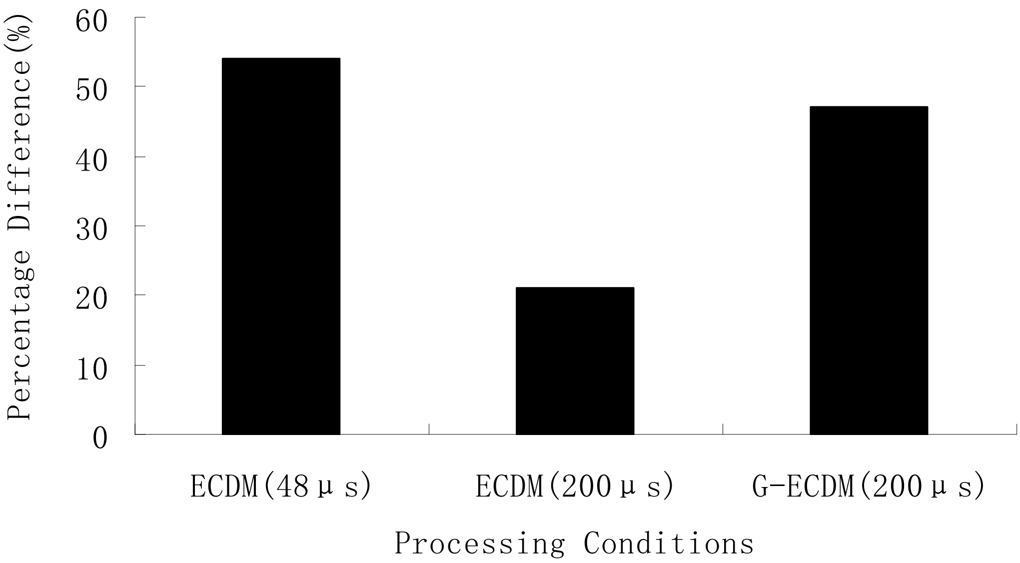

(b)

Fig. 7.29 (a) Crater volume, and (b) percentage difference in crater volume between positive and negative polarity surfaces for different processing conditions

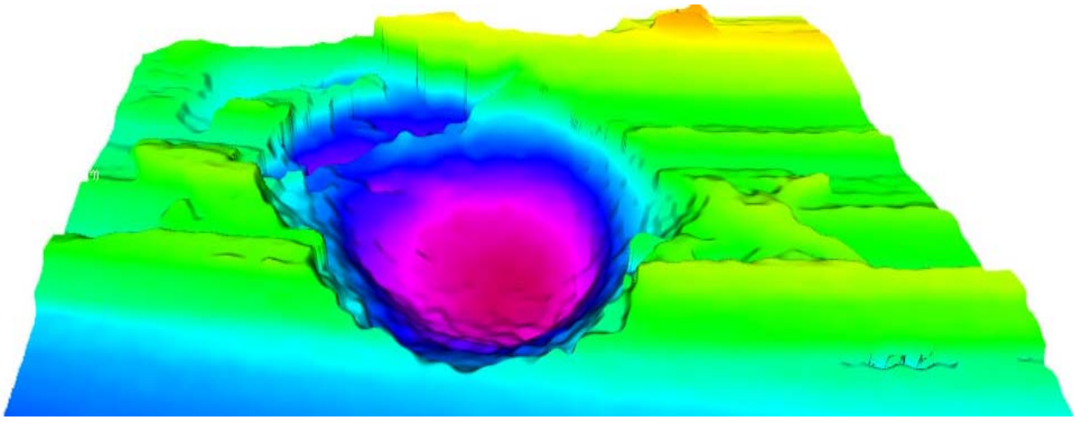

(a)

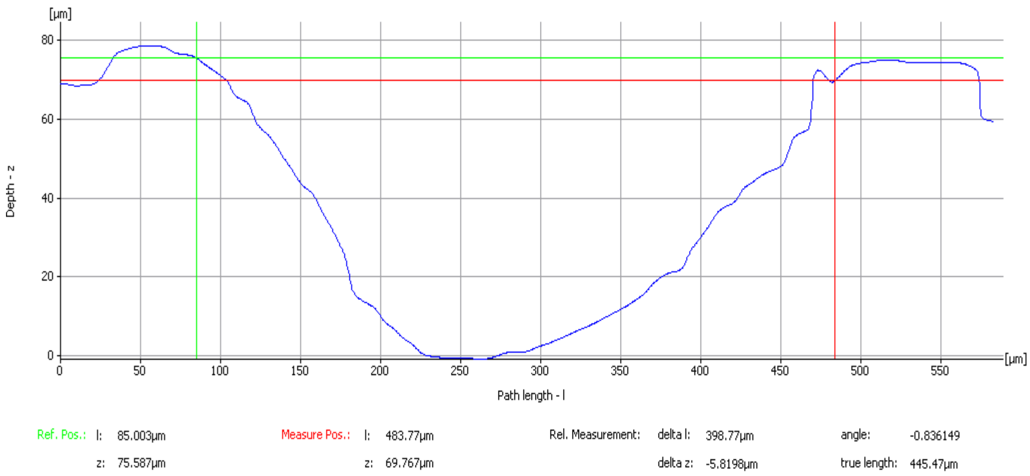

(b)

Fig. 7.30 3-D re-construction of (a) a crater generated on the positive polarity surface under G-ECDM condition with a pulse duration of 200µs, (b) a cross-sectional profile of the crater

7.4 Summary

With the aid of grinding action in ECDM, the MRR would increase, this is made possible because the chip adhered to the cathode tool could be removed by

EDM sparks. This is particularly applicable for machining conditions where a high EDM peak current is used. The EDM spark thus serves the role of tool cleaning and inhibits short circuiting from occurring. The EDM spark that occurs between the chip and the anode did not cause damage at the interface between the diamond grit and the binding material. In order to increase the removal volume of the clogged material, the tool should have positive polarity. However, the clogged material also provides protection to the tool, thus long tool life is expected of the G-ECDM process. However, a good balance between tool cleaning and protection must be reached in order that the G-ECDM process can be operated effectively.

CHAPTER 8

CONCLUSIONS

A Grinding-aided Electrochemical Discharge Machining (G-ECDM) process has been successfully developed to raise the material removal rate and to improve the surface quality in the machining of particulate reinforced aluminium composites over those of the conventional EDM and ECDM processes. A G-ECDM system has been successfully designed and built. Both the theoretical and experimental analyses on the material removal mechanism of ECDM and G-ECDM have been conducted. Moreover, the tool performance of the G-ECDM process was analysed. The main findings of this research work are summarised as follows:

(A) ECDM

(i) A model to reveal the electric field acting on the hydrogen bubbles in ECDM of particulate reinforced MMCs has been established. The model was found capable of predicting the position of the maximum field strength on the bubble surface as well as the critical breakdown voltage for spark initiation, for a given processing condition. A set of experiments was conducted to verify the theoretical breakdown voltage, and the results agreed well with the predicted values.

(ii) The experimental results also showed that an increase in current, duty cycle, pulse duration or electrolyte concentration would promote the occurrence of arcing in ECDM. Moreover, by studying the waveform of ECDM and surface craters, it can be confirmed that the discharge action is in the form of an arc.

(iii) The relative importance of the various processing parameters on material removal rate was established. As far as MRR is concerned, the applied current was found to be the most influential factor among current, pulse duration and electrolyte concentration. The results of the study also showed that although ECDM could achieve a reasonably high MRR when compared to the EDM process, the machined surface quality needs to be improved.

(B) G-ECDM

(i) The material removal mechanism of G-ECDM of particulate reinforced MMCs has been modelled. The individual contribution of ECM and EDM to the material removal rate has been established. The theoretical results show that ECM *per se* does not contribute significantly to the overall high material removal rate of the G-ECDM process. The main role of the electrochemical effect is to allow spark initiation to occur in a relatively large discharge machining gap which facilitates the removal of the reinforcement particles.

(ii) When grinding is incorporated with the ECDM process, both the MRR and the molten material throw-out coefficient were significantly increased.

(iii) Within the scope of this study, the maximum MRR occurred at an electrolyte concentration of around 1.25%, and it appears that a concentration higher or lower than this level would result in a lower MRR. The experimental results also showed that the MRR of G-ECDM increased with an increase in the processing current.

(iv) During G-ECDM of the composite, unstable conditions could occur. However, the spinning effect of the tool-electrode could restore the stable machining condition.

(v) A preliminary study of the quality of the machined surface of the ECDM and G-ECDM specimens showed that the surface roughness of the latter can be 10 times smaller than that of the former. Moreover, when machining composites of SiC reinforced Al-alloys, unlike the ECDM process, the harmful Al_4C_3 phase was not detected.

(C) Tool Performance

(i) In G-ECDM, though the grinding action could cause tool clogging, the clogged material could be removed by the action of electrical discharging, thus a stable processing condition might be maintained. Moreover, a more effective tool cleaning effect could be obtained using positive electrode polarity. On the other hand, the clogged material also provides protection to the tool, thus long tool life is expected of the G-ECDM process. Therefore, a good balance between tool cleaning and protection must be reached in order that the G-ECDM process can be operated effectively.

(ii) Although there was a relatively high detachment rate of the diamond grits at the early stage of the machining, the grit volume of the tool appeared to become rather stable after the run in period. This means that the tool life of the G-ECDM tool is primarily governed by the tool wear of the diamond grit itself.

CHAPTER 9

FUTURE WORK

Although a G-ECDM process has been developed for shaping difficult-to-machine materials, and a systematic study had been conducted to study the material removal mechanism of G-ECDM process, at the end of this study a number of questions remain unanswered, and require further examination. The following lists some important subjects/issues that are considered to be in need of further investigation.

(i) In the present study, only some simple cylindrical types of drill tools were used. In order that the G-ECDM process is to be adopted by industry, it must prove itself to be a flexible process capable of machining different shapes and geometries. Therefore, other forms of tools, such as flexible wires, should be designed based on the basic principle of G-ECDM.

(ii) Although the results of the present study showed that G-ECDM can produce a better surface finish on Al-MMC materials than EDM and ECDM can offer, a complete understanding on the effects of processing conditions, including the size and amount of the diamond abrasive phase, on surface roughness and quality is still lacking. Moreover, other abrasive phases, such as cubic boron nitride, could be considered for the fabrication of the tool electrode.

(iii) The fluid flow induced by the rotational tool has found can increase the throw out volume of molten material. However, the actual mechanism is still not clear, and this requires to be analysed.

(iv) It would be a great asset if sparking under the dynamic condition of a rotating tool can be captured by a high speed camera. This achievement would in no doubt provide valuable information for understanding the sparking behaviour of G-ECDM.

(v) A separate study is required to examine the tool wear mechanism as well as tool life.

(vi) In this study only particulate reinforced aluminium alloys have been investigated, it is necessary to demonstrate that G-ECDM is also suitable for shaping other types of MMCs, such as long and short fibres composites.

REFERENCES

[1] W. Speer and O.S. Es-Said. Applications of an aluminum-beryllium composite for structural aerospace components. Engineering Failure Analysis, (2004) 11, 895-902.

[2] J.M. Kunze and C.C Bampton. Challenges to developing and producing MMCs for space applications. Journal of the Minerals, Metals and Materials Society (JOM), (2001) 53, 22-25.

[3] M.A. Occhionero and R.W. Adams. AlSiC, and AlSiC hybrid composites for flip chips, optoelectronics, power, and high brightness LED thermal management solutions. The 6th International Conference on Electronics Packaging Technology, ShenZhen, China, (2005) Aug. 30-Sept. 2, 576-580.

[4] C. Zweben. Advanced electronic packaging materials. Advanced Materials and Processes, (2005) 163, 33-37.

[5] P.K. Rohatgi, D. Weiss, and N. Gupta. Applications of fly ash in synthesizing low-cost MMCs for automotive and other applications. Journal of the Minerals, Metals and Materials Society (JOM), (2006) 58, 71-76.

[6] K. Xiu, Q.C. Jiang, B.X. Ma, Y. Wang, L. Sui and E.Y. Shang. Fabrication of TiCp/Mg composites by powder metallurgy. Journal of Materials Science, (2006) 41, 1663-1666.

[7] Q.C. Jiang, H.Y. Wang, B.X. Ma, Y. Wang and F. Zhao. Fabrication of B_4C participate reinforced magnesium matrix composite by powder metallurgy. Journal of Alloys and Compounds, (2005) 386, 177-181.

[8] K.S. See and T.A. Dean. The effects of the disposition of SiC particles on the forgeability and mechanical properties of co-sprayed aluminium-based MMCs. Journal of Materials Processing Technology, (1997) 69, 58-67.

[9] M. Mizumoto, H. Ezaki and A. Kagawa. Fiber orientation control and evaluation of characteristics of short fiber reinforced metal matrix composite fabricated by low-pressure infiltration process. Materials Science Forum, (2005) 475-479, 2559-2562.

[10] M.S. Yong and A.J. Clegg. Process optimisation for a squeeze cast magnesium alloy metal matrix composite. Journal of Materials Processing Technology, (2005) 168, 262-269.

[11] Y.B. Liu, S.C. Lim, L. Lu and M.O. Lai. Recent development in the fabrication of metal matrix-particulate composites using powder metallurgy techniques. Journal of Materials Science, (1994) 29, 1999-2007.

[12] G.A. Chadwick and T.M. Yue. Principles and applications of squeeze casting. Metals and Materials, (1989) 1, 6-12.

[13] N. Tomac and K. Tønnessen. Machinability of particulate aluminium matrix composites. Annals CIRP, (1992) 41, 55-58.

[14] W.S. Lau, T.M. Yue and M. Wang. Ultrasonic-aided laser drilling of aluminium-based metal matrix composites. Annals CIRP, (1994) 43, 177-180.

[15] T.M. Yue, and W.S. Lau. Pulsed Nd: YAG laser cutting of SiC/Al-Li metal matrix composite. Materials and Manufacturing Processes, (1996) 11, 17-29.

[16] E. Savrun and M. Taya. Surface characterization of SiC wisker/2124 aluminium and Al_2O_3 composites machined by abrasive water jet. Journal of Materials Science, (1988) 23, 1453-1458.

[17] S. Durante, G. Rutelli and F. Rabezzana. Aluminum based MMC machining with diamond coated cutting tools. Surface & Coatings Technology, (1997) 94-95, 632-640.

[18] G.E. D'Errico and R. Calzavarini. Turning of metal matrix composites. Journal of Materials Processing Technology, (2001) 119, 257-260.

[19] R. Polini, A. Allegri, S. Guarino, F. Quadrini, H. Sein and W. Ahmed. Cutting force and wear evaluation in peripheral milling by CVD diamond dental tools. Thin Solid Films, (2004) 469–470, 161-166.

[20] X. Ding, W.Y.H. Liew and X.D. Liu. Evaluation of machining performance of MMC with PCBN and PCD tools. Wear, (2005) 259, 1225-1234.

[21] R.M. Hooper, J.L. Henshall and A. Klopfer. The wear of polycrystalline diamond tools used in the cutting of metal matrix composites. Journal of Refractory Metals & Hard Materials, (1999) 17, 103-109.

[22] A.R. Chambers. The machinability of light alloy MMCs. Journal of Composites, Part A, (1996) 27, 143-147.

[23] M. Chen, X.G. Jian, F.H. Sun, B. Hu and X.S. Liu. Development of diamond coated drills and their cutting performance. Journal of Materials Processing Technology, (2002) 129, 81-84.

[24] R.T. Coelho, S. Yamada, D.K. Aspinwall and M.L.H. Wise. The application of polycrystalline diamond (PCD) tool materials when drilling and reaming aluminium based alloys including MMC. International Journal of Machine Tools & Manufacture, (1995) 35, 761-774.

[25] J.P. Davim. Diamond tool performance in machining metal matrix composites. Journal of Materials Processing Technology, (2002) 128, 100-105.

[26] Y.M. Quan. Study on the cutting mechanism of SiC particle-reinforced aluminium matrix composites and hypereutectic AL-Si alloy. PhD thesis of South China University of Technology, 1996.

[27] Y.M. Quan and Z.H. Zhou. Tool wear and its mechanism for cutting SiC particle reinforced aluminium matrix composites. Journal of Materials Processing Technology, (2000) 100, 194-199.

[28] I. Ciftci, M. Turker and U. Seker. Evaluation of tool wear when machining SiCp-reinforced Al-2014 alloy matrix composites. Materials and Design, (2004) 25, 251-255.

[29] Y. Sahin, M. Kok and H. Celik. Tool wear and surface roughness of Al_2O_3 particle reinforced aluminium alloy composites. Journal of Materials Processing Technology, (2002) 128, 280-291.

[30] X.P. Li and W. K. H. Seah. Tool wear acceleration in relation to workpiece reinforcement percentage in cutting of metal matrix composites. Wear, (2001) 247, 161-171.

[31] J. P. Davim and A. M. Baptista. Relationship between cutting force and PCD cutting tool wear in machining silicon carbide reinforced aluminium. Journal of Materials Processing Technology, (2000) 103, 417-423.

[32] J.T. Lin, D. Bhattacharyya and C. Lane. Machinability of a silicon carbide reinforced aluminium metal matrix composite. Wear, (1995) 181-183, 883-888.

[33] N.P. Hung, F.Y.C. Boey, K.A. Khor, Y.S. Phua and H.F. Lee. Machinability of aluminum alloys reinforced with silicon carbide particulates. Journal of Materials Processing Technology, (1996) 56, 966-977.

[34] M. El-Gallab and M. Sklad. Machining of Al/ SiC particulate metal matrix composites Part 1: Tool performance. Journal of Materials Processing Technology, (1998) 83, 151-158.

[35] J.P. Davim. Design of optimization of cutting parameters for turning metal matrix composites on the orthogonal arrays. Journal of Materials Processing

Technology, (2003) 132, 340-344.

[36] D.Z. Wang, H.M. Liu, R.D. Han and Z.Z.Zheng. A study on a friction formula between tool and chip and wear characteristics when cutting SiC reinforced aluminum composite. Tribology, (2000) 20(2), 85-89 .

[37] M.S. El-Gallab, and M. Sklad. Machining of Al/ SiC particulate metal matrix composites Part 2: Workpiece surface integrity. Journal of Materials Processing Technology, (1998) 83, 277-285.

[38] L. luliano, L. Settineri and A. Gatto. High speed turning experiments on metal matrix composites. Composites Part A, (1998) 29, 1501-1509.

[39] Y.M. Quan. Deformation of cutting zone of the hard particle reinforced metal matrix composites. Journal of South China University of Technology (natural science), (1998) 26(4), 27-32.

[40] J.T. Lin, D. Bhattacharyya and W.G. Ferguson. Chip formation in the machining of SiC particle reinforced aluminium matrix composites. Composites Science and Technology, (1998) 58, 285-291.

[41] Y.M. Quan. Cutting process and chip appearance of aluminum matrix composites reinforced by SiC particle. Journal of Materials Machining Technology, (1999) 91, 231-235.

[42] Z.F. Yue and Z.Y. Lv. A phenomenal model for the plastic response of particle reinforced composites. Materials for mechanical engineering, (1995) 19(3),

11-14.

[43] S. S. Joshi, N. Ramakrishnan and P. Ramakrishnan. Analysis of chip breaking during orthogonal machining of Al/ SiCp composites. Journal of Materials Machining Technology, (1999) 88, 90-96.

[44] J. P. Davim and C. A. Conceição António. Optimal drilling of particulate metal matrix composites based on experimental and numerical procedures. International Journal of Machine Tools & Manufacture, (2001) 41, 21-31.

[45] H. Chandrasekaran and J.O. Johansson. The role of material and grinding parameters in grinding of alumina fibre reinforced aluminium alloys. Proceedings of Machining of Advanced Materials, Gaithersburg, USA, July, (1993), 20–22.

[46] A. Di Ilio and A. Paoletti. Wheel topography evaluation during the grinding of SiC reinforced aluminium. Proceedings of the First World Conference on Integrated Design and Process Technology, Austin, 6–9 December, (1995), 70–76.

[47] A. Di Ilio, A. Paoletti, V. Tagliaferri and F. Veniali. An experimental study on grinding of SiC reinforced aluminium. International Journal of Machine Tool and Manufacture, (1996) 36 (6), 673–685.

[48] A. Di Ilio, A. Paoletti, V. Tagliaferri and F. Veniali. Grindability evaluation of SiC reinforced aluminium alloys. Proceedings of the XIXth Scientific

Conference of Abrasive Technology, Lodz, 10–13 September, (1996), 47–55.

[49] Z.W. Zhong and N.P. Hung. Grinding of alumina/ aluminum composites. Journal of Materials Processing Technology, (2002) 123, 13-17.

[50] A Di Ilio and A. Paoletti. A comparison between conventional abrasives and superabrasives in grinding of SiC aluminium composites. International Journal of Machine Tool and Manufacture, (2000) 40, 173-184.

[51] Y.C. Zhou, S.G. Long and Y.W. Liu. Thermal failure mechanism and failure threshold of SiC particle reinforced metal matrix composites induced by laser beam. Journal of Mechanics of materials, (2003) 35, 1003-1020.

[52] F. Müller and J. Monaghan. Non-conventional machining of particle reinforced metal matrix composites. Journal of Materials Processing Technology, (2001) 118, 278-285.

[53] F. Mülle and J. Monaghan.. Non-conventional machining of particle reinforced metal matrix composite. International Journal of Machine Tools and Manufacture, (2000) 40, 1351-1366.

[54] L. Hong, R.M. Vilar and W. Youming. Laser beam processing of a SiC particulate 6061 aluminium metal matrix composite. Journal of Materials Science, (1997) 32, 5545-5550.

[55] C. Hu and T.N. Baker. A new aluminium silicon carbide formed in laser processing. Journal of Materials Science, (1997) 32, 5047-5051.

[56] M. Ramulu and M. Taya. EDM machinability of SiCw/Al composites. Journal of Materials Science, (1989) 24, 1103-1108.

[57] A. Dvivedi, P. Kumar and I. Singh. Experimental investigation and optimisation in EDM of Al 6063 SiCp metal matrix composite. International Journal of Machining and Machinability of Materials, (2008) 3, 293-308.

[58] F. Müller and J. Monaghan. Electro discharge machining of a particle reinforced metal matrix composite. The 12th International Symposium for Electromachining, Aachen, Germany, (1998) May 11-13, 513-522.

[59] F. Müller. Electro discharge machining of particle reinforced metal matrix composites. PhD Dissertation, Trinity College, Dublin, Ireland, (1999).

[60] T.M. Yue and Y. Dai. Wire electrical discharge machining of Al_2O_3 particle and short fibre reinforced Al-based composites. Materials Science and Technology, (1996) 12, 831-835.

[61] B. Mohan, A. Rajadurai and K.G. Satyanarayana. Electric discharge machining of Al–SiC metal matrix composites using rotary tube electrode. Journal of Materials Processing Technology, (2004) 153-154, 978-985.

[62] B.H. Yan, H.C. Tsai, F.Y. Huang and L.C. Lee. Examination of wire electrical discharge machining of Al_2O_3p/6061Al composites. International Journal of Machine tools & Manufacture, (2005) 45, 251-269.

[63] G.S. Liu, B. Zhao, G.F. Gao and F Jiao. Research on the characteristics of the

cutting force in the vibration cutting of a particle-reinforced metal matrix composites SiCp/Al. Journal of Materials Processing Technology, (2002) 129, 196-199.

[64] C.C. Wang and B.H. Yan. Blind-hole drilling of Al_2O_3 6061Al composite using rotary electro-discharge machining. Journal of Materials Processing Technology, (2000) 102, 90-102.

[65] B.H. Yan, C.C. Wang, H.M. Chow and YC Lin. Feasibility study of rotary electrical discharge machining with ball burnishing for Al_2O_3 6061Al composite. International Journal of Machine Tools & Manufacture, (2000) 40, 1403-1421.

[66] P. Narender Silngh, K. Raghukandan, M. Rathinasabapathi and B.C. Pai. Electric discharge machining of Al–10%SiCp as-cast metal matrix composites. Journal of Materials Processing Technology, (2004) 155-156, 1653-1657.

[67] M. Ramulu, G. Paul and J. Patel. EDM surface effects on the fatigue strength of a 15 vol% SiCp/Al metal matrix composite material. Composite Structures, (2001) 54, 79-86.

[68] J.F. Wilson. Practice and theory of electrochemical machining. Robert E Krieger Publishing Company, Malabar, Florida, (1982).

[69] J.Y. Wang and J.W. Xu. Principle and application of ECM. National Defence

Industry Press, (2001).

[70] D. Zhu. The latest advances and the principal issues in ECM. Electromachining & Mould, (2000) 1, 11-16.

[71] A.E. Debarr and D.A. Oliver. Electrochemical machining, Macdonald & Co Ltd. (publisher), (1968).

[72] C.G. Zhang, J. Miu, C.S. Liu, D.X.Fu and B.Zhao. Status and development of pulse electrochemical machining. Tool Engineering, (2007) 41, 19-23.

[73] J. Kozak, K. P. Rajurkar and Y. Makkar. Selected problems of micro-electrochemical machining. Journal of Materials Processing Technology, (2004) 149(1-3), 426-431.

[74] E.S. Lee, S. Y. Baek and C. R. Cho. A study of the characteristics for electrochemical micromachining with ultrashort voltage pulses. International Journal of Advance Manufacture Technology, (2007) 31, 762-769.

[75] M. Sen and H. S. Shan. A review of electrochemical macro-to micro-hole drilling processes. International Journal of Machine Tools and Manufacture, (2005) 45(2), 137-152.

[76] L.H. Hihara and P. Panquites IV. Method of electrochemical machining (ECM) of particulate metal-matrix composites (MMCs). United States Patent (no.6110351), (2000).

[77] H. El-Hofy and J.A. McGough. Evaluation of an apparatus for

electrochemical arc wire-machining. Journal of Engineering for Industry, Transactions ASME, (1988) 110(2), 119-123.

[78] J.W. Xu, N.Z. Yun, J.Y.Wang, J.A.Tian and W.J. Xu. Electrochemical Machining Technology. National Defence Industry Press, (2008).

[79] V. K. Jain, P.M. Dixit, P.M. Pandey. On the analysis of the electrochemical spark machining process. International Journal of Machine Tools and Manufacture, (1999) 39(1), 165-186.

[80] A. Kulkarni, R. Sharan and G.K. Lal. An experimental study of discharge mechanism in electrochemical discharge machining. International Journal of Machine Tools and Manufacture, (2002) 42(10), 1121-1127.

[81] Q.H. Zhang, J.H. Zhang, S.F. Ren, J.X. Deng and X. Ai. Study on technology of ultrasonic vibration aided electrical discharge machining in gas. Journal of Materials Processing Technology, (2004) 149(1-3), 640-644.

[82] N.M. Abbas, D.G. Solomon and M.F. Bahari. A review on current research trends in electrical discharge machining (EDM). International Journal of Machine Tools and Manufacture, (2007) 47(7-8), 1214-1228.

[83] J. Kozak and K.E Oczoś. Selected problems of abrasive hybrid machining. Journal of Materials Processing Technology, (2001) 109(3), 360-366.

[84] G.F. Benedict. Nontraditional Manufacturing Processes, Marcel Dekker, Inc. New York·Basel, (1987).

[85] A. Hasçalık and U. Çaydaş. A comparative study of surface integrity of Ti–6Al–4V alloy machined by EDM and AECG. Journal of Materials Processing Technology, (2007) 190(1-3), 173-180.

[86] S. Zaborski, M. Łupak and D. Poroś. Wear of cathode in abrasive electrochemical grinding of hardly machined materials. Journal of Materials Processing Technology, (2004) 149(1-3), 414-418.

[87] H El-Hofy. Advanced Machining Processes Nontraditional and Hybrid Machining Processes, McGraw-Hill, (2005).

[88] I.M. Crichton and J.A. McGough. Studies of the discharge mechanisms in electrochemical arc machining. Journal of Applied Electrochemistry, (1985) 115, 113–119.

[89] I. Basak and A. Ghosh. Mechanism of spark generation during electrochemical discharge machining: a theoretical model and experimental investigation. Journal of Materials Processing Technology, (1996) 62, 46–53.

[90] K. Allesu, A. Ghosh and M.K. Muju. A preliminary qualitative approach of a proposed mechanism of material removal in electrical machining of glass. European Journal of Mechanical Engineering, (1991) 36(3), 201-207.

[91] R. Wüthrich and V. Fascio. Machining of non-conducting materials using electrochemical discharge phenomenon – an overview. International Journal of Machine Tools and Manufacture, (2005) 45, 1095-1108.

[92] A.F. Nikiforov and V.B. Uvarov. Special Functions of Mathematical Physics, Birkhäuser, Basel · Boston, (1988).

[93] X.Q. Yang and K.M. Huang. The new method to calculate the complex

effective permittivity of mixed aqueous electrolyte solution at microwave frequency. Chinese Journal of Acta Electronica Sinica, (2006) 34, 356-360.

[94] J.W. Liu, T.M. Yue and Z.N Guo. Wire electrochemical discharge machining of Al_2O_3 particle reinforced aluminum Alloy 6061. Materials & Manufacturing Processes, (2009) 24(4), 446-453.

[95] Z.D. Liu. Research on cooling liquid used in super-high thickness workpiece cutting of HSWEDM. Electromachining & Mould, (2006) 1, 25-27.

[96] C.P. Lin. Determined eccentric travelling distance of electrode-wire for punching & blanking die in WEDM. Electromachining and Mould, (2006) (S1), 67-69.

[97] S.L. Ma. Research of the mechanism of material removal erosion based on single pulse in EDM. Dissertation of Masters Degree, Harbin Institute of Technology, (2006).

[98] S.K. Hargrove and D. Ding. Determining cutting parameters in wire EDM based on workpiece surface temperature distribution. International Journal of Advanced Manufacturing Technology, (2007) 34(3-4), 295-299.

[99] M.G. Xu. Study on the new combined machining technology and mechanism of ultrasonic vibration assisted electrical discharge machining in gas medium. PhD Dissertation, Shandong University, (2007).

[100] V. Yadava, K.L. Bhondwe and G. Kathiresan. Finite element prediction of material removal rate due to electro-chemical spark machining. International Journal of Machine Tools & Manufacture, (2006) 46, 1699-1706.

[101] V. Yadava, V.K. Jain and P.M. Dixit. Thermal stresses due to electrical discharge machining. International Journal of Machine Tools & Manufacture,

(2002) 42, 877-888.

[102] Y.J. Chen, L. Gu and J.F. Guan. Research on natural convection thermodynamic model of hydro-pneumatic spring. Journal of System Simulation, (2008) 20(5), 4198-4206.

[103] E.M. Bazelyan and Yu.P. Raizer. Spark Discharge, CRC Press, (1998).

[104] C. A. Harper. Hand Book of Ceramics, Glasses, and Diamonds. McGraw-Hill Company, (2001).

[105] H.E. Boyer and T.L. Gall. Metals Handbook, American Society for Metals, (1992).

[106] Q.H. Zhang and R. Du. An investigation of ultrasonic-assisted electrical discharge machining in gas. International Journal of Machine Tools & Manufacture, (2006) 42, 1582-1588.

[107] J.C. Rebelo and A. Dias. Influence of EDM pulse energy on the surface integrity of martensitic steels. Journal of Materials Processing Technology, (1998) 84(1-3), 90-96.

[108] S.H. Yeo, W. Kurnia and P.C. Tan. Electro-thermal modelling of anode and cathode in micro-EDM. Journal of Physics D: Applied Physics, (2007) 40, 2513-2521.

[109] W. ZHAO. Research on the corrosion of electrodes and its theory foundation in EDM. PhD Dissertation, Northwestern Polytechnical University, China, (2003).

APPENDIX A

Control program written for the control of the spindle movement of the G-ECDM tool

```
Option Explicit
Dim CHColor(8) As ColorConstants
Dim LoopAcqStatus As Integer

Dim X As Long
Dim Y As Long
Dim s    As Long
Dim z As Long
Dim vol As Single
Dim voltage As Single
Dim cs As Single
Const XCH As Integer = 0
Const YCH As Integer = 1
Const ZCH As Integer = 2
'Const UCH As Integer = 4
'Const VCH As Integer = 0

Dim dirx As Integer
Dim diry As Integer
Dim dirz As Integer
'Dim diru As Integer
'Dim dirv As Integer

Dim nspeedx As Long
Dim nspeedy As Long
Dim nspeedz As Long
'Dim nspeedu As Long
'Dim nspeedv As Long

Dim nlongx As Long
Dim nlongy As Long
Dim nlongz As Long
'Dim nlongu As Long
'Dim nlongv As Long

Dim nposx As Double
Dim nposy As Double
Dim nposz As Double
'Dim nposu As Double
'Dim nposv As Double
```

```
Dim modex As Integer
Dim modey As Integer
Dim modez As Integer


Private Sub AcqCardInitial()
      Dim i As Integer

        ChannelNum = IDTS_SysInit(pSI, 0)                    If ChannelNum = &HFF
Then
              MsgBox
              End
         End If
            AcqStatus = 0


   For i = 0 To 17
     If pSI.clk_tab(i) > 0 Then RateCombo.AddItem Str(pSI.clk_tab(i))
  Next i
  RateCombo.Text = RateCombo.List(0)
  ad.CurChanID = 0
  ad.AcqRate = pSI.clk_tab(0)

For i = 0 To 15
     If pSI.range_tab(i) > 0 Then CHRangeCombo.AddItem Str(pSI.range_tab(i))
  Next i

  For i = 0 To ChannelNum - 1
        CHSetCombo.AddItem Str(i)
        CHShowCombo.AddItem Str(i)
        TrigCHCombo.AddItem Str(i)
        ChanSet(i).CoupleID = 0
        ChanSet(i).RangeID = 0
        ChanSet(i).RangeVal = pSI.range_tab(ChanSet(i).RangeID)
  Next i

        CHSetCombo.Text = CHSetCombo.List(0)
        CHShowCombo.Text = CHShowCombo.List(0)
        TrigCHCombo.Text = TrigCHCombo.List(0)
        CHRangeCombo.Text = CHRangeCombo.List(0)
  'ad.RangeVal = pSI.range_tab(ChanSet(ad.CurChanID).RangeID)

  CHTrigCombo.Text = CHTrigCombo.List(0)
  CouplingCombo.Text = CouplingCombo.List(0)
```

```
  Call AddLength
  LengthCombo.Text = LengthCombo.List(0)
  DelayCombo.Text = DelayCombo.List(2)
  ad.Length = Val(LengthCombo.Text)
  ad.Delay = Val(DelayCombo.Text)
  Trigger.Mode = 0


End Sub

Private Sub AddLength()
        Dim i As Integer
        Dim addValue As Long

                i = 0
                addValue = 1024
                While addValue <= pSI.maxsmplength
                        LengthCombo.AddItem Str(addValue)
                        i = i + 1
                        addValue = 1024 * 4 ^ i
                Wend
End Sub
Private Sub RunAcq()

        Dim i As Integer

       Call IDTS_SetAcqRate(ad.AcqRate, 100#)

               Call IDTS_SetAcqFrame(ad.Length, ad.Delay)

        Call IDTS_SetAcqTrigger(Trigger.Mode, Trigger.Ch, Trigger.Level)
        For i = 0 To ChannelNum - 1
            Call IDTS_SetChannelParam(i, ChanSet(i).RangeID, ChanSet(i).CoupleID)

        Next i

          StopAcqCmd.Enabled = True
        LoopAcqCmd.Enabled = False
        SingleAcqCmd.Enabled = False
        AcqFrame.Enabled = False
        CHFrame.Enabled = False

        Call IDTS_Acq
        Timer1.Enabled = True
        AcqStatus = 1
End Sub
```

```
Private Sub TerminateAcq()

        AcqLed.BackColor = &H808080
        Timer1.Enabled = False
        StopAcqCmd.Enabled = False
        LoopAcqCmd.Enabled = True
        SingleAcqCmd.Enabled = True
        AcqFrame.Enabled = True
        CHFrame.Enabled = True
        Call IDTS_StopAcq
        AcqStatus = 0

End Sub

Private Sub AcqCardExit()

        Timer1.Enabled = False
        Call IDTS_StopAcq
        Call IDTS_SysFinally

        End

End Sub


Private Sub PaintWaveform()
    Dim j, dotnum, l As Integer
    Dim dot1, dot2 As Single
    Dim compress As Long, DaLength As Long



       Call IDTS_GetAcqFrame(ad.Length, ad.Delay)

       Call                    IDTS_GetChannelParam(ad.CurChanID,
ChanSet(ad.CurChanID).RangeID, ChanSet(ad.CurChanID).CoupleID)

        compress = (ad.Length - 1) / 16384 + 1
        dotnum = ad.Length / compress
        l = IDTS_Pack(ad.CurChanID, ad.data(0), -1, compress, ad.Delay, dotnum)

         ad.RangeVal = pSI.range_tab(ChanSet(ad.CurChanID).RangeID)
         Osc.Scale (0, ad.RangeVal)-(dotnum, -ad.RangeVal)
         Osc.Cls
         dot1 = ad.data(0) * ad.RangeVal / 32768#
```

```
            UpVoltLabel.Caption = ad.RangeVal
            LowVoltLabel.Caption = -ad.RangeVal
            TimeStartLabel.Caption = Format(ad.Delay / ad.AcqRate * 1000,
"0.000")
            TimeEndLabel.Caption = Format((ad.Length + ad.Delay) / ad.AcqRate *
1000, "0.000")
            dot1 = ad.data(0) * ad.RangeVal / 32768#
            voltage = dot1
            txtVoltRead.Text = Format(dot1, "###0.00")
            For j = 1 To dotnum - 1
                 dot2 = ad.data(j) * ad.RangeVal / 32768#
                 Osc.Line (j - 1, dot1)-(j, dot2), ad.Color
                 dot1 = dot2
             Next j
End Sub



Private Sub CHLabel_DblClick(Index As Integer)

       CHShowCombo.ListIndex = Index

End Sub


Private Sub CHRangeCombo_Click()
  Dim chan As Integer

            chan = CHSetCombo.ListIndex
            ChanSet(chan).RangeID = CHRangeCombo.ListIndex
            ChanSet(chan).RangeVal = pSI.range_tab(ChanSet(chan).RangeID)

End Sub



Private Sub CHSetCombo_Click()
     Dim chan As Integer

          chan = CHSetCombo.ListIndex
          CHRangeCombo.ListIndex = ChanSet(chan).RangeID
          CouplingCombo.ListIndex = ChanSet(chan).CoupleID

End Sub
```

```
Private Sub CHShowCombo_Click()

        ad.CurChanID = CHShowCombo.ListIndex
        ad.Color = CHColor(ad.CurChanID)
       If AcqStatus = 0 And ad.Length > 0 Then Call PaintWaveform

End Sub

Private Sub CHTrigCombo_Click()

                Trigger.Mode = CHTrigCombo.ListIndex
                If Trigger.Mode > 1 Then
                      TrigCHCombo.Enabled = True
                      TrigLevel.Enabled = True
                Else
                      TrigCHCombo.Enabled = False
                      TrigLevel.Enabled = False
                End If

End Sub

Private Sub Command2_Click()
      DIOfrm.Show vbModal, Me
End Sub

Private Sub Slider1_Click()

End Sub

Private Sub CouplingCombo_Click()
        Dim chan As Integer

                chan = CHSetCombo.ListIndex
                ChanSet(chan).CoupleID = CouplingCombo.ListIndex
End Sub

Private Sub DelayCombo_Click()

                ad.Delay = Val(DelayCombo.Text)

End Sub

Private Sub ExitCmd_Click()
```

```
            Call AcqCardExit
        Demofrm.Hide
        If d1000_check_done(0) = 0 Or d1000_check_done(1) = 0 Or
d1000_check_done(2) = 0 Then
        'd1000_decel_stop 0
        d1000_decel_stop 0
        d1000_decel_stop 1
        d1000_decel_stop 2
        End If
          d1000_board_close
        End
End Sub

Private Sub Form_Load()
Dim i As Integer

        For i = 0 To 3
        CHColor(i) = CHShape(i).FillColor
          CHColor(i + 4) = CHColor(i)
        Next i
        Call OscInit
          Call AcqCardInitial
    'Cancel As Integer
      Dim nCard As Integer
      d1000_board_close
      nCard = d1000_board_init()
      'If d1000_set_sd(0, 1) Then MsgBox "ok"
If nCard < 1 Then
            MsgBox, vbOKOnly,
Else
    Call d1000_set_pls_outmode(0, 0)
    Call d1000_set_pls_outmode(1, 0)
    Call d1000_set_pls_outmode(2, 0)
End If
End Sub

Private Sub Form_Unload(Cancel As Integer)
            Call AcqCardExit
    If d1000_check_done(0) = 0 Or d1000_check_done(1) = 0 Or
d1000_check_done(2) = 0 Then
    d1000_decel_stop 0
    d1000_decel_stop 1
    d1000_decel_stop 2
    End If
        d1000_board_close
End Sub
```

```
Private Sub LengthCombo_Click()

        ad.Length = Val(LengthCombo.Text)

End Sub

Private Sub LoopAcqCmd_Click()

LoopAcqStatus = 1
nspeedx = Val(Text_nspeedx.Text)
nlongx = Val(Text_nlongx.Text)

nspeedy = Val(Text_nspeedy.Text)
nlongy = Val(Text_nlongy.Text)

nspeedz = Val(Text_nspeedz.Text)
nlongz = Val(Text_nlongz.Text)
Call RunAcq
'tmrRead.Enabled = True



If Check_x.Value = 1 Then

    If (Option_fx = True) Then
    dirx = -1
    End If
    If (Option_zx = True) Then
    dirx = 1
    End If

    If Option_dx = True Then
            d1000_start_s_move 0, nlongx * dirx, 10, nspeedx, 0.1
    End If
    If Option_lx = True Then
            d1000_start_sv_move 0, 10, nspeedx * dirx, 0.1
    End If
  End If

If Check_y.Value = 1 Then

    If (Option_fy = True) Then
    diry = -1
```

```
        End If
        If (Option_zy = True) Then
        diry = 1
        End If

        If Option_dy = True Then
                d1000_start_s_move 1, nlongy * diry, 10, nspeedy, 0.1
        End If
        If Option_ly = True Then
                d1000_start_sv_move 1, 10, nspeedy * diry, 0.1
        End If
    End If

    If Check_z.Value = 1 Then

        If (Option_fz = True) Then
        dirz = -1
        End If
        If (Option_zz = True) Then
        dirz = 1
        End If

        If Option_dz = True Then
                d1000_start_s_move 2, nlongz * dirz, 10, nspeedz, 0.1
        End If
        If Option_lz = True Then
                d1000_start_sv_move 2, 10, nspeedz * dirz, 0.1
        End If
    End If

End Sub

Private Sub RateCombo_click()

         ad.AcqRate = Val(RateCombo.Text)

End Sub

Private Sub SingleAcqCmd_Click()

        LoopAcqStatus = 0
        Call RunAcq

End Sub

Private Sub StopAcqCmd_Click()
```

```
        Call TerminateAcq


If d1000_check_done(0) = 0 Or d1000_check_done(1) = 0 Or d1000_check_done(2)
= 0 Then
    'd1000_decel_stop 0
    d1000_decel_stop 0
    d1000_decel_stop 1
    d1000_decel_stop 2
End If

End Sub

Private Sub Timer1_Timer()

        Dim Ch As Integer, tmp As Integer
        Dim a As Double
    Dim n As Long
    Dim nspeed As Long
    Dim nback As Long
    Dim min As Single
    Dim naxis As Single
    Dim p As Single
                tmp = IDTS_StatusCheck()
                Select Case tmp
                        Case 0:
                                AcqLed.BackColor = vbRed
                                LedLabel.Caption
                        Case 1:
                                AcqLed.BackColor = vbGreen
                                LedLabel.Caption
                        Case &HFF:
                                Timer1.Enabled = False
                                AcqLed.BackColor = &H808080
                                LedLabel.Caption
                                Call PaintWaveform

                                If LoopAcqStatus = 1 Then
                                        Call IDTS_Acq
                                        Call MoveAndRead
                                        Timer1.Enabled = True
                                Else
                                        Call TerminateAcq
                                End If
                        Case -1:
```

```
                MsgBox
            End Select


End Sub



Private Sub TrigCHCombo_Click()

          Trigger.Ch = TrigCHCombo.ListIndex
          TrigLevel.Value = 0
          Call TrigLevel_Change

End Sub

Private Sub TrigLevel_Change()

Dim i As Integer, vr As Single

            vr = TrigLevel.Value / 128# * ChanSet(Trigger.Ch).RangeVal
            Trigger.Level = TrigLevel.Value + 128
            TrgLabel.Caption = Format(vr, "0.000") & "V"

End Sub





Private Sub Command3_Click()
     d1000_set_command_pos 0, 0
     d1000_set_command_pos 1, 0
     d1000_set_command_pos 2, 0
     d1000_set_command_pos 3, 0
End Sub

Private Sub Check_x_Click()
If Check_x.Value = 1 Then
    Frame_fx.Enabled = True
    Frame_mx.Enabled = True
    Text_nspeedx.Enabled = True
    Text_nposx.Enabled = True
 Else
    Frame_fx.Enabled = False
    Frame_mx.Enabled = False
```

```
      Text_nspeedx.Enabled = False
      Text_nposx.Enabled = False
  End If
End Sub


Private Sub Option_dx_Click()
If Option_dx.Value = True Then
      Text_nlongx.Enabled = True
End If
End Sub
Private Sub Option_lx_Click()
If Option_lx.Value = True Then
      Text_nlongx.Enabled = False
End If
End Sub


Private Sub Check_y_Click()
  If Check_y.Value = 1 Then
      Frame_fy.Enabled = True
      Frame_my.Enabled = True
      Text_nspeedy.Enabled = True
      Text_nposy.Enabled = True
Else
      Frame_fy.Enabled = False
    Frame_my.Enabled = False
      Text_nspeedy.Enabled = False
      Text_nposx.Enabled = False
  End If
End Sub
Private Sub Option_dy_Click()
If Option_dy.Value = True Then
      Text_nlongy.Enabled = True
End If
End Sub
Private Sub Option_ly_Click()
If Option_ly.Value = True Then
      Text_nlongy.Enabled = False
End If
End Sub



Private Sub Check_z_Click()
  If Check_z.Value = 1 Then
```

```
      Frame_fz.Enabled = True
      Frame_mz.Enabled = True
      Text_nspeedz.Enabled = True
      Text_nposz.Enabled = True
Else
      Frame_fz.Enabled = False
    Frame_mz.Enabled = False
      Text_nspeedz.Enabled = False
      Text_nposz.Enabled = False
  End If
End Sub
Private Sub Option_dz_Click()
If Option_dz.Value = True Then
      Text_nlongz.Enabled = True
End If
End Sub
Private Sub Option_lz_Click()
If Option_lz.Value = True Then
      Text_nlongz.Enabled = False
End If
End Sub


Private Sub Text_naxis_Change()
Dim naxis As Single
naxis = Val(Text_naxis.Text)

If naxis = 0 Then
    Frame_x.Enabled = False
Else
    Frame_x.Enabled = True
End If

If naxis = 1 Then
    Frame_y.Enabled = False
  ' Frame_u.Enabled = False
Else
    Frame_y.Enabled = True
    'Frame_u.Enabled = True
End If

If naxis = 2 Then
    Frame_z.Enabled = False
Else
    Frame_z.Enabled = True
End If
```

```
'If naxis = 0 Then
'    Frame_v.Enabled = False
'Else
'    Frame_v.Enabled = True
'End If

End Sub
Private Sub Timer2_Timer()
Dim naxis As Single
naxis = Val(Text_naxis.Text)
Text_nposx.Text = Str(d1000_get_command_pos(0))
Text_nposy.Text = Str(d1000_get_command_pos(1))
Text_nposz.Text = Str(d1000_get_command_pos(2))
'Text_nposu.Text = Str(d1000_get_command_pos(2))
'Text_nposv.Text = Str(d1000_get_command_pos(0))
Text_nposcontrol.Text = -Str(d1000_get_command_pos(naxis))
Text_cs.Text = cs
End Sub


Private Sub MoveAndRead() 'Move() 'tmrRead_Timer()
   Dim a As Double
   Dim n As Long
   Dim nspeed As Long
   Dim nback As Long
   Dim min As Single
   Dim naxis As Single
   Dim p As Single
   n = Val(Text_n.Text)
   'j = 0
   'i = 0
   nspeed = Val(Text_ncontrol.Text)
   nback = Val(Text_nback.Text)
   min = Val(Text_nmin.Text)
   naxis = Val(Text_naxis.Text)
   z = Val(Text_l.Text)


   s = -d1000_get_command_pos(naxis)
If s >= z Then
   d1000_decel_stop naxis
Else

   X = X + 1
```

```
  If voltage > 1.5 Then
        vol = vol + voltage
        Y = Y + 1
  End If
  'MsgBox i
  If X = n Then
    If Y = 0 Then
    a = 0
    Else
    a = vol / Y
    End If
    Text1.Text = Format(Y, "###0.0")
    Text2.Text = Format(a, "###0.00")
    X = 0
    vol = 0
    Y = 0

    If a < min Then '
      d1000_start_s_move naxis, nback, 10, BackSpd, 0.1
        Do
        DoEvents
        Loop While (d1000_check_done(naxis) = 0)
        d1000_start_s_move naxis, nback * (-1), 10, BackSpd, 0.1
        Do
        DoEvents
        Loop While (d1000_check_done(naxis) = 0)
        cs = cs + 1
        nspeed = nspeed * (1 - 0.01)
        If nspeed <= 0 Then
            nspeed = Val(Text_ncontrol.Text)
        End If
        Text_ncontrol.Text = CStr(nspeed)
    Else
        d1000_start_sv_move naxis, 1, -nspeed, 0.01
        nspeed = nspeed * (1 + 0.01)
        Text_ncontrol.Text = CStr(nspeed)
        If nspeed > MaxSpdZ Then
            nspeed = MaxSpdZ
        End If

Private Sub OscInit()
  Dim i As Integer, xDis As Integer, yDis As Integer
  Dim Linelength As Integer, Lineheight As Integer

  Linelength = Osc.Width
  Lineheight = Osc.Height
```

```
 xDis = Linelength / 10
 yDis = Lineheight / 6

     For i = 1 To 5
        Load GridLine(i)
        GridLine(i).X1 = 0
        GridLine(i).X2 = Linelength
        GridLine(i).Y1 = yDis * i
        GridLine(i).Y2 = GridLine(i).Y1
        GridLine(i).Visible = True
    Next i

     For i = 1 To 9
        Load GridLine(i + 5)
        GridLine(i + 5).X1 = xDis * i
        GridLine(i + 5).X2 = GridLine(i + 5).X1
        GridLine(i + 5).Y1 = 0
        GridLine(i + 5).Y2 = Lineheight
        GridLine(i + 5).Visible = True
    Next i

End Sub
```